

THÈSE

DE DOCTORAT DE L'UNIVERSITÉ PARIS.DIDEROT (Paris 7)

Spécialité
Champs, Particules, Matière

présenté par

Aion VIANA

pour obtenir le grade de

DOCTEUR EN SCIENCES

**Indirect searches of dark matter,
and the galactic center at very high
energy with H.E.S.S.**

Directeur de thèse : Emmanuel MOULIN

soutenue le 9 juillet 2012

Jury :

George F. SMOOT	(président)
François MONTANET	(rapporteur)
Joseph SILK	(rapporteur)
Pierre-Olivier LAGAGE	(examinateur)
Pascal VINCENT	(examinateur)
Jean-François GLICENSTEIN	(invité)
Didier VILANOVA	(invité)

*For my parents, for Júlia,
and for Heeya.*

Acknowledgements

To begin with, I would like to express my deepest gratitude to my Ph.D thesis advisor, Emmanuel Moulin, who so enthusiastically guided me through this endeavour during the past three years. His encouragement, persistence, and faith in me kept me constantly engaged in my research, and his personal generosity helped make my time at CEA-Saclay very pleasant.

I am very grateful to Ursula Bassler, director of the Particle Physics Division (SPP, *Service de Physique des Particules*) at the Institute of Research into the Fundamental Laws of the Universe (IRFU, *Institut de Recherche sur les lois Fondamentales de l'Univers*) of the CEA, for welcoming me in this laboratory during my Ph.D thesis graduation.

I would like to thank my committee members, George F. Smoot (president of the committee), Pierre-Olivier Lagage, Pascal Vincent, Jean-François Glicenstein and Didier Vilanova for the privilege of having them read my thesis with such interest and for their participation at my Ph.D thesis defense. In particular, I thank François Montanet and Joseph Silk for having accepted to be referees of my manuscript. All their comments and suggestions substantially improved the quality of the manuscript.

I thank the whole H.E.S.S. group at the IRFU, Jean-François Glicenstein, Pierre Brun, Clementina Medina, Bernard Peyaud, Karl Kosack and Denis Wouters, for providing a stimulating and fun environment in which to learn and grow. A special thanks to Jean-François, for all the inspiring and insightful discussions we had, and for his wise advices, as he was always available for my questions and generously gave me his time and vast knowledge.

More generally, I would like to thank the H.E.S.S. collaboration, and in special those physicists I had the opportunity to work and exchange ideas; Werner Hoffmann,

Bernard Degrange, Berrie Giebels, Andreas Zech, Catherine Boisson, Christian Stegmann, Gérard Fontaine, Goetz Heizelmann, Pascal Vincent, Ullrich Schwanke, Agnieszka Jacholkowska and Wilfried Domainko. Also, I wish to thank all the H.E.S.S. Ph.D and post-doc students I had the pleasure to meet all over Europe for the H.E.S.S. collaboration meetings, my special thanks to François Brun, Matteo Cerruti, Hélène Laffon, Jonathan Biteau, Matthieu Vivier, Aldée Charbonnier, Jean-Philippe Lenain, Björn Opitz, Daniil Nekrassov, Fabio Acero, Ryan Chaves and Anna Barnacka.

My appreciation also extends to my laboratory colleagues. A special thank you to my office room-mate, Michael Macaire, and the Ph.D and post-doc students of the SPP, Nicolas, Cecile, Eve, Lea, Flor, Vincent, Laurent, Matthieu, Somnath, Timothee, Jessica, Bruno, Nicolas and Pierre. I really enjoyed the pleasant atmosphere and our long Friday lunches.

For their support, encouragement and companionship, I would like to thank my Brazilian friends for our shared experiences in France during the past six years, Renné, Jambon, Malade, Fou, Jong, João Pedro and Luciana. And also to all the friends I made along the way, too numerous to name here, but equally important.

Above all, I would like to thank my parents and my sister, for their unconditional support and love. For them, I take the liberty to write a little something in Portuguese:

Agradeço enfim, a meus pais e minha irmã por sempre terem me apoiado em todos os meus empreendimentos, e pelo amor incondicional que sempre me deram. Sem vocês não teria chegado aonde estou; segurando o martelinho. Essa tese a vocês também é dedicada.

Lastly, I thank Heeya - this thesis also belongs to you.

Contents

Acknowledgements	ii
Introduction	xi
I Very high energy γ-ray astronomy	1
1 γ-ray emission above 100 GeV	3
1.1 Non-thermal phenomena and γ -ray emission processes	5
1.1.1 Charged particles acceleration	5
1.1.2 γ -ray emission processes	7
1.2 Where to look for very high energy γ -rays?	10
1.2.1 Galactic sources	10
1.2.2 Extragalactic sources	15
2 γ-ray detection techniques	17
2.1 The high-energy domain by satellites	18
2.2 Ground-based Cherenkov telescopes	20
2.2.1 Electromagnetic air showers	21
2.2.2 Hadronic air showers	22
2.2.3 Cherenkov radiation from air showers	22
2.2.4 Extensive air shower arrays	23
2.2.5 The imaging atmospheric Cherenkov technique	25
2.3 IACTs around the world: present and future	28

3	H.E.S.S.: The High Energy Stereoscopic System	31
3.1	The H.E.S.S. experiment	32
3.1.1	The site	32
3.1.2	The telescopes	32
3.1.3	The cameras	35
3.2	Data analysis	37
3.2.1	Data taking	37
3.2.2	Data quality selection	38
3.2.3	γ -ray selection and reconstruction	40
3.2.4	Residual hadronic background estimate	46
3.3	Spectral reconstruction	54
3.3.1	Effective detection area	55
3.3.2	Energy resolution	56
3.3.3	Maximum-likelihood method	57
3.3.4	Systematic errors	61
II	Indirect dark matter searches through gamma-rays	63
4	Cold Dark Matter	65
4.1	Dark Matter cosmology	66
4.1.1	Standard cosmological model	66
4.1.2	Relic density of dark matter	68
4.2	Evidences in the Universe	70
4.2.1	Rotation curves of galaxies	71
4.2.2	Gravitational lensing	72
4.2.3	Primordial Big-Bang Nucleosynthesis	73
4.2.4	CMB observations and the Silk damping	74
4.3	Dark matter density distribution in the Universe	77
4.3.1	Cosmological N-body numerical simulations	77
4.3.2	Distribution in different scales	79
4.4	Dark matter candidates	83
4.4.1	Neutrinos	83
4.4.2	Supersymmetric dark matter	85

4.4.3	Universal extra dimension	86
5	Exclusion and sensitivity limits to dark matter annihilation	91
5.1	γ -ray flux from dark matter annihilation	95
5.2	Dark matter halo modelling	96
5.2.1	Halo profile parameters determination	99
5.2.2	Dark matter halo substructures	103
5.3	γ -ray final spectra	105
5.4	γ -ray flux enhancement effects	106
5.4.1	Radiative correction : Internal Bremsstrahlung	106
5.4.2	Inverse compton process	108
5.4.3	The Sommerfeld effect	112
5.5	Limits on the dark matter annihilation cross section	114
5.5.1	Exclusion limits	115
5.5.2	Sensitivity limits	116
6	Dark matter towards Sculptor and Carina dwarf galaxies	117
	Introduction	118
6.1	H.E.S.S. observations and data analysis	119
6.2	γ -rays flux upper-limits	122
6.3	Dark matter halo modelling	123
6.4	Exclusion limits on the dark matter annihilation cross section	126
6.4.1	Generic case for exclusion limits	126
6.4.2	Enhancement effects for the exclusion limits	129
6.5	Summary and conclusion	133
7	Prospects for the CTA towards dwarf galaxies	137
	Introduction	138
7.1	CTA effective area	138
7.2	The Sagittarius dwarf galaxy	140
7.3	Modelling the Sagittarius dwarf dark matter halo	140
7.4	Exclusion and sensitivity limits to dark matter annihilation cross section	142
7.4.1	Sensitivity calculation and background estimates	142
7.4.2	Upper limits on the dark matter annihilation cross section	143

7.5	Astrophysical background emission	147
7.5.1	Millisecond pulsars in M54	148
7.5.2	Intermediate-Mass Black hole	150
7.6	Sensitivities predictions for Sculptor and Segue 1	150
7.7	Summary and conclusion	152
8	Gamma-rays from the Fornax galaxy cluster	155
	Introduction	156
8.1	Target selection and dark matter content	157
8.1.1	Dark matter in the Fornax galaxy cluster	158
8.1.2	Dark matter halo substructures	160
8.2	Astrophysical non-thermal emission from Fornax	162
8.3	H.E.S.S. observations and data analysis	165
8.3.1	Fornax galaxy cluster observation by H.E.S.S.	165
8.3.2	Data analysis	165
8.4	Gamma-ray flux upper limits	167
8.5	Exclusion limits on dark matter annihilations	168
8.5.1	γ -ray flux enhancements	169
8.5.2	Inverse Compton emission	171
8.5.3	Enhancement from dark matter substructures	173
8.6	Summary and conclusion	173
III	The Galactic Center region	177
9	The Galactic Center inner 500 pc	179
	Introduction	180
9.1	Morphology and main components of the Galactic Center region	180
9.1.1	Central region morphology in radio	180
9.1.2	Central region morphology in X-rays	182
9.1.3	Central molecular zone	186
9.1.4	Sgr A complex	188
9.2	Gamma-ray emissions from the Galactic Center region	197
9.2.1	HESS J1745-290: counterparts and spectrum	197

9.2.2	The diffuse emission from the Galactic Center Ridge	200
10	Analysis of the VHE diffuse emission in the Galactic Center region	203
10.1	Update on the Galactic Center observations	204
10.1.1	Data selection	204
10.1.2	HESS J1745-290 data analysis and spectrum	205
10.2	Subtraction of the diffuse spectral contamination	208
10.2.1	Diffuse emission spectrum	209
10.2.2	A Diffuse model	212
10.2.3	Final spectrum	214
10.2.4	A closer look on the highest energy events	215
10.3	Spectral morphology of the diffuse region	217
10.3.1	Spectral analysis of annular regions around the Galactic Center	218
10.3.2	Systematics uncertainties on the energy cut-off reconstruction	219
10.3.3	Sagittarius B, C and D spectra	220
10.4	Summary and conclusion	221
	General conclusion	225
	List of Figures	227
	List of Tables	233
	References	235

Introduction

Astrophysical observations of very high energy (VHE) γ -rays play a crucial role in the exploration of non-thermal phenomena in the Universe in their most extreme and violent forms. It can also provide unique information about exotic Particle Physics phenomena beyond the Standard Model of Particle Physics, which at even higher energies complements the studies performed at particle accelerators such as the Large Hadron Collider (LHC). For instance, an intense γ -ray production might be expected from the annihilation of non-baryonic dark matter under some circumstances. Indeed, since the discovery that various luminous objects (stars, gas clouds, globular clusters, or entire galaxies) move faster than one would expect if they felt the gravitational attraction of only other visible objects, with the addition of the most recent observations of the cosmic microwave background (CMB) radiation, supernova distance measurements, and large scale galaxy surveys, there are compelling evidences that dark matter exists in the form of non-baryonic and weakly interacting massive particles (WIMPs).

Numerical N-body simulations of hierarchical formation of structures in the Universe suggest that dark matter is distributed as halos surrounding galaxies and galaxy clusters. Observations of dynamical tracers of the gravitational potential of galaxies (and galaxy clusters) also corroborate with the existence of a large amount of dark matter to explain their velocity dispersions. In many Particle Physics models beyond the Standard Model, dark matter particle candidates can self-annihilate in dense environments, and produce γ -rays as a sub-product of the annihilation process. Therefore one of the main goals of γ -ray astronomy is to observe structures in which dark matter is expected to be highly concentrated in order to detect a possible annihilation signal. Historically, the first astrophysical source to be considered as a good candidate possessing a strong dark matter annihilation signal was the Galactic Center. However various observations in radio, microwave, infrared, X-rays and γ -rays in the past decades revealed an enormous

concentration of emissions in almost every waveband coming from the Galactic Center inner region. For instance, the H.E.S.S. array of Cherenkov telescopes detected a very strong γ -ray signal coming from the Galactic Center region, including a point-like source coincident in position with Sgr A* and a region of diffuse radiation (diffuse emission). Although there exist astrophysical scenarios which can explain such emissions, the exact underlying processes are still under debate. In order to disentangle a dark matter annihilation signal from the overall emission of the Galactic Center region, it is crucial to first have a better understanding of the ongoing astrophysical processes in this region. Finally, astronomical objects with low astrophysical γ -ray background, such as the dwarf galaxies satellites of the Milky Way, or galaxy clusters with a low cosmic-ray content, are the most promising targets for searches for γ -rays from dark matter annihilation.

This thesis presents a study on indirect searches of dark matter through VHE γ -rays towards dwarf galaxies and galaxy clusters, and the analysis of the Galactic Center at VHE with the H.E.S.S. instrument. The following manuscript is organized in three parts. **The first part** presents a general introduction to the γ -ray astronomy. The non-thermal phenomena that may lead to the emission of VHE γ -rays, as well as the main γ -ray astrophysical sources are first described in Chapter 1. In Chapter 2, an overview of the γ -ray detection techniques is given. All the data used in this work was collected by the H.E.S.S. array of imaging atmospheric Cherenkov telescopes (IACTs): the instrument and the detection technique are introduced in Chapter 3. In this chapter the data analysis procedure, including methods for the rejection and subtraction of hadronic background and the reconstruction of energy spectra, is described.

The second part is devoted to the study of the indirect searches of dark matter through VHE γ -rays. First, in Chapter 4, an overview on the actual cold dark matter paradigm is given. Chapter 5 presents a detailed description of the methodology developed to extract constraints from γ -ray observations on dark matter astrophysical and particle physics models. Constraints on a dark matter annihilation signal are obtained following this methodology to the H.E.S.S. observations of the Sculptor and Carina dwarf galaxies, which are reported in Chapter 6. In Chapter 7 the sensitivity of the future Cherenkov Telescope Array (CTA) to a dark matter annihilation signal towards the tidal disrupted Sagittarius dwarf galaxy, and the ultra-faint dwarf galaxy Segue 1, are presented. The Chapter 8 reports on the observations in VHE γ -rays of the Fornax galaxy cluster, and constraints on several dark matter properties are derived.

The third and final part of the manuscript addresses the Galactic Center region. A first introductory chapter (Chapter 9) describes in details the structure and morphology of the Galactic Center region at different wavelengths relevant for non-thermal phenomena. In the same chapter, the VHE γ -ray observations of the Galactic Center region, including all the published results from H.E.S.S. and other ground-based Cherenkov telescopes, are summarized and discussed. Chapter 10 presents the analysis of the entire H.E.S.S. data set of the Galactic Center region from 2004 to 2011. The spectra of both the central VHE γ -ray source and the diffuse emission are updated. The spectral subtraction of the diffuse component under the central γ -ray source is performed, allowing to recover the intrinsic spectrum of the central source. A study on the spectral morphology of the whole diffuse emission region in VHE γ -rays is conducted and the results are presented at the end of the chapter.

Part I

Very high energy γ -ray astronomy

Chapter 1

γ -ray emission above 100 GeV

Contents

1.1	Non-thermal phenomena and γ-ray emission processes	5
1.1.1	Charged particles acceleration	5
1.1.2	γ -ray emission processes	7
1.2	Where to look for very high energy γ-rays?	10
1.2.1	Galactic sources	10
1.2.2	Extragalactic sources	15

Introduction

The γ -ray astronomy is intrinsically related to the problem of the origin of cosmic rays (CRs). The history of cosmic rays begins in the early twentieth century when it was realized that electroscopes discharged even if they were kept shielded from natural sources of radioactivity. It was Victor Franz Hess who, in 1912, discovered in balloon ascents that the ionization even increases when going up in the atmosphere. He found that electroscopes discharged twice as fast at 5300 meters altitude than at sea level and attributed this to extraterrestrial radiation of very high penetration power - the cosmic rays (Hess [1] 1912). Today it is well established that an intense flux of charged and neutral cosmic particles exists and arrives isotropically at Earth. Their main constituents are the normal nuclei as in the standard cosmic abundances of matter, with some enhancements for the heavier elements; there are also electrons, positrons and antiprotons. The known spectrum extends over energies from a few tens of MeV to 300 EeV ($= 3 \times 10^{20}$ eV). For most parts the spectrum is well described by a single power law with index -2.7. The cosmic-ray spectrum reveals two distinct features, the *knee* and the *ankle* at $\sim 10^{15}$ eV and $\sim 10^{18}$ eV, respectively. At the knee the spectrum steepens, at the ankle it hardens again. It is generally believed that cosmic rays up to the ankle are of Galactic origin, whereas beyond the ankle they are produced and accelerated outside the Galactic disk.

Nevertheless the exact origin of these CRs is still under debate. The main obstacle is the diffusion of charged particles in the interstellar magnetic fields. Once the cosmic rays are injected into the interstellar medium at the acceleration site, they are deflected by Lorentz forces thereby losing directional information. From the isotropically arriving charged radiation no information about the source direction can be inferred on Earth. For this reason, neutral CR particles, such as γ -rays play a crucial role in the exploration of the CRs origins, since they propagate freely in space from the source without deflection in the interstellar and intergalactic magnetic fields. Generally, the observational γ -ray astronomy can be divided into 5 areas - low (LE: below 50 MeV), high (HE: 50 MeV - 100 GeV), very high (VHE: 100 GeV - 100 TeV), ultra high (UHE: 100 TeV - 100 PeV), and finally extremely high (EHE: above 100 PeV) energies.

This chapter first reviews the non-thermal phenomena that may lead to the emission of VHE γ -rays. The astrophysical γ -ray sources, where non-thermal particle acceleration mechanisms are most likely ongoing, are briefly described.

1.1 Non-thermal phenomena and γ -ray emission processes

The power-law behavior of the energy spectrum of CRs up to extremely high energies indicates that such a radiation originates from non-thermal acceleration processes rather than from black-body radiation of thermal processes. Indeed, the hottest objects observed in the universe emit thermal radiation with energies extending up to the hard X-ray range of ≈ 10 keV. Therefore, any radiation exceeding these energies must be created in non-thermal processes [2]. The production of VHE γ -rays is related to the interaction of highly relativistic charged particles with ambient radiation fields and matter of the interstellar medium. The exact production mechanism depends on the astrophysical conditions and the type of particle which is accelerated (electrons¹ or hadrons).

1.1.1 Charged particles acceleration

Charged particles are accelerated in astrophysical sources mainly by two mechanisms:

- very intense magnetic field, such as in pulsars;
- Fermi acceleration mechanisms;

Fermi particle acceleration (Fermi [3], 1949) is essentially based on the fact the energetic particles (with velocity $v \sim c$) can gain energy by elastically scattering off magnetic turbulence structures or irregularities moving with some velocity \mathbf{u} . Historically it was proposed by E. Fermi in 1949 to explain the origin of CRs as being from Galactic origin. E. Fermi realized that, if interstellar magnetic field disturbances have converging motions, then the CRs have systematic energy gains proportional to the flow velocity difference. This has been called the *first-order Fermi process*. However at that time, it was difficult to figure out whether this kind of process could be so frequent in the interstellar medium to account for the generation of the CR spectrum. Then Fermi devised

¹The term *electron* stands here for both electrons and positrons.

the *second order process* which consists in considering a set of random magnetohydrodynamic disturbances; he was thinking about interstellar clouds. Second order Fermi acceleration thus represents a classical example of a stochastic acceleration process due to many small, nonsystematic energy changes. The average energy gain $\langle \Delta E/E \rangle$ per collision is second order in u/c , i.e.,

$$\frac{\langle \Delta E \rangle}{E} \propto \left(\frac{u}{c}\right)^2, \quad (1.1)$$

when averaged over all momentum directions [2]. Unfortunately the irregular motion of the interstellar clouds u is generally too slow, and thus the second order Fermi is typically not very efficient.

First order Fermi acceleration theories were developed in the 1970's [4, 5, 6, 7], motivated in particular by the fact that acceleration in supernova remnant non-relativistic shocks would be particularly efficient, because the motions are not random. Assuming a strong (non-relativistic) shock wave propagating through the plasma, in the frame of the shock the conservation relations imply that the upstream velocity u_u (ahead of the shock) is much higher than the downstream velocity u_d (behind the shock), so that the two regions may be regarded as two converging flows. Hence, in the upstream rest frame the plasma from the other side of the shock (downstream) is always approaching with velocity $u = u_u - u_d$, so that to first order there are only head-on/approaching collisions for particles crossing the shock front. The acceleration process, although stochastic, thus always leads to a gain in energy, so that for magnetic turbulence structures virtually comoving with the plasma flow, the energy gain at every crossing of the shockwave becomes first order in u/c , i.e.,

$$\frac{\langle \Delta E \rangle}{E} \propto \left(\frac{u}{c}\right). \quad (1.2)$$

The energy spectrum of a population of charged particles accelerated following a Fermi process, with unmodified conditions¹, follows a power-law distribution. The first order Fermi process usually generates a power-law spectrum with spectral index $\gtrsim 2$. The observed values of the spectral indexes coming from supernova remnants are

¹For example, energy losses of the shock wave in first order Fermi acceleration, or non-linear feedback processes might induce a deviation from a power-law behavior in the charged particles energy spectrum.

generally close to this lower-bound value, although energy dependent losses due to the propagation of these CRs in the interstellar medium on large distances might induces softer observed spectrum, with a typical spectral index of ~ 2.7 .

1.1.2 γ -ray emission processes

Synchrotron radiation

Charged particles propagating in an electromagnetic field are deflected by Lorentz forces and loose their energy through synchrotron radiation. The characteristic energy E_{syn} of the synchrotron emission of a charged particle of mass m and energy E propagating in a magnetic field B can be expressed as [8, 9]

$$E_{\text{syn}} = 3\mu_{\text{B}} \left(\frac{E}{mc^2} \right)^2 B \sin \theta, \quad (1.3)$$

where $\mu_{\text{B}} = e\hbar/2m_e$ is the Bohr magneton. Energy losses through synchrotron emission are thus proportional to BE^2m^{-2} .

For instance, in the case of the Crab nebula, electrons are accelerated to energies up to a few PeV (10^{15} eV) in a magnetic field of $100 \mu\text{G}$ ¹. Hence, the typical energy of a emitted synchrotron photon is of the order of a few MeV. In order to produce γ -rays in the TeV energy scale by synchrotron emission in a source like the Crab nebula, electrons would have to be accelerated to energies of the order of tens of PeV. However, due to synchrotron energy losses during the acceleration, such energies cannot be reached [9]. Nevertheless, in the presence of very intense magnetic fields, such as those in the neighborhood of some neutron stars or black holes ($\sim 10^{12}$ G), electrons with energies of only a few GeV could produce γ -rays at the TeV energy range.

Energy losses through synchrotron emission are weaker for more massive particles, like protons or atomic nuclei. In fact, in order to emit γ -rays at the TeV energy range, it would be necessary to accelerate protons up to energies of 10^{16} eV in a magnetic field of the order of 10 G. Thus standard values of magnetic fields in astrophysical γ -ray sources, which are inferior to 10 G, do not allow to explain the TeV γ -ray emission by synchrotron

¹For comparison, the Earth magnetic field is about 0.5 G (Gauss).

losses. On the other hand, most of the radio and X-ray emission of astrophysical objects are explained by these synchrotron processes. In the case of a population of charged particles with an energy spectrum following a power-law distribution $E^{-\alpha}$, the synchrotron energy spectrum also follows a power-law distribution but with a spectral index of $(\alpha + 1)/2$ [10].

Bremsstrahlung

Bremsstrahlung, or “braking radiation”, is an electromagnetic radiation produced by the deceleration of a charged particle when deflected by the Coulomb field of another charged particle, typically an electron by an atomic nucleus. The moving particle loses kinetic energy, which is converted into a photon because energy is conserved. Bremsstrahlung produces a continuous spectrum, which becomes more intense and shifts toward higher frequencies when the energy of the accelerated particles is increased. For instance, a charged particle accelerated to an energy E emits photons with an average energy of $E/3$ [10]. Therefore, electrons and protons with energies at the tens of TeV energy range can produce TeV γ -rays through bremsstrahlung radiation. The efficiency of this process depends on the density of charged particles and nuclei in the propagation environment.

Inverse Compton scattering

Charged particles propagating through radiation fields may lead to a γ -ray emission by Inverse Compton (IC) up-scattering of background photons. The angle-averaged total cross section of IC scattering depends only on the product of the energies of the interacting charged particle E_c and that of the target photons ϵ , $\kappa_0 = E_c\epsilon/m_c^2$, where m_c is the charged particle mass. In the non-relativistic regime, $E_c\epsilon \ll m_c^2$, it approaches the classical Thompson cross section $\sigma_{\text{IC}} \approx \sigma_{\text{T}}(1 - 2\kappa_0)$, while in the ultra-relativistic regime, $E_c\epsilon \gg m_c^2$, it decreases with κ_0 as $\sigma_{\text{IC}} \approx (3/8)\sigma_{\text{T}}\kappa_0^{-1} \ln(4\kappa_0)$. The latter effect (also referred as to the Klein-Nishina cut-off) significantly limits the maximum energy of the up-scattered photon. In the Thompson regime the average energy of the up-scattered photon is $E_\gamma \approx \epsilon E_c^2/m_c^2$. The energy losses of a charged particle due to IC are thus proportional to $N_\epsilon E_c^2 \epsilon m^{-2}$ in the Thompson regime, where

N_ϵ is the target photons density [9, 10].

For a power-law distribution of charged particles, $dN_c/dE_c \propto E_c^{-\alpha}$, the resulting γ -ray energy spectrum in the Thompson regime has a power-law form with a photon index $(\alpha + 1)/2$. In the ultra-relativistic regime, also called the Klein-Nishina regime, the γ -ray spectrum is noticeably steeper, $dN_\gamma/dE_\gamma \propto E_\gamma^{-(\alpha+1)} \ln(\kappa_0 + \text{const})$ [9].

The interaction of relativistic charged particles with radiation fields through IC scattering provides one of the principal γ -ray production processes in astrophysics. It works effectively almost everywhere, from compact objects like pulsars and active galaxy nuclei to extended sources like supernova remnants and galaxy clusters [9]. Because of the universal presence of the 2.7 K cosmic microwave background (CMB) radiation, as well as low gas densities (infrared radiation field) and low magnetic fields (optical radiation fields), IC scattering proceeds with very high efficiency in the intergalactic medium over the entire γ -ray domain. Indeed, electrons with energies of about 100 TeV up-scattering CMB photons can lead to the emission of γ -rays in the TeV energy range. The exact IC scattering calculation is detailed in the Section 5.4.2, in the case of electrons and positrons coming from dark matter particles annihilation, interacting with the CMB radiation field.

π_0 decay

Inelastic collisions of relativistic protons and nuclei with ambient nucleons or radiation (proton-proton and proton-photon reactions) yield pions, kaons and hyperons, that then decay to produce HE photons and leptons [9]. For high proton energies, the probability of creation of the three species of pions (π_0 , π^+ and π^-) is almost the same. The neutral π_0 provide the main channel of conversion of the kinetic energy of protons to γ -rays. The π_0 has a mean lifetime of $t_{\pi_0} = 8.4 \times 10^{-17}$ s and thus immediately decays to two γ -rays (with 98.8% of branching ratio). The decays of charged pions ($t_{\pi^\pm} = 2.6 \times 10^{-8}$ s) lead to muons and neutrinos with spectra quite similar to the spectrum of accompanying π_0 -decay γ -rays. Therefore this process is very interesting, in the sense that a joint detection of neutrinos and γ -rays would be a clear signal that CR acceleration processes

are ongoing in local astrophysical sources. The distinct feature of the spectrum of π_0 -decay γ -rays is a maximum at $E_\gamma = m_\pi/2 \simeq 67.5$ MeV, independent of the energy distribution of π_0 , and consequently of the parent protons.

Dark matter annihilation

The main part of the matter density of the universe consists of an unknown component, called *dark matter*, and only a small fraction consists of baryonic matter (see chapter 4). The dark matter is often described as being composed of *weakly interacting massive particles* (WIMPs). The annihilation of such WIMPs would lead to a flux of particles, among of which γ -rays are of the most interest. Chapter 4 and chapter 5 describe in detail the dark matter paradigm and the dark matter particle annihilation processes leading to γ -ray signals, respectively.

1.2 Where to look for very high energy γ -rays?

The first source to be ever detected in the γ -ray domain was the diffuse Galactic plane emission by the satellite OSO-3 (Clark et al. [11]). It is in fact the most abundant source of high energy γ -ray in the sky, accounting for almost 80% of all the γ -rays detected by the modern satellites, such as the Fermi-LAT (see Section 2.1). The origin of this emission is related to almost all the processes of γ -ray production described in the previous section, when applying them to the interaction of CRs with the matter and the radiation fields in the interstellar medium of the Galaxy. In the VHE γ -ray domain ($\gtrsim 100$ GeV), the first source to be detected was the Crab nebula in 1989 by the Whipple telescope [12]. The most recent catalogues of γ -ray sources contain, in July 2012, about 1873 sources in the GeV energy domain (Nolan et al. [13]) and about 136 sources in the TeV energy domain [14]. These sources can be both from Galactic and extragalactic origin.

1.2.1 Galactic sources

Shell-type supernova remnants

All stars above an original mass of more than $8 M_\odot$ are expected to explode at the end of their life-time, after they have exhausted nuclear burning; the observable effect of such an explosion is called a supernova. A supernova is first categorized as either

a Type I or Type II, then sub-categorized based on more specific traits. Supernovae belonging to the general category Type I lack hydrogen lines in their spectra; in contrast to Type II supernovae which do display lines of hydrogen. The Type I category is sub-divided into Type Ia, Type Ib and Type Ic supernovae. Type Ia supernovae are a particular category of supernovae formed in binary systems, in which a white dwarf accretes matter from a companion until it reaches a mass limit and explodes. This category of supernovae produces consistent peak luminosity because of the uniform mass of white dwarfs that explode via the accretion mechanism. The stability of this value allows these supernovae to be used as standard candles for cosmology to measure the cosmological expansion rate (Hubble parameter), since the observed brightness of the supernovae depends primarily on the distance to their host galaxies. Stars with original masses superior to 8 solar masses produce Type II, Ib, and Ic supernovae.

In Type II supernovae, when the mass of the star inert core exceeds the Chandrasekhar limit of about $1.4 M_{\odot}$, electron degeneracy alone is no longer sufficient to counter gravity. A cataclysmic implosion takes place within seconds, in which the outer core reaches an inward velocity of up to 23% of the speed of light and the inner core reaches temperatures of up to 10^{11} K. The collapse is halted by neutron degeneracy, causing the implosion to bounce outward. The energy of this expanding shock wave is sufficient to detach the surrounding stellar material, forming a supernova explosion. The ejecta material forms the so called shell-type *SuperNova Remnant* (SNR) [9].

When the ejected material meets the interstellar medium a new shock wave is created, which loses energy with time. A γ -ray emission is produced in the interface of the ejecta and the interstellar medium, by proton-proton interactions or inverse Compton scattering of relativistic charged particles accelerated through first-order Fermi processes. H.E.S.S. was the first telescope to have detected a γ -ray emission at the TeV energy range coming from a shell-type SNR. After the initial detection of the shell-type SNR RXJ1713.7-3946 [15](Figure 1.1a), several others SNR detections of TeV γ -rays were reported, such as the SNR RXJ0852.0-4622 [16] (Figure 1.1a), also called Vela Junior, and the SN 1006 [17] which exploded very recently, in the year 1006.

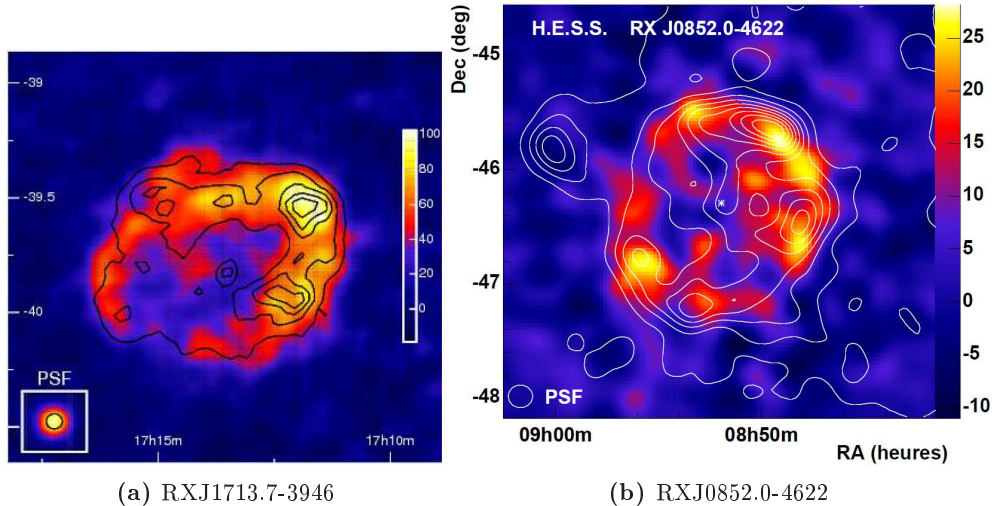


Figure 1.1: Shell-type supernova remnants RXJ1713.7-3946 [15] (a) and RXJ0852.0-4622 [16] (b), detected by H.E.S.S. in 2004 and 2005, respectively. The black (a) and white (b) contours indicates the X-ray morphology of these sources.

Pulsars

In general when the progenitor star is below about $20 M_{\odot}$ the degenerate remnant of a core collapse is a neutron star, with masses between 1 to 2 solar masses. The neutron star retains most of its angular momentum, and since it has only a tiny fraction of its progenitor’s radius (about 10 kilometers), it is formed with very high rotation speed, thus characterizing a so-called *pulsar*. The rotation period of such objects is very short: from a few milliseconds to a few seconds. Pulsars possess a very strong bipolar electromagnetic field (up to 10^{12} G) which is not necessarily aligned along the rotation axis of the neutron star, and thus the magnetic axis spins along with the rotation. Particles are accelerated along the magnetic axis, producing two beams of radiation. The misalignment between the magnetic and rotational axis causes the beam to be seen once for every rotation of the neutron star, which leads to the “pulsed” nature of its appearance. These objects were discovered accidentally in 1967 by Antony Hewish and Jocelyn Bell at Cambridge, from observations at radio wavelength of the pulsar PSR 1919+21. About 1800 pulsars have been observed so far at radio wavelength. At the GeV energy domain, the EGRET satellite observed only 6 pulsars, but recently the Fermi-LAT satellite has increased this number to more than 50 detected pulsars. VHE

γ -rays from pulsars had never been observed until very recently, when a pulsed γ -ray emission from the Crab pulsar was detected by the VERITAS [18] and MAGIC [19] experiments, extending up to at least 400 GeV. Moreover the collective emission of high energy γ -rays from a population of milisecond pulsars in globular clusters has been claimed to be detected by *Fermi-LAT* [20], and the emission in the VHE energy range has been predicted by several models for these objects [see for instance, 21, 22, 23]. Recently the H.E.S.S. telescope has detected a VHE γ -ray emission coming from the direction of globular cluster Terzan 5 [24], which could be explained as coming from the collective emission of milisecond pulsars. Globular clusters could be a new class sources at the VHE regime.

Pulsar wind nebula or plerions

Some pulsars are associated to supernova remnants presenting a very intense synchrotron emission coming from the interior of a nebula. This nebula is powered by strong electron and positron winds coming from the pulsar. The pulsar wind creates a shock wave (distinct from the original supernova shock wave) in the interior of the SNR shell, accelerating electrons to relativistic velocities, and thus producing very high energy γ -rays through IC scattering. A famous example of plerion is the Crab nebula, which was the first TeV source to be detected and it used to serve as prototypical pulsar wind nebula. The Crab nebula had played an important role in γ -ray astronomy because it was believed to have a stable γ -ray flux at time scales superior to year, and thus it was used as reference for calibration of γ -ray detectors. However the stability of the Crab nebula VHE γ -ray emission was challenged very recently with the detection of a γ -ray flare by the Fermi-LAT [25] at the hundreds of MeV energy range, and as already mentioned the detection of the pulsed emission of the Crab central pulsar between 50-400 GeV by IACTs [18, 19]. The multi-wavelength spectrum of the Crab nebula is shown in Figure 1.2. The spectrum was measured from radio to TeV energies. The bump at lower energies, from radio to a few hundreds of MeV, is due to synchrotron emission of electrons, and the IC scattering of the same electrons leads to the second bump at energies from a few GeV to tens of TeV [26].

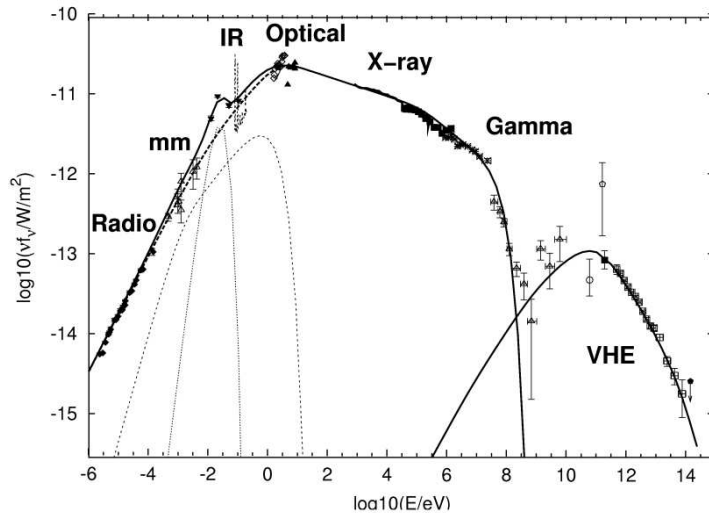


Figure 1.2: Crab nebula emission model. The multiwavelength data is superposed to the model for comparison. The solid line is the model, which is the sum of a synchrotron component (thick dashed), a thermal component (short dashed), and a non-thermal synchrotron component at mm wavelengths (long dashed). Extracted from Ref. [26].

X-ray binaries

Galactic X-ray binaries are binary systems containing a compact object (the primary: a black hole, neutron star, or white dwarf) and a normal star (the secondary). The compact primary accretes matter from a stellar wind of the secondary or by direct mass transfer from the surface of the secondary, if the secondary has expanded so far that matter on a section of its surface becomes gravitationally bound to the primary. Due to angular-momentum conservation, the matter accreting onto the primary settles in an accretion disk, where viscous stresses heat the material to millions of K. At such temperatures, the disk is radiating primarily in X-rays, hence the name “X-ray binaries”. In addition to the thermal X-ray emission which one expects from the standard accretion disk, X-rays binaries are also potential sources of γ -rays. If the primary is a black hole, the binary system is often called microquasar due to its similitude to quasars, and a relativistic jet of particles can emit VHE γ -rays through the interaction of this jet with the secondary photon radiation fields. If the primary is a neutron star, the system might emit through a similar mechanism to the pulsar wind nebula, where in this case a stationary shock wave is formed between the neutron star wind and the secondary wind. The first X-ray binary system to be detected in VHE γ -rays was LS 5039 [27],

showing a periodic emission of 3.907 ± 0.001 days correlated to the orbital period of the system, which was also detected by Fermi-LAT [28] at GeV energies but anti-correlated to the TeV emission. Only three others X-ray binary systems were detected to date (July 212) in the TeV energy domain, which are: LSI + 61-303 [29], PSR B1259-63 [30] and more recently HESS J0632+057 [31].

1.2.2 Extragalactic sources

Active galactic nuclei

Active galactic nuclei (AGN) are the most luminous persistent sources of electromagnetic radiation in the universe. They manifest themselves through extremely luminous emission from the nuclear region of a galaxy, which often extends far into the X-ray and γ -ray bands. The radiation from AGN is believed to be a result of accretion of mass by a supermassive black hole at the center of the host galaxy. In many of these sources, relativistic outflows (jets) are observed which are probably powered by the mass accretion onto the black hole. AGNs detected in the TeV energy domain are generally blazars, for which the angle between the jet and line-of-sight is relatively small. Those blazars are often observable in all wavelength bands - from radio waves to γ -rays-, are rapidly variable, emit polarized, non-thermal optical light, and their total energy output is often dominated by their high-energy emission in X-rays and γ -rays. For instance, H.E.S.S. has observed the active galaxy M 87 [32] and the blazar PKS 2155-304 [33] which revealed strong variabilities in 2005 and 2006, respectively, and for which simultaneous observations at other wavelengths were performed in order to obtain better constraints to the emission models. Also, an impressive multiwavelength monitoring campaign on M 87 followed the first detection of VHE γ -rays and a flare was simultaneously detected in 2010 at VHE γ -rays (by MAGIC, VERITAS and H.E.S.S.), X-rays (by Chandra), and radio (by 43 GHz Very Long Baseline Array, VLBA) [34].

γ -ray bursts

γ -ray bursts (GRBs) are short emissions of γ -rays which can last from ten milliseconds to several minutes, and are very intense in low energy γ -rays (between 100 keV and 1 MeV). The initial burst is usually followed by a longer-lived “afterglow” emitted at longer wavelengths (X-ray, ultraviolet, optical, infrared, microwave and radio) [35].

1. γ -ray emission above 100 GeV

GRBs were first detected in 1967 by the Vela satellites, a series of satellites designed to detect covert nuclear weapons tests. However over 30 years after their discovery, the source of these GRBs is still unidentified. Only in 1997 the BeppoSAX satellite detected the first X-ray afterglows with a rapidly following up by multiwavelength observations [36]. Their redshifts were measured thanks to optical spectroscopy with large ground-based telescopes, showing that GRBs take place at cosmological distances (i.e. gigaparsecs). At these distances GRBs are the most powerful explosions in the Universe. These discoveries, and subsequent studies of the galaxies and supernovae associated with the bursts, clarified the distance and luminosity of GRBs, definitively placing them in distant galaxies and connecting long GRBs with the deaths of massive stars [35]. However, the exact nature of GRB progenitors and the primary mechanism driving GRB explosions are still largely unknown. No GRB has been detected in the VHE γ -ray domain by ground-based Cherenkov telescopes. Nevertheless, recently the Fermi-LAT has detected emissions in the high energy domain (superior to 100 MeV) coming from about ten GRBs, in particular a photon with an energy of $33.4_{-3.5}^{+2.7}$ GeV was detected coming from the GRB 090902B¹ [38].

¹Such high energy photons coming from GRB are useful probes for fundamental Physics studies, such as test of possible Lorentz symmetry invariance violations [37].

Chapter 2

γ -ray detection techniques

Contents

2.1	The high-energy domain by satellites	18
2.2	Ground-based Cherenkov telescopes	20
2.2.1	Electromagnetic air showers	21
2.2.2	Hadronic air showers	22
2.2.3	Cherenkov radiation from air showers	22
2.2.4	Extensive air shower arrays	23
2.2.5	The imaging atmospheric Cherenkov technique	25
2.3	IACTs around the world: present and future	28

2. γ -ray detection techniques

The γ -ray astronomy presents some particular characteristics that distinguish it from other wavelength domains :

- γ -rays from space can not be directly detected on the ground because they get absorbed in the Earth's atmosphere;
- the γ -ray fluxes are very small and decrease rapidly with energy. The spectra follow approximately a power-law over a large energy range, and with a spectral index around -2;
- since the wavelength of γ -rays is of the order of interatomic distances, unlike optical light and X-rays, γ -rays cannot be captured and reflected in mirrors. New techniques were thus developed, inspired by those used in particle physics detectors, in order to detect γ -rays.

Two different detection strategies are used: the first one consists using detectors embarked on satellites for the detection of high energy γ -rays in the range of 10 MeV to 100 GeV, and the second consists in building ground based detectors of the sub-products of the interaction between γ -rays, with energies superior to a few tens of GeV, and the atmosphere. Both strategies are complementary in energy, covering the energy domain from high energy to very high energy γ -rays. In this chapter an overview of the γ -ray detection techniques is done, where an emphasis is given on the imaging atmospheric Cherenkov technique.

2.1 The high-energy domain by satellites

High energy γ -ray detectors embarked on satellites, such as EGRET¹[39], Fermi² (originally called GLAST³, see Figure 2.1b) [40], AGILE⁴ or AMS-02⁵ [41] observe γ -rays from a few MeV to hundreds of GeV. They are composed by several particle physics sub-detectors, namely a particle tracking detector, an electromagnetic calorimeter and

¹EGRET : Energetic Gamma Ray Experiment Telescope

²Fermi : Fermi Gamma Ray Space Telescope

³GLAST : Gamma-Ray Large Area Space Telescope

⁴AGILE : Astro-rivelatore Gamma a Immagini LEggero is a small satellite launched in 2007, operating in the energy band of 30 MeV - 30 GeV

⁵Alpha Magnetic Spectrometer is a charged particles detector for the cosmic ray flux measurements. It also detects γ -rays in the energy band of 10-300 GeV.

an anticoincidence detector (see Figure 2.1a).

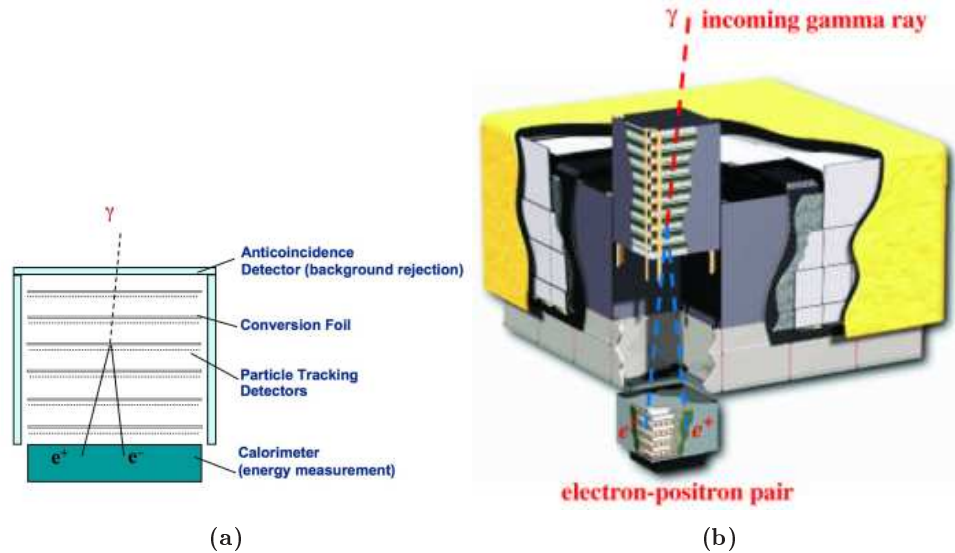


Figure 2.1: (a) Schematic view of a γ -ray detector embarked in satellites. (b) Cutaway view of the Fermi-LAT instrument [40].

The **anticoincidence detector** is made of a scintillating material, normally placed around the tracking detector forming an active veto. Incoming γ -rays pass freely through the anticoincidence detector, while charged cosmic rays cause a flash of light, allowing efficient identification of the relatively rare γ -rays, which have a flux 10^5 less intense than the charged CRs. The **tracking detector** consists of several layers of a dense material that converts an incoming γ -ray into pairs of electrons and positrons (e^-/e^+). Between these layers, detectors of charged particles are placed, allowing the progress of the particles to be tracked, and thus the direction of the γ -ray to be reconstructed. The tracking detector of EGRET was a spark chamber consisting of many plates of metal and gases such as helium or neon, which significantly limited the performances of EGRET, specially in terms of dead time of the system. The tracking detectors of Fermi, AGILE and AMS-02 are silicon strip detectors which have better performances than spark chambers. Finally the charged particles are stopped by a thick **electromagnetic calorimeter** which measures the total energy deposit. The information from the anticoincidence detector, tracker and calorimeter is combined to estimate

2. γ -ray detection techniques

the energy and direction of the γ -ray.

Instrument	EGRET (1991-200)	Fermi-LAT (2008-...)
Energy range	30 MeV - 30 GeV	100 MeV- 300 GeV
Angular resolution/ γ	5.5° (100 MeV) 0.5° (5 GeV)	3.5° (100 MeV) 0.12° (10 GeV)
Energy resolution	20-25%	~ 10%
Effective area	10 ³ cm ²	10 ⁴ cm ²
Field of view	0.6 sr	2.4 sr
Sensitivity	5.4×10 ⁻⁸ cm ⁻² s ⁻¹ (E ≥ 100 MeV) 1.2×10 ⁻⁸ cm ⁻² s ⁻¹ (E ≥ 1 GeV)	1.5×10 ⁻⁹ cm ⁻² s ⁻¹ (E ≥ 100 MeV) 1.5×10 ⁻⁹ cm ⁻² s ⁻¹ (E ≥ 1 GeV)
Dead time	0.1 s	100 μ s

Table 2.1: Performances comparison between EGRET [39] and Fermi-LAT [40].

Table 2.1 compares the performances of EGRET and Fermi Large Area Telescope (Fermi-LAT)¹. These two experiments represent the old and the new generation of space telescopes for the detection of high energy γ -rays. At the end of EGRET mission and after nine years of service, about 271 sources were detected, of which 170 were unidentified. The first Fermi-LAT catalog [42], after only 11 months of data taking, contains 1451 sources detected and characterized in the 100 MeV to 100 GeV range. A second Fermi-LAT catalog [13] has recently been released after 24 months of activity, and it contains 1873 detected sources, of which 127 as being firmly identified and 1170 as being reliably associated with counterparts of known or likely γ -ray-producing source classes.

2.2 Ground-based Cherenkov telescopes

The direct detection of cosmic γ -rays by satellite experiments can observe γ -rays up to about 100 GeV, but due to a strongly decreasing flux of CRs with energy, their detection area, typically of the order of 1 m², is not sufficient for detection of particles with even higher energies. Therefore, for higher energies, indirect measurements by means of the Earth's atmosphere as calorimeter are required. Whenever a high-energy

¹The Fermi Gamma Ray Space Telescope is composed of two instruments: a main Large Area Telescope (LAT), which provides sensitivity to γ -rays in the energy range of about 20 MeV to about 300 GeV, and a detector of transient sources, the Gamma-ray Burst Monitor (GBM) which is sensitive to X-rays and γ -rays with energies between 8 keV and 40 MeV.

cosmic-ray nucleus or γ -ray hits the top of the terrestrial atmosphere it sets off a cascade of secondary particles, produced in interactions of the primary particle and in turn of the secondary particles with molecules and atoms in air. The cascade is called an *air shower*. It can have two different components depending on the type of the primary particle. In case of a photon or an electron a shower of electromagnetic nature is initiated¹. In case of proton and nucleus, like for the overwhelming part of the cosmic rays, interactions via the strong and the weak force will occur beside the electromagnetic processes, and hadronic, as well as electromagnetic, sub-showers evolve. Two different methods can be used to detect the passage of an air shower: one can look for the charged particles in the shower directly through extensive air shower arrays (EAS arrays), or one can look for the Cherenkov light generated by the charged particles in the atmosphere through imaging atmospheric Cherenkov telescopes (IACTs). Thus in the energy range between ~ 100 GeV and ~ 100 TeV, indirect detection is carried out by ground based telescopes. The detection area of such instruments exceeds the detection area of satellite experiments by up to six orders of magnitude, thus accounting for the decreasing flux of very high-energy particles.

2.2.1 Electromagnetic air showers

High energy electrons and photons penetrating in the atmosphere generate an electromagnetic air shower. In case of a photon, the interaction with the Coulomb electromagnetic field of an air nuclei leads to an electron-positron (e^\mp) pair creation, occurring after the traversed mean free path of $7/9X_0$, with $X_0 = 37.2 \text{ g cm}^{-2}$ being the radiation length for electrons, whereas the interaction of an incoming electron with an air nuclei leads to irradiations of an energetic photon due to bremsstrahlung process. These two processes are responsible for a subsequent exponential rise of the particle number during the shower development, until the mean energy of particles drops below 80 MeV and energy losses due to ionization start to become dominant. The shower has reached its maximum particle number at this stage, no new particles will be created any more. The trajectories of the created particles remain close to the direction of the incident one, however due to multiple Coulomb-scattering of created

¹Note that for UHE and EHE photons a hadronic component in the shower cannot be excluded, due to photonuclear processes.

e^\pm -pairs electromagnetic showers get a certain lateral extent, which is, however, small compared to its longitudinal extent which accounts to several kilometers, as it can be seen in Figure 2.2. Electromagnetic showers initiated by γ -rays with energies between 100 GeV and 1 TeV reach their maximum development at an altitude of about 10 kilometers, with a lateral extension of about 50 meters.

2.2.2 Hadronic air showers

Although the development of hadronic air showers is similar to that of electromagnetic ones, since its constituent quarks also undergo strong interactions, both types differ significantly in some aspects. For a hadronic shower, the dominant process for creation of secondary particles is hadronization, in which further hadronic particles like mesons and baryons are produced. Due to meson decays into leptons and photons, the induced air shower has three components, an electromagnetic, a hadronic and a leptonic component. The mass of particles, created in strong interactions, is much higher than the mass of electrons, thus the electrons receive higher transverse momenta by inelastic scattering resulting in a much larger lateral extension of hadronic showers, compared to the electromagnetic one (see Figure 2.2 (a) and (b)). Besides, complex multi-particle processes in contrast to the dominant three-particle processes in electromagnetic showers cause larger fluctuations in hadronic showers and make them less regular, while for electromagnetic showers mainly three-particle processes play a role, as explained above. Moreover, a part of the energy of a hadronic shower is carried away by muons and neutrinos, created in charged mesons decay, whereas the energy of electromagnetic showers mostly remains in its constituent particles. These different characteristics affect the properties of the subsequently produced Cherenkov radiation, which is discussed in the following.

2.2.3 Cherenkov radiation from air showers

Most secondary particles of extensive air showers have high-relativistic energies. Thus, charged shower particles will move with a velocity larger than the local phase velocity of light and emit Cherenkov radiation. The opening angle θ of the radiation cone, with respect to the propagation direction, depends on the air refraction index, $n(\lambda)$ (λ is

the radiation wavelength), and it can be calculated as:

$$\cos \theta = \frac{c}{n(\lambda)v} \sim \frac{1}{n(\lambda)} \text{ for } v \sim c, \quad (2.1)$$

where v is the velocity of the particle. At an altitude of about 10 km in the air, $\theta \approx 1 - 2^\circ$. The energy threshold of production of Cherenkov light is defined as the energy for which the velocity of the particle becomes similar to that of the light in the air. For electrons, such threshold varies between 20 and 40 MeV during the shower development. This value is very close to the critical energy where energy losses due to ionization start to become dominant, thus the e^\pm with these energies almost do not emit Cherenkov radiation.

At observation level the light cones emitted by electrons in different heights superimpose resulting in an almost homogeneous light distribution in a circle with radius between 80 m and 150 m (in case of an electromagnetic shower) around the shower axis. The Cherenkov photons arrive within a very short time interval of the order of 10 nanoseconds. If all the particles emitting Cherenkov light would move parallel and close to the shower axis, there would be no light outside the maximum radius. However, due to multiple scattering (as mentioned above), the light distribution is smeared out. This can be seen in Figure 2.2 which compares distribution of light on the ground for a simulated electromagnetic (c) and hadronic shower (d). One can see the smearing effect for the electromagnetic shower, also the distinct circle of the maximum radius is visible. In contrast to that stands the image for the hadronic case which exhibits heterogeneous, asymmetric structures reflecting the differences in the shower development as described above. Faint circles originating from the various electromagnetic sub-showers occur. The total number of Cherenkov photons reaching the ground amounts to 100 photons per m^2 for a 1 TeV γ -ray. Such a low number of photons makes a large collecting area and fast electronics required for the detection of Cherenkov light from particle cascades in the atmosphere.

2.2.4 Extensive air shower arrays

One way to measure air showers is to deploy an array of particle counters on the ground and directly observe the charged particles in the shower once they reach ground level. They are called Extensive Air Shower arrays (EAS arrays). Traditionally an air

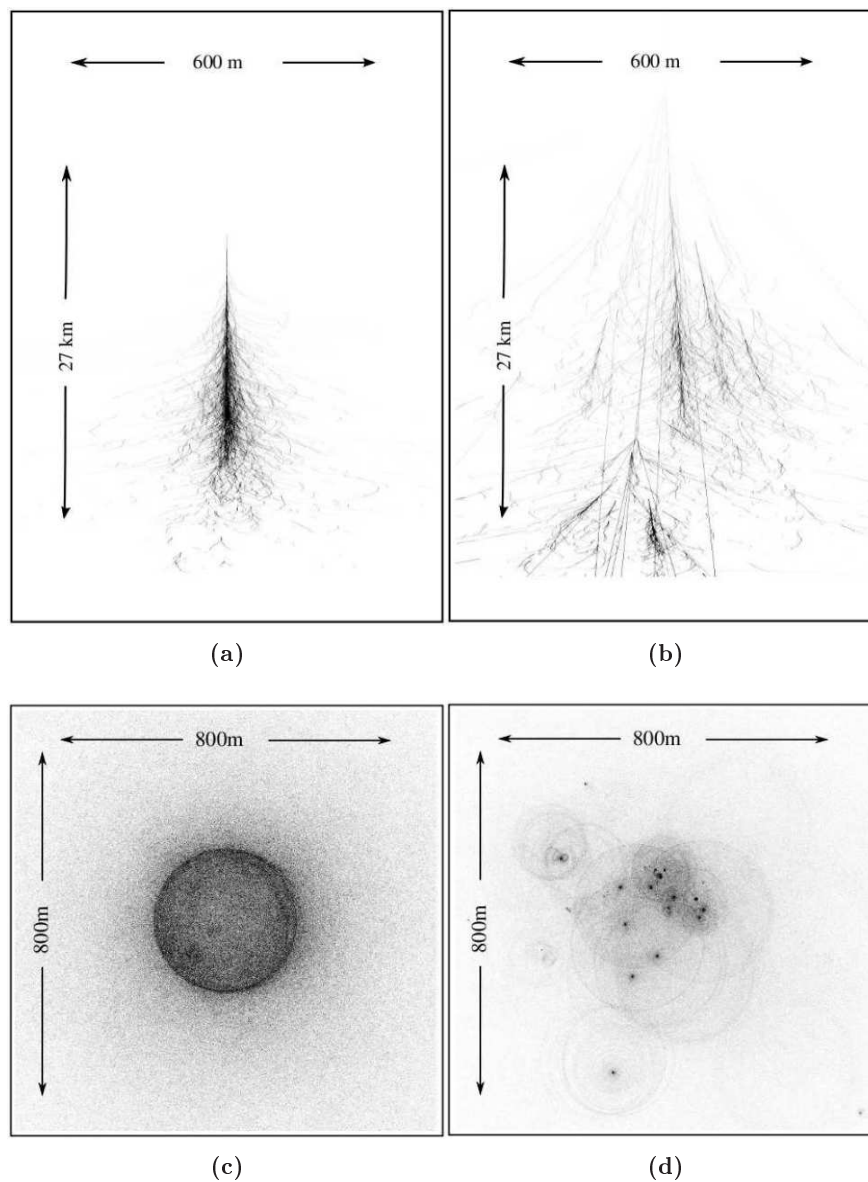


Figure 2.2: Comparison between shower shapes induced by a γ -ray (a) and by a proton (b). The distribution of Cherenkov light on the ground, emitted by relativistic shower constituents, images the shape of the shower, yielding a regular circular shape for γ -rays (c), while Cherenkov light from a proton shower has a rather disperse distribution (d), where the sub-shower are clearly seen. Credits to Konrad Bernlöhner.

shower array is composed of a sparse array of plastic scintillators which emit a short burst of UV light when they are penetrated by a charged particle. However, they are

very inefficient detectors of the γ -rays in the air showers. The main challenges of the EAS approach are the rejection of the CR background and directional and energy reconstruction using the exponentially decreasing tail of particles detected well beyond the shower maximum. Because the scintillators cover less than 1% of the total area of the array, traditional EAS arrays have rather high energy thresholds, and high altitudes are therefore critical to achieve low (< 1 TeV) thresholds with such instruments.

Alternatively, the particle detectors can be tanks full of water. When particles from the shower pass through the water they emit Cherenkov light, which are then detected by photomultipliers placed around the tanks of water. Such arrays are called water Cherenkov detectors. Unlike IACTs, EAS arrays can operate under all conditions, night or day, and they have a very wide (~ 1 steradian) field of view. By using buried counters they can detect the muons in air showers generated by cosmic-ray nuclei, the rejection of the hadronic background is based on the muon content of showers and/or the distribution of shower particles on the ground. However, this method of distinguishing between γ -rays and nuclear cosmic rays is not as efficient as the imaging method used by IACTs. The most recent generation of EAS array observing in the TeV energy domain includes the ARGO-YBJ [43] and the Milagro [44] experiments. Milagro achieves its best background rejection power and sensitivity in the regime above 10 TeV. The next generation consists on the High-Altitude Water Cherenkov Observatory [45], or HAWC, which is currently under construction and will be sensitive to γ -rays from 100 GeV to 100 TeV, and the Large High Altitude Air Shower Observatory (LHAASO [46]), which is in its preparatory phase and it is projected to be sensitive to γ -rays from 30 GeV and 100 TeV.

2.2.5 The imaging atmospheric Cherenkov technique

Cherenkov light, emitted by constituents of a particle cascade, carries information about properties of the primary particle, i.e. its type, energy and incident direction. In order to determine these characteristics with sufficient precision, telescopes with mirror areas of the order of ~ 100 m² are placed on the ground to collect the Cherenkov photons. These are subsequently reflected onto a camera, that is sensitive and fast enough to be able to detect such weak Cherenkov flashes of about 10 ns duration. Such cameras are comprised of highly sensitive photo-multiplier

2. γ -ray detection techniques

tubes (PMTs), which are capable to provide the required sensitivity and time resolution.

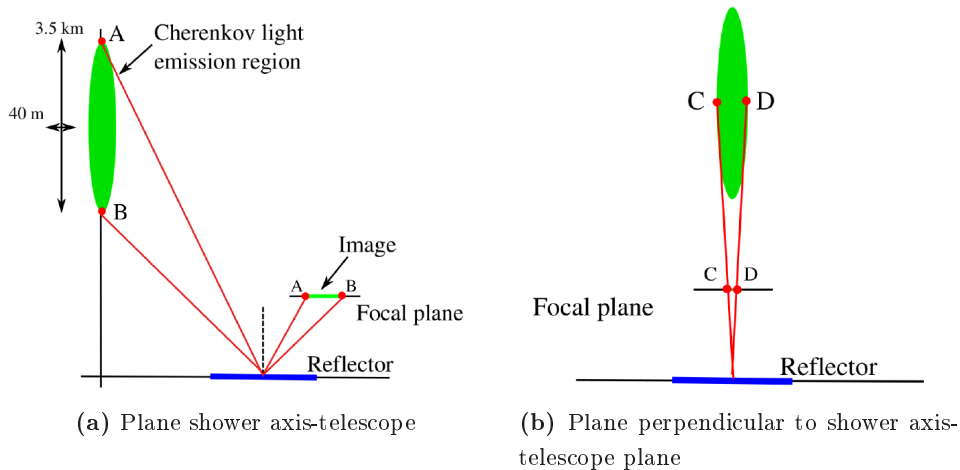


Figure 2.3: Illustration of the imaging principle used in IACTs: The longitudinal extension of the shower defines the length of the image in a Cherenkov camera, while its latitude extent defines its width. The angle between the shower and the axis defines the position of the shower image in the camera plane. Image taken from [47].

Figure 2.3 shows a sketch which explains the shape of the light distribution in a Cherenkov camera. It is evident, that the resulting image on the camera is a two-dimensional projection of the corresponding particle shower. Its shape is ellipsoidal and thus characterized by the long (major) and short (minor) axes. The size of the major axis, also called the length of the image, is determined by the angle between the observation position and the shower direction, while the size of the minor axis (width of the shower) is determined by the lateral extension of the particle cascade. As described above, electromagnetic showers have a smaller lateral extent, compared with hadronic ones, hence usually images from hadronic showers have a larger width, in this way offering a selection criterium for the rejection of the hadronic background. Figure 2.4 presents real images from the H.E.S.S. cameras. The γ -ray events on top have a clear line shape, while the events on the bottom are more diffuse and extended, which are typical of hadronic showers. The image on bottom right shows a signature of local muons which have a narrow Cherenkov light cone. These muons are created in sub-showers from hadronic origin, and trigger only a single telescope with a ring-like

shape.

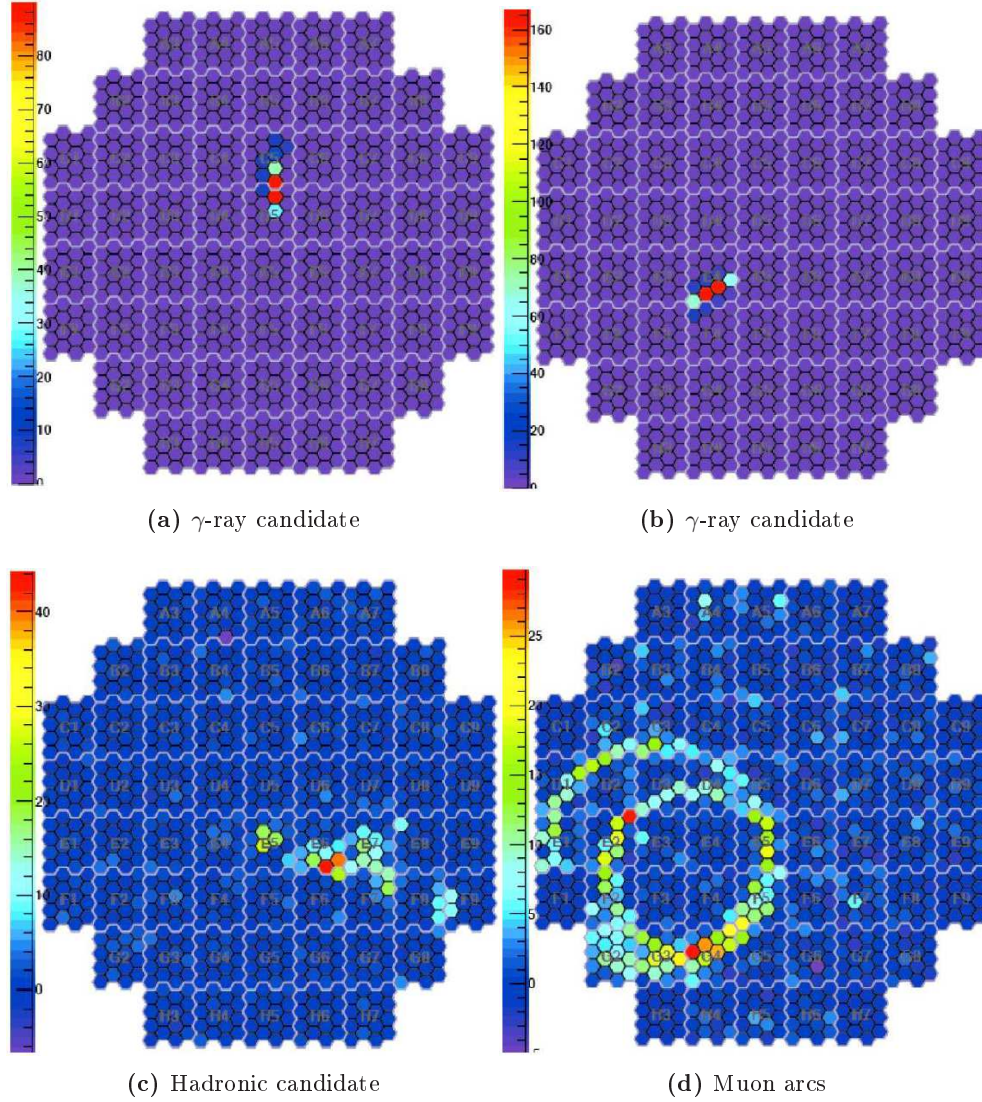


Figure 2.4: Examples of air showers images observed in the H.E.S.S. cameras. In (a) and (b) two images of showers initiated by γ -ray candidates. In (c) an image of a probable hadronic shower. In (d) an image of two muon arcs, related to hadronic showers. The color scale represents the number of photo-electrons in the camera pixels. Image taken from Ref. [48].

The major axis of a shower image in the camera points towards the incident direction of the primary particle, which can in principle be reconstructed by a single

telescope. However, operating multiple telescopes proved to improve the performance concerning the direction reconstruction. Moreover, the irregular shape of hadronic showers leads to deviating images between individual telescopes, yielding an improved background rejection potential for a multiple-telescope array.

2.3 IACTs around the world: present and future

The IACT technique was pioneered by the Whipple collaboration [12] which was the first to detect a source of VHE γ -rays with this technique, the Crab nebula, in 1989. The HEGRA collaboration [49] took the next step in 1996 with the installation of an array of 5 Cherenkov telescopes to perform stereoscopic observations of air showers. This approach of simultaneous observations with more than one telescope has different advantages: the trigger threshold of the system can be lowered since a trigger coincidence of multiple telescopes can be required which drastically reduces random triggers of night-sky background (NSB) light and single-telescope triggers by local muons. As a result the telescopes can be operated with reduced energy thresholds. Another advantage of having multiple views of the same air shower is that the amount of information is increased which improves the reconstruction of the shower geometry (and thereby the direction of the primary) and of the primary energy. Finally, viewing the shower from different sides improves the rejection of the dominant background, hadronic cosmic rays, given that on average γ -ray induced showers are much more regular and symmetric than cosmic-ray showers. All of the experiments of the current generation of IACT experiments, H.E.S.S. [50], MAGIC [51], VERITAS [52], and CANGAROO-III [53], take or plan to take the stereoscopic approach, aiming at energy thresholds¹ of 50 GeV to 100 GeV. The main characteristics of these experiments are described in Table 2.2. The H.E.S.S. array of telescopes is presented in detail in the next chapter (Chapter 2).

¹The “energy threshold” of a detection system is usually quoted as the energy of the maximum of the Crab nebula spectrum multiplied by the effective area of the instrument. It typically defines the transition region between the steeply rising part and the nearly constant part of the acceptance. However, it is important to notice that individual events may be detected at energies well below this energy threshold definition.

2.3 IACTs around the world: present and future

Instrument	Site	Alt. [m]	N_{tel}	S_{tel} [m ²]	S_{tot} [m ²]	N_{pix}	FoV [°]	E_{th} [TeV]
H.E.S.S.	Namibia (S)	1800	4	107	428	960	5	0.1
VERITAS	Mont Hopkins (N)	1275	4	106	424	299	3.5	0.1
MAGIC	La Palma (N)	2225	2	234	468	574	3.5	0.06
CANGAROO-III	Woomera (S)	160	4	57	230	427	4	0.4
Whipple	Mont Hopkins (N)	2300	1	75	75	379	2.3	0.3
HEGRA	La Palma (N)	2200	5	9	43	271	4.3	0.5
CAT ¹	Targassone (N)	1650	1	18	18	600	4.8	0.25

Table 2.2: Comparative table of different IACTs. The first four lines are the current generation of IACTs, while the three last are the old generation of IACTs. The first column gives the experiment name. The second column gives the site of construction with the hemisphere in parenthesis. The third column shows the altitude of the site. N_{tel} , S_{tel} and S_{tot} are the number of telescopes in the array, the surface of each telescope, and the total surface of the array, respectively. N_{pix} indicates the number of pixels in the camera. FoV is the total field of view on a fixed position in the sky. E_{th} is the typical instrument energy threshold for observations at zenith.

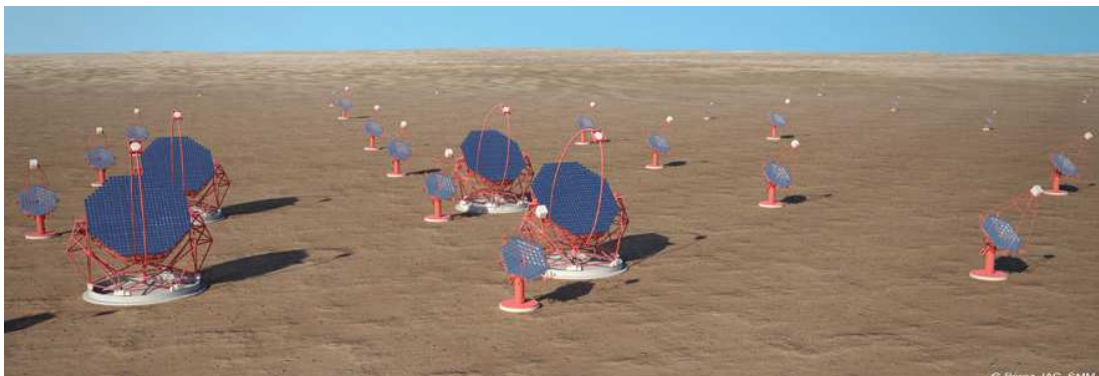


Figure 2.5: Artistic view of the Cherenkov Telescope Array (CTA). Credits to G. Perez.

In the very near future (Summer 2012) the H.E.S.S. telescope array will enter in its second phase. A fifth large telescope is under construction in the center of the H.E.S.S. array, which will not only increase the sensitivity in the currently accessible energy regime, but will in addition lower the energy threshold of the system down to ~ 30 GeV. In the long run, the plan for the next generation of IACTs, the Cherenkov Telescope Array (CTA, 2010), involves building two large arrays (see Figure 2.5), one in each hemisphere, with an order of magnitude more telescopes than current instruments. This future instrument is expected to increase the flux sensitivity by a factor of 10

2. γ -ray detection techniques

compared to current instruments, and enlarge the accessible energy range both towards the lower and higher energies, from ~ 10 GeV to ~ 100 TeV. Based on the current CTA design study, a factor of about ten in effective area, and a factor of two better in hadron rejection and angular resolution are expected. The flux sensitivity as function of the energy of the current and future IACTs is compared with the space telescopes in Figure 2.6.

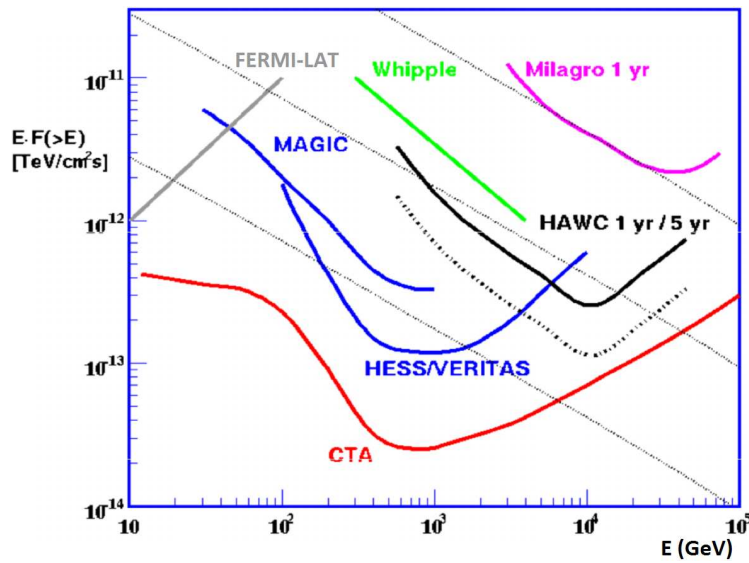


Figure 2.6: Sensitivity as function of the energy of current and future IACTs. Also for comparison, the sensitivities of the Fermi-LAT satellite and EAS arrays (Milagro and the upcoming HAWC) are plotted.

¹CAT : Cherenkov Array at Themis [55]. French IACT experiment started in 1996 detecting and identifying very high energy γ -rays in the range 200 GeV - 20 TeV.

Chapter 3

H.E.S.S.: The High Energy Stereoscopic System

Contents

3.1	The H.E.S.S. experiment	32
3.1.1	The site	32
3.1.2	The telescopes	32
3.1.3	The cameras	35
3.2	Data analysis	37
3.2.1	Data taking	37
3.2.2	Data quality selection	38
3.2.3	γ -ray selection and reconstruction	40
3.2.4	Residual hadronic background estimate	46
3.3	Spectral reconstruction	54
3.3.1	Effective detection area	55
3.3.2	Energy resolution	56
3.3.3	Maximum-likelihood method	57
3.3.4	Systematic errors	61

3. H.E.S.S.: The High Energy Stereoscopic System

The High Energy Stereoscopic System (H.E.S.S.)[\[50\]](#) consists of four identical imaging atmospheric Cherenkov telescopes, designed for observations of astrophysical sources emitting VHE γ -ray radiation in the energy range between ~ 100 GeV and ~ 100 TeV. This chapter describes in detail the H.E.S.S. telescope array. The first section describes the H.E.S.S. experiment, where details about the telescopes and cameras are given. The data taking and analysis are described in the second section. The spectral reconstruction procedure is detailed in the last section.

3.1 The H.E.S.S. experiment

The first H.E.S.S. observations were conducted in summer 2002, when the construction of the first telescope was completed. From December 2003 on, observations have been carried out with the completed 4-telescope array. A fifth telescope is being placed in the center of the array for the second phase of the H.E.S.S. experiment, H.E.S.S.-II. The new telescope consists of a 28m-diameter dish, equipped with almost 600 m² of mirrors. The telescope structure is under construction, with the mount and dish structure already on site. The drive systems are ready, as well as the entire set of mirror facets. The camera is on site and is being mounted [\[50\]](#). (see [Figure 3.1](#)).

3.1.1 The site

The H.E.S.S. array is located in the Khomas Highland of Namibia ($23^{\circ}16'18''$ South, $16^{\circ}30'00''$ East) at an altitude of 1800 m above sea level. The site was chosen due to its excellent astronomic conditions, in particular a cloudless sky is present for $\sim 54\%$ of all moonless nights and the humidity hardly reaches 90% for almost all nights, thus enabling safe operation of electronic equipment. Besides, the location in the southern hemisphere allows observations of the most part of the Milky Way, including the Galactic disk and Galactic Center regions (see [Chapter 10](#)).

3.1.2 The telescopes

The four identically designed IACTs of the H.E.S.S. I array are placed on a square of 120 m side length. The geometrical configuration of the array was determined in order

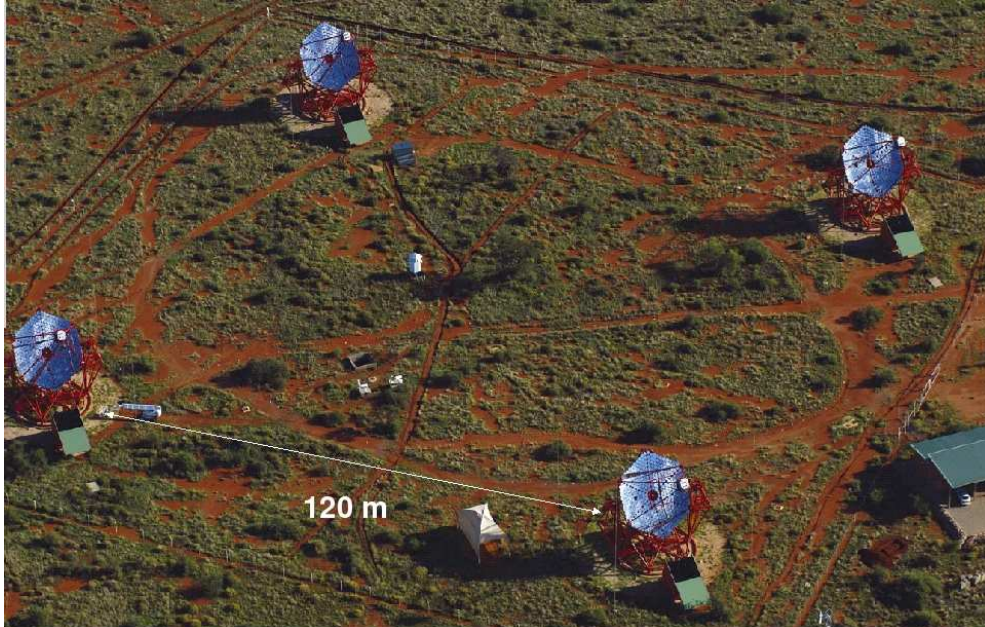


Figure 3.1: Aerial view of the H.E.S.S. telescope array, located in the Khomas Highland of Namibia at an altitude of 1800 m above sea level. The four identically designed telescopes are placed on a square of 120m side length.

to:

- **maximize the number of collected photons**, since as already mentioned before (see Section 2.2), at 1800 m of altitude, the radius of the Cherenkov light pool from electromagnetic showers on the ground extends up to ~ 120 m;
- **optimize the stereoscopic trigger conditions**. A minimum trigger condition that at least two telescopes trigger at a given time window (see more details about the trigger in the paragraph 3.1.3) is applied. The separation between two telescopes for which the effective detection area of γ -rays with energies above 100 GeV is maximum is about 100 m;
- **optimize the muon background rejection**. Indeed, a 100 m separation between telescope allows to minimize the probability that a muon event trigger several telescopes at the same time.

Each of the telescopes consists of a mirror dish of 13 m in diameter, its support structure and a camera. On each dish, 382 spherical mirrors are arranged in a

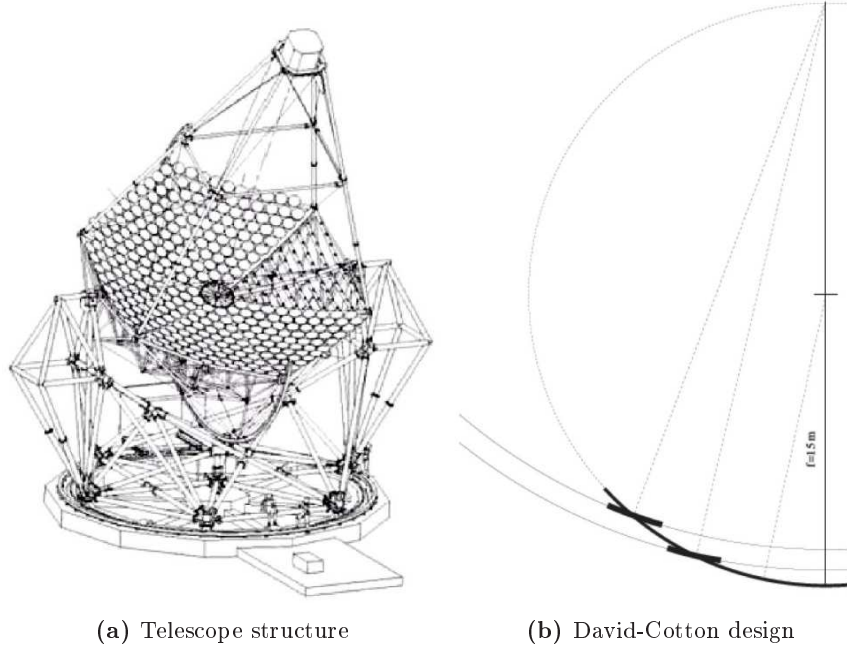


Figure 3.2: H.E.S.S. telescope structure and the David-Cotton design principle for the mirrors arrangement. Taken from Ref [56].

Davies-Cotton design [57] with a total mirror area of $\sim 107 \text{ m}^2$ and a focal length of 15.2 m (see Figure 3.2). At the peak of the Cherenkov light on the ground, at wavelength $\sim 330 \text{ nm}$, the reflectivity of the mirrors accounts to 80%. The optical point spread function (PSF) is found after alignment of individual mirror, and it usually defines the angular resolution after analysis [58]. The PSF of one of H.E.S.S. telescopes is represented in Figure 3.3a. Different quantities are used to quantify its width. These include the rms (root-mean-square) width σ_{proj} of the projected distributions on a given axis (radial or tangential), and the radius r_{80} of a circle around the center of gravity of the image, containing 80% of the total intensity. Figure 3.3b shows the measured width of the PSF as function of the angular distance to the optical axis. It lies between 0.25 mrad on-axis and 1.8 mrad at the edge of the field of view [58].

The rotation of the telescopes in azimuth direction is performed on a circular steel rail of 13.6 m in diameter, while rotation in altitude is done by friction drive systems acting on altitude rails at $\approx 7 \text{ m}$ radius from the axes, with a maximum rotation

velocity of $100^\circ/\text{min}$ in both directions. The total weight of the dish and its support structure is ~ 60 t, ensuring a sufficient rigidity of the telescope. The pointing of each telescope is monitored by two optical CCD cameras, and with all systems in use, the pointing accuracy of the H.E.S.S. array can be reduced from $28''$, being the standard pointing accuracy, to $9''$ for selected strong sources [see, for instance, 59].

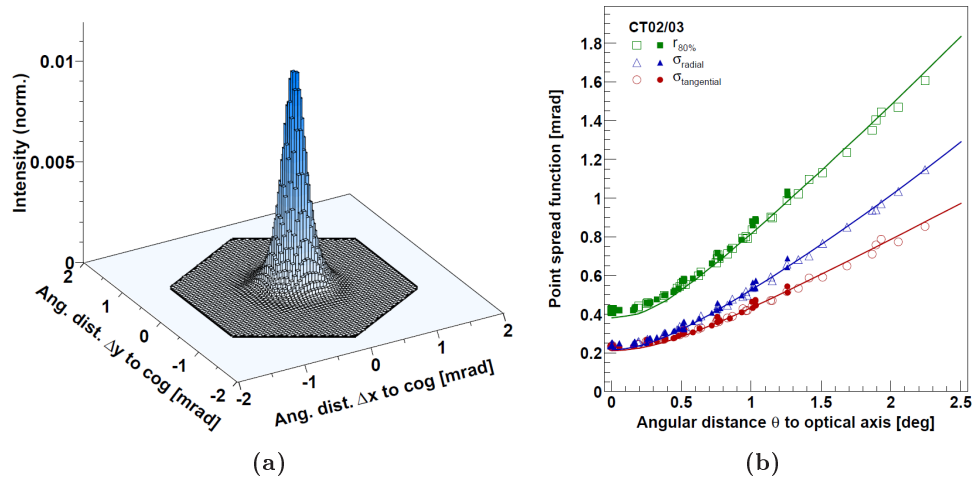


Figure 3.3: (a) Representation of the point spread function of a point-like source. This corresponds to the image of a star on the camera of the telescope CT3 of H.E.S.S.. The boxes correspond to the camera CCD pixels. (b) Width of the point spread function as function of the angular distance θ to the optical axis. Different measures of the width are shown (see text for details). Full symbols represent the CT3 telescope and open circles the CT2 telescope of H.E.S.S.. Extracted from Ref. [58].

3.1.3 The cameras

General description

The H.E.S.S. cameras were conceived for detection of short and weak Cherenkov light flashes [60]. Thus several criteria had to be fulfilled during the camera conception:

- small pixel size in order to obtain a good image quality (~ 1.8 mrad);
- large field of view ($\sim 5^\circ \times 5^\circ$) for extended sources observations and blind searches of astrophysical sources;
- a fast trigger system;

3. H.E.S.S.: The High Energy Stereoscopic System

- a fast electronic system for the data acquisition in order to maximize the background suppression.

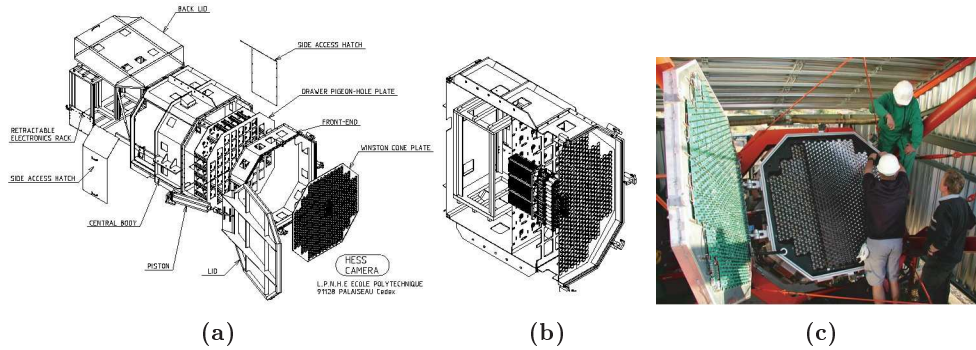


Figure 3.4: Mechanics of the H.E.S.S. camera: (a) exploded view, showing all elements (b) cut-through view of a closed camera with three drawers in place (c) H.E.S.S. camera photography during the placement of the Winston cones. Extracted from Ref. [60].

The cameras have 1.5 m of length for 1.6 m of width, and a total weight of 900 kg each. They are equipped with fast and sensitive photo-multiplier tubes (PMTs). Each of H.E.S.S. cameras comprises 960 of such PMTs, each one subtending a field of view of 0.16° , and thus a total field of view of a H.E.S.S. camera of $5^\circ \times 5^\circ$. In order to reduce light losses, Winston cones are installed in front of each PMT, focusing the incident light into the active volume of PMTs (see Figure 3.4). The signals coming from PMTs are captured using analog memories, Analog Ring Sampling (ARS), which sample the signal every nanosecond and which keeps the last 128 ns of signal history in a circular buffer. Every 16 PMTs are integrated to a module (drawer), of a total of 60 individual drawers for a camera, containing also trigger and readout electronics and the high voltage supply (see Figure 3.5) [61]. The readout time is adjusted to 16 ns, thus taking into account the short duration of a Cherenkov pulse and reducing background photons from the night sky. More details about the cameras and the calibration of the cameras are given in [60] and [61], respectively.

Trigger system

The system trigger requires the simultaneous detection of air showers by several telescopes at the hardware level. This requirement allows a suppression of background



Figure 3.5: Photography of a H.E.S.S. camera drawer. The PMTs can be seen on the right. Ref. [61].

events, which in turn leads to a lower system energy threshold for the detection of γ -rays. The trigger of the H.E.S.S. experiment consists of two levels, a telescope trigger and a central trigger system [62].

As far as the telescope trigger is concerned, it is implemented by dividing the camera into 64 overlapping trigger sectors. A telescope trigger signal is generated, if more than 3 pixels within such a sector receive a signal of more than 4 photo-electrons (p.e.) within a time window of 1.5 ns. The frequency of telescope triggers depends, beside atmospheric conditions, on the zenith angle of observations and has a rate between 300 Hz and 500 Hz. The telescope trigger signal is subsequently sent to the hardware central trigger, located in the control building on the site. The central trigger checks, whether at least two telescope trigger signals arrive within a time window of 80 ns. If this is the case, the central trigger sends a readout signal to the telescopes, and the information of the individual telescopes is subsequently read out and stored on the data acquisition system on the H.E.S.S. site. The requirement of at least two triggered telescopes reduces the system trigger rate to ~ 150 -200 Hz and effectively discriminates against Cherenkov light from muons, mostly seen only by single telescopes. For more details see [62].

3.2 Data analysis

3.2.1 Data taking

H.E.S.S. carries out observations of γ -ray sources only during moonless nights, with good weather conditions, and with the Sun at more than 18° below the horizon. Under

3. H.E.S.S.: The High Energy Stereoscopic System

these conditions the observation time amounts to a maximum of ~ 1700 hours per year, while the mean total data taking time is ~ 1000 hours per year. The light from the Moon would severely influence the sensitivity of the telescopes, making the detection of the Cherenkov light from VHE photons at energies close to the energy threshold of 100 GeV impossible, thus only some data taking for calibration purposes is possible. The observations are split in 28 minutes runs, during which a potential target is tracked on the sky. Different observation strategies are used by H.E.S.S.:

- **ON-OFF strategy** : the telescope pointing alternates between the studied source position (*ON*-position) and a position out of the source (*OFF*-position), offset by 30 minutes in right ascension but with the same declination as the putative source. This *OFF*-position run begins approximatively 30 sidereal minutes before or after the start of the *ON*-position run so that the telescope tracks the same range of elevation and azimuth. This allows a robust hadronic background estimation (see paragraph 3.2.4) on the same region in the sky, and thus with similar atmospheric and night sky brightness conditions. The disadvantage of this strategy is that only half of the available observation time is used on the target.
- **Wobble mode strategy** : the center of the camera points to a direction slightly offset from the target position (typically $\pm 0.5^\circ$ for a point-like source). The hadronic background can thus be estimated in the same field-of-view. An eventual disadvantage of this technique is the impossibility of having background estimation for extended sources with sizes similar or larger than the H.E.S.S. field-of-view.

3.2.2 Data quality selection

The data, recorded during γ -ray observations, need to be prepared for analysis. Therefore, observation runs are first checked for the stability of the system performance. This means that besides the hardware performances, also the stability of the weather conditions is checked, since the atmosphere is used as a calorimeter and is thus an integral part of the detection system.

Atmospheric control

The air-showers development strongly depends on the atmospheric conditions. In particular, the atmosphere transparency has a direct effect on the amount of Cherenkov light that reaches the ground. The presence of clouds is the most visible phenomenon, but the presence of aerosols also decreases its transparency. Atmospheric monitoring is thus necessary for the data selection, in order to reduce the systematic error on the analysis procedure. Different instruments are used for the atmospheric monitoring and their data are recorded on the database after every observations. For instance, each telescope is equipped with infrared radiometers to measure the effective sky temperature in the field of view of the telescope. Clouds in the field of view manifest themselves through an increased sky temperature. A weather station measures permanently the temperature and pressure on the ground level, and the wind speed and direction. An infrared LIDAR (Ceilometer, 95 nm) is used as an active cloud sensor scanning the sky with a laser beam and detecting light backscattered by clouds and aerosol. And finally a transmitter was recently installed to measure the atmosphere transparency at ~ 500 m of elevation above the ground level at different wavelengths (390, 455, 505 and 910 nm).

Standard data-quality selection

The standard data-quality selection which will be used for all the H.E.S.S. analyses presented in this work follows the following criteria:

- trigger condition of 3 pixels with more than 4 p.e. within a camera sector, and at least two telescope trigger signals arriving within a time window of 80 ns.
- number of disabled PMTs (which are represented as “broken” pixels on the camera) due to hardware failures or bright stars in the field of view not exceeding 10%.
- global temperature variation of the cameras, measured by radiometers, not exceeding 10%.
- global trigger rate superior to 200 Hz.
- variation on the individual trigger rate of each telescopes inferior to 10%.

A full description of calibration steps can be found in Rolland [63] (2005).

3.2.3 γ -ray selection and reconstruction

Air showers and detector simulations

In the absence of a test beam, the data analysis methods are based on the comparison between observed images on the cameras and images generated by simulations. Simulations of air showers initiated by γ -rays are essential for improving the detection and spectral reconstruction of γ -ray sources. Additionally, simulations of hadronic showers are used for validation of the detector response, since most of the actual acquired data contains events initiated by hadrons.

Electromagnetic showers simulations are produced using a Monte Carlo technique, including all the different particle interaction processes during the shower development in the atmosphere (energy loss through ionization, bremsstrahlung, e^+/e^- annihilation, inelastic diffusion...). Several shower generators are used in the H.E.S.S. collaboration, in particular CORSIKA [64] and KASKADE [65]. Atmospheric models are based on the temperature and pressure profiles measured in Windhoek between January and July 1999. Seasonal atmospheric condition oscillations induce changes on the density of Cherenkov light at the ground level, which can reach 15-20% at the H.E.S.S. site.

The detector is simulated taking into account all the analysis chain. The full telescope structure is simulated, each mirror being individually modelled. The mirror reflection on the Winston cones, followed by the PMTs readout and electronic signal reconversion to be finally treated by the data acquisition electronics, are all modelled and included in the simulations. More details about the detector simulation can be found in [66].

Second moments or Hillas parameters technique

As described in Sec. 2.2, electromagnetic and hadronic air showers exhibit a quite different shape, therefore parameters like length and width of the corresponding image on the camera can be used for discriminating between air showers induced by γ -rays (and electrons) and hadronic CRs. This idea was first proposed by Hillas in 1985 for the WHIPPLE experiment [67], where the images were parametrized as ellipses with the intensity on the major and minor axis following a Gaussian distribution. This

parametrization yields a set of Hillas parameters, which are illustrated in Figure 3.6 and defined by:

- the nominal distance, D , between the center of gravity (CoG) of the shower image and the real source position (pointing position) on the camera;
- the length l and width w of the shower, defined as the length of the major and minor axes, respectively;
- the overall image intensity amplitude;
- the angular distance θ the reconstructed position and real positions of the source on the camera;
- the angle α between the major axis and the axis linking the CoG to the real source position. This parameter is usually only used for mono-telescope observations.

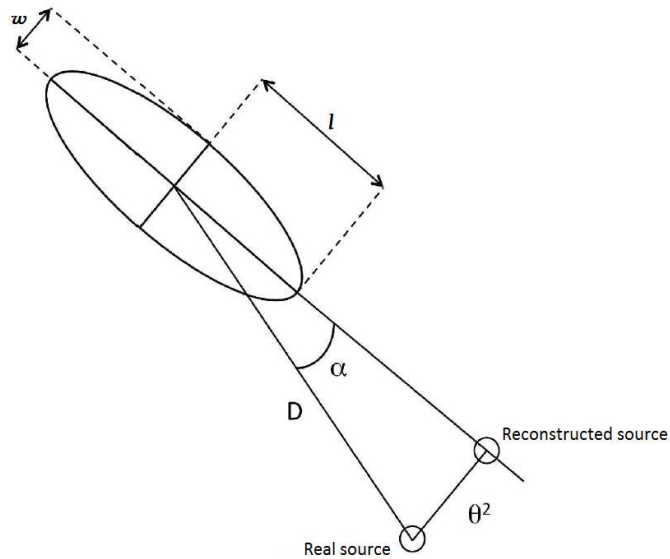


Figure 3.6: Illustration of the Hillas parameters for a elliptical image. The parameters are defined in section 3.2.3.

The reconstructed parameters l and w of individual shower images are used in order to obtain a discrimination between γ -rays and hadrons showers. In order to account for intrinsic fluctuations of photon emission during the shower development, these parameters are renormalized to the mean expected value for a shower with the same amplitude, zenith angle and impact parameters. The expected values are found after simulations.

3. H.E.S.S.: The High Energy Stereoscopic System

The renormalized variables are called the *Scale Width* (SW) and the *Scale Length* (SL) and they are found by

$$SW = \frac{w - \langle w \rangle}{\sigma_w} \quad \text{and} \quad SL = \frac{l - \langle l \rangle}{\sigma_l}, \quad (3.1)$$

where $\langle w \rangle$ and $\langle l \rangle$ are the mean reconstructed values, and σ_w and σ_l are their respective spread for simulated showers assuming a Gaussian distribution. In stereoscopic mode, the values of these variables for each telescope are combined and a mean value can be found (*Mean Scale Width/Length*):

$$MSW = \frac{\sum N_{tels} SW}{N_{tels}} \quad \text{and} \quad MSL = \frac{\sum N_{tels} SL}{N_{tels}}, \quad (3.2)$$

where N_{tels} corresponds to the number of telescopes triggered for a given event. The distribution of these parameters for simulated γ -rays, protons and data from empty regions in the sky (off-data) is shown in Fig. 3.7.

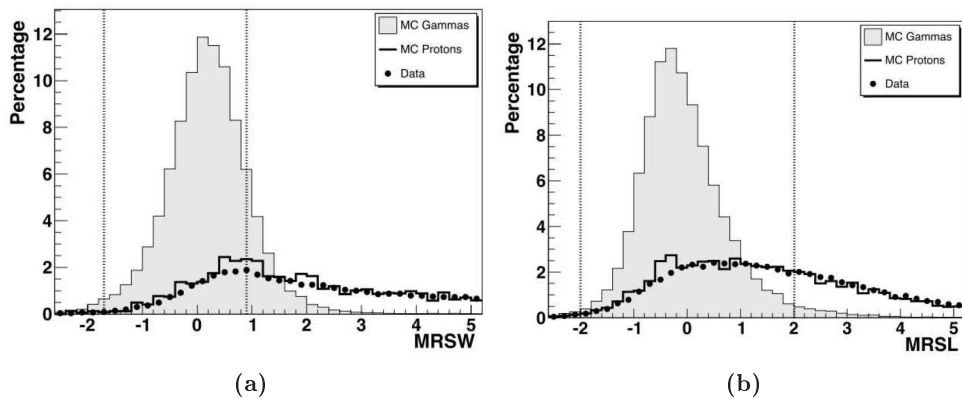


Figure 3.7: Distributions of mean (a) reduced scaled width (MRSW) and (b) mean reduced scale length parameters (MRSL) for simulated γ -rays and protons, and data taken from empty regions in the sky (off-data). The simulations were performed at a zenith angle of 20° . Proton and off-data distribution show a nice agreement, leading to the conclusion that the distributions are understood and can be used as selection variables. The standard cut values are indicated by vertical lines. Image taken from Ref. [68].

The distributions for simulated γ -ray events are highly concentrated around 0, whereas the distributions for simulated protons exhibit a much more extended shape, being in good agreement with off-data, which almost entirely consists of hadronic CRs. In the same figure, cut values, introduced to reject the most part of the hadronic background, both for MSW and MSL distributions, are depicted by vertical lines. The

standard cuts for H.E.S.S. analysis are

$$-2 \leq MSW \leq 0.9 \quad \text{and} \quad -2 \leq MSL \leq 2. \quad (3.3)$$

These values were optimized for a source with a flux of the order of 10% of the flux from the Crab nebula and a spectral index of $\Gamma = -2.6$. In addition, these Hillas parameters contain the necessary information to reconstruct the incident direction and the energy of the primary particle as well. Since for all events at least two telescopes exist, which have observed the same particle shower, the determination of the particle incoming direction is possible by intersecting the major axes of the reconstructed ellipses. If N_{tels} telescopes have triggered for the same shower, the number of intersection points is $N_{tels}(N_{tels} - 1)/2$, *i.e.*, one intersection point for a two-telescope event and six intersection points for a four-telescope event. In case $N_{tels} > 2$, the direction is reconstructed by calculating a weighted mean [68]. The more telescopes have seen the shower, the more accurate is the direction reconstruction. The energy of the primary particle is determined by the comparison between the observed image and simulated images with the same impact parameters and intensity in the Hillas ellipse. A large number of showers initiated by γ -rays is simulated for different discrete values of energy, impact parameter, zenith angle, off-axis angle and optical efficiency. The simulated photons are then reconstructed with the same algorithm as for the real data, and the results are stored in *look-up* tables. The event energy is then found by interpolation between the observed Hillas parameters and the tables.

Semi-analytical model

The analysis by semi-analytical model is based on a comparison of the recorded Cherenkov light distributions of photon-induced electromagnetic showers in the camera, *i.e.* the shower images, with calculated shower images from a model of the Cherenkov light distribution in electromagnetic showers. This analysis technique was pioneered by the CAT experiment [69], and it was improved by the H.E.S.S. collaboration (*Model analysis*) [70]. The calculated shower images are derived from Monte Carlo simulations of the Cherenkov light distribution of charged particles in electromagnetic showers taking into account the atmospheric density profile, atmospheric absorption, etc. The Cherenkov light distribution of the shower is determined by the longitudinal, lateral,

3. H.E.S.S.: The High Energy Stereoscopic System

and angular distributions of charged particles in the shower, as well as their energy spectra. These distributions are parametrised to yield an analytical description of the shower, *i.e.* the *shower model*. The mirror asynchronicity and their reflectivity, the quantum efficiency of the PMTs, as well as the signal integration window are all included in the simulations. Additionally, the contribution of the night sky background noise in every pixel of the camera is modelled on the basis of a detailed statistical analysis.

The semi-analytical model predicts the amount of Cherenkov light μ_i expected on a pixel i of the camera. This quantity depends on several parameters, which are:

- the primary γ -ray energy E_γ ;
- the coordinates of the impact point of the Cherenkov front on the ground with respect to the center of the camera, or impact parameters, (X_γ, Y_γ) of the shower initiated by the primary γ -ray¹;
- the zenith angle $\theta_{z,\gamma}$ of the primary photon;
- the azimuthal angle ϕ_γ of the primary photon with respect to the telescope pointing direction;
- the PMTs response to a unique photon σ_γ , calculated for each pixel of the camera;
- the pixel i pedestal width $\sigma_{p,i}$.

The latter accounts for the residual light that falls into each pixel due to the night sky background light and electronic noise. A *telescope log-likelihood* function is defined for a signal x_i , seeing by each pixel i of the camera, as

$$\ln L = -2 \sum_i \ln P(x_i, \mu_i, \sigma_{p,i}, \sigma_\gamma), \quad (3.4)$$

where $P(x_i, \mu_i, \sigma_{p,i}, \sigma_\gamma)$ is the probability to observe a signal x_i on a pixel i with a pedestal width $\sigma_{p,i}$ and a response to a unique photon σ_γ , when a signal μ_i is expected. Its value is given by the convolution between a Poisson distribution of photo-electrons and the PMTs resolution σ_γ .

The minimization of the log-likelihood function gives best fit parameters E_γ , X_γ , Y_γ , $\theta_{z,\gamma}$ and ϕ_γ for a given triggered event. A fitting quality variable G is defined

¹The XY plan is defined at the ground level.

(*goodness of fit*), in order to create a discrimination criteria between showers initiated by γ -rays or hadrons. This variable is defined as the sum, normalized over all pixels, of the differences between the likelihood function $\ln L$ and its expectation value $\overline{\ln L}$:

$$G = \frac{\ln L - \overline{\ln L}}{\sqrt{2 \times N_{\text{dof}}}}, \quad (3.5)$$

where $N_{\text{dof}} = N_{\text{pixels}} - 5$ is the number of degrees of freedom of a fitting procedure with 5 parameters by log-likelihood minimization. The choice of G as discriminating variable comes from the analytical calculation of the likelihood logarithmic average $\overline{\ln L}$. Indeed the distribution of $\overline{\ln L}$ follows a χ^2 law with N_{dof} degrees of freedom. Thus the expected distribution of G must be close to a Gaussian distribution with mean 0 and standard deviation 1. In order to fully exploit the differences between the γ and hadron-induced showers, individual pixels contributing to the goodness of fit are classified into two different groups at the end of the fit:

- Pixels belonging to the *shower core*, defined as pixels whose predicted amplitude is above 0.01 p.e., are grouped together with three rows of neighbours around them to construct a variable named *ShowerGoodness* (SG). Due to the large reduction of the number of degrees freedom, this variable is more sensitive than the Goodness to discrepancies between the model prediction and the actual shower images.
- Remaining pixels, denoted as *background pixels*, are grouped together to construct a variable named *BackgroundGoodness* (BG), which is sensitive to hadronic clusters outside the main image, and other irregularities.

In stereoscopic mode these variables are averaged for all telescopes detecting the event. The new variables are the *Mean Scaled Shower Goodness* (MSSG) and the *Mean Scaled Background Goodness* (MSBG), which have a better discrimination strength than the *Goodness* variable alone. The analysis method using these variables is called *Model++*. The distribution of the *Shower Goodness* variable for data from empty regions in the sky (background), γ -rays coming from the blazar PKS 2155-304 and simulated γ -rays is shown in Fig. 3.8. It is clear that by introducing a cut value most part of the hadronic background can be rejected. The H.E.S.S. standard cut for analysis is

$$-2 \leq MSSG \leq 0.6. \quad (3.6)$$

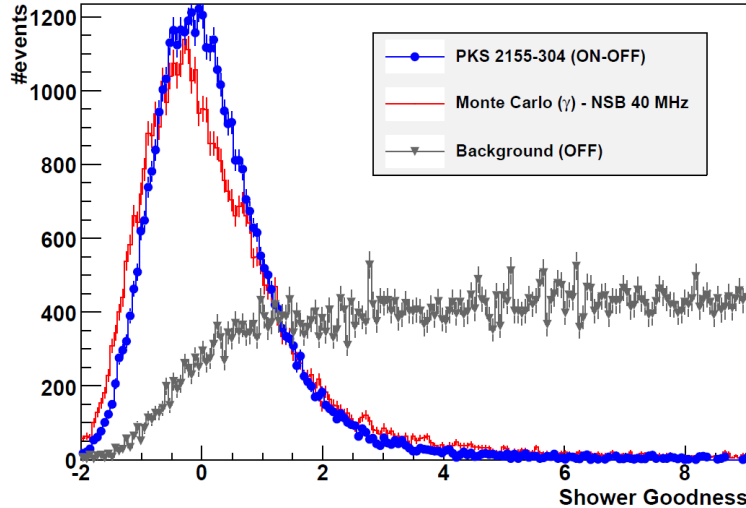


Figure 3.8: Distribution of Shower Goodness for real data taken on the blazar PKS 2155-304 (blue point for excess events, grey triangles for background events), compared with a simulation of γ -rays (red histogram) with a similar night sky background level. From Ref. [70].

In order to efficiently improve the hadronic background rejection, secondary cuts are added to the γ -ray selection procedure. The set of cuts which defines the *Standard cuts configuration* of the H.E.S.S. *Model++* analysis are the following [70]:

- A minimum image amplitude of 60 photoelectrons per telescope;
- A maximal nominal distance (distance between the center of the shower image to the center of the camera) inferior to 2° ;
- At least two telescopes passing the previous shape cuts;
- A maximum MeanScaleShowerGoodness (MSSG) of 0.6;
- A reconstructed primary interaction depth t_0 between -1 and $4 X_0$ ¹;
- For a point-like emission search, a squared angular distance cut of $\theta^2 \leq 0.01 \text{ deg}^2$.

3.2.4 Residual hadronic background estimate

The previous selection methods allow to select only showers which have similar characteristics to an electromagnetic shower. The selected events are defined as γ -candidates (or γ -like events). However, due to the actual large flux of hadrons reaching the Earth,

¹ X_0 is represented in radiation length. The atmosphere has ~ 28 radiation length.

statistically, a residual number of showers initiated by hadrons still remains among the selected event. Such events strongly resemble an electromagnetic shower and are undistinguishable from true γ -ray events. In order to estimate this residual background several methods were developed, making use of the fact that the hadronic background is isotropic. Figure 3.9 shows the event distribution as function of the squared angular distance to the blazar PKS 2155-304, which is point-like source [70]. The residual background can be clearly seen for angular distances $> 0.01 \text{ deg}^2$. The region $\leq 0.01 \text{ deg}^2$ is defined as the ON-region, where the point-like γ -ray source is expected to be located. In order to perform an estimation of the residual hadronic background under the central source, OFF regions are defined. These regions must be chosen so that the observing conditions and telescope sensitivity are as similar as possible to those of the ON region.

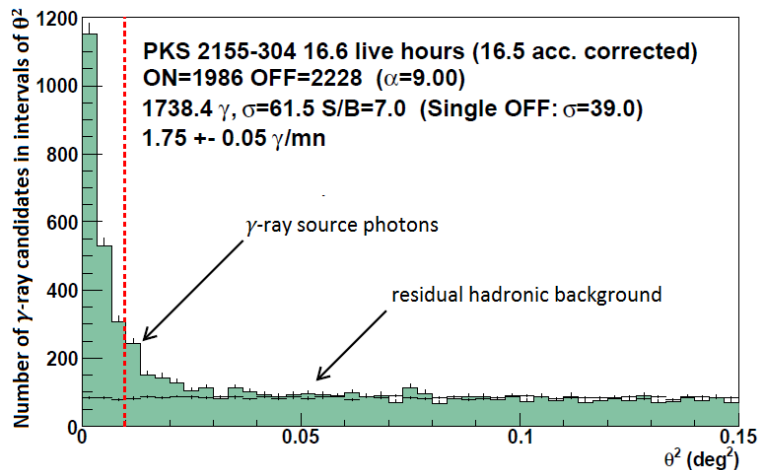


Figure 3.9: Squared angular distribution (θ^2) obtained on the blazar PKS 2155-3042. The number of events coming from the γ -ray source is measured for distances $\theta^2 < 0.01 \text{ deg}^2$ (red line), defined as the ON region. The residual hadronic background is clearly seen for $\theta^2 > 0.01 \text{ deg}^2$. From Ref. [70].

The telescope sensitivity to γ -rays is called acceptance, and it is defined as the probability for a given event to trigger the camera and pass the γ -ray selection cuts. Its estimation depends on several instrumental effects, like the camera response inhomogeneities, the mirror reflectivity, and thus it is not homogenous over the whole cameras field-of-view. Therefore, any acceptance measurement needs to be performed

3. H.E.S.S.: The High Energy Stereoscopic System

on a field-of-view with an homogenous and isotropic γ -ray background. The methods applied by the H.E.S.S. collaboration first calculate the acceptance on each camera and then translates it on the field-of-view acceptance. Because the presence of a γ -ray source would forbid the acceptance calculation during an observation, two methods were developed in order to circumvent this problem. The first one relies on the assumption that the acceptance of the detector is radially symmetric around the observation position, and the second one uses bi-dimensional maps of detected γ -candidates and hadrons-candidates.

Radial acceptance

Figure 3.10 illustrates the radial acceptance calculation. In *Wooble* mode observations, the acceptance on a called *exclusion region* of radius d (larger or equal to the ON region radius)¹, surrounding the ON region is calculated assuming that the camera response is radially symmetric around its center. A weight w is defined for each γ -candidate on the camera as

$$w = \frac{\pi}{\pi - \theta}, \quad (3.7)$$

where θ is the angle between the reconstructed γ direction and the source (see Figure 3.10). If the circle of radius r (distance between the reconstructed γ direction and the center of the camera) does not intersect the exclusion region, a weight $w = 1$ is attributed to the γ -candidate. On the other hand, if the circle intersects the exclusion region, the weight is given by Eq. 3.7 and it represents the inverse of the circle fraction which does not intersect the exclusion region ($w > 1$).

The main advantage of this method is that it can be applied run-by-run, thus automatically taking into account variations from run to run due to different sky night background or zenith angle. Also it can be applied to a single observation run, *i.e.*, it does not require a large number of data for the acceptance calculation (as it is the case for the bi-dimensional acceptance method). But it relies on the quite strong assumption that the camera acceptance is purely radial, which might be wrong.

¹This exclusion region is defined as a region which cannot be used for hadronic background estimation. Indeed, due to the HESS angular resolution, some true γ events leaks out of the ON region and should not be miscounted as hadronic background.

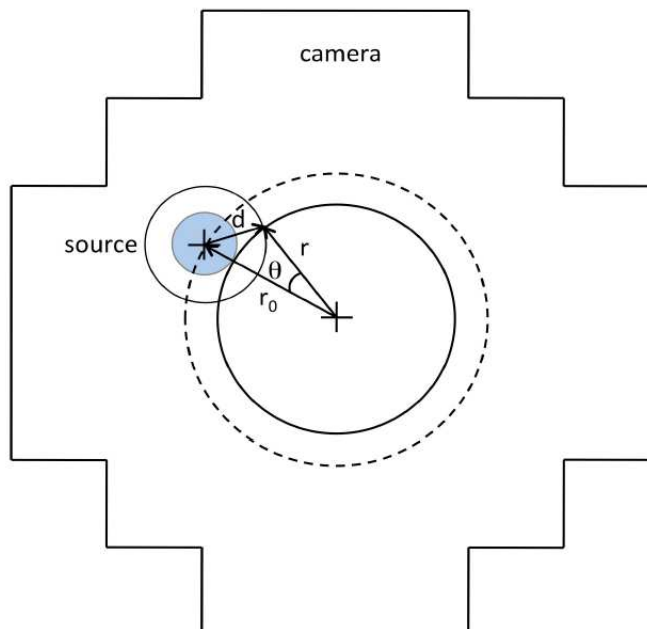


Figure 3.10: Illustration of the radial acceptance calculation method. The distance of between the reconstructed γ direction and the center of the camera is given by r , and the distance between the source position and the center of the camera is given by r_0 . The radius of the exclusion region surrounding the source is defined by d .

Indeed, non-operational pixels and inhomogeneous pixel responses are often present, implying on a anisotropic response of the camera. Also if several sources are found in the field-of-view, exclusion regions need to be defined for each source, which turns the method to be very time consuming.

Bi-dimensional acceptance

The bi-dimensional acceptance method does not suffer of the same difficulties as the radial acceptance method. On the other hand, this method requires a large number of events, in order to reduce Poisson fluctuations of the hadronic background.

First, an *exposition map* is calculated centered on the center of the camera (camera reference frame). The exposition map calculation procedure is illustrated in Figure 3.11. For each data run, two hadronic background map are created, with

and without the exclusion regions around the sources positions, and then summed for all runs on the same region. The ratio between these maps defines the exposition map, which basically gives the observation time fraction spent by each pixel out of the exclusion regions. In the case of a single run, the exposition map would have a value 0 inside the exclusion regions and 1 everywhere else. For several data runs, the time fraction will have an intermediary value between 1 and 0 due to the displacement of the sources on the camera during several data takings (see Figure 3.11).

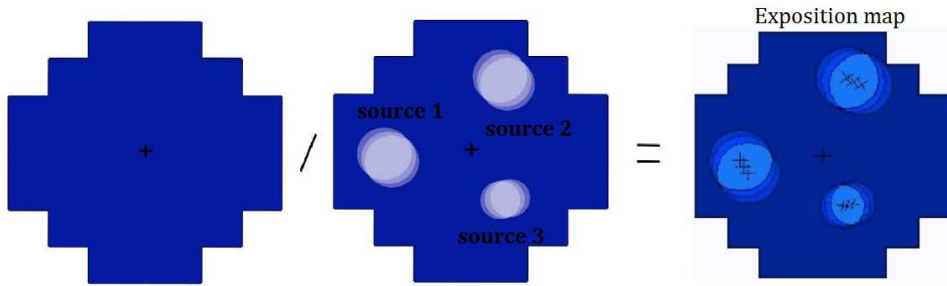


Figure 3.11: Schematic illustration of the exposition map calculation. The first two map represent the hadronic background maps, with and without the exclusion regions around the sources positions.

Second, a γ -events map is created for each data run, using all γ -candidates out of the exclusion regions, and then summed for all data runs (see Fig. 3.12). The bi-dimensional acceptance is found by dividing the events map by the exposition map. The same procedure can be used to derive the hadronic background bi-dimensional acceptance. Once the acceptance map is found on the camera reference frame for each observation run, a conversion is done in order to obtain the acceptance on the field-of-view reference frame (centered on the source).

Geometrical “ON-OFF” background techniques

Once the telescope acceptance on the field-of-view is calculated, OFF regions can be safely defined in order to estimate the residual background in the ON region. Several geometric configurations for the OFF region can be defined, under the condition that ON and OFF region have similar acceptances. For this reason, OFF regions are generally chosen within a similar distance to center of the camera as the ON region. Figure 3.13

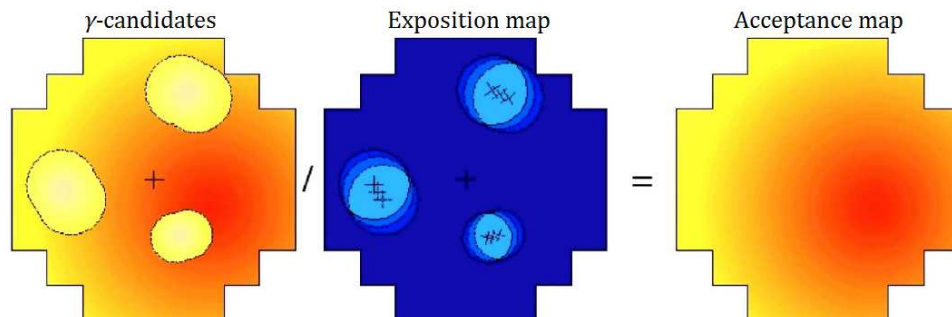


Figure 3.12: Schematic illustration of the bi-dimensional acceptance map calculation. The γ -ray candidates map and exposition map are used.

shows a schematic illustration of the different regions defined for the background estimate:

- **reflected background** : uses OFF regions symmetrically opposed to the ON region, with respect to the center of the camera;
- **multiple-off background** : uses non-overlapping OFF regions placed around the observation position at the same offset as the ON region;
- **ring-segment background** : similar to the multiple-off, but instead of several OFF regions uses a ring centered on the observation position with a radius equal to the offset;
- **full-ring background** : uses a ring around the ON region as OFF region. This OFF region is selected only once for the total data analysis of a particular source and is valid of all runs, independent of the actual observation position. Since the definition of this OFF region does not depends on the observation offset, this method is applied mainly in cases when the source is too close to the observation position and there exist nearby sources. It is used, in particular, for the Galactic Center data analysis (chapter 10).

The estimate on the number of residual hadronic events under the central source can thus be performed by taking into account the ratio between the ON and OFF region surfaces. The statistical uncertainty on the background estimation decreases if large OFF region surfaces are taken. The number of residual background events is also

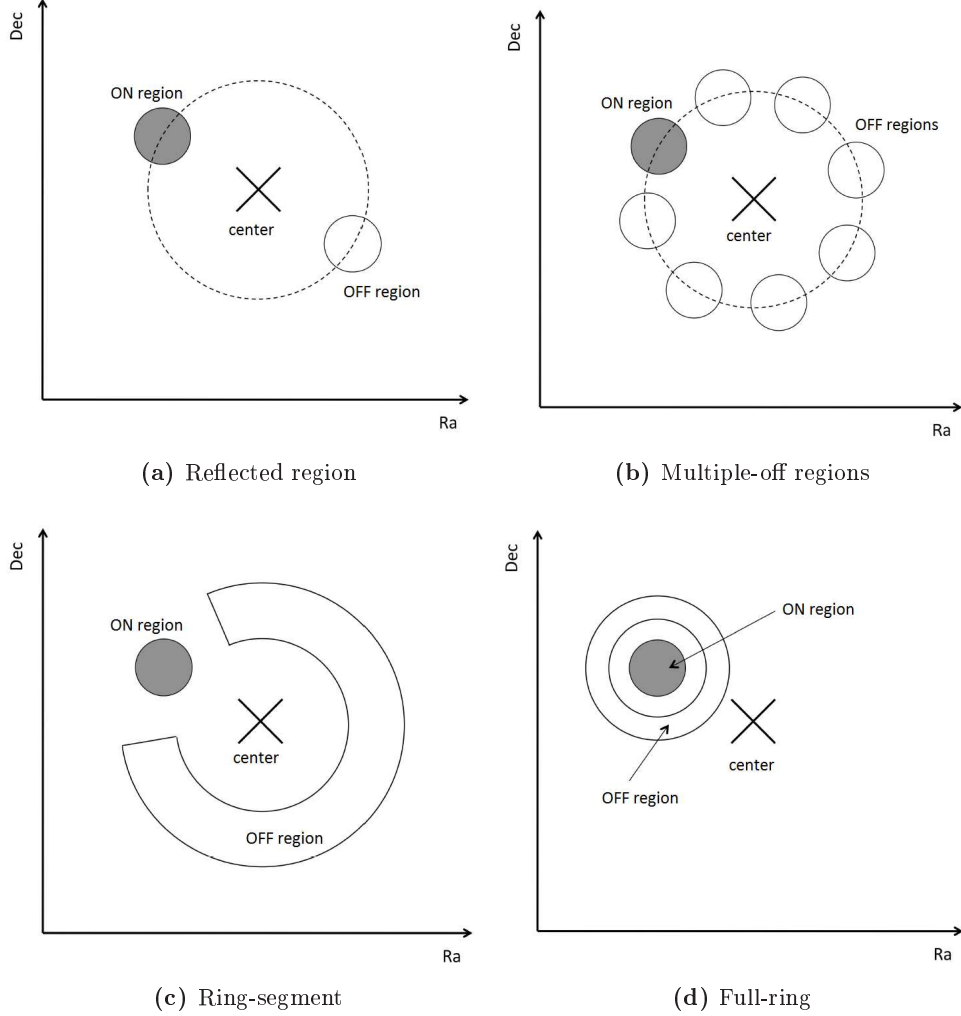


Figure 3.13: Different OFF regions definitions for the residual hadronic background estimate. The ON regions are indicated in gray areas, and the OFF regions in white. Adapted from Ref. [48].

corrected from differences between acceptances in the ON and OFF regions. Finally, the number of γ -ray excess N_γ in the ON region is found by

$$N_\gamma = N_{\text{ON}} - \alpha N_{\text{OFF}}, \quad (3.8)$$

where N_{ON} and N_{OFF} are the number of γ -candidates in the ON and OFF regions, respectively. The normalisation factor α includes the ratio between the ON and OFF regions surfaces and differences between acceptances of these regions. For a detailed

comparison between the different techniques see Ref. [71].

Template background technique

The template background model invokes a different philosophy to that of geometric background models. Instead of using spatially distinct OFF regions, this technique employs as a background estimate hadron-like events with reconstructed directions overlapping the source of interest. Such events can form a suitable *template* of response for γ -like events. This method is illustrated in Figure 3.14, and can be used for both Hillas and Model analysis. In the γ -ray selection parameters space, the parameters range which is fully dominated by hadronic background is defined as the “OFF-regime”. Similarly, the parameters range fully dominated by γ -candidates is defined as the “ON-regime”. The number of OFF events N_{OFF} is then calculated by counting all the events in source region (geometrical ON region), but in the OFF-regime of the parameters space. The γ -ray excess N_γ is then defined in same way as for the geometric background technique, where α in this case is the ratio between the acceptances for γ -candidates and hadrons.

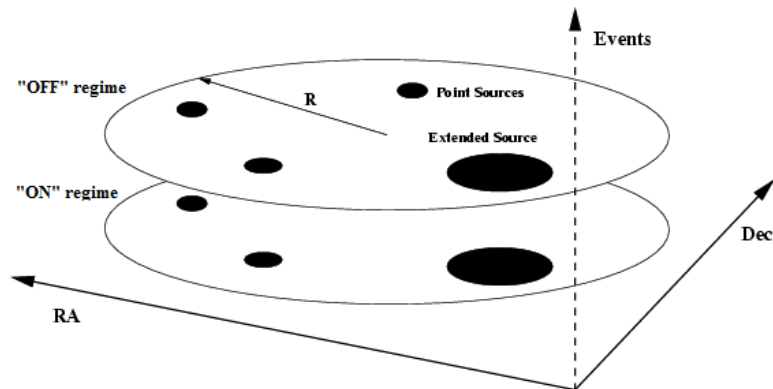


Figure 3.14: Illustration of the template background geometry with the field of view (radius R). The ON and OFF regions are spatially coincident but differ in the γ -ray selection parameters space.

The template background technique is very useful for blind searches of γ -ray sources, where neither the position or extension of the sources are known previously. This method will be used in particular for the extended analysis of the Fornax galaxy cluster (chapter 8). A disadvantage of this technique is that it needs the hadronic background acceptance map, and since the position of primary hadrons are badly reconstructed, the

3. H.E.S.S.: The High Energy Stereoscopic System

hadronic background acceptance map calculation suffers from much more systematical uncertainties than the γ -ray acceptance map calculation. Another source of systematical uncertainty can also come from the fact that the background estimation is performed in the same region as the source, and thus it does not take into account possible inhomogeneities that might exist in the hadronic background sky. The template background technique is described in more details in Ref. [72].

Significance calculation

In order to estimate whether the number of γ -candidates detected in the source (ON) region is a significant signal detection, a comparison with the residual number of background events in the same region has to be done. The statistical significance of a source candidate is determined using the number of ON and OFF events (N_{ON} and N_{OFF}) as well as the normalisation factor α (Li & Ma 1983 [73]):

$$S = \sqrt{2} \left[N_{\text{ON}} \ln \frac{1 + \alpha}{\alpha} \left(\frac{N_{\text{ON}}}{N_{\text{ON}} + N_{\text{OFF}}} \right) N_{\text{OFF}} \ln (1 + \alpha) \left(\frac{N_{\text{OFF}}}{N_{\text{ON}} + N_{\text{OFF}}} \right) \right]^{1/2}. \quad (3.9)$$

A significance superior to 5 is required to declare a significant detection. The significance distribution S measured in absence of a signal reflects the statistical fluctuation of the hadronic background and it follows a Gaussian with mean 0 and standard deviation 1. It is important to notice that the significance of a true signal will increase proportionally to $\sqrt{T_{\text{obs}}}$, where T_{obs} is the observation time.

3.3 Spectral reconstruction

The spectral reconstruction method used in this work¹ is a “forward-folding” method based on a maximum-likelihood procedure, comparing the energy distributions of ON and OFF events to pre-defined spectral shapes. Generally in VHE γ -ray astronomy the emission comes from particle acceleration processes and non-thermal photon emission (see chapter 1.1). The γ -ray flux in such processes is predicted to decrease following an power-law behavior $dN/dE \propto E^{-\Gamma}$, where Γ is the spectral index. However cut-offs and

¹Another method used by the H.E.S.S. collaboration is based on a “unfolding” method, and it is described in details in [47] (called “Method A” in the work).

curvatures might be present in the energy distribution of certain sources. Such features can be intrinsic to the acceleration mechanism of the source, or related to energy absorptions processes during the photon propagation in the interstellar or intergalactic medium. For instance, the energy spectrum of an hypothetical self-annihilation of dark matter particles should follow an power-law with an energy cut-off at the particle mass.

In order to properly reconstruct the energy distribution of detected γ -candidates, knowledge of detector energy resolution and acceptance as function of the energy, zenith angle of observation, source off-set (for observations in Wooble mode) and optical efficiency (which can varies with time due to the mirrors degradation) is needed. Therefore shower simulations for discrete values of the energy, zenith angle, off-set and optical efficiency are performed. Both the energy resolution and acceptance are extracted after the γ -ray selection cuts, so their values will depend on the analysis technique used in the simulations.

3.3.1 Effective detection area

The detector acceptance as function of the energy is expressed in terms of the effective detection area, or collection area. This effective area is defined by

$$A_{eff} = \int dS \epsilon(\vec{r}, E_{true}, \theta_z, \theta_d, \mu), \quad (3.10)$$

where $\epsilon(\vec{r}, E_{true}, \theta_z, \theta_d, \mu)$ accounts for the detector efficiency in collecting a true primary γ -ray of impact parameter \vec{r} and energy E_{true} , for a zenith angle of observation θ_z , observation off-set θ_d and an optical efficiency μ .

Figures 3.15a and 3.15b show the effective area as function of the primary γ -ray energy, for different zenith angles and off-set. With increasing zenith angle the Cherenkov light cone travels increasingly larger distances until the observation level is reached and widens correspondingly. As a consequence the Cherenkov radius on ground, in a plane perpendicular to the shower axis, also increases. In this case, not only the probability of detection of showers energetic enough to trigger the telescopes at high θ_z increases, but also a large number of low-energy γ -rays not being energetic enough to trigger the telescopes are lost. This behavior is clearly seen in Fig 3.15a. Similar explanation can be derived for the acceptance behavior at high source off-sets. In this case, only energetic enough γ -rays are able to trigger the telescopes when a

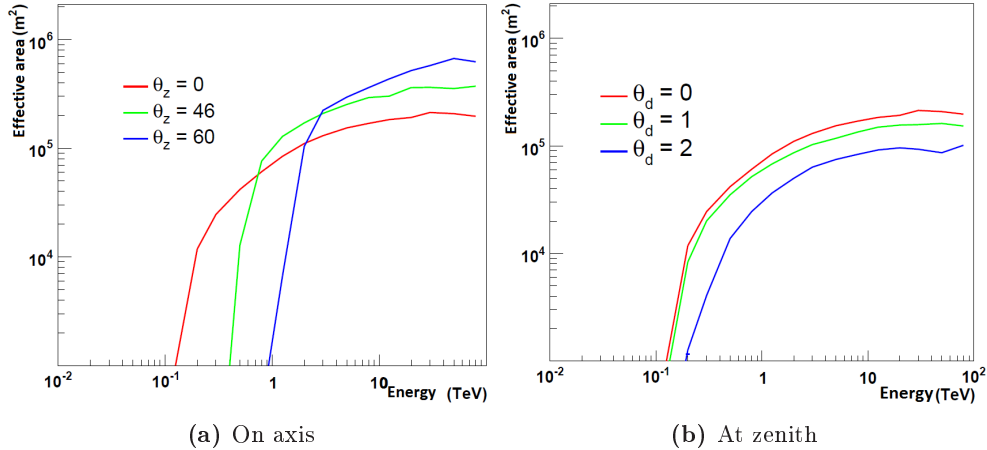


Figure 3.15: Effective area as function of the energy. (a) Effective area, on axis, as function of the energy for three different zenith angle of observation. (b) Effective area at zenith angle of observation for three different off-sets. Adapted from Ref. [48].

significant part of their light cone falls outside of the telescope camera field-of-view. Besides, the fact that a significant part of their Cherenkov light cone is missing reduces the γ -ray reconstruction and selection efficiency. The effective area thus decreases at higher energies. The same effect takes place for γ -rays with energies $\gtrsim 10$ TeV, even with no off-set, since their Cherenkov radius on ground can also be larger than the field-of-view. Effective areas for both the Hillas and Model analysis methods are calculated and stored in look-up tables, which can later be recovered for each data spectral reconstruction.

3.3.2 Energy resolution

The probability to reconstruct a γ -ray event at an energy E_{reco} , when the true primary γ -ray energy is E_{true} , defines the energy resolution and bias of the instrument for a given analysis method. These probabilities are estimated in the same way as the acceptance, through simulations using discrete values of the zenith and off-set angles, and then stored in look-up tables. The evolution of the energy resolution as function of the primary γ -ray energy, represented in terms of $\Delta E/E_{\text{true}}$, where $\Delta E = (E_{\text{true}} - E_{\text{reco}})$, is presented in Figure 3.16 for observations at zenith [70]. The energy resolution is better than 15% for the whole energy range (from 80 GeV up to more than 20 TeV),

with biases not exceeding 5% in the central range. For the very central energy range (500 GeV to more than 10 TeV), the energy resolution is better than 10% and reaches values as low as 7 to 8%. Larger energy biases appear at very low energy (up to 20% at 80 GeV), due to trigger selection effects.

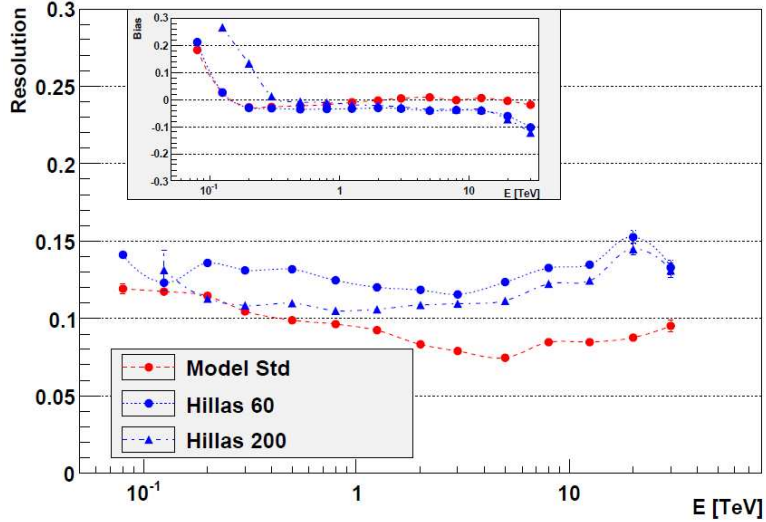


Figure 3.16: Energy resolution (main plot) and bias (inset) as function of energy, at zenith, obtained for standard cuts Model, and the standard and hard cuts (minimum image amplitude of 200 photoelectrons) Hillas parameters based analyses. From Ref. [70].

3.3.3 Maximum-likelihood method

This method is based on a global forward-folding method, using the knowledge of the detector response (γ -ray effective detection area and energy resolution), as well as a parameterization of the spectral shape. The spectral shape is convoluted with the detector response and the energy distribution which is obtained is compared with the actual measured energy distribution. A maximum-likelihood method, assuming that the number of ON and OFF γ -ray events follows a Poisson distribution, is then applied in order to recover the values of the most probable spectral shape parameters and their covariance matrix, used for the errors estimate.

The number of ON and OFF γ -ray events passing the selection cuts is first separated in the following sets of parameters intervals,

3. H.E.S.S.: The High Energy Stereoscopic System

- reconstructed energy intervals $\Delta_{i_e} = [\tilde{E}_{i_e}^{\min} - \tilde{E}_{i_e}^{\max}]$;
- zenith angle intervals $\Delta_{i_z} = [\theta_{i_z}^{\min} - \theta_{i_z}^{\max}]$;
- off-set intervals $\Delta_{i_d} = [\delta_{i_d}^{\min} - \delta_{i_d}^{\max}]$;
- optical efficiency intervals $\Delta_{i_r} = [\mu_{i_r}^{\min} - \mu_{i_r}^{\max}]$.

The predicted number of γ -rays $S_{i_e, i_z, i_d, i_r}^{\text{pred}}$ for each interval $\Delta_{i_e, i_z, i_d, i_r} = \{\Delta_{i_e} \otimes \Delta_{i_z} \otimes \Delta_{i_d} \otimes \Delta_{i_r}\}$ is calculated by

$$S_{i_e, i_z, i_d, i_r}^{\text{pred}} = T_{ON} \int_{\tilde{E}_{i_e}^{\min}}^{\tilde{E}_{i_e}^{\max}} d\tilde{E} \int_0^{\infty} dE \left[\frac{dN}{dE} \right]^{\text{pred}} \times A_{\text{eff}}(E, \bar{\theta}_{i_z}, \bar{\delta}_{i_d}, \bar{\mu}_{i_r}) P(E, \tilde{E}, \bar{\theta}_{i_z}, \bar{\delta}_{i_d}, \bar{\mu}_{i_r}), \quad (3.11)$$

where $(dN/dE)^{\text{pred}}$ is the assumed spectral shape, $\bar{\theta}_{i_z}$, $\bar{\delta}_{i_d}$ and $\bar{\mu}_{i_r}$ are the mean value of the zenith angle, off-set and optical efficiency, respectively, in the corresponding intervals. A_{eff} is the effective detection area of γ -ray photons with true energy E , $P(E, \tilde{E}, \bar{\theta}_{i_z}, \bar{\delta}_{i_d}, \bar{\mu}_{i_r})$ is the probability function to reconstruct a γ -ray photon of true energy E at an energy \tilde{E} ¹, and T_{ON} is the observation time in the ON region. The mean predicted number of events in the ON region $\hat{n}_{i_e, i_z, i_d, i_r}$ can be expressed as

$$\hat{n}_{i_e, i_z, i_d, i_r} = S_{i_e, i_z, i_d, i_r}^{\text{pred}} \times (1 + \beta) \times \hat{p}_{i_e, i_z, i_d, i_r}, \quad (3.12)$$

where $\hat{p}_{i_e, i_z, i_d, i_r}$ is mean predicted number of events in the OFF region and $\beta = T_{ON}/T_{OFF}$. Assuming that the observed numbers n_{i_e, i_z, i_d, i_r} and p_{i_e, i_z, i_d, i_r} have Poissonian probability distributions $P(n_{i_e, i_z, i_d, i_r})$ and $P(p_{i_e, i_z, i_d, i_r})$, respectively, the likelihood function is as follows:

$$\mathcal{L}(\{\Lambda\}, \hat{p}_{i_e, i_z, i_d, i_r}) = \prod_{i_e, i_z, i_d, i_r} P(n_{i_e, i_z, i_d, i_r}) P(p_{i_e, i_z, i_d, i_r}), \quad (3.13)$$

where $\{\Lambda\}$ is the set of parameters of the assumed spectral shape. The quantities $\hat{p}_{i_e, i_z, i_d, i_r}$, which are unknown, and $\{\Lambda\}$ can be determined by maximizing the function \mathcal{L} for all the intervals $\Delta_{i_e, i_z, i_d, i_r}$. A more precise study of this maximum-likelihood procedure with the H.E.S.S. data can be found in Ref. [63].

¹The symbols for true energy E_{true} and reconstructed energy E_{reco} were changed in order to not overcharge the formulas.

This method allows to test any spectral shape. The commonly tested spectral shapes are a power-law,

$$\frac{dN}{dE} = \Phi_0 \times \left(\frac{E}{E_{\text{norm}}} \right)^{-\Gamma}, \quad (3.14)$$

a log-parabolic power-law,

$$\frac{dN}{dE} = \Phi_0 \times \left(\frac{E}{E_{\text{norm}}} \right)^{-\Gamma - \beta \times \ln(E/E_{\text{norm}})}, \quad (3.15)$$

and a power-law with exponential cut-off,

$$\frac{dN}{dE} = \Phi_0 \times \left(\frac{E}{E_{\text{norm}}} \right)^{-\Gamma} \times e^{-\frac{E}{E_c}}, \quad (3.16)$$

where Φ_0 is the flux normalisation in $\text{TeV}^{-1} \text{m}^{-2} \text{s}^{-1}$, E_{norm} is the energy normalisation at 1 TeV, Γ the spectral index, β the curvature parameter, and E_c the exponential cut-off energy.

In order to estimate the quality of the fit, a equivalent χ^2 is calculated¹. Also associated residuals are often plotted, which are defined as

$$R = \frac{\hat{n}_{i_e}^{\text{pred}} - n_{i_e}^{\text{obs}}}{\hat{n}_{i_e}^{\text{pred}}}, \quad (3.17)$$

where $\hat{n}_{i_e}^{\text{pred}}$ and $n_{i_e}^{\text{obs}}$ are the predicted and observed number of γ -rays in the interval Δ_{i_e} , respectively. Ideally for a good fit, this distribution should follows a Gaussian distribution of mean 0 and standard deviation 1.

Calculation of spectral points

Spectral points are defined from the fitted spectrum and not the reverse. These points are simply a representation of the quality of the fitting and available statistics, which should not be confused with experimental data points on which the spectrum curve is fitted. In particular, their position in energy and flux will depend on the fitted spectrum.

The reconstructed energy intervals Δ_{i_e} are first grouped in new intervals Δ'_{i_e} , so that the mean signal significance in each of these intervals is superior to 3σ . The mean

¹ $\chi^2 = -2 \times \ln \mathcal{L}_{\text{max}}$

3. H.E.S.S.: The High Energy Stereoscopic System

true energy of each new interval is then calculated by (averaged for all zenith angle intervals Δ_{iz} and off-set intervals Δ_{id} in the field of view) :

$$\langle E \rangle_{\Delta'_{ie}} = \frac{\sum_{\Delta_{ie} \subset \Delta'_{ie}} \left[\int_{\tilde{E}_{ie}^{\min}}^{\tilde{E}_{ie}^{\max}} d\tilde{E} \int_0^{\infty} dE \times E \times \left[\frac{dN}{dE} \right]^{\text{pred}} \times A_{eff}(E) P(E, \tilde{E}) \right]}{\sum_{\Delta_{ie} \subset \Delta'_{ie}} \left[\int_{\tilde{E}_{ie}^{\min}}^{\tilde{E}_{ie}^{\max}} d\tilde{E} \int_0^{\infty} dE \left[\frac{dN}{dE} \right]^{\text{pred}} \times A_{eff}(E) P(E, \tilde{E}) \right]}. \quad (3.18)$$

For each new interval, the observed number of γ -rays $n_{i'_e}^{\text{obs}}$, and the predicted number of γ -rays $\hat{n}_{i'_e}^{\text{pred}}$, are calculated, using the effective area and energy resolution in the interval. The ratio between these two quantities is used as a normalization for the spectral point flux with respect to the fitted spectrum flux at the calculated mean true energy. The spectral point flux is given by

$$F \left(\langle E \rangle_{\Delta'_{ie}} \right) = \left[\frac{dN}{dE} \right]^{\text{pred}} \left(\langle E \rangle_{\Delta'_{ie}} \right) \times \frac{n_{i'_e}^{\text{obs}}}{\hat{n}_{i'_e}^{\text{pred}}}. \quad (3.19)$$

The asymmetrical confidence interval on this flux is calculated using the methods of Feldman & Cousins [74]. If the flux is compatible with 0, an upper-limit is given. The spectral point in the reconstructed energy interval Δ'_{ie} is then placed at the true energy $\langle E \rangle_{\Delta'_{ie}}$, with its corresponding flux F and errors.

Light curves

In order to follow a source activity, light curves can be constructed. They are defined as the integrated flux above certain energy E_0 (E_0 is generally defined as the highest energy threshold¹ among all the observations). The integration can be performed for any time range, from a few minutes to several days.

The light curve determination is performed after the previously described spectral reconstruction procedure. Thus it depends on the assumed spectral shape. The procedure is similar to the spectral reconstruction method, but this time the spectral parameters are fixed at the values found with the previous maximum-likelihood estimate, and only the flux normalisation Φ_0 is found after a new maximum-likelihood

¹The energy threshold for an observation is defined as the energy for which the acceptance of the instrument as function of the energy reaches 20% of its maximum value.

estimate for each time interval.

3.3.4 Systematic errors

The efficiency of the spectral reconstruction method was studied in detail in Ref. [63]. Several sources of systematic errors were found to influence the spectral parameters estimate.

Source of error	Spectral index	Flux
PMTs lost of gain	< 1%	+5%
Broken pixels	< 1%	< 1%
Azimuth angle	$\pm 2\%$	$\pm 7\%$
NSB	< 1%	< 1%
Atmospheric conditions	negligible	$\pm 15\%$

Table 3.1: Main sources of systematic errors and their value for the reconstruction of the spectral index and fluxes. Ref. [63].

The most important are:

- **variation of the detector calibration parameters** : the effective detection area and energy resolution are calculated for an ideal camera operational condition, *i.e.*, without broken pixels and for nominal values of the PMTs gain. These parameters do not reflect the actual operational state of the cameras.
- **azimuth distribution of the observation** : The electromagnetic showers development as function on the azimuth angle can vary due to the interaction of charged particles with the Earth magnetic field. This effect is specially important for low energy γ -rays and is not generally taken into account in the showers simulations.
- **night sky background (NSB)** : The night sky brightness is an important source of background. Imprecise estimates of the NSB variations with the position in the sky is a source of systematic error. For instance, the NSB photon rate for sources on the galactic plane (~ 100 MHz) is more intense than for extragalactic sources (~ 40 MHz for the blazar PKS2155-304).

3. H.E.S.S.: The High Energy Stereoscopic System

- **atmospheric conditions** : the spectral analysis is based on a simplified atmospheric model, where the atmosphere characteristics do not vary with time. This is definitely not the case for actual observations. However since the installation of more precise instruments of atmospheric monitoring in the weather station of the H.E.S.S. site, this source of systematic error was significantly reduced.

Table 3.1 summarizes the main sources of systematic errors, together with their amplitudes on the reconstructed values of spectral index and flux. The sum of all systematic errors are found to be about 20% for the flux, and ± 0.1 for the spectral index.

Part II

Indirect dark matter searches through gamma-rays

Chapter 4

Cold Dark Matter

Contents

4.1	Dark Matter cosmology	66
4.1.1	Standard cosmological model	66
4.1.2	Relic density of dark matter	68
4.2	Evidences in the Universe	70
4.2.1	Rotation curves of galaxies	71
4.2.2	Gravitational lensing	72
4.2.3	Primordial Big-Bang Nucleosynthesis	73
4.2.4	CMB observations and the Silk damping	74
4.3	Dark matter density distribution in the Universe	77
4.3.1	Cosmological N-body numerical simulations	77
4.3.2	Distribution in different scales	79
4.4	Dark matter candidates	83
4.4.1	Neutrinos	83
4.4.2	Supersymmetric dark matter	85
4.4.3	Universal extra dimension	86

It is generally accepted nowadays that the matter density of the universe mainly consists of an unknown component, called the Dark Matter (DM). The first observations suggesting the existence of DM were measurements of a large velocity dispersion of the members of the Coma galaxy cluster by Zwicky in 1933 [75]. Similarly, the problem of galactic rotation curves - the circular velocity of stars at large distances to the galactic center was found “too fast” to be explained by Newtonian dynamics with the visible matter - can be traced back to Babcock’s measurements of the Andromeda galaxy in 1939 [76]. In the late 1970’s and early 1980’s the so-called cold dark matter (CDM) paradigm appeared [77], where in this context, cold means matter moving with non-relativistic velocities when structures formed in the universe. The recent impressive amount of data from studies of the cosmic microwave background (CMB) radiation, supernova distance measurements, and large scale galaxy surveys have together solidified the Standard Model of cosmology, where structures formed through gravitational amplification of small density perturbations with the help of cold dark matter. Without the existence of dark matter the formation of structures in the present universe is hard to be explained, given the small amplitude of density fluctuations inferred from anisotropies of the CMB [78].¹

This chapter gives an overview on the CDM paradigm. The standard model of cosmology is described in the first section. The experimental evidences in favor of the existence of dark matter are presented next. Then the predicted distribution of dark matter in the present Universe is discussed in Section 4.3. In the end some of the main candidates from particle Physics models which were proposed in the literature to account for the dark matter are presented.

4.1 Dark Matter cosmology

4.1.1 Standard cosmological model

The present *Standard Model* of Cosmology which is most accepted is the Standard Big-Bang model, first proposed by Friedmann and Lemaître in the 1920’s. This scenario

¹Although the *hot* dark matter scenario is mainly excluded by several cosmological reasons, warm dark matter (WDM) is still a viable candidate to account for the dark matter relic density, under some particular assumption. For a review on the topic see Ref. [79].

describes the evolution of the Universe from a once very hot and dense state, and its expansion to a much cooler present state. The formulation of the Big-Bang model is based on the solution of the Einstein's equations for an isotropic and homogeneous universe. Although this is definitely not true on galactic scales and smaller, the distribution of matter seems to become more and more smooth on large scales. For instance, on the largest observable scales, probed by the CMB radiation, isotropy and homogeneity is realized at the level of 10^{-5} . Given isotropy and homogeneity, the overall geometry and evolution of the Universe is described by a space-time metric found by Friedmann, Lemaître, Robertson and Walker (FLRW), for which the line element is expressed as

$$ds^2 = c^2 dt^2 - a(t)^2 \left[\frac{dr^2}{1 - kr^2} + r^2 d\Omega \right], \quad (4.1)$$

where $a(t)$ is the so-called scale factor and the constant k , describing the spatial curvature, can take only the discrete values $+1$, -1 , or 0 corresponding to closed, open, or spatially-flat geometries, respectively. The Einstein equations can be solved with this metric, one of its components leading to the Friedmann equation

$$\Omega(t)_{\text{tot}} - 1 = \frac{k}{H(t)^2 a(t)^2}, \quad (4.2)$$

where $H(t) = \dot{a}(t)/a(t)$ is the Hubble parameter, which is defined as the expansion rate of the scale factor, and Ω_{tot} is the total average energy density of the Universe ρ_{tot} in units of its critical density ρ_c ¹:

$$\Omega_{\text{tot}} \equiv \frac{\rho_{\text{tot}}}{\rho_c} \quad \text{and} \quad \rho_c \equiv \frac{3H^2}{8\pi G_{\text{N}}}. \quad (4.3)$$

The critical density is defined as the energy density for which the Universe is flat ($k = 0$). The current value of the Hubble parameter and the energy density will be noted as H_0 and Ω_0 . Observations gives $k \approx 0$ ($\Omega_0 \approx 1$), *i.e.*, a geometrically flat universe on large scales, to good accuracy. Moreover, theoretical inflation models, where the Universe has passed by a period of accelerated expansion in its early stages, so far have provided a good description on how the Universe can automatically generate a negligible spatial

¹ $\rho_c^0 = 2.775 \times 10^{11} h^2 \text{ M}_{\odot} \text{Mpc}^{-3} = 1.053 \times 10^{-5} h^2 (\text{GeV}/c^2) \text{ cm}^{-3}$ [80]

4. Cold Dark Matter

curvature [81, 82]. The total energy density of the Universe can be decomposed into several components,

$$\Omega_{\text{tot}} = \Omega_{\text{m}} + \Omega_{\Lambda} + \Omega_{\text{r}}, \quad (4.4)$$

where Ω_{m} is the total present matter density, Ω_{Λ} the cosmological constant density (vacuum energy density) and Ω_{r} the radiation density.

Assuming that a non-zero cosmological constant, and a matter density composed by baryons and cold dark matter (and neutrinos, since they have non-zero mass), give rise to the so-called Λ CDM model of cosmology. This model is completely determined by the energy density distribution of the Universe. The current observational data are consistent with the Λ CDM model. The Λ CDM parameters are obtained via several astrophysical observations, amongst which the most important are: the CMB temperature anisotropies and power spectrum, Type Ia supernovae luminosity observations, abundance of primordial elements and the study of galaxies distribution in large structures, in particular their power spectrum oscillations due to the baryon acoustic oscillations (BAOs) [83]. The most recent results on the $(\Omega_{\text{m}}, \Omega_{\Lambda})$ are shown in Figure 4.2 [84]), and the full set of parameters are shown in Table 4.1 [80].

Parameter	Symbol	Value
Hubble parameter	h	0.704 ± 0.025
Cold dark matter density	Ω_{cdm}	$\Omega_{\text{cdm}}h^2 = 0.112 \pm 0.006$
Baryon density	Ω_{b}	$\Omega_{\text{b}}h^2 = 0.0225 \pm 0.0006$
Cosmological constant	Ω_{Λ}	0.73 ± 0.03
Radiation density	Ω_{r}	$\Omega_{\text{r}}h^2 = 2.47 \times 10^{-5}$
Neutrino density	Ω_{ν}	$\Omega_{\nu}h^2 \lesssim 0.07$ (95% C.L.)

Table 4.1: Most recent set of cosmological parameters. The values are obtained using a fit of a spatially-flat Λ CDM cosmology with a power-law initial spectrum (source Ref. [80]).

4.1.2 Relic density of dark matter

The simplest models of cold dark matter assume that the present relic value of CDM energy density was thermally produced, i.e., the DM particles number density was

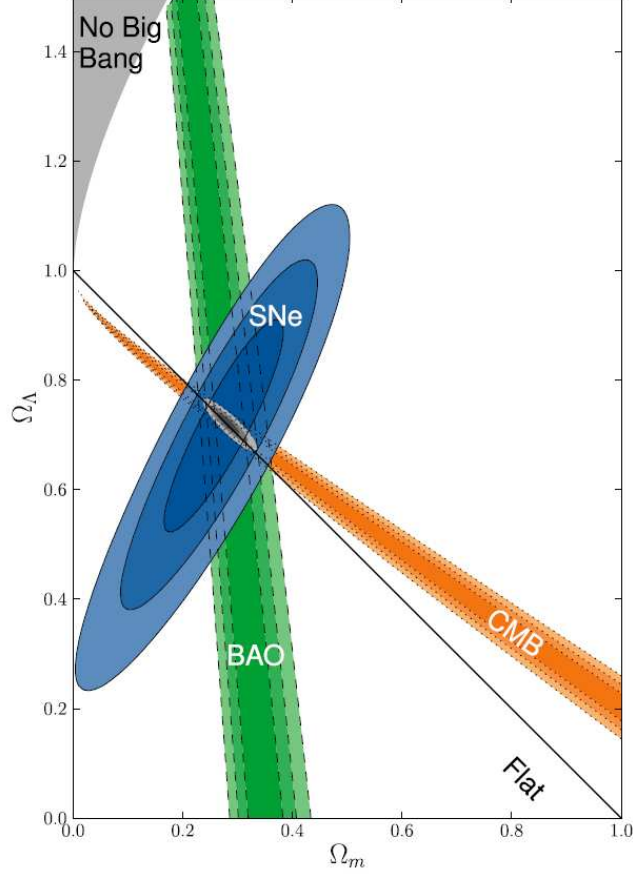


Figure 4.1: Contours at 68.3%, 95.5% and 99.7% confidence levels in the $(\Omega_m, \Omega_\Lambda)$ plane from recent supernovae data (blue solid lines), baryon acoustic oscillations (green dashed), and CMB peak positions (orange dotted). These plots are all assuming a Λ CDM cosmological model. Plot taken from Ref. [84].

§frozen \check{T} at some particular value after they were in thermal and chemical equilibrium with the hot §soup \check{T} of Standard Model (SM) particles after inflation [85]. Most of the more natural candidates to a DM particle are weakly interacting massive particles (WIMPs) χ , i.e. particles which do not have electromagnetic nor strong interactions with standard matter. In most of the DM particle models, WIMPs are generally particles with masses roughly between 10 GeV and a few TeV, and with cross sections of approximately weak strength. WIMPs can self-annihilate with their antiparticle to give SM particle-antiparticle pairs $\chi\bar{\chi} \rightarrow \psi\bar{\psi}$. Within standard cosmology with an expanding Universe, the evolution of number density of WIMPs n_χ is described by the

4. Cold Dark Matter

Boltzmann equation,

$$\frac{dn_\chi}{dt} + 3Hn_\chi = -\langle\sigma_{\text{ann}}v\rangle \times ((n_\chi)^2 - (n_\chi^{\text{eq}})^2), \quad (4.5)$$

where $\langle\sigma_{\text{ann}}v\rangle$ is the total annihilation cross section multiplied by velocity, brackets denote thermal average, H is Hubble constant, and n_χ^{eq} is the number density at thermal equilibrium. The term proportional to $3Hn_\chi$ expresses the dilution that automatically comes from the Hubble expansion. The condition that the interactions maintain equilibrium is that the interaction rate $\Gamma = n_\chi\langle\sigma_{\text{ann}}v\rangle$ is larger than the expansion rate of the universe $\Gamma > H$. Hence the annihilations stop changing the dark matter number density when $\Gamma \sim H$, that is when $n_\chi\langle\sigma_{\text{ann}}v\rangle \sim H$, basically defining the freeze-out. After freeze-out, the co-moving WIMP density remains essentially constant; if the Universe evolved adiabatically after WIMP decoupling, this implies a constant WIMP number to entropy density ratio. Freeze-out happens at temperature $T_F \sim m_\chi/20$ almost independently of the properties of the WIMP [81]. Their present relic density is then approximately given by (ignoring logarithmic corrections) :

$$\Omega_{\text{CDM}}h^2 \simeq \frac{3 \times 10^{-27} \text{cm}^3 \text{s}^{-1}}{\langle\sigma_{\text{ann}}v\rangle}. \quad (4.6)$$

Using the actual value of the CDM relic energy density $\Omega_{\text{CDM}}h^2 = 0.11$, this implies a DM annihilation cross section of $\langle\sigma_{\text{ann}}v\rangle \sim 2.8 \times 10^{-26} \text{cm}^3 \text{s}^{-1}$. The fact that this corresponds to what one gets with a weak interaction cross section (gauge couplings) for particles of mass around typical electroweak interaction magnitude (a few hundred of GeV) is sometimes coined the ‘‘WIMP miracle’’.

4.2 Evidences in the Universe

The most compelling pieces of evidence in favor of dark matter are [86]:

- the anomalous behaviour of the rotation curves of galaxies,
- strong gravitational lensing effects,
- primordial Big Bang Nucleosynthesis, and
- CMB measurements of the cosmological parameters and Silk damping.

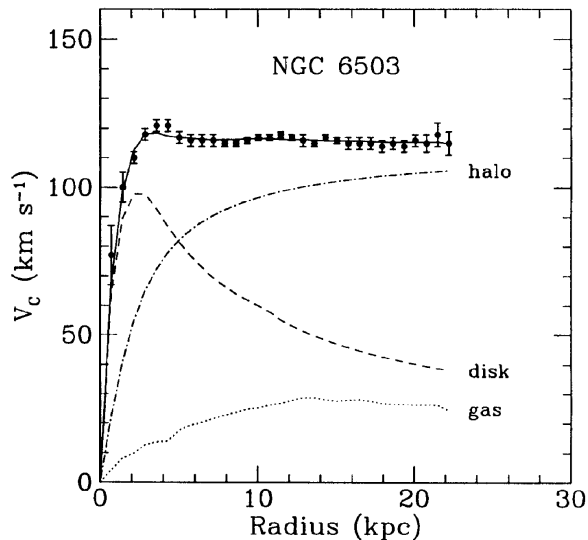


Figure 4.2: Rotational curve of the NGC6503 galaxy, broken down to its individual components. For small radii, gravitational potential stems from the matter in the galactic disk, whereas for larger radii the influence of the DM halo is clearly dominant. Figure is taken from Ref. [87].

4.2.1 Rotation curves of galaxies

The most convincing and direct evidence for dark matter on galactic scales comes from the observations of the rotation curves of galaxies, namely the graph of circular velocities of stars and gas as a function of their distance from the galactic center [88]. Indeed, according to the Kepler law, rotation curves of galaxies should decrease with the distance r to the center of the galaxy beyond the optical disc, as

$$v(r) = \sqrt{\frac{GM(r)}{r}} \quad (4.7)$$

while observation indicate that they remain constant far from the galactic center. Here, as usual, $M(r) = 4\pi \int \rho(r)r^2 dr$, and $\rho(r)$ is the mass density profile. One way to solve this problem is to postulate the existence of a dark halo of mass $M_{\text{dark}}(r)$ which increases proportionally to the distance r from the center of the galaxy¹.

¹Another way to solve the problem would be through modifications of Newton's law of gravity. This approach is commonly referred as Modified Newtonian dynamics (MOND) [89].

4.2.2 Gravitational lensing

Strong gravitational lensing magnifies and distorts light from a source, generating \tilde{U} depending on the case \tilde{U} Einstein rings, luminous arcs or even multiple images. This effect is used to estimate the dark matter distribution in clusters of galaxies and it revealed that the mass enclosed in such clusters is clearly dominated by a dark component [90]. Although this definitely indicates that there is more dark matter than luminous matter in clusters, this method does not give a precise information on the nature of dark matter (Fig. 4.3).

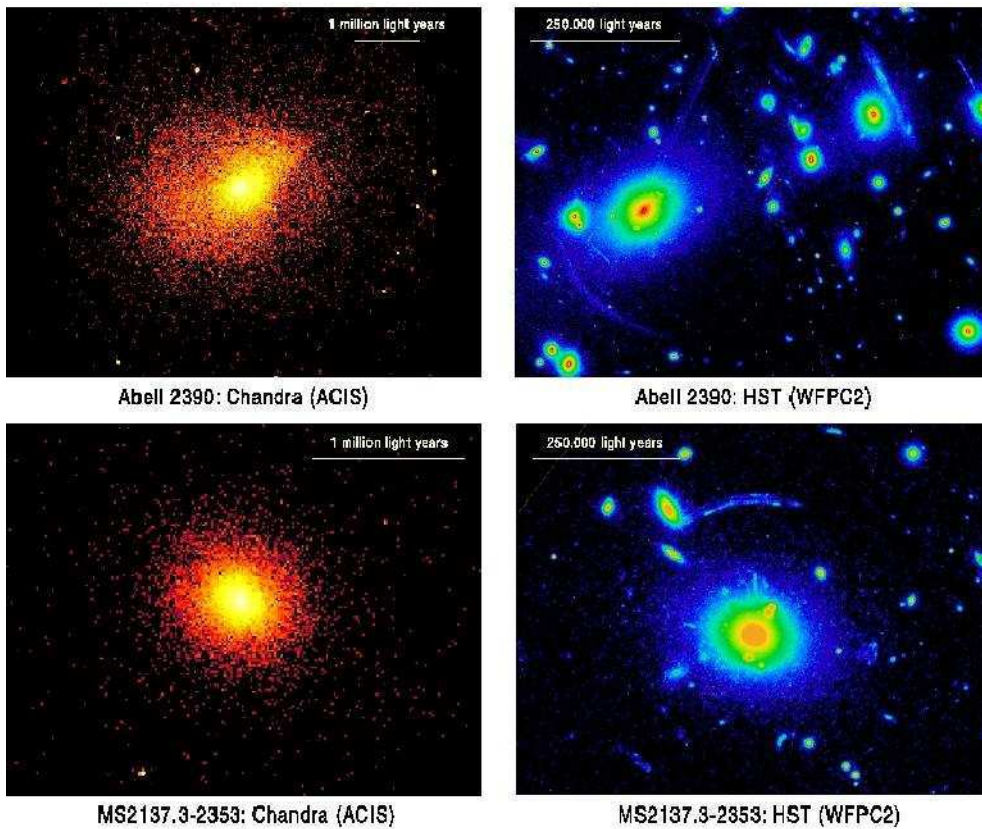


Figure 4.3: Chandra X-ray (left) and Hubble Space Telescope Wide Field Planetary Camera 2 optical (right) images of Abell 2390 ($z = 0.230$) and MS2137.3-2353 ($z = 0.313$). The gravitational arcs are clearly seen in the Hubble images. Extracted from Ref. [88].

A particularly compelling example involves the bullet cluster (1E0657-558) which recently (on cosmological time scales) passed through another cluster. As a result,

the hot gas, traced by its X-ray emission, which forms most of the clusters baryonic mass was shocked and decelerated, whereas the galaxies in the clusters proceeded on ballistic trajectories. Gravitational lensing shows that most of the total mass also moved ballistically, indicating that DM self-interactions are indeed weak (see Fig. 4.4)¹.



Figure 4.4: Composites image of the Bullet cluster (1E 0657-56) of an X-ray image from the Chandra X-Ray Observatory and a visible light image from the Hubble Space Telescope. The pink clumps are hot gas in the X-ray image that contain most of the normal baryonic matter in the two colliding clusters. The blue areas, on the other hand, show where the mass in the clusters is concentrated based on measurements of gravitational lensing in the optical image. The blue and pink regions are clearly separated, indicating that most of the mass in the clusters is dark matter. Figure extracted from Ref. [91].

4.2.3 Primordial Big-Bang Nucleosynthesis

An essential element of the standard cosmological model is Big-Bang nucleosynthesis (BBN), the theory which predicts the abundances of the light element isotopes D, ^3He , ^4He , and ^7Li [80]. Nucleosynthesis takes place at a temperature scale of order 1 MeV.

¹Interestingly, MOND theories cannot explain this results without the introduction of a new massive particle.

4. Cold Dark Matter

The nuclear processes lead primarily to ${}^4\text{He}$, with a primordial mass fraction of about 25%. Lesser amounts of the other light elements are produced: about 10^{-5} of D and ${}^3\text{He}$ and about 10^{-10} of ${}^7\text{Li}$ by number relative to H. The abundances of the light elements depend almost solely on one key parameter, the baryon-to-photon ratio η . The nucleosynthesis predictions can be compared with observational determinations of the abundances of the light elements. Consistency between theory and observations leads to a conservative range of η (see Figure 4.5):

$$5.1 \times 10^{-10} < \eta < 6.5 \times 10^{-10}. \quad (4.8)$$

On the other hand, η is related to the baryons energy density Ω_b by

$$\Omega_b h^2 = 3.66 \times 10^7 \eta, \quad (4.9)$$

which gives a value of $\Omega_b h^2 \simeq 0.02$. Hence, for $h = 0.7$, the baryon fraction is of the order of $\Omega_b \sim 0.04$: approximately only four percent of the universe density is due to ordinary matter. Moreover this value is about five times smaller than the observed present total matter density $\Omega_m h^2 \simeq 0.13$. Thus a significant matter content of the Universe has to come from a non-baryonic dark component.

4.2.4 CMB observations and the Silk damping

As already mentioned the analysis of CMB anisotropies enables accurate testing of cosmological models and puts stringent constraints on cosmological parameters. The observed temperature anisotropies are usually expanded in spherical harmonics [88] as

$$\frac{\delta T}{T}(\theta, \phi) = \sum_{l=2}^{+\infty} \sum_{m=-l}^{+l} a_{lm} Y_{lm}(\theta, \phi), \quad (4.10)$$

where $Y_{lm}(\theta, \phi)$ are spherical harmonics. The variance C_l of a_{lm} is given by

$$C_l \equiv \langle |a_{lm}|^2 \rangle \equiv \frac{1}{2l+1} \sum_{m=-l}^l |a_{lm}|^2. \quad (4.11)$$

If all perturbations in the universe are stochastic and Gaussian, as appears to be the case, all of the information contained in CMB maps can be compressed into the power spectrum, essentially giving the behavior of C_l as a function of l . Usually plotted is $l(l+1)C_l/2\pi$ (see Fig. 4.6). Assuming a cosmological model (Λ CDM for example)

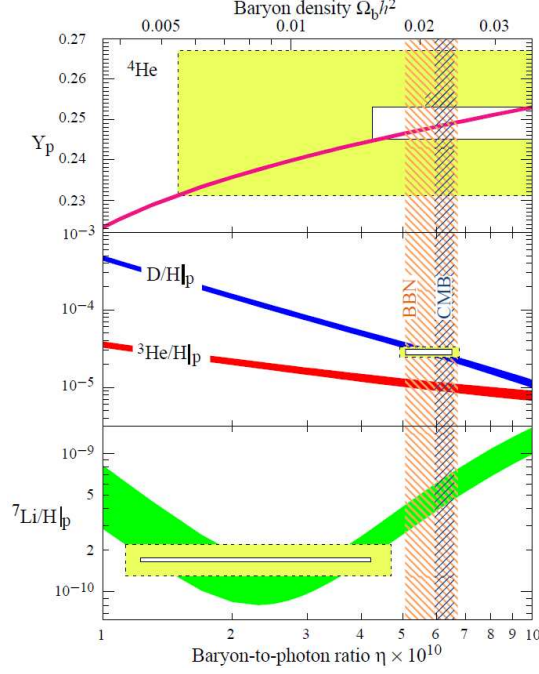


Figure 4.5: The abundances of ${}^4\text{He}$, D, ${}^3\text{He}$, and ${}^7\text{Li}$ as predicted by the standard model of Big-Bang nucleosynthesis - the bands show the 95% C.L. range. Boxes indicate the observed light element abundances (smaller boxes: $\pm 2\sigma$ statistical errors; larger boxes: $\pm 2\sigma$ statistical and systematic errors). The narrow vertical band indicates the CMB measure of the cosmic baryon density, while the wider band indicates the BBN concordance range (both at 95% C.L.). Extracted from Ref. [80].

with a fix number of parameters, the best-fit parameters can be determined from the peak of the N-dimensional likelihood surface. Several effects need to be taken into account in order to match a theoretical power spectrum to the observed one, and a full understanding of the cosmological perturbations evolution during several stages of the Universe history is needed.¹ With the analysis of the WMAP data alone the abundances of baryons and matter in the Universe were found

$$\Omega_b h^2 = 0.024 \pm 0.001 \quad \Omega_m h^2 = 0.14 \pm 0.02, \quad (4.12)$$

which implies a large amount of non-baryonic matter to account for it. The value of $\Omega_b h^2$ thus obtained is consistent with the results from Big Bang nucleosynthesis.

¹A full description of the CMB theory goes beyond the scope of this work, but excellent introductions to CMB theory can be found in the literature [see for instance, 80, 92].

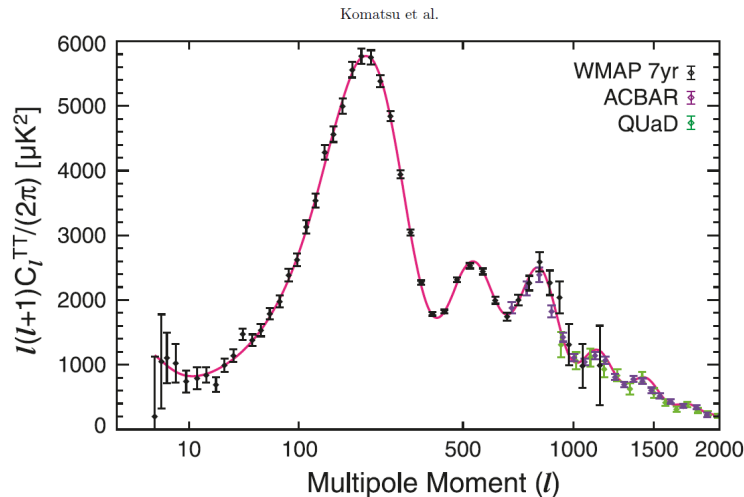


Figure 4.6: The WMAP 7-year temperature power spectrum [93], along with the temperature power spectra from the ACBAR¹ [94] and QUaD [95] experiments. The ACBAR and QUaD data is only showed at $l \geq 690$, where the errors in the WMAP power spectrum are dominated by noise. The solid line shows the best-fitting 6-parameter flat Λ CDM model to the WMAP data alone. Extracted from Ref. [83].

An interesting effect affecting the CMB temperature spectrum is the so-called Silk damping effect. In cosmological theory, diffusion damping, also called photon diffusion damping, is a physical process which reduced anisotropies in the early universe, making the universe itself and the cosmic microwave background radiation (CMB) more uniform. This question was first addressed by Misner in 1967 [96] who wondered whether or not the neutrino-electron interactions could damp the small matter fluctuations introduced by Peebles in 1965 [97] to explain the formation of large-scale structures. J. Silk noticed in 1967 and 1968 [98, 99] that electromagnetic interactions, which happened just after the photons left the thermal equilibrium of the initial hot \S soup \check{T} (photon decoupling), could damp the baryonic fluctuations up to 1 Mpc. This basically means that no (or too few) Milky Way-size galaxy should have formed. Hence the Silk damping forbids the hypothesis of a baryonic matter dominated Universe and, in fact, can be seen as the first theoretical evidence in favor of non baryonic dark matter [86]. Indeed by postulating that the Universe is dominated by a neutral weakly-interacting massive particle, the gravitational potentials created by the latter would not undergo the Silk damping, thus allowing the existence of gravitational structures smaller than 1 Mpc. The Silk damping can be easily seen in the suppression of power peaks at small scale

($l \gtrsim 800$) on Figure 4.6.

4.3 Dark matter density distribution in the Universe

4.3.1 Cosmological N-body numerical simulations

The hierarchical formation of structures is due to the gravitational amplification of primordial density fluctuations during the Universe expansion. Theoretical approaches are far from being sufficient to describe the actual large scale distribution in the Universe, since the action of many physical processes like gas dynamics, radiative cooling, photoionization, recombination and radiative transfer would have to be properly treated and are rather complicated to be treated analytically. N-body numerical simulations are thus used in order to model the structures formation from density fluctuations in a non-linear regime. Notable examples of simulations are the Aquarius Project [100] and the Via Lactea Project [101]. Figure 4.7 presents a composite image of the projected dark matter density-square maps of the simulated Milky Way-size halo Via Lactea-1 at the various epochs.

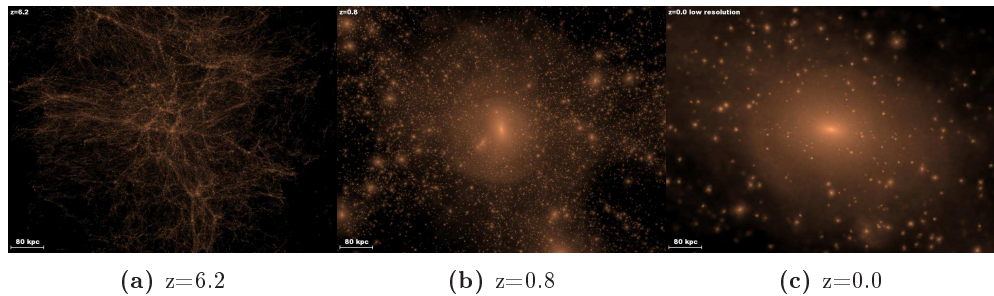


Figure 4.7: Projected DM density-square maps of the simulated Milky Way-size halo Via Lactea-1. Cubes of 800 proper kpc are shown at different redshifts z , always centred on the main progenitor halo.

The evolution of structures is then approximated with non-linear gravitational clustering from specified initial conditions of dark matter particles and can be refined by introducing the effects of gas dynamics, chemistry, radiative transfer and other astrophysical processes. However until very recently simulations used only CDM, and thus include only the gravitational force. Incorporating baryons into the simulations

4. Cold Dark Matter

dramatically increases their complexity and in the past, radical simplifications of the underlying physics was made. The reliability of an N-body simulation is measured by its mass and length resolution. The mass resolution is specified by the mass of the smallest (Elementary) particle considered, being the scale below which fluctuations become negligible. Length resolution is limited by the so-called softening scale, introduced to avoid infinities in the gravitational force when elementary particles collide [88].

N-body simulations of cosmological structures with CDM agree in general that DM is distributed in the form of halos surrounding galaxies and galaxy clusters. However N-body simulations tend to predict DM halo profiles which are too cuspy at the innermost parts of the halo. Meaning that the DM density distribution increases too fast at distances close to the center. This result appears to be in disagreement with the flat cores observed in astrophysical systems, such as low surface brightness galaxies [102]. Only results from more recent N-body simulations suggest actually a lack of a definite inner slope: the density profile of the now better resolved DM haloes would continue to flatten with decreasing radius (e.g., Navarro et al. 2004; Merritt et al. 2005, 2006; Graham et al. 2006). In fact, in galaxies, groups and clusters the central regions are dominated by the baryons. Predictions on the dark matter and total mass distribution require a realistic treatment of the baryons and their dynamical interactions with the dark matter. However very recent attempts to include the effect of baryons in the DM halo formation, such as H_2 and metal cooling, star formation (SF) and supernovae-driven gas outflows [103, 104], are not yet conclusive.

Moreover recent cosmological N-body simulations, such as Aquarius [100] and Via Lactea [101], have suggested the presence of dark matter substructures in the form of self-bound overdensities within the main halo of galaxies. These substructures may play an important role in DM searches through γ -rays as it will be treated in the next chapter. Also the most used predicted DM halo profiles are going to be discussed in the next chapter.

4.3.2 Distribution in different scales

- Milky Way

The central part of the Milky Way (MW) DM halo profile is still very uncertain. However microlensing optical depth observations of the center of the Galaxy by EROS-II showed that the matter distribution is dominated by baryons [105]. The modelisation of the bulge and the galactic disk gives a good estimation of the visible matter contribution to the rotation curve of the Milky Way. The DM halo can be then be deduced, and it is well fitted by an isothermal halo distribution with a flat density distribution towards the center [106]. However, due to the uncertainties on the DM density distribution in the inner kiloparsec of the MW, several DM density profiles were used in the literature and normalized to the local DM density (see Fig 4.8).

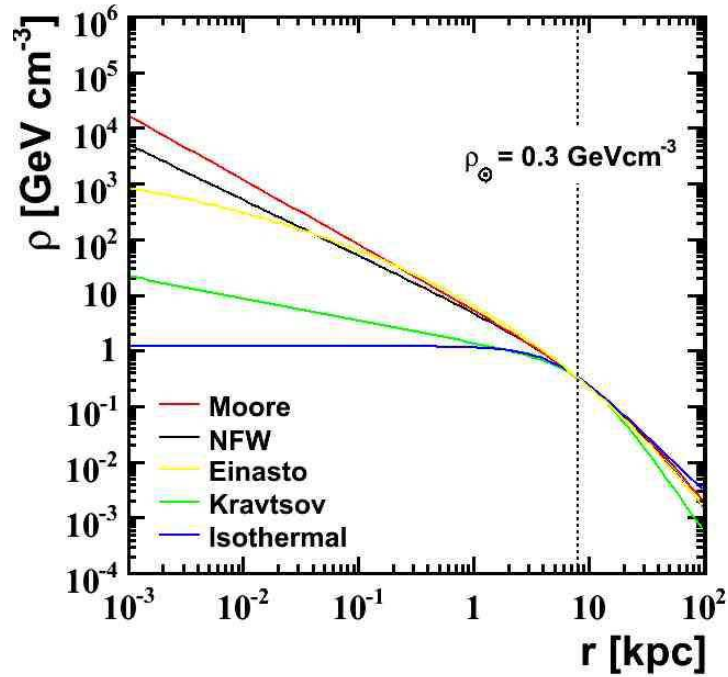


Figure 4.8: DM density distribution of the MW normalized to the local DM density $\rho_{\odot} = 0.3 \text{ GeV cm}^{-3}$ ¹. Several DM density profiles are used. For more details about the different density profiles parameterizations, see Section 5.2.

¹The local dark matter density can be constrained through a determination of the dependence of the gravitational potential on distance above the mid-plane of the disk, from measuring the kinematics

4. Cold Dark Matter

Recently, near-infrared high-resolution imaging and spectroscopic observations of individual stars, as close as a few light days from the galactic center, were carried out at Keck [108] and ESO/VLT telescopes [109]. The analysis of the orbital parameters of such stars suggest the existence of a Super Massive Black Hole (SMBH) lying at the center of the Galaxy, with a mass of $(2.87 \pm 0.15) \times 10^6 M_\odot$ [110]. It has been proposed that (see e.g. Ref. [111]), under certain assumptions, the process of adiabatic accretion of DM by SMBH would produce a “spike” in the center of the halo, modifying the DM density profile for distances inferior to 1 kpc. If the SMBH grew to its final size in the simplest possible way \tilde{U} via spherically symmetric infall of gas \tilde{U} it would pull the dark matter and increase its density in the process [111, 112]. In the limit that the growth timescale of the SMBH is long compared with orbital periods, this scenario predicts a final density (of stars or dark matter) near the SMBH of

$$\rho_f(r) \approx \rho_i(r_f)(r/r_f)^{-\gamma_f}, \quad \gamma_f = 2 + 1/(4 - \gamma_i), \quad (4.13)$$

where $\rho_i \propto r^{-\gamma_i}$ is the pre-existing density profile and $r_f \approx 0.2r_h$, with r_h being the SMBH gravitational influence radius¹. Gondolo and Silk [113] have estimated that such a steep DM density profile near the SMBH would imply very high rates of DM self-annihilation signals, which would significantly improve the possibility of detection of such signals coming from the GC.

• Dwarf galaxies, satellites of the Milky Way

The Milky Way has tens of very faint satellite galaxies with luminosities of the order of $10^6 L_\odot$ down to $10^3 L_\odot$. These dwarf galaxies are very hard to be detected, and only recently they were discovered by survey programs as 2MASS and SDSS [114, 115]. The predictions of N-body simulations that dark matter substructures should exist in the Galaxy, suggest that such dwarf galaxies may be the most massive manifestation of these DM substructures. However, the number of detected dwarf galaxies are still too few compared to the N-body simulations predictions, configuring the so-called “missing satellites” problem [116].

of stars. The most recent studies found a dark matter density of $0.3 \pm 0.1 \text{ GeV cm}^{-3}$ [107].

¹ $r_h = GM_{\text{SMBH}}/\sigma^2$, where M_{SMBH} is the SMBH mass and σ^2 is the one-dimensional rms velocity of stars in the spheroid.

Dwarf galaxies of the Local Group can be classified into two types, based on their luminosity and morphology: dwarf elliptical galaxies and dwarf spheroidal galaxies. Measurements of the stars dynamics within dwarf galaxies and their surface luminosity showed that these object have a high mass-to-light ratio ($M/L_V \sim 10 - 100$), thus gravitationally dominated by DM [117, 118]. However, due to tidal forces from the Milky Way, the DM halo of dwarf galaxies might have been modified from what is predicted by N-body numerical simulations. Indeed, the last estimations of DM density distributions inside several dwarf galaxies from the measurements of their stars velocity dispersion have been well described by both cuspy or cored DM halo profiles (see Figure 4.9).

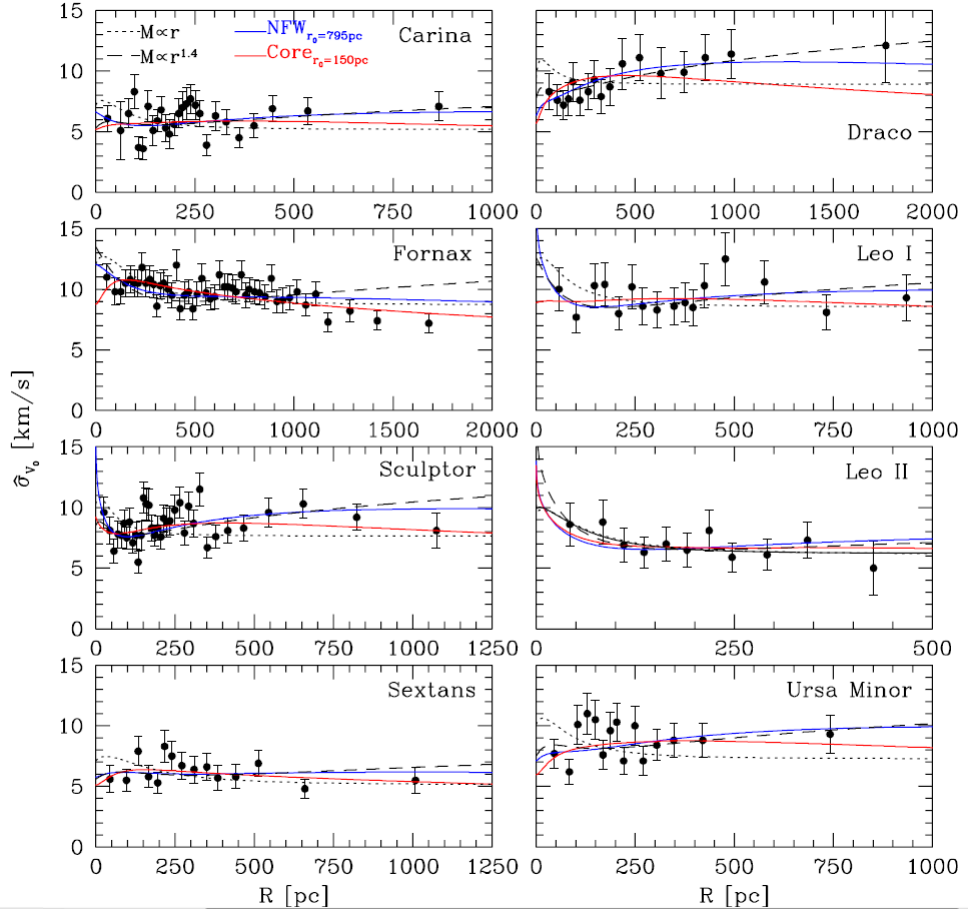


Figure 4.9: Projected velocity dispersion profiles for eight bright dwarf spheroidal galaxies. Overplotted are profiles calculated from NFW and cored halos (see chapter 5 for the parameterization of these profiles). In general both cuspy and cored DM halo profiles can well describe the stellar dynamics inside dwarf galaxies. Extracted from Ref. [119].

- **Galaxy clusters scale**

The mass of a cluster can be determined via several methods, including application of the virial theorem to the observed distribution of radial velocities of gravitational tracers, by weak and strong gravitational lensing, and by studying the profile of X-ray emission that traces the distribution of hot emitting gas in rich clusters. Combining X-ray and gravitational lensing measurements allowed to estimate the existence of a substantial amount of dark matter in clusters. Plus, the distortion of the images of background objects due to the gravitational mass of a cluster can be used to infer the shape of the potential well. Finally, the fraction of baryons inside a cluster, crucial to disentangle the contributions of ordinary (visible) and dark matter, can also be inferred through the so-called *Sunyaev-Zel'dovich effect* by which the cosmic microwave background gets spectrally distorted through Compton scattering on hot electrons [88]. A different approach is to use Jeans equation solutions (see Section 5.2.1 for details) from the observation of dynamical tracers of the gravitational potential of the cluster halo, such as stars, globular clusters, planetary nebulae or galaxies. This method is limited by the observability of such tracers, but can yield less model-dependent and more robust modeling of the DM distribution. Figure 4.10 shows the radial mass profile of the galaxy M87 located at the center of the Virgo galaxy cluster, obtained with several different tracers at different distance scales from its center.

The DM halo distribution within galaxy clusters appears to be well reproduced by N-body numerical simulations at large radii [121, 122, 123, 124, and references therein]. However, it is unclear whether there is agreement with the predicted profiles in the inner parts of clusters. For instance, gravitational lensing measurements appear to be in conflict with spherically symmetric cuspy DM halo profiles [125]. In addition it has been shown that the influence of baryon infall in the DM gravitational potential can still flatten the DM density distribution in the inner regions of galaxy clusters [see, for instance, 126]. On the other hand, recent Chandra observations of X-ray emission from Abell 2029 suggest a full compatibility of dark matter distributions with cuspy profiles. In this work both cored and cuspy profiles are going to be used in order to describe the DM density distribution inside galaxy clusters (see chapter 8).

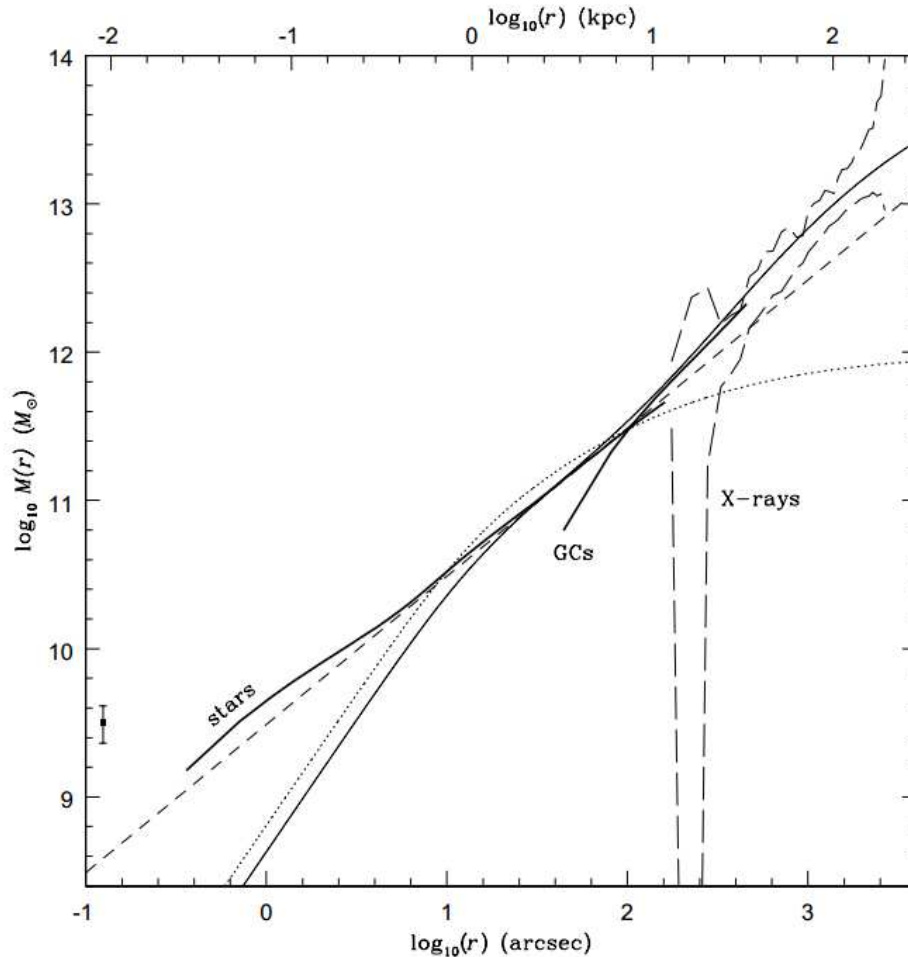


Figure 4.10: Radial mass profile of M87 located at the center of the Virgo galaxy cluster. The heavy solid lines show estimates from the Jeans equations using the stars and globular clusters separately. The long-dashed lines show confidence limits from X-ray analysis. The best orbit models fitted to the combined star and GC data for an isothermal DM halo profile (dashed line) and a NFW DM halo profile (light solid line) are also plotted. Extracted from Ref. [120].

4.4 Dark matter candidates

4.4.1 Neutrinos

The first natural candidate which was proposed to account for the DM particle were the neutrinos. In the Standard Big-Bang cosmological model, knowing the CMB temperature $T_\gamma = 2.725$ K, if neutrinos have mass in the range 5×10^{-4} eV to 1 MeV, the

4. Cold Dark Matter

density parameter of neutrinos is predicted to be [127]

$$\Omega_\nu h^2 = \frac{\sum m_\nu}{93\text{eV}}, \quad (4.14)$$

where the sum is over all families with mass in that range. Results on atmospheric and Solar neutrino oscillations [128] imply non-zero mass-squared differences between the three neutrino flavors. The most stringent upper bounds on the ν mass were obtained in the Troitzk [129] and Mainz [130] by measuring the spectrum of electrons near the end point in ^3H β -decay experiments at

$$m_\nu < 2.05\text{ eV (95\%C.L.)}. \quad (4.15)$$

The above upper limit applies to all three mass eigenvalues [80], since the mass differences among them must be very small to explain solar ($\Delta m^2 \approx 7 \times 10^{-5}\text{ eV}^2$) and atmospheric ($\Delta m^2 \approx 3 \times 10^{-3}\text{ eV}^2$) neutrino anomalies. This implies an upper bound on the total relic density of

$$\Omega_\nu h^2 \lesssim 0.07, \quad (4.16)$$

which means that neutrinos are simply not abundant enough to be the dominant component of dark matter. Additionally, being relativistic collisionless particles, neutrinos would erase (moving from high to low density regions) fluctuations below a scale of $\sim 40\text{ Mpc}(m_\nu/30\text{ eV})$, called the free-streaming length [88]. This would imply that big structures would have to be formed first in the formation history of structure in the Universe. The fact that the Milky Way appears to be older than the Local Group, and the discrepancy between the predicted late formation of galaxies, at redshift $z \lesssim 1$, against observations of galaxies around $z > 4$, is a further argument against neutrinos as a viable dark matter candidate [88].

Another possibility to explain the DM still in the neutrino sector is the existence of states of relativistic neutrinos (antineutrinos), which are predominantly right-handed (left-handed). At present there is no compelling evidence for their existence. If such neutrinos exist they should not interact with matter through standard weak interactions [80], but only communicate with the rest of the neutrino sector through fermion mixing, therefore called “sterile” or “inert” neutrinos. They are limited by a variety of observational data [131], but it seems that, e.g, a region below 10 keV for

very small mixing angles is allowed.

In this work, however, constraints on DM scenarios are going to be derived in the energy range scale of a few hundreds of GeV up to tens of TeV. So neutrinos are not going to be tested in the present work. The next sections describe the two most broadly used DM particle candidates, coming from extensions of the Standard Model (SM) of particle physics, which predict viable DM particles with masses in the range of a few GeV to tens of TeV.

4.4.2 Supersymmetric dark matter

Supersymmetry (SUSY) is a generalization of the space-time symmetries of quantum field theory that transforms fermions into bosons and vice versa. Supersymmetry is an ingredient in many superstring theories which attempt to unite all the fundamental forces of nature, including gravity. In most versions of the low-energy theory there is, to avoid, for example, excessive baryon number violating processes, a conserved multiplicative quantum number, R-parity [85]:

$$R = (-1)^{3(B-L)+2S}, \quad (4.17)$$

where B is the baryon number, L the lepton number and S the spin of the particle. This implies that $R = +1$ for ordinary particles and $R = -1$ for supersymmetric particles. This means that supersymmetric particles can only be created or annihilated in pairs in reactions of ordinary particles. It also means that a single supersymmetric particle can only decay into final states containing an odd number of supersymmetric particles. In particular, this makes the lightest supersymmetric particle (LSP) stable, since there is no kinematically allowed state with negative R-parity which it can decay to, and thus making it an excellent dark matter candidate [85].

A disadvantage of a full supersymmetric model (even making the particle content minimal, the Minimal Supersymmetric Standard Model, MSSM) is that the number of free parameters is excessively large - of the order of 100. Therefore, most treatments have focused on constrained models, such as minimal supergravity (mSUGRA) models [132], which is a constrained MSSM and where one has the opportunity to explain

4. Cold Dark Matter

electroweak symmetry breaking by radiative corrections caused by running from a grand-unification scale down to the electroweak scale.

The MSSM is minimal in the sense that it contains the smallest possible field content necessary to give rise to all the fields of the Standard Model. The procedure to derive the MSSM is the following

- Each gauge field is associated to a fermionic superpartner. Gluons, W^\pm and B bosons then get fermionic partners called *gluinos* (\tilde{g}), *winos* (\tilde{W}^i) and *binos* (\tilde{B}), respectively. The common name for all partners of gauge fields is the *gaugino*.
- Each fermion is associated to a scalar partner, *i.e.*, quarks and leptons get scalar partners called *squarks* and *sleptons*.
- One additional Higgs field is introduced (for a total of two Higgs doublets, corresponding to five physical Higgs states) and to each Higgs boson a spin 1/2 *Higgsino* is associated. This is done to give masses to both up and down-type quarks upon electroweak symmetry breaking and also preserve supersymmetry [88]. Introducing another Higgs doublet also makes the theory anomaly free.

The resulting particle content of the theory is shown in Figure 4.11.

The nature of the LSP in the MSSM is constrained by many observations. It cannot have a non-zero electric charge or color, or it would have condensed with baryonic matter to produce heavy isotopes, in conflict with observations. Among the neutral candidates, the lightest neutralino is most promising candidate for DM particle, with possibilities for discovery in direct detection [85] and in various channels of indirect detection (γ -rays for example).

4.4.3 Universal extra dimension

Kaluza-Klein (KK) particles are new particles which appear in extra dimensions theories. In such theories the usual 4-dimension space-time is seen as a structure, called *brane*, which is embedded in a $(3+\delta+1)$ space-time called the *bulk*. Generally, in most of the extra dimensions scenarios (see for instance Arkani-Hamed, Dimopoulos and Dvali (ADD) [133] or Randall-Sundrum [134] scenarios), the SM fields are confined

Standard Model particles and fields		Supersymmetric partners			
Symbol	Name	Interaction eigenstates Symbol	Name	Mass eigenstates Symbol	Name
$q = d, c, b, u, s, t$	quark	\tilde{q}_L, \tilde{q}_R	squark	\tilde{q}_1, \tilde{q}_2	squark
$l = e, \mu, \tau$	lepton	\tilde{l}_L, \tilde{l}_R	slepton	\tilde{l}_1, \tilde{l}_2	slepton
$\nu = \nu_e, \nu_\mu, \nu_\tau$	neutrino	$\tilde{\nu}$	sneutrino	$\tilde{\nu}$	sneutrino
g	gluon	\tilde{g}	gluino	\tilde{g}	gluino
W^\pm	W -boson	\tilde{W}^\pm	wino	} $\tilde{\chi}_{1,2}^\pm$	chargino
H^-	Higgs boson	\tilde{H}_1^-	higgsino		
H^+	Higgs boson	\tilde{H}_2^+	higgsino		
B	B -field	\tilde{B}	bino	} $\tilde{\chi}_{1,2,3,4}^0$	neutralino
W^3	W^3 -field	\tilde{W}^3	wino		
H_1^0	Higgs boson	\tilde{H}_1^0	higgsino		
H_2^0	Higgs boson	\tilde{H}_2^0	higgsino		
H_3^0	Higgs boson				

Figure 4.11: Standard Model particles and their superpartners in the MSSM. Extracted from Ref. [88].

in the brane and only gravity can propagate in the bulk. Scenarios in which all fields are allowed to propagate in the bulk are called Universal Extra Dimensions (UED).

Extra dimensions are compactified on circles (or other topology) of some size R , and a general feature of extra-dimensional theories is that upon compactification of the extra dimensions, all of the fields propagating in the bulk have their momentum quantized in units of $p^2 \sim 1/R^2$. The result in UED model is that for each SM field, a set of Fourier expanded modes, called Kaluza-Klein (KK) states, appears as a series (called a tower) of states with masses $m_n = n/R$, where n labels the mode number (see Figure 4.12). These KK states are also called KK particles.

The lightest KK particle (LKP) is an interesting, viable particle dark matter candidate arising from UED models. For the LKP to be a well-motivated dark matter candidate, it should be electrically neutral and non-baryonic. Thus, the most promising candidates in the minimal treatment of radiative corrections of UED picture are first level KK modes of the neutral hypercharge gauge bosons (analogues of the KK modes of the photon and Z), called $\tilde{B}^{(1)}$ particle and the KK neutrino, $\nu^{(1)}$. However, KK neutrinos were found to generate unacceptably large rates in direct detection experiments in [136]. Here the $\tilde{B}^{(1)}$ particle is taken as the LKP.

4. Cold Dark Matter

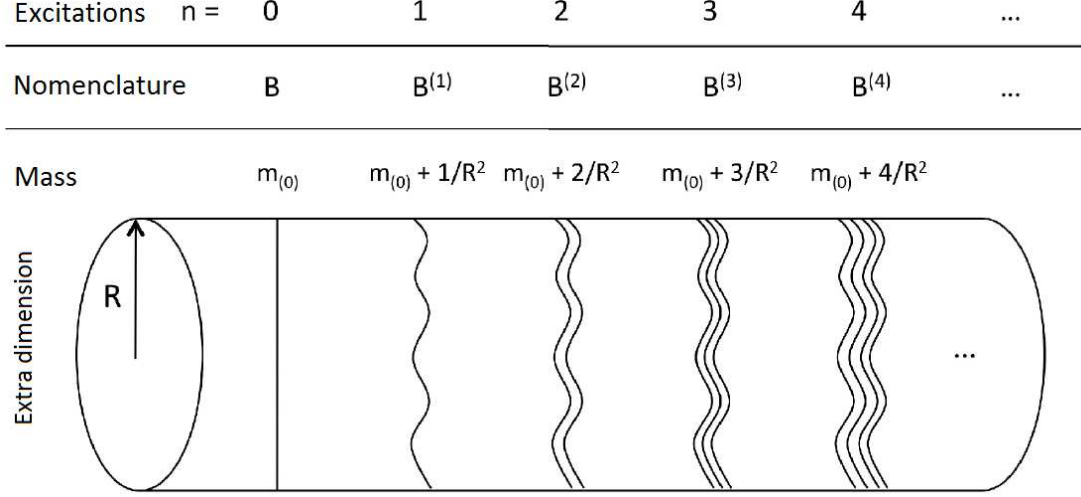


Figure 4.12: Representation of different Kaluza-Klein states. Here only one compactified extra dimension is represented. Figure adapted from Ref. [135].

The relic density of $\tilde{B}^{(1)}$ was calculated by Servant and Tait [136], who found that it is compatible with the measured Ω_{CDM} if its mass (which is inversely proportional to the compactification radius R) lies in the range of 400 to 1200 GeV [136]. The spectrum of first level KK states has been calculated to one loop by Cheng et al. [137]. The branching ratios for $\tilde{B}^{(1)}$ annihilation (see Table 4.2) are almost independent of the particle mass. Unlike in the case of supersymmetry, the bosonic nature of the LKP means that there will be no chirality suppression in its annihilations, and thus can annihilate efficiently to fermion-fermion pairs. In particular, since the annihilation cross section is proportional to hypercharge of the final state, a large fraction of LKP annihilations produce charged lepton pairs.

Annihilation channel	Branching ratio
charged lepton pairs	59%
quark pairs	35%
neutrino pairs	4%
Gauge bosons	1.5%
Higgs boson	0.5%

Table 4.2: Branching ratios of the different annihilation channels of the $\tilde{B}^{(1)}$ particle.

The predicted $\tilde{B}^{(1)}$ self-annihilation cross section has been calculated in [136] in a minimal UED framework, and is given by

$$\langle\sigma v\rangle \approx \frac{95g_1^4}{324\pi m_{\tilde{B}^{(1)}}^2} \simeq 0.4 \times 10^{-26} \text{cm}^3 \text{s}^{-1} \left(\frac{1 \text{TeV}}{m_{\tilde{B}^{(1)}}} \right)^2, \quad (4.18)$$

where g_1 is the gauge coupling of the $U(1)_Y$. However these predictions can change in extensions of this UED model [138], where for example the mass splitting between the LKP and the next lightest KK particle is too small. The evolution of the predicted $\langle\sigma v\rangle$ as function of this mass splitting is showed in Figure 4.13.

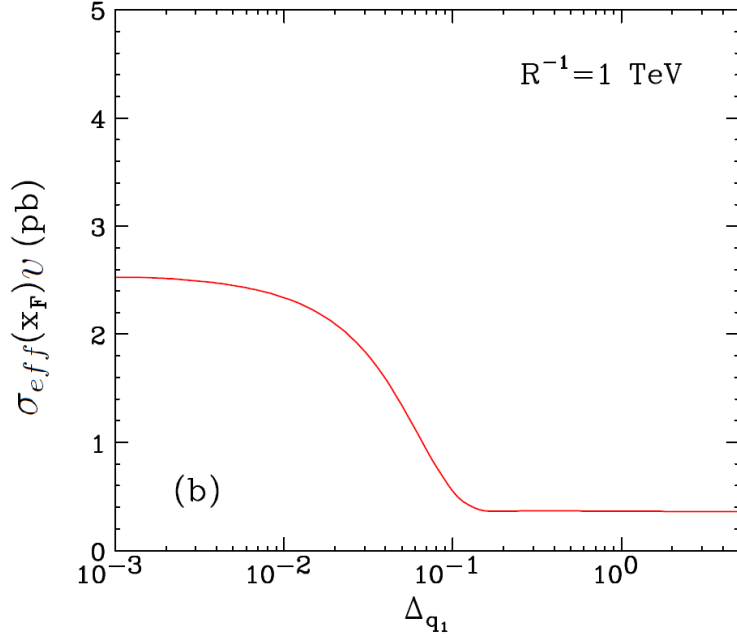


Figure 4.13: LKP effective annihilation cross section $\sigma_{eff}v$ as a function of the mass splitting Δ_{q_1} between the LKP and the next LKP, for a extra dimension of $R^{-1} = 1$ TeV. Figure adapted from Ref. [138].

4. Cold Dark Matter

Chapter 5

Exclusion and sensitivity limits to dark matter annihilation

Contents

5.1	γ-ray flux from dark matter annihilation	95
5.2	Dark matter halo modelling	96
5.2.1	Halo profile parameters determination	99
5.2.2	Dark matter halo substructures	103
5.3	γ-ray final spectra	105
5.4	γ-ray flux enhancement effects	106
5.4.1	Radiative correction : Internal Bremsstrahlung	106
5.4.2	Inverse compton process	108
5.4.3	The Sommerfeld effect	112
5.5	Limits on the dark matter annihilation cross section	114
5.5.1	Exclusion limits	115
5.5.2	Sensitivity limits	116

Introduction

The Standard Model of Cosmology assumes that in the early Universe dark matter particles, in the form of WIMPs, were produced in collisions between particles of the thermal plasma during the radiation-dominated era. Production and annihilation of DM particle pairs into Standard Model (SM) particles were the main reactions taking place and controlling the initial thermal equilibrium. After freeze out, DM pair annihilation becomes greatly suppressed. However, even if nowadays its impact on the dark matter relic density must be negligible, dark matter still annihilates and may be observable in dense environments. Dark matter may therefore be detected indirectly: dark matter pair-annihilates somewhere, creating as sub-product of annihilation SM particles, which might then be detected. There are many indirect detection methods being pursued. Their relative sensitivities are highly dependent on which WIMP candidate is being considered, and the systematic uncertainties and difficulties in determining backgrounds also vary greatly from one method to another (see Feng [139]). Among the sub-products used as probes for indirect DM searches the predominant are neutrinos, positron and electrons, and γ -rays.

Searches for neutrinos coming from DM annihilation have been performed by several experiments. Constraints on the DM particle annihilation cross section were derived by the IceCube Collaboration [140] from the null excess of neutrinos coming from the annihilation of DM particles in the Galactic halo (see figure 5.1a). Searches for neutrinos have the peculiarity of probing not only the DM annihilation cross section, but also the scattering cross section of a DM particle when looking towards the Sun. The idea behind is the following: when WIMPs pass through the Sun, they may scatter and be slowed below escape velocity. Over the lifetime of the Sun, a sufficient density of WIMPs may have accumulate in its center so that an equilibrium is established between their capture and annihilation rates. Although most of their annihilation products are immediately absorbed, neutrinos are not. Some of the resulting neutrinos then travel to the Earth, where they can be efficiently identified using large volume neutrino detectors. Under some general assumptions the neutrino signal is completely determined by the capture rate in the Sun, that is, the scattering cross section. The Super-Kamiokande, IceCube, and AMANDA Collaborations have looked for excesses of neutrinos from the

Sun with energies in the range $10 \text{ GeV} \lesssim E_\nu \lesssim 1 \text{ TeV}$. Their null results provide the leading bounds on spin-dependent scattering cross sections, as seen in Fig. 5.1. These experiments are just beginning to probe relevant regions of supersymmetric and UED parameter space [139, 141].

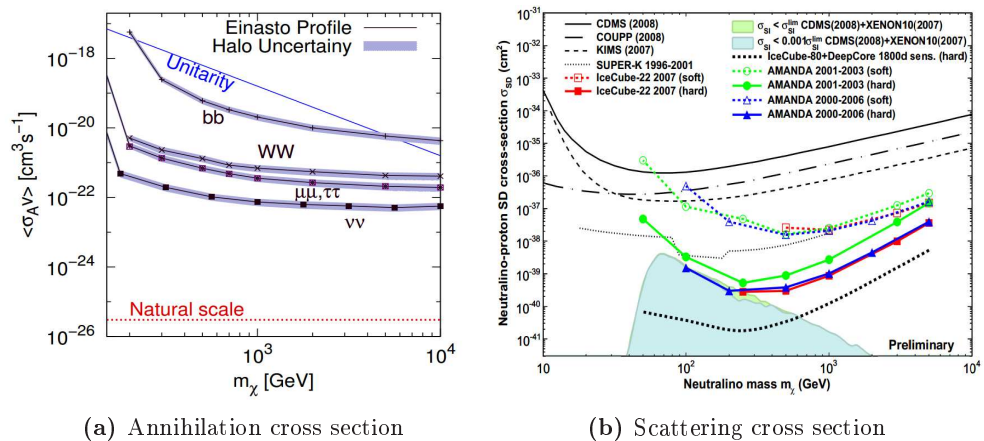


Figure 5.1: The current status of searches for dark matter using high-energy neutrinos. Left: Upper limit on the dark matter self annihilation cross section for five different annihilation channels for a Einasto DM Galactic halo density profile (see Section 5.2 for more details) with IceCube. Also shown are the natural scale (red dotted line), for which the WIMP is a thermal relic, and unitarity bound (blue line). From Ref. [140]. Right: Upper limits on spin-dependent WIMP-proton cross sections as function of the WIMP mass from several neutrino detectors (CDMS, IceCube, Super-K, KIMS and COUPP), along with preliminary limits from AMANDA and the projected 10-year sensitivity of IceCube with DeepCore are presented. The shaded regions are predictions for neutralino dark matter in the general minimal supersymmetric standard model with $0.05 < \Omega_{\text{cdm}} h^2 < 0.20$. For the data and references see Ref. [142].

Recent measurements of cosmic electron and positron spectra with energies between 10 GeV and 1 TeV by PAMELA [143], ATIC [144], H.E.S.S. [145] and *Fermi*-LAT [146] have been explained in terms of DM annihilation primarily into leptonic final states (to avoid an over-production of anti-protons). These data are shown in Figure 5.2, and reveal an excess above an estimate of the expected background, as modeled by a cosmic-ray diffusion simulations (GALPROP [147]). The PAMELA experiment measures only the flux of positron, and the ATIC and Fermi experiments are unable to distinguish positrons from electrons, and so constrain the total e^+e^- flux. The excess seen by ATIC was first in good agreement with the PAMELA data, however such

5. Exclusion and sensitivity limits to dark matter annihilation

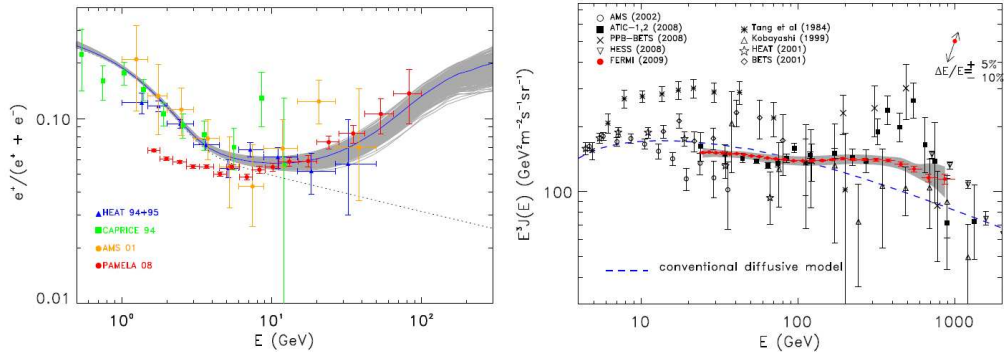


Figure 5.2: Left: the cosmic positron fraction measured by PAMELA and other experiments and the predictions of pulsars with various parameters (grey contours) (94). Right: the total e^+e^- flux measured by ATIC, Fermi, and other experiments [150]. In both cases, the dashed contours represent the predicted backgrounds from GALPROP [147].

prominent excess was not confirmed by neither the Fermi-LAT data, which has much higher statistics, nor the H.E.S.S. measurements. These results thus exacerbate the PAMELA discrepancy. However the PAMELA data was found to be consistent with standard expectations from nearby pulsars and supernova remnant, and thus may also have other more natural explanations than DM particles annihilation. Despite the astrophysical explanations, one may explore the possibility that the positron excesses arise from dark matter annihilation and constraints are derived for this scenario, for instance, in chapter 8 (see also [148] and [149] for more details).

The present work focus on the search for secondary γ -rays from annihilations of DM particles. The main advantages of this powerful indirect detection technique are:

- (i) γ -rays do not suffer deviation of their trajectories from propagation effects,
- (ii) the γ -ray signal should be proportional to the square of the DM density, and
- (iii) characteristic features such as bumps, steps or cut-offs may be present in the energy spectrum, given by the fact that no more energy than DM particle mass per particle can be released in the annihilation of two non-relativistic DM particles.

On the other hand γ -rays are also abundantly produced by astrophysical sources in electromagnetic and hadronic processes, thus the unambiguous identification of a DM emission above such astrophysical background is difficult, as it will be seen later. Imaging atmospheric Cherenkov telescopes (IACTs) such as HESS [50], MAGIC [51] and VERITAS [52], are particularly well suited for deep searches of targeted objects

because of their large effective areas ($\sim 10^5 \text{ m}^2$ above 100 GeV). However, since IACTs are multipurpose astrophysical experiments and have a relatively short duty cycle (~ 1000 hours/year), the observation time dedicated to these objects is typically limited to a few tens of hours per year.

Up to date no clear detection of a γ -ray signal coming from a DM annihilation has been confirmed. In the absence of a significant signal, constraints on DM models, from astrophysics and particle physics, can be derived. This chapter describes each step of the methodology used in order to extract these constraints, from the predicted γ -ray flux from DM annihilation to upper limits on the DM annihilation cross section from γ -ray observations.

5.1 γ -ray flux from dark matter annihilation

The γ -ray flux from the annihilations of DM particles of mass m_{DM} in a DM halo is given by a particle physics term times an astrophysics term:

$$\frac{d\Phi_\gamma(\Delta\Omega, E_\gamma)}{dE_\gamma} = \frac{1}{8\pi} \underbrace{\frac{\langle\sigma v\rangle}{m_{\text{DM}}^2} \frac{dN_\gamma}{dE_\gamma}}_{\text{Particle Physics}} \times \underbrace{\bar{J}(\Delta\Omega)\Delta\Omega}_{\text{Astrophysics}}, \quad (5.1)$$

where the astrophysical factor is defined as

$$\bar{J}(\Delta\Omega) = \frac{1}{\Delta\Omega} \int_{\Delta\Omega} d\Omega \int_{\text{l.o.s.}} \rho^2[r(s)] ds = \frac{J(\Delta\Omega)}{\Delta\Omega}. \quad (5.2)$$

In equation 5.2 the squared density distribution of DM (ρ^2) is integrated along the line of sight (l.o.s.) and over the solid angle $\Delta\Omega$. For point-like source search, for example, the solid angle is fixed as the angular resolution of the telescope. For the H.E.S.S. experiment $\Delta\Omega = 10^{-5}$ sr. The models that describe how DM is distributed in gravitational halos are detailed in the next section (Sect.5.2). The particle physics term contains the DM particle mass, m_{DM} , the velocity-weighted annihilation cross section, $\langle\sigma v\rangle$, and the differential γ -ray spectrum from all final states weighted by their corresponding branching ratios, dN_γ/dE_γ . The γ -ray final spectra for different DM annihilation models are addressed in Sect. 5.3. Some particular models that could give rise to an enhancement to the γ -ray annihilation flux are treated independently in

Sect. 5.4.

5.2 Dark matter halo modelling

Dark matter is predicted to be distributed in dark halos surrounding structures as small as globular cluster to as large as clusters of galaxies. The models which describe the DM density profiles of halos are motivated by both observation and numerical simulations. The choice of this model is the crux of most of the DM analyses in the literature, and many models exist. These can be broadly distinguished in two groups: halo models with a core, and halo models with a cusp.

Isothermal and pseudo-isothermal profile:

The simplest density profile one can derive is the based on the isothermal sphere model. This model allows to reproduce the flat rotation curves observed in spiral galaxies. The isothermal profile [151] is described by

$$\rho_{\text{ISO}}(r) = \frac{V_c^2}{4\pi G r^2}, \quad (5.3)$$

where V_c is the circular velocity and G the gravitational constant. However this profile is known to overestimate the mass and rotational velocity in the central parts of observed galaxies because of the singular density behavior when $r \rightarrow 0$. In order to describe a central component and to avoid the density singularity in $r = 0$, a non-singular pseudo-isothermal profile is often used in actual analysis. This profile can be expressed as

$$\rho_{\text{pISO}}(r) = \rho_0 \frac{r_c^2}{(r_c^2 + r^2)}, \quad (5.4)$$

where ρ_0 is the central DM density and r_c is a core radius.

Navarro, Frenk and White (NFW) profile:

A large number of cosmological N-body numerical simulations suggest the existence of a universal dark matter profile, with the same shape for all halo masses. The usual

parametrisation for the dark matter halo density in this case is a cusped profile, called Navarro, Frenk and White (NFW) profile [152], with the mass density given by

$$\rho_{\text{NFW}}(r) = \frac{\delta_c \rho_c^0}{(r/r_s)(1+r/r_s)^2}, \quad (5.5)$$

where r_s is a scale radius, ρ_c^0 the present critical density of the Universe ¹ and δ_c a characteristic over-density, defined by $\delta_c = \Delta_v c^3 g(c)/3$. The term Δ_v is fixed by defining the halo mass as the amount of matter contained in a spherical region of radius R_v (virial radius), whose mean density is $\Delta_v \rho_c^0$. A common value for Δ_v is $\Delta_v = 200$, which is derived from a cosmological scenario of a flat universe with a non-zero cosmological constant. The term in the numerator of Eq. 5.5 is often expressed as $\rho_s = \rho_c^0 \delta_c$. Here $c = R_v/r_s$ is the concentration parameter of the halo and $g(c) = (\ln(1+c) - c/(1+c))^{-1}$.

The NFW profile is characterized by the logarithmic slope $d \ln \rho / d \ln r = -3$ at $r \gg r_s$ and a divergence in the inner parts with $d \ln \rho / d \ln r = -1$, leading to an infinite density in the center. Note however that this does not imply an infinite γ -ray flux, since the value of \bar{J} is finite.

Burkert profile:

The NFW profile appears to well reproduce the DM halo distribution within large gravitational structures like galaxy clusters and large elliptical galaxies [121, 122, 123, 124, and references therein]. However central density cusps as predicted by the NFW profile are hard to verify in normal spiral galaxies as their inner parts are gravitationally dominated by baryons. In addition cores are effectively observed in small systems like dwarf galaxies, where the inner parts would be better described by a pseudo-isothermal profile. In order to overcome these difficulties, a purely phenomenological density distribution has been proposed in Burkert (1996) [153], called the ‘‘Burkert’’ profile, parametrised as

$$\rho_B(r) = \frac{\rho_0 r_c^3}{(r+r_c)(r^2+r_c^2)} \quad . \quad (5.6)$$

¹ $\rho_c^0 = 2.775 \times 10^{11} h^2 \text{ M}_\odot \text{Mpc}^{-3} = 1.053 \times 10^{-5} h^2 (\text{GeV}/c^2) \text{ cm}^{-3}$ [80]

5. Exclusion and sensitivity limits to dark matter annihilation

ρ_0 and r_c are free parameters which represent the central density and a scale or cored radius, respectively. This revised density law resembles an isothermal profile in the inner regions ($r \ll r_c$) and predicts a finite central density ρ_0 . On the other hand at large radii ($r \gg r_c$) it has a logarithmic slope $d \ln \rho / d \ln r = -3$, in agreement with the predictions of numerical simulations.

Einasto profile:

The density profiles of the dark matter halos formed in N-body simulations of hierarchical clustering have traditionally been fitted by essentially broken power law formulas. Recent simulations (Power et al. 2003; Reed et al. 2004) suggest that halo density profiles are better represented by a function with a continuously-varying slope. Navarro et al. (2004) proposed the fitting function

$$\frac{\ln \rho_e}{\ln r} = -2 \left(\frac{r}{r_{-2}} \right)^\alpha \quad (5.7)$$

which corresponds to the called Einasto density profile¹ with the form,

$$\rho_E(r) = \rho_{-2} \exp\left\{ \frac{-2}{\alpha} \left[\left(\frac{r}{r_{-2}} \right)^\alpha - 1 \right] \right\}, \quad (5.8)$$

where r_{-2} and ρ_{-2} are the radius and density at which the logarithmic slope of the density is -2, respectively, and α is a parameter describing the degree of curvature of the profile.

In principle all the above mentioned are potentially good profiles to describe DM distribution in haloes at any scale, from dwarf galaxies to galaxy clusters. Even in general, as already mentioned at the last chapter, numerical simulation with cusp profiles will tend to describe most precisely large scale distributions, while cored profiles are in better agreement with the observation of smaller scale objects, the dynamical history of each object will be the decisive component that will finally privilege one or another. In this sense there are evidences of galaxy cluster which are better described by cored profiles as well as dwarf galaxies well described by a NFW profile [see for

¹This density law was first introduced by Einasto (1965) who used it to describe the distribution of old stars within the Milky Way.

instance [118](#), [123](#)]. Both cuspy and cored profiles are considered in the DM analysis presented in this work.

5.2.1 Halo profile parameters determination

Given a hypothesis about the DM halo profile of an object, one need to find the set of parameters for each halo profile assumption that best fits the data. Two cases are described here, the first case relies on both simulations and observations, the second case describes a more generic method based only on observations.

NFW profile case

The NFW profile in Eq. [5.5](#) can be completely defined by any set of two parameters without a bijective relation between them, for example, (δ_c, r_s) , (ρ_s, r_s) or (c, R_v) . A very useful set of parameters however is the concentration parameter c and the virial mass M_v , which can be expressed as

$$M_v^{\text{NFW}} = \frac{4\pi}{3} \Delta_v \rho_c^0 R_v^3. \quad (5.9)$$

Several cosmological numerical simulations have found the concentration c to correlate with the halo virial mass M_v in the mass range $10^{11} - 10^{14} h^{-1} M_\odot$. An example of this correlation is given in Jing and Suto [[154](#)] (see also [[155](#)] for the exact formula) for haloes of galaxies at the scale of dwarf galaxies up to the scale of a Milky-Way (MW) galaxy, where

$$c = 10.23 \left(\frac{hM_v}{10^{12} M_\odot} \right)^{-0.088}. \quad (5.10)$$

Another correlation can found in [[156](#)] which can be applied to MW-like galaxies up to the most massive galaxy clusters, $(0.06 - 20) \times 10^{14} M_\odot$. In this case the correlation is found to be

$$c = 9.0 \left(\frac{hM_v}{10^{14} M_\odot} \right)^{-0.172}. \quad (5.11)$$

As it can be seen in Figure [5.3](#), where both equation are plotted, less massive objects are expected to have higher concentrations.

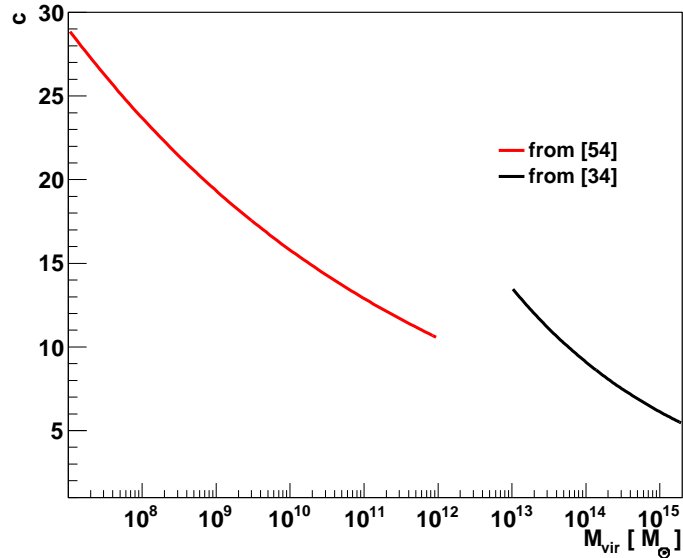


Figure 5.3: Concentration parameter c as function of the virial mass M_{vir} for the equations 5.10 (red line) and 5.11 (black line).

If applied, these correlations make the NFW model completely defined by one parameter, e.g., the virial mass M_v . The virial mass on the other hand can be determined by independent methods, all based on relations linking mass to some observable. Among the observables that trace the virial mass, an example, which is applied in the case of galaxy clusters, is the X-ray temperature of the intracluster gas. Assuming hydrostatic equilibrium and an isothermal gas (which is taken as the total average gas temperature), the relation can be simply written as [124]

$$\kappa_B T = \frac{GM_v \mu m_p}{2R_v} = (8.2 \text{ keV}) \left(\frac{M_v}{10^{15} h^{-1} M_\odot} \right)^{2/3}, \quad (5.12)$$

where T is the global cluster temperature, κ_B the Boltzmann constant and μm_p is the mean mass per particle in the gas. Realistic departures from hydrostatic equilibrium can be assessed with simulations of structure formation that include hydrodynamics, but they do not have a large effect on the mass-temperature relation [e.g. 124]. Another methods to derive the virial mass include a fixed mass-to-light ratio M/L correlation to the total luminosity or the velocity dispersion of stars [e.g. 157], direct measurements of the rotation curves from different tracers [e.g. 158, 159, 160], kinematics of stellar

populations [e.g. 157, 161, 162] and H I gas in galaxies [e.g. 163, 164], or gravitational lensing [e.g. 165, 166].

General case: solving the Jeans equation

One way to constrain the density distribution is to solve the Jeans equation relating the gravitational potential to various intrinsic velocity moments, which are in turn related to the observed velocity moments of some tracer. The Jeans equation is a particular case of the collisionless Boltzmann equation written in the velocity moment space. For spherical systems it has the form [151]

$$\frac{d(\rho_* \langle v_{r,*}^2 \rangle)}{dr} + \frac{\rho_*}{r} [2 \langle v_{r,*}^2 \rangle - \langle v_{\theta,*}^2 \rangle - \langle v_{\varphi,*}^2 \rangle] = -\rho_* \frac{d\Phi}{dr} = -\rho_* \frac{V_c^2}{r}, \quad (5.13)$$

where ρ_* is the density of the tracer, $\langle v_{r,*}^2 \rangle$, $\langle v_{\theta,*}^2 \rangle$ and $\langle v_{\varphi,*}^2 \rangle$ are the tracer second moments in the (r, θ, φ) directions, respectively, and Φ and V_c are the potential and the circular velocity of the total mass distribution. Considering a galaxy whose velocity structure is invariant under rotation about its center, $\langle v_{\theta,*}^2 \rangle = \langle v_{\varphi,*}^2 \rangle$. In the absence of net streaming motions in any of the directions, $\langle v_{i,*}^2 \rangle = \sigma_i^2$, where σ_i is the velocity dispersion in the direction i . The Jeans equation thus becomes

$$\frac{1}{\rho_*} \frac{d(\rho_* \sigma_{r,*}^2)}{dr} + \frac{2\beta(r) \sigma_{r,*}^2}{r} = -\frac{d\Phi}{dr} = -\frac{GM(< r)}{r^2} = -\frac{V_c^2(r)}{r}, \quad (5.14)$$

where β is the velocity anisotropy parameter, defined as $\beta = 1 - \sigma_{\theta}^2 / \sigma_r^2$, assuming $\sigma_{\theta}^2 = \sigma_{\varphi}^2$. Note that $\beta = 0$ if the velocity ellipsoid is isotropic, $\beta = 1$ if the ellipsoid is completely aligned with the radial direction, and $\beta < 0$ for tangentially anisotropic ellipsoids. A even simpler rewriting of the Jeans equation where the dependencies are explicit is:

$$M(< r) = \frac{V_c^2(r)r}{G} = -\frac{r\sigma_{r,*}^2}{G} \left(\frac{d \ln \rho_*}{d \ln r} + \frac{d \ln \sigma_{r,*}^2}{d \ln r} + 2\beta(r) \right). \quad (5.15)$$

The Jeans equation relates observable quantities like the density distribution of the tracer and its radial velocity dispersion profile to quantities of interest such as the total mass distribution. Knowing $\rho_*(r)$ and $\beta(r)$, and assuming a mass model, one can derive the predicted radial velocity dispersion profile for the mass model under consideration

5. Exclusion and sensitivity limits to dark matter annihilation

and compare it to the observed radial velocity dispersion profile of the tracer. However, knowledge of the velocity anisotropy parameter requires proper motion measurements of the individual stars and at the moment this is possible only in the Solar Neighbourhood. Therefore in practise one uses parametrizations for how β varies with r . The general solution of Eq. 5.15 is [167]

$$\sigma_{r,*}^2(r) = \frac{1}{\rho_* e^{\int 2\beta dx}} \int_x^\infty \rho_* V_c^2 e^{\int 2\beta dx''} dx', \quad x = \ln r. \quad (5.16)$$

The observables are the surface brightness and the line-of-sight velocity dispersion of the tracer population. The latter is related to the radial velocity dispersion by

$$\sigma_{los}^2(R) = \frac{2}{\Sigma_*(R)} \int_R^\infty \frac{\rho_*(r) \sigma_{r,*}^2 r}{\sqrt{r^2 - R^2}} \left(1 - \beta \frac{R^2}{r^2}\right) dr, \quad (5.17)$$

where R is the projected radius (on the sky) and $\Sigma_*(R)$ is the mass surface density of the tracer, which can be deduced from the surface brightness following a mass-to-light relation. The circular velocity $V_c(r)$ is associated to the DM halo density profile assumption. For example, for a pseudo-isothermal profile the circular velocity is given by

$$V_c^2(r) = 4\pi G r_c^2 \rho_0 \left(1 - \frac{r_c}{r} \arctan \frac{r}{r_c}\right), \quad (5.18)$$

and for the NFW profile by

$$V_c^2(s) = \frac{V_{vir}^2 g(c)}{s} \left[\ln 1 + cs - \frac{cs}{1 + cs} \right], \quad (5.19)$$

where V_{vir} is the circular velocity at the virial radius and $s = r/R_{vir}$.

The methodology used to find each set of parameters for each halo profile consists of comparing the observed line-of-sight velocity dispersion of the tracer, σ_{los} , for each distance bin with that predicted for the various models. Minimizing the χ^2 between the model and the data provides the best set of profile parameters.

Velocity anisotropy: As already mentioned, the variation of the velocity anisotropy with radius is not known. In order to compare the observations to the model predictions two hypotheses are often used: considering β as constant with radius; or using the Osipkov-Merritt parametrization [168, 169] for β :

$$\beta_{OM} = r^2 / (r^2 + r_a^2) \quad (5.20)$$

where r_a is the anisotropy radius. In the Osipkov-Merritt parametrization the anisotropy is always ≥ 0 , i.e. it is never tangential. The central regions are isotropic, and for $r_a \rightarrow \infty$ the anisotropy becomes purely radial. At $r = r_a$, $\beta = 0.5$. The smaller r_a , the faster the anisotropy becomes very radial. Models with large r_a correspond to models with almost isotropic behavior.

Jeans degeneracy: From the equations above it is however clear that different combinations of the density and anisotropy profiles can produce the same l.o.s. velocity dispersion profile, the so-called “mass-anisotropy” or Jeans degeneracy [170]. The best observational constraint for lifting the Jeans degeneracy on the other hand would be some handle on the proper motions of tracers. Alternatively, with a data set consisting of discrete tracers, the precisely measured differential distances (which ultimately yield the distances to the center of the system) can also break the Jeans degeneracy (cf., Watkins et al. 2010 [171]). Unfortunately, with the current and near-future observational capabilities, their uses are mostly limited to very near-by objects. Another recent method (Battaglia et al. 2008 [172]) consists in considering not one, but two different tracers population of the cluster gravitational potential, so that there are two observables (the l.o.s. velocity dispersion profiles of the two tracers) to solve for the two unknowns, $\rho(r_n)$ and $\beta(r_n)$. Since $\rho(r_n)$ must be the same for both tracers, but $\beta(r_n)$ can in principle be different, the degeneracy is only partially broken, however the constraints on the dynamics of the system are significantly stronger than with a single tracer.

5.2.2 Dark matter halo substructures

Numerical simulations of galactic halos predict a population of subhalos that could contribute to the overall astrophysical factor (eq. 5.2). The substructure enhancement over the smooth host halo contribution along the line of sight and inside a solid angle of observation $\Delta\Omega$ is defined as $B_{\text{sub}}(\Delta\Omega) = 1 + \mathcal{L}_{\text{sub}}(\Delta\Omega)/\mathcal{L}_{\text{sm}}(\Delta\Omega)$, where $\mathcal{L}_{\text{sm/sub}}(\Delta\Omega)$ denotes the annihilation luminosity of the smooth host halo and the additional contribution from substructures, respectively. A quantification of the substructure flux contribution to the total γ -ray flux was computed from the Aquarius simulation by [173]. The annihilation luminosity is defined by:

5. Exclusion and sensitivity limits to dark matter annihilation

$$\mathcal{L}_{\text{sm/sub}}(\Delta\Omega) = \Delta\Omega \times \overline{\mathcal{J}}_{\text{sm/sub}}(\Delta\Omega) = \int_{\Delta\Omega} d\Omega \int_{\text{l.o.s.}} dl \times \rho_{\text{sm/sub}}^2[r(l)], \quad (5.21)$$

where $\rho_{\text{sm/sub}}$ is the DM density distribution of the smooth halo and substructures, respectively. In order to perform the l.o.s. integration over the subhalo contribution, an effective substructure density $\tilde{\rho}_{\text{sub}}$ is parametrized following [100] and [173] as:

$$\tilde{\rho}_{\text{sub}}^2(r) = \frac{A(r) 0.8C \mathcal{L}_{\text{sm}}(R_{\text{vir}})}{4\pi r^2 R_{\text{vir}}} \left(\frac{r}{R_{\text{vir}}} \right)^{-B(r)}, \quad (5.22)$$

where

$$A(r) = 0.8 - 0.252 \ln(r/R_{\text{vir}}) \quad (5.23)$$

and

$$B(r) = 1.315 - 0.8(r/R_{\text{vir}})^{-0.315}. \quad (5.24)$$

$\mathcal{L}_{\text{sm}}(R_{\text{vir}})$ is the smooth halo luminosity within the virial radius R_{vir} . The normalization is given by $C = (M_{\text{min}}/M_{\text{lim}})^{0.226}$, where $M_{\text{min}} = 10^5 M_{\odot}$ is the minimum substructure mass resolved in the simulation and M_{lim} is the intrinsic limiting mass of substructures, or free-streaming mass.

Effect of the virial radius

It is important to notice that numerical simulations of galactic halos are scale invariant. The total contribution of substructures to the overall γ -ray flux is normalised at the DM halo virial radius. Integrating eq. 5.21 in the local frame of reference for the whole volume up to the virial radius give the maximum annihilation luminosity from substructures as function of the smooth halo luminosity, $\mathcal{L}_{\text{sub}}(R_{\text{vir}}) = 0.8C \mathcal{L}_{\text{sm}}(R_{\text{vir}})$. The maximum substructure enhancement over the smooth host halo contribution is then $B_{\text{sub}}(R_{\text{vir}}) = 1 + 0.8C$. An example of this effect for the same object is given in Sect. 8.1.2 in the case of the Fornax galaxy cluster, where the use of different methods to derive the virial mass gives different values of the latter.

Effect of the limiting mass of substructures M_{lim}

The kinetic decoupling of weakly interacting massive particles (WIMPs) in the early universe sets a scale that can directly be translated into a small-scale cutoff in the spectrum of matter density fluctuations. With decoupling temperatures of several MeV to a few GeV, Bringmann [174] found the smallest protohalos to be formed range between 10^{-11} and almost 10^{-3} solar masses depending on the particle DM model. A conventional value for this quantity is $M_{\text{lim}} = 10^{-6} M_{\odot}$ [175]. Very small M_{lim} would imply in a large number of substructures in DM haloes, and thus a large expected γ -ray signal. Assuming a specific DM model, a constraint on M_{lim} was derived by Pinzke et al. [173] using EGRET γ -ray upper limits on the Virgo cluster and a lower bound was placed at $M_{\text{lim}} = 5 \times 10^{-3} M_{\odot}$. Nevertheless, in this work both limiting mass values are used to derive DM annihilation constraints, $M_{\text{lim}} = 10^{-6} M_{\odot}$ and $M_{\text{lim}} = 5 \times 10^{-3} M_{\odot}$.

5.3 γ -ray final spectra

In any theory that predicts a viable DM candidate, each pair of DM particles that disappears through annihilation give rise to pairs of Standard Model particles in final states of annihilation, like gauge bosons, leptons or quarks. The subsequent chain of hadronisation, annihilations and decays of these SM particles will finally produce secondary photons. The total photon energy distribution in the rest frame of the annihilation pair can be generally written in the form

$$\frac{dN_{\gamma}^{\text{tot}}}{dE_{\gamma}} = \sum_f B_f \left(\frac{dN_{\gamma,f}^{\text{sec}}}{dE_{\gamma}} + \frac{dN_{\gamma,f}^{\text{line}}}{dE_{\gamma}} \right), \quad (5.25)$$

where B_f denotes the branching ratio into the annihilation primary channel f . The term $dN_{\gamma,f}^{\text{sec}}/dE_{\gamma}$ encodes the contribution from secondary photons, produced in each annihilation channel. The self-annihilation of MSSM neutralinos, for example, will give rise in general to a continuous γ -ray spectrum from the decay of neutral pions, which are produced in the hadronisation process of final-state quarks and gauge bosons. The last term in the above equation $dN_{\gamma,f}^{\text{line}}/dE_{\gamma}$ gives the contribution from the direct annihilation into photons, $\gamma\gamma$ or $Z\gamma$, which result in a sharp line feature. However since DM particles cannot be charged, these processes are typically loop-induced or otherwise highly suppressed, and are not treated in this work. The exact γ -ray spectrum and

5. Exclusion and sensitivity limits to dark matter annihilation

annihilation branching ratios will depend on the chosen underlying parameters of the DM particle model and particle mass.

Nevertheless, in order to avoid the choice of a preferred DM particle model, DM annihilation spectra are presented here in a model-independent way, i.e. for given pure annihilation channel (100% of branching ratio in one channel) and DM particle mass. The first Kaluza-Klein (KK) mode of the hypercharge gauge boson $\tilde{B}^{(1)}$ will be the only exception. In the minimal UED framework, which is used here, the $\tilde{B}^{(1)}$ particle have fixed annihilation branching ratios which are independent of its mass. The branching ratios of the different annihilation channels of the $\tilde{B}^{(1)}$ are presented in Table 4.2 of chapter 4. Figure 5.4 shows different annihilation spectra for 1 TeV mass dark matter particles. Spectra of DM particles annihilating into $\mu^+\mu^-$, $b\bar{b}$, W^+W^- and $\tau^+\tau^-$ pairs are calculated using the *Mathematica* code from [176]. For Kaluza-Klein $\tilde{B}^{(1)}$ annihilation, PYTHIA 6.225 [177] was used to compute the spectra [136].

A distinct general feature of the DM annihilation spectra is the sharp step or cut-off close to the DM particle mass. Such spectral end point features are of the utmost importance for fitting data in indirect DM searches through γ -rays. Plus they emphasize the necessity of complementary studies from different classes of γ -ray experiments, satellites *versus* IACTs. Indeed, the detection of these features could provide a clear distinction between an annihilation signal and a standard astrophysical signal [see, for instance, 178]), and for this reason they are often referred as *smoking-gun* signatures. Another *smoking-gun* signatures include monochromatic γ -ray lines, as well as pronounced bumps, which are present in some DM models (an example is given in the Sect. 5.4). These models can only be tested by satellite telescopes for DM particle masses up to a few hundreds of GeV. IACTs observation can provide well-complementary searches for such features at DM particle masses higher than a few hundreds of GeV .

5.4 γ -ray flux enhancement effects

5.4.1 Radiative correction : Internal Bremsstrahlung

Whenever DM particles annihilate into pairs of charged particles $X\bar{X}$, this process will with a finite probability automatically be accompanied by internal bremsstrahlung

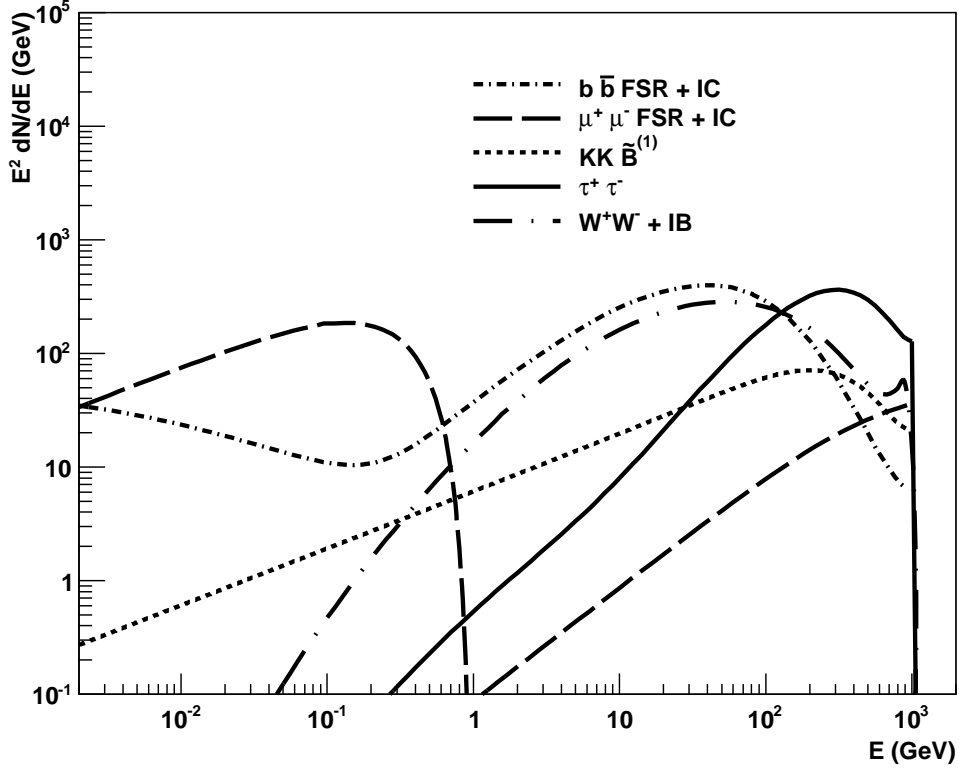


Figure 5.4: Photon spectra for 1 TeV dark matter particles self-annihilating in different channels obtained with the Monte Carlo simulation program PYTHIA (version 8.135, [179]) from Ref. [176]. Spectra from DM annihilating purely into $\tau^+\tau^-$ (black solid line) and W^+W^- (long-dashed dotted line) are shown. The latter shows the effect of Internal Bremsstrahlung (IB) occurring for the W^+W^- channel. The γ -ray spectrum from the annihilation of $\tilde{B}^{(1)}$ hypergauge boson pairs arising in Kaluza-Klein (KK) models with UED is also plotted (dotted line). Annihilation spectrum into $b\bar{b}$ including the inverse Compton (IC) scattering contribution is also plotted (dot-dashed line). The long dashed line shows the photon spectra from final-state radiation (FSR) and the inverse Compton (IC) scattering contribution in the case of DM particles annihilating into muon pairs, which was analytically and numerically calculated independently (see Section 5.4.2 for more details on the calculation).

(IB), i.e. the emission of an additional photon in the final state. These electromagnetic radiative corrections will give rise to two particular photon emissions, as visualized in Fig 5.5, one may distinguish between photons directly radiated from the external legs (final state radiation, FSR) and photons radiated from virtual charged particles (virtual

5. Exclusion and sensitivity limits to dark matter annihilation

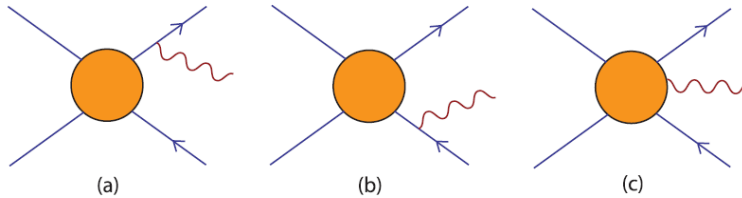


Figure 5.5: Types of diagrams that contribute to the first order QED corrections to WIMP annihilations into a pair of charged particle final states. The leading contributions to diagrams (a) and (b) are universal, referred to as final state radiation (FSR). Internal bremsstrahlung from virtual particles (or virtual internal bremsstrahlung, VIB) is indicated in diagram (c).

internal bremsstrahlung, VIB). What is called IB photons will be the total contribution from both FSR and VIB photons [180, 181]. Internal bremsstrahlung processes can contribute significantly to the γ -ray spectrum [180, 181] yielding a detectable $\tilde{\Gamma}$ bump $\tilde{\Gamma}$ near the highest energy. Adding this effect to the continuous spectrum of secondary γ -rays from pion decay, the total spectrum is given by

$$\frac{dN_\gamma}{dE_\gamma} = \frac{dN_\gamma^{\text{sec}}}{dE_\gamma} + \frac{dN_\gamma^{\text{IB}}}{dE_\gamma}. \quad (5.26)$$

The magnitude of this effect depends on the intrinsic properties of the dark matter particle model. Bringmann et al. [181] provide an approximation that is valid for wino-like neutralinos [182] which annihilates purely into W^+W^- . The IB spectrum in this case can be expressed as

$$\frac{dN_{W^+W^-}^{\text{IB}}}{dx} = \frac{\alpha_{\text{em}}}{\pi} \frac{4(1-x+x^2)^2}{(1-x+\epsilon/2)x} \times \left[\log \left(2 \frac{1-x+\epsilon/2}{\epsilon} \right) - 1/2 + x - x^3 \right], \quad (5.27)$$

where $\epsilon = m_W/m_{\text{DM}}$, m_W is the W particle mass, m_{DM} is the DM particle mass, and $x = E_\gamma/m_{\text{DM}}$. The annihilation spectrum for a 1 TeV wino is shown in Figure 5.6.

5.4.2 Inverse compton process

Every time a DM particle annihilation has electrons or positrons in the final states of annihilation, the propagation of these particles may lead to an additional γ -ray emission component by Inverse Compton (IC) up-scattering of background photons, such as those of the cosmic microwave background (CMB). If the electron/positron energy loss time scale is much shorter than the spatial diffusion time scale, the IC contribution to the

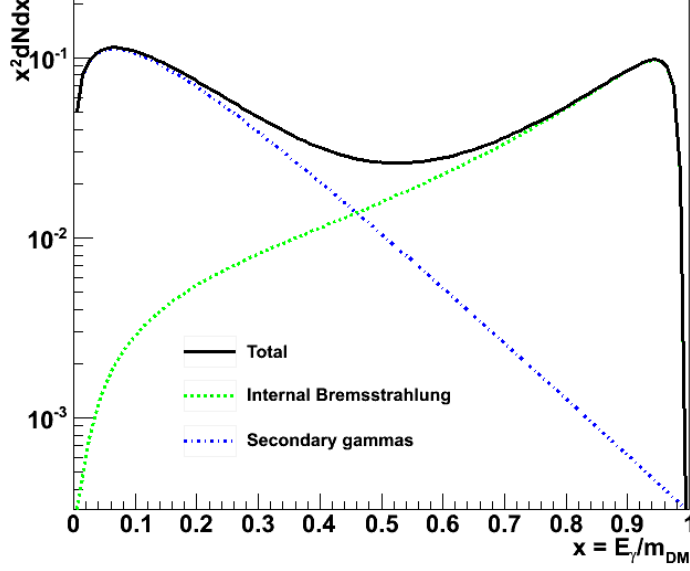


Figure 5.6: γ -ray spectrum for 1 TeV wino. The contributions from IB and secondary photons is indicated separately.

γ -ray flux may be significant. In galaxy clusters, for example, the energy loss term is dominated by the IC component [121]. The total γ -ray spectrum is then given by

$$\frac{dN_\gamma}{dE_\gamma} = \frac{dN_\gamma^{\text{sec}}}{dE_\gamma} + \frac{dN_\gamma^{\text{IC}}}{dE_\gamma} . \quad (5.28)$$

DM particles annihilating purely into $\mu^+\mu^-$ or W^+W^- will have a significant amount of electrons in the final states coming from muon and pion decays.

Let E_e be the energy of electrons and positrons, ϵ that of the target photons and E_γ the energy of the scattered photon. The IC component of the annihilation spectrum can be calculated by

$$\frac{dN_\gamma^{\text{IC}}}{dE_\gamma}(E_\gamma) = \int dE_e \frac{dn_e}{dE_e}(E_e) P_{IC}(E_\gamma, E_e), \quad (5.29)$$

where

$$P_{IC}(E_\gamma, E_e) = c \int d\epsilon n_\gamma(\epsilon) \sigma_{KN}(E_\gamma, E_e, \epsilon) \quad (5.30)$$

is the IC power, which is obtained by convolving the IC cross section σ_{KN} (differential Klein-Nishina cross section) with the differential target photon number density $n_\gamma(\epsilon)$.

5. Exclusion and sensitivity limits to dark matter annihilation

In the case of IC up-scattering on the CMB $n_\gamma(\epsilon)$ is the black body spectrum of the 2.73K CMB photons. The Klein-Nishina formula [151] has the form

$$\sigma_{KN}(E_\gamma, E_e, \epsilon) = \frac{3\sigma_T(m_e c^2)^2}{4\epsilon E_e^2} G(q, \Gamma_e), \quad (5.31)$$

where σ_T is the Thompson cross section and

$$G(q, \Gamma_e) \equiv \left[2q \ln q + (1 + 2q)(1 - q) + \frac{(\Gamma_e q)^2 (1 - q)}{2(1 + \Gamma_e q)} \right] \quad (5.32)$$

with $\Gamma_e = 4\epsilon E_e / (m_e c^2)^2$ and $q = E_\gamma / [\Gamma_e (E_e - E_\gamma)]$. Finally, the total equilibrium distribution of the electrons plus positrons is given by

$$\frac{dn_e}{dE_e}(E_e) = \frac{1}{b(E_e)} \int_{E_e}^{m_{DM}} dE'_e \frac{dN_e}{dE_e}(E'_e), \quad (5.33)$$

where dN_e/dE_e denotes the differential spectra of electrons plus positron from an DM particle annihilation event, and

$$b(E_e) = \frac{4\sigma_T c}{3(m_e c^2)^2} E_e^2 \approx 2.67 \times 10^{-17} (E_e / \text{GeV})^2 \text{ GeV/s} \quad (5.34)$$

is the typical energy loss rate of an electron or positron up-scattering in a radiation field with average energy $\bar{\epsilon} = 2.73 = 0.235$ meV.

Electron spectra of DM particles annihilating into $\mu^+\mu^-$ and $b\bar{b}$ pairs are calculated using the *Mathematica* code from [176]. Using these spectra the IC emission is calculated for different DM particle masses. Figure 5.4 shows the total annihilation spectrum for 1 TeV DM particle. Due the cross section suppression when electrons/positrons are too energetic, also referred as suppression in the Klein-Nishina regime $\epsilon E_e \gg (m_e c^2)^2$, IC emission is only very significative for energies inferior to $E_\gamma^{\text{IC}} \approx \epsilon (m_{DM}/2m_e)^2$ [2]. This means that, given the energy range sensible to IACTs (like H.E.S.S.), the IC component will only be contributing significantly to the total γ -ray flux for DM particle masses $m_{DM} > 10$ TeV.

It is important to notice however that a suppression of the IC signal might occur if (i) the spatial diffusion time scale of electrons/positrons is too short compared to the IC energy loss time scale, or (ii) because of a local magnetic field synchrotron losses, averaged over the entire volume of the object, are comparable or more significant than

IC losses. The first case effectively happens in small scale objects such as dwarf galaxies. In this class of objects the electrons will diffuse out of the system before it can efficiently interact through IC. On the other hand, for large scale object such as galaxy clusters the effect of electrons escaping the diffusion region was shown to be negligible[121]. Indeed, as it can be seen in Fig. 5.7, a comparison among the time scales for the energy losses due to various mechanisms (as labeled in the figure) and the time scale for diffusion in a cluster of typical size $R_{\text{vir}} = 1$ Mpc shows that the energy losses are dominated by IC losses for electrons in the GeV-TeV energy range.

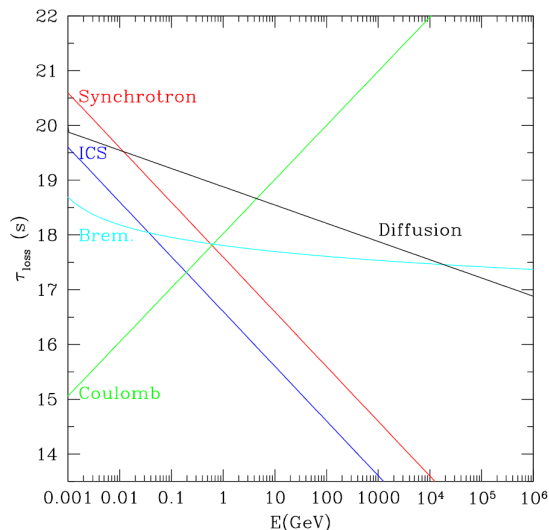


Figure 5.7: A comparison between the time scales for the energy losses due to various mechanisms (as labeled in the figure) and the time scale for diffusion (black solid curve) in a cluster of size $R_{\text{vir}} = 1$ Mpc. A uniform magnetic field of value $B = 1\mu\text{G}$ and a thermal gas density $n = 1.3 \times 10^{-3}\text{cm}^{-3}$ have been assumed in the computations. Figure extracted from Colafrancesco et al. [121].

The condition for case (ii) amounts to the existence of an effective average magnetic field \bar{B} in the object which have a value $\bar{B} \gtrsim B_{\text{CMB}} \simeq 3.2\mu\text{G}$, the latter quantity being the amplitude of a magnetic field having the same energy density as the CMB. While such large magnetic fields are possible, they are unlikely to uniformly populate the galaxy clusters considered in this study (cf. Fornax galaxy cluster in chap. 8). If, however, this were the case, the suppression in the IC signal would be on the order of $(B_{\text{CMB}}^2/\bar{B}^2)$.

5.4.3 The Sommerfeld effect

The DM annihilation cross section can be enhanced, with respect to its primordial value $\langle\sigma v\rangle_0$ during thermal freeze-out, in the presence of the so-called Sommerfeld effect. This is a non-relativistic effect which arises when two DM particles interact in an attractive potential and it is particularly effective in the very low-velocity regime. From the point of view of quantum field theory, this Sommerfeld enhancement corresponds to the summation of a series of ladder diagrams where the scalar state is repeatedly exchanged (see Fig. 5.8). The idea that the γ -ray flux from DM annihilations can be enhanced in this way was first proposed in the seminal paper by Hisano et al. (2004) [183].

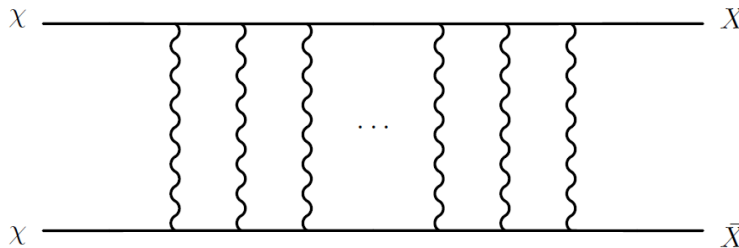


Figure 5.8: Ladder diagram giving rise to the Sommerfeld enhancement for DM particle (χ) $\chi\chi \rightarrow X\bar{X}$ annihilation, via the exchange of gauge bosons. Ref. [184]

In DM haloes where the relative velocity between the DM particles may be sufficiently low, the Sommerfeld effect can substantially boost the annihilation cross section [184]. The actual velocity-weighted annihilation cross section of the neutralino can then be enhanced by a factor S defined as

$$\langle\sigma v\rangle = S(\beta, m_{\text{DM}}) \langle\sigma v\rangle_0, \quad (5.35)$$

where the value of S depends on the DM particle mass and relative velocity $\beta = v/c$. The Sommerfeld enhancement can be obtained solving the $l = 0$ Schrödinger equation for the reduced two-body wave function $\Phi(r)$:

$$\left(\frac{1}{m_{\text{DM}}} \frac{d^2}{dr^2} - V(r) \right) \Phi(r) = -m_{\text{DM}} \beta^2 \Phi(r), \quad (5.36)$$

with the boundary condition $\Phi'(\infty)/\Phi(\infty) = im_{\text{DM}}\beta$. The Sommerfeld factor S is then given by $S = |\Phi(0)/\Phi(\infty)|^2$. Particles interacting through a Yukawa-like potential,

$$V(r) = -\frac{\alpha}{r} e^{-m_\nu r}, \quad (5.37)$$

are considered. Here m_V is the exchanged boson mass and α the coupling constant.

The Sommerfeld enhancement is effective in the low-velocity regime, and disappears ($S = 1$) in the limit $\beta \rightarrow 1$. In general, one can distinguish two distinct behaviors, resonant and non-resonant, depending on the value of the annihilating particle mass and the relative velocity β [184]. In the non-resonant case, the cross section is enhanced for $\beta < \alpha$, with $S = \pi\alpha/\beta$ up to a saturation value, roughly given by $S_{\max} \sim 6\alpha m_V/m_{\text{DM}}$. This value occurs for $\beta \sim 0.5m_V/m_{\text{DM}}$. In the resonant case, occurring for particular values of the mass of the annihilating particle, the cross section follows the non-resonant behavior until $\beta \simeq \sqrt{\alpha m_V/m_{\text{DM}}}$; below this critical value, the enhancement grows like $1/\beta^2$ before saturating. The Sommerfeld boost can then reach values as large as 10^5 for a DM particle mass of order 4.5 TeV [184]. These different behaviors can be observed in left figure of Fig. 5.9 when considering DM particles annihilating purely into a W bosons. The peak position in the series of resonances is approximatively given by $4.5\text{TeV}n^2$, where n is an integer. The attractive potential created by the exchange of Z gauge bosons implies $\alpha = 1/30$ and $m_V = 90$ GeV.

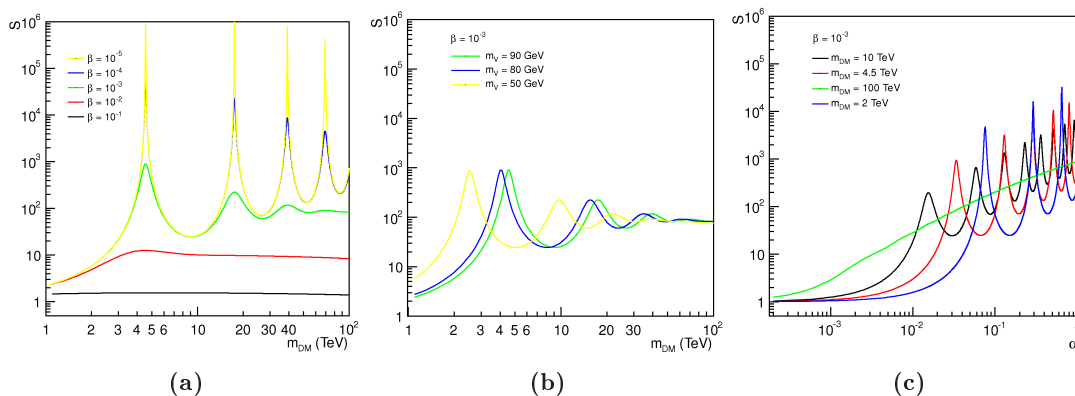


Figure 5.9: Sommerfeld effect dependence with respect to the relative velocity β (a), the exchanged boson mass m_V (b) and the coupling constant α (c).

A more general case of the enhancement by the Sommerfeld effect can be treated by changing the exchanged boson mass and the coupling constant accordingly. The position of the resonances is qualitatively driven by m_V/α [184]. Increasing the boson mass shifts the resonance to higher DM masses since the the weak coupling constant

5. Exclusion and sensitivity limits to dark matter annihilation

is only a slowly varying function of the boson mass. Simultaneously, once the relative velocity and the DM particle mass are fixed, the value of the enhancement close to the resonance grows roughly linearly with the boson mass [184]. The behavior of the Sommerfeld effect with respect to the exchanged boson mass and the coupling constant are presented in Fig. 5.9.

The relative velocity, or velocity dispersion, between the DM particles in galactic haloes is assumed here as having the same value as the velocity dispersion of the gravitational tracers, such as stars, globular clusters or galaxies, in the case of galaxy clusters. The later assumption is plausible due to the large relaxation time scales of galaxy clusters, galaxies and dwarf galaxies. The relaxation time being sufficiently long, the velocity dispersion of the tracers was not significantly perturbed by other objects in the system. The velocity dispersion is then still very close to the initial value, which can be assumed to be the same for DM and other gravitational bound objects.

5.5 Limits on the dark matter annihilation cross section

Constraints on a DM particle scenario from γ -rays observations can be derived comparing the number of detected γ -ray events $N_\gamma^d(\Delta\Omega)$ in a region $\Delta\Omega$ with the number of events expected from an assumed γ -ray emission scenario $N_\gamma^e(\Delta\Omega)$ in this same region. The number of expected signal events is calculated by:

$$N_\gamma^e(\Delta\Omega) = T_{\text{obs}} \int_0^\infty A_{\text{eff}}(E_\gamma) \frac{d\Phi_\gamma}{dE_\gamma}(E_\gamma, \Delta\Omega) dE_\gamma, \quad (5.38)$$

where T_{obs} is the observation time, and $A_{\text{eff}}(E_\gamma)$ is the effective area of the detector as a function of the γ -ray energy. The predicted γ -ray flux from DM annihilation Eq. 5.1 in then replaced in Eq. 5.38. Comparing the expected number of γ -rays with the number of detected events and assuming a DM density distribution, one can constraint the DM particle physics scenario through the remaining pair of parameters ($\langle\sigma v\rangle, m_{DM}$):

$$\langle\sigma v\rangle = \frac{8\pi}{\bar{J}(\Delta\Omega)\Delta\Omega} \times \frac{m^2 N_\gamma^d}{T_{\text{obs}} \int_0^m A_{\text{eff}}(E_\gamma) \frac{dN_\gamma}{dE_\gamma}(E_\gamma) dE_\gamma}. \quad (5.39)$$

However in real observations the number of detected γ -rays is always subject to background contamination and up-to-date no γ -ray signal from a DM annihilation has

been significantly detected from any astrophysical source. In case of no significant γ -ray signal, an upper limit on the detected number of γ -rays ($N_{\gamma}^{95\%C.L.}$ for upper limit at 95% confidence level) can be derived based on the background level contamination. Replacing the number of detected γ -rays by the upper limit on this number, an upper limit on the velocity-weighted annihilation cross section is directly obtained as function of the DM particle mass, spectrum and density distribution. Two kinds of limits can be extracted from γ -ray observations. The first are exclusion limits for a DM model, which can be derived from actual observations where no significant γ -ray signal has been detected. The second are sensitivity limits for future observations.

5.5.1 Exclusion limits

In order to estimate whether the number of events detected in the region of interest, signal or ON region, is a significant signal detection, a comparison with the estimated number of background events in the same region needs to be done. In IACTs observations the background is measured simultaneously with the signal but in a different region, OFF region, and then renormalised by the factor α which is the ratio between the OFF/ON region sizes. The significance of a signal is given by the formula 3.9, where a significance superior to 5 is required to declare a significant detection.

In case of no significant signal detection (Eq. 3.9) an upper limit on the number of true γ -rays in the ON region is calculated using the methods of Feldman & Cousins [74] or Rolke et al. [185]¹. These methods allow to estimate a confidence interval and fixing the confidence level (C.L.) at 95% the number of γ -rays at 95% confidence level (C.L.), $N_{\gamma}^{95\%C.L.}$ is found for given N_{ON} , N_{OFF} and α (see Section 3.2 for details).

¹Both methods are fully frequentist constructions, where the limit calculations make use of a profile likelihood method. The Feldman & Cousins is usually used in case of no (or negligible) uncertainties in nuisance parameters. However it does not handle background expectations or signal efficiencies which are known only with some limited accuracy, which might be the case for some IACTs observations. In these cases, Rolke et al. [185] is applied. See [185] for more details.

5.5.2 Sensitivity limits

In the case where the background cannot be measured experimentally, future experiments for example, it can still be estimated assuming that the background consists of misidentified hadron showers. The estimate of the expected number of background events in the signal region can be determined using the following expression [see Ref. 186]:

$$\frac{d^2\Phi_{\text{had}}}{d\Omega dE_\gamma} = 8.2 \times 10^{-8} \epsilon_{\text{had}} \left(\frac{E_\gamma}{1\text{TeV}} \right)^{-2.7} [\text{TeV}^{-1}\text{cm}^{-2}\text{s}^{-1}\text{sr}^{-1}], \quad (5.40)$$

where ϵ_{had} is the hadron detection efficiency. To take into account the performance of the future IACTs the hadron rejection is taken at the level of 90%, which corresponds to $\epsilon_{\text{had}} = 0.1$ and it is twice as good as the current instruments like H.E.S.S.. This parametrisation gives remarkable agreement with CTA background simulations [187], but since CTA is still in the conception phase this value can become better and thus the value $\epsilon_{\text{had}} = 0.1$ can be considered as a conservative one.

In the case of 95% C.L. sensitivity calculations, $N_\gamma^{95\% \text{C.L.}}$ is calculated assuming that only hadronic background events are detected and misidentified with γ -rays. The number of background events N_{OFF} is calculated by integrating the background event flux given in Eq. (5.40) after multiplication by the effective area of the detector and the observation time. Then the method of Rolke et al. [185] (or Feldman & Cousins [74]) is applied with $N_{\text{ON}} = N_{\text{OFF}}$.

Finally the 95% C.L. limit on the velocity-weighted annihilation cross section is given by the following expression:

$$\langle\sigma v\rangle_{\text{min}}^{95\% \text{C.L.}} = \frac{8\pi}{\bar{J}(\Delta\Omega)\Delta\Omega} \times \frac{m^2 N_\gamma^{95\% \text{C.L.}}}{T_{\text{obs}} \int_0^m A_{\text{eff}}(E_\gamma) \frac{dN_\gamma}{dE_\gamma}(E_\gamma) dE_\gamma}, \quad (5.41)$$

which will be used to derive all the exclusion and sensitivities limits in the next chapters.

Chapter 6

Dark matter constraints towards the Sculptor and Carina dwarf spheroidal galaxies

Contents

Introduction	118
6.1 H.E.S.S. observations and data analysis	119
6.2 γ-rays flux upper-limits	122
6.3 Dark matter halo modelling	123
6.4 Exclusion limits on the dark matter annihilation cross section	126
6.4.1 Generic case for exclusion limits	126
6.4.2 Enhancement effects for the exclusion limits	129
6.5 Summary and conclusion	133

Introduction

The Dwarf Spheroidal Galaxies (dSphs) of the Local Group are the most commonly studied satellites of the Milky Way and assumed to be gravitationally bound dominantly by Dark Matter (DM). Although the predicted very high energy (VHE, $E \gtrsim 100$ GeV) γ -ray flux from DM annihilation from dwarf galaxies is smaller compared to the expected DM annihilation γ -ray flux from denser regions of DM such as the Galactic Center, these galaxies are promising targets for searches for γ -rays from DM annihilation since they are environments with a favorably low astrophysical γ -ray background. The galaxies themselves are expected to contain no astrophysical γ -ray sources since no recent star formation activity gives rise to VHE γ -rays (supernova remnants, pulsar wind nebula, etc.) and little or no gas acting as target material for cosmic rays has been measured [188]. Additionally their position at high galactic latitude is well separated from the numerous sources of VHE γ -rays harbored in the Galactic plane. Also at such high altitudes no detectable contamination due to diffuse VHE γ -ray emission is expected, which in any case has shown up so far only from the Galactic Center region [189].

The H.E.S.S. array of Cherenkov telescopes has already observed dSphs and the collaboration has published results on the Sagittarius dSph [190, 191] and the overdensity Canis Major [192]. In January 2008 H.E.S.S. launched observation campaigns on the Sculptor and Carina dSphs, which are among the most luminous dSphs near the Milky Way (see Table 6.1 for coordinates and distances). The Sculptor dSph was discovered in 1938 [193], and was the first example of this type of galaxy in the vicinity of the Milky Way. The Carina dSph was discovered in 1977 [194]. The best estimates of the orbits of the two dSphs show that Carina is likely to be more tidally disrupted than Sculptor [195, 196], leading to higher uncertainties for the DM content of the Carina dSph than of the Sculptor.

This chapter presents the results of a search for VHE γ -rays from DM annihilation from the Sculptor and Carina dSphs. The work presented here has been published in the *Astroparticle Physics Journal* [197]. The chapter is organized as follows: in Section 6.1 the analysis of the data is presented, from which upper limits on the γ -ray flux are extracted assuming power-law spectra and DM annihilation spectra

Galaxy	Sculptor	Carina
RA	01 ^h 02 ^m 19 ^s .2	06 ^h 41 ^m 36 ^s .0
Dec.	−33° 33′ 00″.0	−50° 58′ 12″.0
Distance (kpc)	79 ± 4	101 ± 5

Table 6.1: Coordinates (taken from [188]) for the Sculptor and Carina dSphs.

are derived for both dSphs (Section 6.2). Then the possibility of giving constraints on the DM particle properties is discussed (Section 6.4), by assuming several DM galactic halo profiles of the dSphs, and considering various possibilities for the DM candidate particle, in particular those that could give rise to an enhancement to the γ -ray annihilation flux. The results obtained are discussed in Section 6.4.2. At the time of the H.E.S.S. publication the *Fermi-LAT* collaboration [198] had published a search for γ -ray emission, in the energy range from 100 MeV to 100 GeV, only from the direction of the Sculptor dSph. The results from *Fermi-LAT* [199] will also be addressed in Section 6.4. However, since the first H.E.S.S. publication, the *Fermi-LAT* collaboration had published another study including constraints on DM annihilation from Carina. These results are now quickly presented and compared to the H.E.S.S. results at Section 6.5.

6.1 H.E.S.S. observations and data analysis

The observations of the Sculptor and Carina dSphs were conducted between January 2008 and December 2009. They were performed in *wobble mode*, i.e. with the target typically offset by 0.7° to 1.1° from the pointing direction, allowing simultaneous background estimation in the same field-of-view (c.f. chapter 3). The data used for the analysis were taken at average zenith angles of $\sim 14^\circ$ and $\sim 34^\circ$ for the Sculptor and Carina dSphs, respectively, leading to different effective energy thresholds. A minimal energy (E_{\min}) is defined as the energy for which the acceptance of the instrument reaches 20% of its maximum value, which for the Sculptor and Carina gives $E_{\min} \sim 220$ GeV and $E_{\min} \sim 320$ GeV, respectively. This minimal energy will be used in section 6.2 for the calculation of the upper limits on the γ -ray flux. The data sets

6. Dark matter towards Sculptor and Carina dwarf galaxies

used for the analysis include only the observation runs that meet the standard quality control criteria described in Section 3.2. The total data set amounts to 11.8 h for Sculptor and 14.8 h for Carina of live time after the quality selection. These parameters are summarized in Table 6.2.

dSph Galaxy	Sculptor	Carina
Observation Period	2008 Oct - 2008 Nov	2008 Jan - 2009 Dec
Live time (h)	11.8	14.8
N_{ON}	117	86
N_{OFF}	2283	1858
α	0.04	0.05
Significance	1.0σ	-1.4σ
$N_{\gamma, \text{tot}}^{95\% \text{ C.L.}}$	32.4	8.6
E_{min} (GeV)	220	320
$N_{\gamma}^{95\% \text{ C.L.}}(E_{\gamma} > E_{\text{min}})$	19.2	10.2

Table 6.2: H.E.S.S. observation characteristics and upper limits on the observed number of γ -rays for the Sculptor and Carina dSphs. N_{ON} and N_{OFF} are the number of γ -ray candidate events in the signal region and in the background region, respectively. α is defined as the ratio of the on-source area to the off-source area. The significance of the excess in the signal region is calculated for the given N_{ON} , N_{OFF} and α . $N_{\gamma, \text{tot}}^{95\% \text{ C.L.}}$ is the 95% confidence level upper limits on the total observed numbers of γ -rays, and $N_{\gamma}^{95\% \text{ C.L.}}(E_{\gamma} > E_{\text{min}})$ is the 95% confidence level upper limits on the observed numbers of γ -rays above the given minimal energy E_{min} for each dSph.

The data are analyzed using the *model analysis* described in the chapter 3 (Model++) with *standard cuts*. The background was determined by the ring-background technique (see 3.2 for more details), calculating the background for each position in the field-of-view using the background rate contained in a ring around the target.

No significant γ -ray excess was found above the estimated backgrounds at the nominal positions of Sculptor and Carina dSphs, as seen in Figure 6.1. The significance of the excess in the 0.1° radius integration area for Sculptor and Carina are $+1.0\sigma$

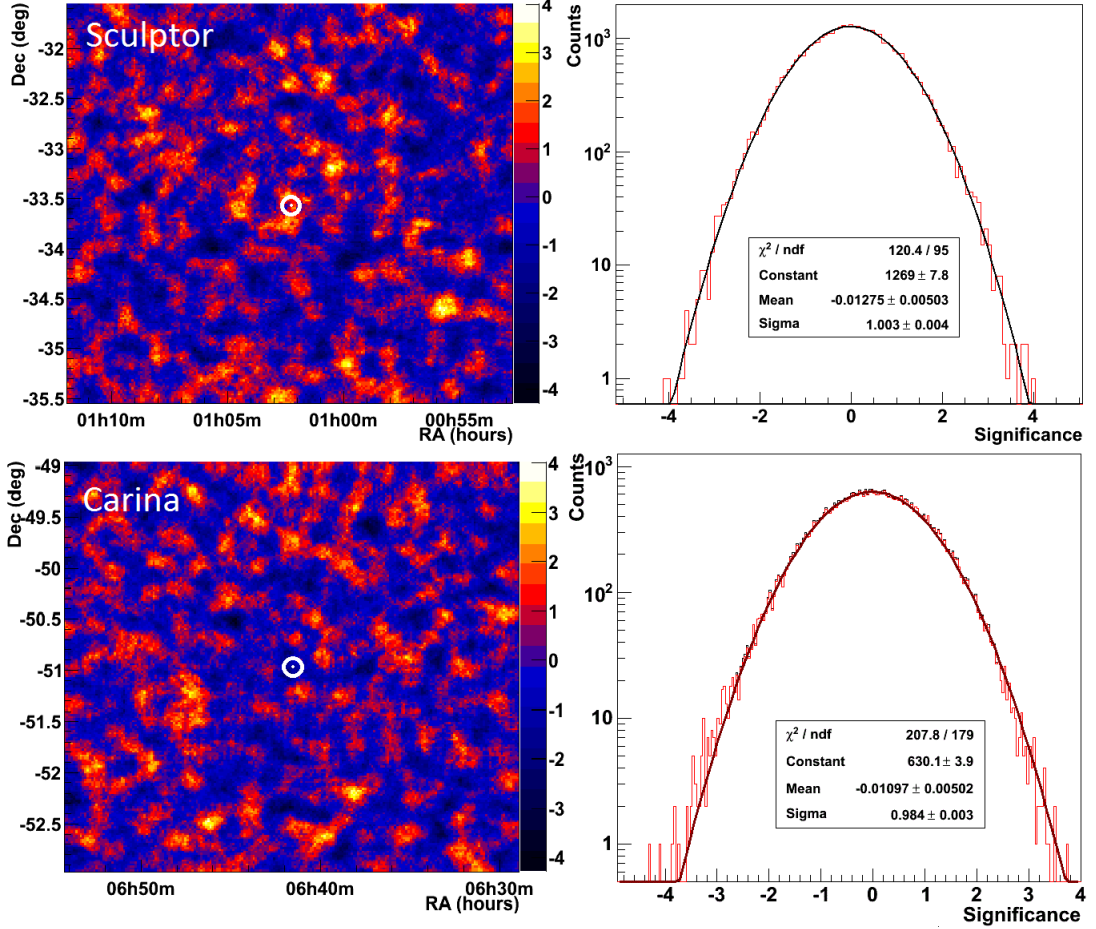


Figure 6.1: Oversampled significance maps (with an integration region of 0.1° , white circle) in equatorial coordinates calculated according to the Li & Ma method [73] in the directions of Sculptor (top left) and Carina (bottom left) dSphs. Distributions of the significance in the maps for the Sculptor (top right) and the Carina (bottom right) dSphs. The solid line is a Gaussian fitted to the data. The significance distribution is well described by a normal Gaussian. No significant excess is seen at the target position.

and -1.4σ , respectively¹. This allows one to set 95% confidence level upper limits on the total observed numbers of γ -rays $N_{\gamma, \text{tot}}^{95\% \text{ C.L.}}$, using the number of γ -ray candidate

¹A sensitivity of 20.1 events is reported for Carina, following the suggestion in Feldman & Cousins [74] in the case where fewer events than the expected background are measured. The sensitivity is defined as the average upper limit (at 95% C.L.) obtained with the expected background and no true excess signal.

events in the signal region N_{ON} , in the background region N_{OFF} , and the ratio α of the on-source area to the off-source area. The limits have also been computed above the given minimal energy E_{min} for each dSph. The $N_{\gamma, \text{tot}}^{95\% \text{ C.L.}}$ and $N_{\gamma}^{95\% \text{ C.L.}}(E_{\gamma} > E_{\text{min}})$ obtained using the method described in Feldman & Cousins [74] are shown in Table 6.2.

6.2 γ -rays flux upper-limits

Upper limits on the number of observed γ -rays above a minimal energy E_{min} can be translated into an upper limit on the observed γ -ray flux Φ_{γ} if the energy spectrum dN_{γ}/dE_{γ} of the source is assumed to be known. The relation is given by

$$\Phi_{\gamma}^{95\% \text{ C.L.}}(E_{\gamma} > E_{\text{min}}) = \frac{N_{\gamma}^{95\% \text{ C.L.}}(E_{\gamma} > E_{\text{min}}) \int_{E_{\text{min}}}^{\infty} dE_{\gamma} \frac{dN_{\gamma}}{dE_{\gamma}}(E_{\gamma})}{T_{\text{obs}} \int_{E_{\text{min}}}^{\infty} dE_{\gamma} A_{\text{eff}}(E_{\gamma}) \frac{dN_{\gamma}}{dE_{\gamma}}(E_{\gamma})}, \quad (6.1)$$

where T_{obs} is the observation time, and $A_{\text{eff}}(E_{\gamma})$ is the effective area of the detector as a function of the γ -ray energy, the zenith angle, the offset of the source from the pointing direction and the selection cuts. By replacing the $N_{\gamma}^{95\% \text{ C.L.}}$ from Section 6.1 (Table 6.2) in equation 6.1, the upper limit on the flux at 95% C.L. is completely determined for an assumed spectrum.

To obtain flux upper limits for standard astrophysical sources, power-law photon flux spectra of index Γ are assumed,

$$\frac{d\Phi_{\gamma}}{dE_{\gamma}} \propto E_{\gamma}^{-\Gamma}. \quad (6.2)$$

The index Γ was varied between 1.8 and 2.4, which correspond to a typical spectral index range for astrophysical sources [200]. The results are summarized in the Table 6.3.

Upper limits on the flux at 95% C.L. for different DM annihilation spectra are considered as a function of the DM particle mass. A parametrization using the average of the WW and ZZ final states was taken from Bergström et al. [186], which

Galaxy	$\Phi_{\gamma}^{95\% \text{ C.L.}}(E_{\gamma} > E_{\min})$ ($10^{-13} \text{ cm}^{-2}\text{s}^{-1}$)
Sculptor ($E_{\min} = 220 \text{ GeV}$)	5.1 - 6.2
Carina ($E_{\min} = 320 \text{ GeV}$)	1.6 - 2.0

Table 6.3: The 95% confidence level upper limits on the γ -ray fluxes above the minimal energy E_{\min} , given in units of $10^{-13} \text{ cm}^{-2}\text{s}^{-1}$, for a power-law model with indices between $\Gamma = 1.8$ and $\Gamma = 2.4$. The lower values of the upper limits are found for the index $\Gamma = 1.8$.

will be used here and in Section 6.4. A comparison with DM particles annihilating purely into $b\bar{b}$ and $\tau^+\tau^-$ is done, using spectra computed with PYTHIA 6.225 [177].

Figure 6.2 shows the calculated upper limit on the flux for both Sculptor and Carina dSphs, which depends on the assumed spectrum and hence on the mass of the neutralino. The results obtained by *Fermi-LAT* [199] for the Sculptor dSph and energies $\gtrsim 100 \text{ MeV}$ are also plotted. As can be seen, for high neutralino masses ($\gtrsim 500 \text{ GeV}$) H.E.S.S. is more sensitive than *Fermi-LAT*. The flux sensitivity is qualitatively driven by the product of the acceptance $A_{\text{eff}}(E_{\gamma})$ times the observation time T_{obs} . Using the acceptances of about $A_{\text{eff}} \sim 10^5 \text{ m}^2$ for H.E.S.S. and of a few m^2 for *Fermi-LAT*, and observation times of about ~ 12 hours for H.E.S.S. and ~ 11 months for *Fermi-LAT*, the ratio between their sensitivities for a given DM mass yields a better sensitivity for H.E.S.S. by a factor of a few hundred, for masses well above the H.E.S.S. threshold.

6.3 Dark matter halo modelling

In order to calculate the exclusion limits on the DM annihilation cross section, one needs to model the density distribution of DM in the observed target that will be used in the astrophysical factor $\bar{\mathcal{J}}$ (eq. 5.2) calculation. Two hypotheses for spherical DM halo profiles are used for Sculptor and Carina: a pseudo-isothermal (pISO) profile (Eq. 5.3), and the *Navarro, Frenk, and White* (NFW) profile (eq. 5.5). Given a hypothesis about the gravitational potential of the galaxy, i.e. its DM halo profile, and about the velocity dispersion anisotropy of its stars, one can obtain the theoretical

6. Dark matter towards Sculptor and Carina dwarf galaxies

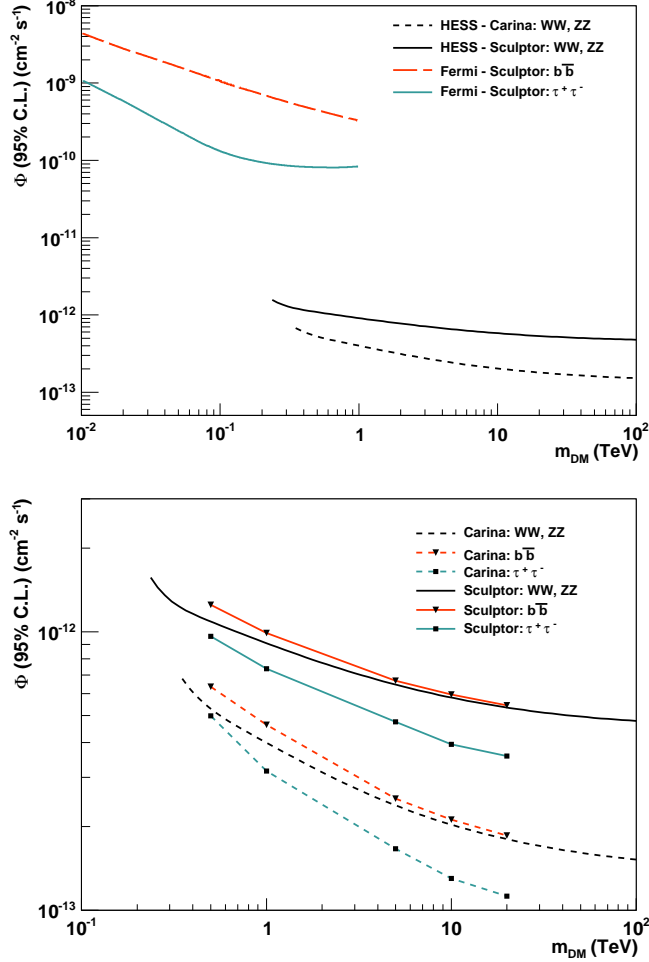


Figure 6.2: (*top*) Upper limits on fluxes at 95% C.L. for the Carina (dashed lines) and Sculptor (solid lines) dSphs obtained with H.E.S.S., for $E > 320$ GeV and $E > 220$ GeV, respectively, as function of the DM mass. The parametrization of the annihilation spectrum using the the average of the WW and ZZ final states is extracted from Bergström et al. [186]. *Fermi-LAT* results for Sculptor [199] with $E \gtrsim 100$ MeV are also plotted for $\tau^+\tau^-$ and $b\bar{b}$ final states [199]. (*bottom*) A zoomed view on the upper limit from H.E.S.S. using in addition various parametrizations for the annihilation spectrum [177].

line-of-sight velocity dispersion, σ_{los} , from the Jeans equation following the procedure described in Sect. 5.2.1. Comparing the observed line-of-sight velocity dispersion of stars for each distance bin with that predicted for the various models, one can find the DM halo parameters that best fit the observations (see Sect. 5.2.1 for more details). This was done in the literature in the both cases of Sculptor and Carina.

Sculptor: The DM halo mass content of Sculptor dSph as well as its profile parameters are estimated in a recent paper [172] and thesis [201], using two RGB (*Red Giant Branch*) stars populations to partially break the Jeans degeneracy in the DM halo modelling (Sect 5.2.1). The last gravitationally bound star was measured at $r_{\text{last}} = 1.8$ kpc, which gives an estimate of the tidal radius [201] and is used in the integration to obtain $\bar{\mathcal{J}}(\Delta\Omega)$. Two hypotheses for the velocity anisotropy profile, $\beta(r)$, were explored in [172]: a radially constant velocity dispersion anisotropy, and a Osipkov-Merritt (OM) velocity dispersion anisotropy [168, 169] (see Sect. 5.2.1). Using the parameters extracted from [201], the astrophysical factor $\bar{\mathcal{J}}$ is computed for eight different Dark Matter halos. The parameters as well as the astrophysical factor are summarized in the Table 6.4.

The large variety of investigated DM halos allows one to encompass the astrophysical uncertainties induced by the modelling. This amounts to a factor of ten for different assumptions. The assumption of an Osipkov-Merritt β induces higher $\bar{\mathcal{J}}$ factor than a constant β , since the central isotropy ($\beta = 0$) in the OM model implies in a slightly higher central density. The main difference however comes from the core radius size r_c , in the pISO profile, and the concentration parameter c which is directly related to the scale radius r_s in the NFW profile. Small values of these radii (or high concentration in the NFW case) gives a higher central density, and thus a higher $\bar{\mathcal{J}}$ factor, than large values of these radii.

Carina: Here, the best fit parameters of each DM halo profile were given for a NFW profile in [118] and for the pseudo-isothermal profile in [117]. The parameters for the NFW profile obtained from [118] are the virial mass $M_v = 2 \times 10^8 M_\odot$ and the star's velocity dispersion anisotropy $\beta(r) = -0.5$. Replacing M_v in Eq. 5.12 of Sect. 5.2.1, the virial radius is found to be $R_v = 12$ kpc. Using the relationship between M_v and the concentration parameter c found in [154] (Eq. 5.10 of Sect. 5.2.1) yields $c \simeq 22$. Finally $r_s = 5.35 \times 10^{-1}$ kpc is obtained using $r_s = c/R_v$ (see Sect. 5.2 for parameters definition). The parameters for a pseudo-isothermal profile with an isotropic velocity dispersion ($\beta(r) = 0$) and consistent with the kinematic data were obtained from [202], see also Figure 4 of [117]. The tidal radius is set arbitrarily to $r_t = 2.0$ kpc. Some works

6. Dark matter towards Sculptor and Carina dwarf galaxies

Sculptor dSph				
Iso Profile	r_c (kpc)	$M_{r_{\text{last}}}$ ($10^8 M_\odot$)	ρ_0 ($10^7 M_\odot \text{kpc}^{-3}$)	\bar{J} ($10^{23} \text{ GeV}^2 \text{cm}^{-5}$)
$\beta = \text{const}$	0.05	1.2	221	2.98
	0.5	3.3	9.13	0.27
$\beta = \beta_{OM}$	0.05	1.3	240	3.49
	0.5	3.4	9.40	0.29
NFW Profile	c	M_v ($10^9 M_\odot$)	r_s (kpc)	\bar{J} ($10^{23} \text{ GeV}^2 \text{cm}^{-5}$)
$\beta = \text{const}$	20	1.9	1.26	2.75
	35	0.59	0.48	5.20
$\beta = \beta_{OM}$	20	2.2	1.32	3.29
	35	0.68	0.51	6.24

Table 6.4: Structural parameters of the eight best fits [172] in the case of a pseudo-isothermal and NFW DM halo profiles for the Sculptor dSph, as well as the corresponding values of the astrophysical factor \bar{J} , for two hypotheses of the velocity anisotropy profile $\beta(r)$, two core radii (pseudo-isothermal) and two concentration parameters (NFW).

claim to observe stars around Carina as far as 3.5 kpc from its center, however it is still an open question whether these are bound or unbound objects [203, 204]. So the choice to arbitrarily set the tidal radius at 2.0 kpc is a conservative one. This value is used in the DM flux calculation to obtain $\bar{J}(\Delta\Omega)$. The parameters of the DM halo profiles as well as the astrophysical factor \bar{J} are summarized in Table 6.5.

6.4 Exclusion limits on the dark matter annihilation cross section

6.4.1 Generic case for exclusion limits

The exclusion limits are calculated following the methodology described in Sect. 5.5 using the Eq. 5.41. The $N_\gamma^{95\% \text{ C.L.}}$ from Sect. 6.1 are used (Table 6.2). A parametrization of dN_γ/dE_γ is taken here from [186] for typical DM particle self-annihilation into WW and ZZ pairs, and calculated from [136] for Kaluza-Klein $\tilde{B}^{(1)}$ self-annihilation.

6.4 Exclusion limits on the dark matter annihilation cross section

Carina dSph				
Iso Profile $\beta = 0$	r_c (kpc)	r_t (kpc)	ρ_0 ($10^8 M_\odot \text{kpc}^{-3}$)	\bar{J} ($10^{22} \text{ GeV}^2 \text{cm}^{-5}$)
	0.22	2.0	1.36	2.01
NFW Profile $\beta = -0.5$	c	M_v ($10^9 M_\odot$)	r_s (kpc)	\bar{J} ($10^{22} \text{ GeV}^2 \text{cm}^{-5}$)
	22	0.20	0.54	4.37

Table 6.5: Structural parameters of the two best fits [117, 118] in the case of a pseudo-isothermal and NFW DM halo profile for the Carina dSph, as well as the corresponding value of the astrophysical factor \bar{J} (see equation 5.2).

The first parametrization was chosen by Bergström et al. [186] in order to establish a benchmark model, which is particularly applied for MSSM neutralino studies. Here this parametrization is used for comparison purposes with past DM exclusion limits publications. The effects of different annihilation channels in the exclusion limits are going to be treated only in chapter 8.

The exclusion curves for a typical DM particle self-annihilation into WW and ZZ pairs are plotted for the Sculptor and Carina dSphs in Figure 6.3 and 6.4 referring to the halo profiles given in the Table 6.4 for Sculptor, and in the Table 6.5 for Carina, respectively. The values of $\langle\sigma v\rangle$ which are above the lines are excluded at 95% C.L. for a given DM halo profile assumption. The *Fermi-LAT* exclusion limit for Sculptor is added extending up to 1 TeV [199], which is based on a NFW profile with $r_s = 0.9$ kpc and $\rho_s = \delta_c \times \rho_c^0 = 3.7 \times 10^7 M_\odot \text{kpc}^{-3}$, and a DM particle parametrization with only $b\bar{b}$ in the final state. Using the parameters r_s and ρ_s from *Fermi-LAT* paper [199], the astrophysical factor with the H.E.S.S. solid angle for point-like observations ($\Delta\Omega = 10^{-5}$ sr) is $\bar{J} = 1.33 \times 10^{23} \text{ GeV}^2 \text{cm}^{-5}$. The resulting H.E.S.S. exclusion limits assuming this specific DM halo profile are plotted (pink dashed line).

Below ~ 1 TeV, the *Fermi-LAT* results provide stronger limits than the H.E.S.S. results. In comparison with the flux sensitivity (Section 6.2), the $\langle\sigma v\rangle$ upper limits also take into account the predicted integrated number of γ -rays in the instrument

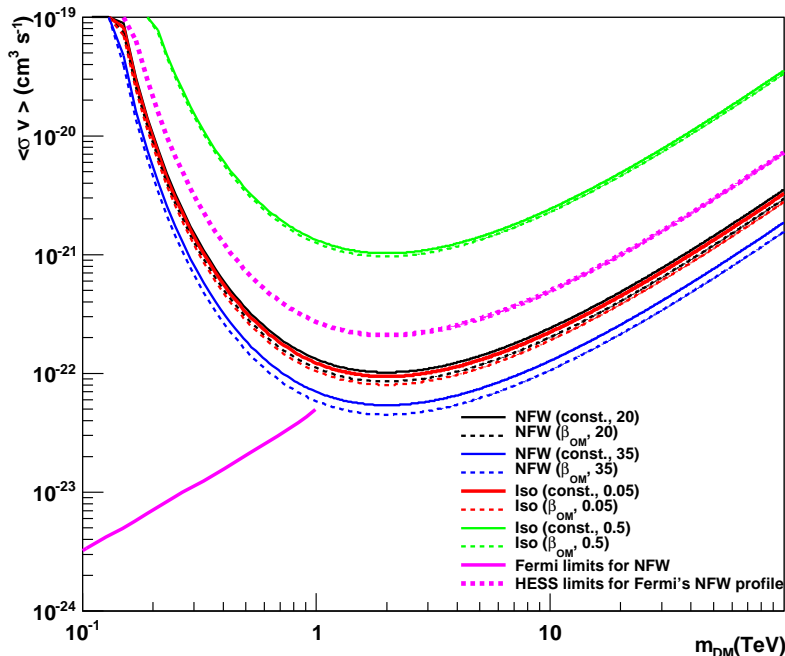


Figure 6.3: Upper limit at 95% C.L. of $\langle\sigma v\rangle$ as function of the DM particle mass for different DM halos of Sculptor dSph. For the NFW halo profile of Sculptor two concentration parameters are used: 20 and 35. For the pseudo-isothermal halo profile two core radii are used: 0.05 kpc and 0.5 kpc. Two hypotheses on the velocity anisotropy parameter are also studied: a constant (solid lines) and an Osipkov-Merritt (dashed lines) anisotropy. The velocity anisotropy and the concentration parameters are given in brackets for the NFW profile. The velocity anisotropy and the core radius are given in brackets for the pseudo-isothermal profile. The *Fermi-LAT* limits [199] for a NFW profile are also plotted as well as the H.E.S.S. limits for this NFW profile ($r_s = 0.9$ kpc and $\rho_s = 3.7 \times 10^7 M_\odot \text{kpc}^{-3}$).

energy range. The predicted number of γ -rays per annihilation event in the *Fermi-LAT* energy range is about 10^3 times higher than the one in the H.E.S.S. energy range. This implies a *Fermi-LAT* limit which is of the order of 10 times better than the one for H.E.S.S., despite the latter's stronger flux sensitivity. *Fermi-LAT* and H.E.S.S. give complementary limits on $\langle\sigma v\rangle$ in the 10 GeV - 100 TeV mass range.

The Figure 6.5 shows the exclusion limits of $\langle\sigma v\rangle$ in the case of the Kaluza-Klein DM particle $\tilde{B}^{(1)}$. The limits are plotted for the Sculptor dSph referring to the halo

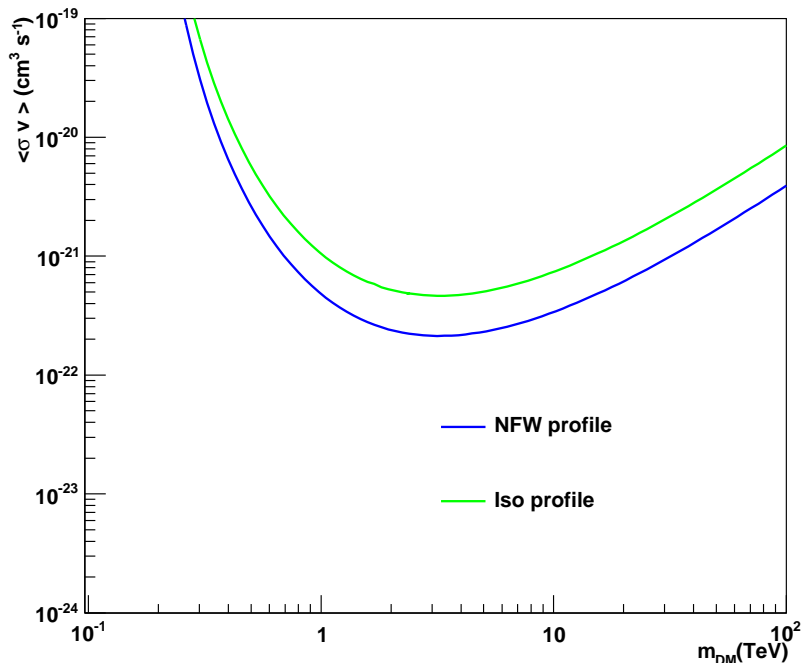


Figure 6.4: Upper limit at 95% C.L. of $\langle\sigma v\rangle$ as function of the DM particle mass for different DM halos for Carina dSph. Both the NFW halo profile and the pseudo-isothermal halo profile of Carina are plotted (see text for parameters).

profiles given in the Table 6.4. In the TeV range the 95% C.L. upper limit on $\langle\sigma v\rangle$ reaches $10^{-23} \text{ cm}^3 \text{s}^{-1}$.

6.4.2 Enhancement effects for the exclusion limits

Three cases that can modify the exclusion limits are considered: two particle physics effects, namely the *Sommerfeld enhancement* (Sect. 5.4.3) and the *Internal Bremsstrahlung* (IB) from the DM annihilation (Sect. 5.4.1), and an astrophysical effect due to the mass distribution of *dark-matter sub-halos*.

The Sommerfeld enhancement

Here two new assumptions were made for the Sculptor’s and Carina’s DM halo composition. The first assumption is to assume the DM particle annihilates to a W boson, which is the case when the neutralino is a pure wino. The second assumption is

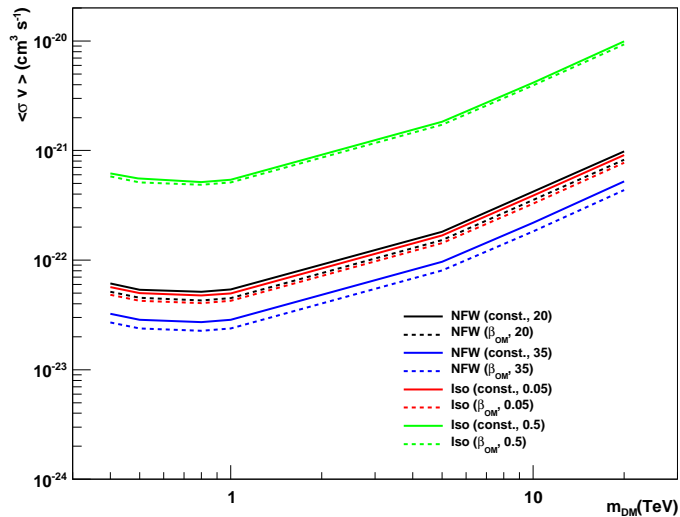


Figure 6.5: Upper limit at 95% C.L. of $\langle\sigma v\rangle$ as function of the Kaluza-Klein DM particle mass for all DM profiles of Sculptor in Table 6.4. The velocity anisotropy and the concentration parameters are given in brackets for the NFW profile. The velocity anisotropy and the core radius are given in brackets for the pseudo-isothermal profile.

to assume that the DM mean velocity inside the halo is the same as for the stars and constant with the radius (for detailed discussion see Section 5.15). The mean velocity dispersion of the stars is $\sigma_V \sim 10.0$ km/s for Sculptor and $\sigma_V \sim 7.5$ km/s for Carina.

In this class of objects, the relative velocity between the DM particles may be sufficiently low so that the Sommerfeld effect can substantially boost the annihilation cross section with respect to its value $\langle\sigma v\rangle_0$ during thermal freeze-out (Section 5.4.3), since it is particularly effective in the very low-velocity regime. The value of the enhancement “S” was numerically calculated following the procedure described in Sect. 5.4.3 where S depends on the DM particle mass and relative velocity. It was then used to improve the 95% C.L. upper limit on the velocity-weighted annihilation cross section, $\langle\sigma v\rangle_{\text{eff}}/S$ as a function of the DM particle mass. The effect of this enhancement is shown in Figure 6.6 for Sculptor and Figure 6.7 for Carina (*bottom*), and for two particular cases of the halo profile models. The predicted $\langle\sigma v\rangle_0$ for a pure wino [182] during thermal freeze-out as well as the typical annihilation cross section

for a thermally produced DM ($\langle\sigma v\rangle_0 \sim 10^{-26} \text{ cm}^3\text{s}^{-1}$ [205]) are also plotted. The Sommerfeld effect allows to exclude some specific wino masses at the level of $\langle\sigma v\rangle_0 \sim 10^{-26} \text{ cm}^3\text{s}^{-1}$.

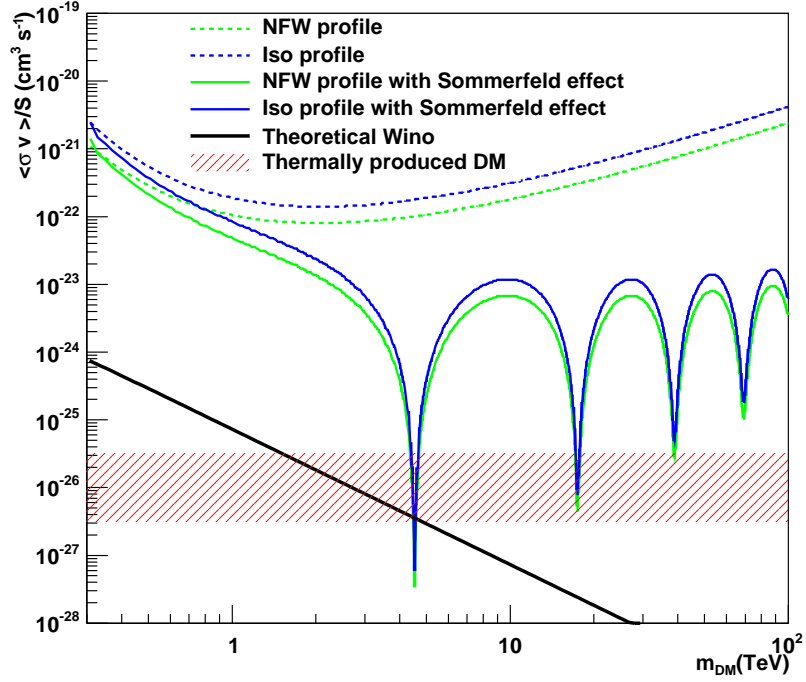


Figure 6.6: Upper limit at 95% C.L. on $\langle\sigma v\rangle/S$ as function of the DM particle mass enhanced by the Sommerfeld effect (see text for more details) for Sculptor. The NFW halo profile as well as the pseudo-isothermal profile are used. The predicted $\langle\sigma v\rangle_0$ for a pure wino [182] (solid black line) as well as the typical cross section for a thermally produced DM (dashed red area) are also plotted.

Internal Bremsstrahlung

Also in the case of a wino annihilation spectrum, the electromagnetic radiative correction to the main annihilation channels into charged particles can give a significant enhancement to the expected γ -ray flux in the observed environment due to internal Bremsstrahlung. This contribution to the annihilation spectrum was computed using the parametrization of [181] for all the wino masses in the H.E.S.S. energy range as

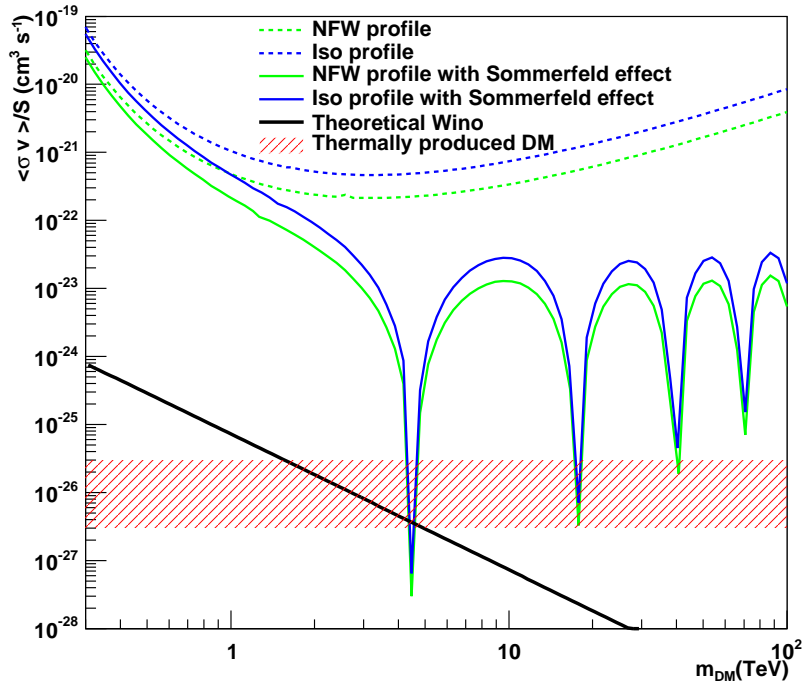


Figure 6.7: Upper limit at 95% C.L. on $\langle \sigma v \rangle / S$ as function of the DM particle mass enhanced by the Sommerfeld effect (see text for more details) for Carina. The NFW halo profile as well as the pseudo-isothermal profile are used. The predicted $\langle \sigma v \rangle_0$ for a pure wino [182] (solid black line) as well as the typical cross section for a thermally produced DM (dashed red area) are also plotted.

already mentioned in Sect. 5.4.1. The enhancement effect on the 95% C.L. upper limit on the velocity-weighted annihilation cross section is shown in Figure 6.8. The joint enhancement due to the Sommerfeld effect and IB is also plotted. The effect of the IB is only significant in the exclusion limits for the low mass DM particle regime.

Enhancement from dark-matter sub-halos

Astrophysical effects may also modify the exclusion limits. Numerical simulations of galactic halos predict a population of subhalos that could contribute to the overall astrophysical factor in equation 5.2. Using the procedures given in Sect. 5.2.2, the contribution to the astrophysical factor by the DM sub-halos population is estimated.

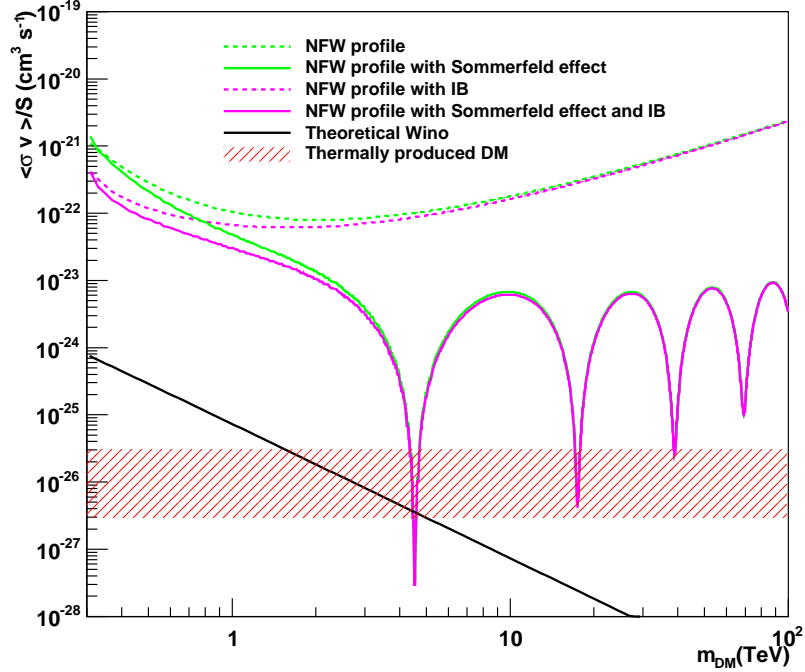


Figure 6.8: Upper limit at 95% C.L. on $\langle\sigma v\rangle/S$ as function of the DM particle mass enhanced by the Sommerfeld effect and the internal Bremsstrahlung (see text for more details) for a NFW profile of Sculptor. The predicted $\langle\sigma v\rangle_0$ for a pure wino (solid black line) as well as the typical cross section for a thermally produced DM (dashed red area) are also plotted.

An enhancement of the astrophysical factor is found to be of a few percent, which is too small to significantly affect the exclusion limits presented.

6.5 Summary and conclusion

Both Sculptor and Carina dSphs are well-studied in multiple wavelengths, providing reasonable measurements of the profile of the DM in their halos. Recent VHE γ -ray observations from H.E.S.S. of both of these objects provide new insight into the DM within them. While no positive DM annihilation signal has been detected, the observations provide constraining limits on dark matter parameters.

6. Dark matter towards Sculptor and Carina dwarf galaxies

Constraints have been obtained for the velocity weighted annihilation cross section $\langle\sigma v\rangle$ as a function of the mass for neutralino and KK DM particles. Concerning Sculptor dSph upper limits on $\langle\sigma v\rangle$ have been obtained in the range of $\sim 10^{-21}$ cm^3s^{-1} to $\sim 10^{-22}$ cm^3s^{-1} for DM particles annihilating into W and Z pairs and $\sim 10^{-21}$ cm^3s^{-1} to $\sim 10^{-23}$ cm^3s^{-1} for KK particles. From the different profile parameters investigated, much better limits are obtained for a NFW profile with a strong concentration parameter $c = 35$ when compared to the limits obtained for a isothermal profile with a large core radius of $r_c = 0.5$ kpc. Also for the Carina Sph better limits for $\langle\sigma v\rangle$ of neutralinos have been obtained for a NFW profile.

The DM halo model induces systematic uncertainties in the exclusion limits: the value of the astrophysical factor can vary over one order of magnitude for a given halo profile in the case of Sculptor. The results presented show that the DM particle models that could satisfy WMAP constraints on the Cold Dark Matter relic density [206] cannot be tested. H.E.S.S. limits are comparable to the limits reported by other IACTs like MAGIC [207] and VERITAS [208] on classic dSphs at the TeV mass range, but weaker than those obtained by *Fermi-LAT* [199] in the GeV mass range. Nevertheless, they are complementary to the *Fermi-LAT* limits in the TeV range. In the WW channel Icecube constraints towards the DM Galactic halo on $\langle\sigma v\rangle$ lie at the level of $\sim 10^{-22}$ cm^3s^{-1} [209]. Finally due to the resonant behavior of the Sommerfeld effect, some specific wino masses can be excluded, and the first experimental constraints have been obtained on the Sommerfeld effect using H.E.S.S. data and DM annihilation spectra.

Since these results from the H.E.S.S. collaboration [197] other studies were performed with H.E.S.S. and *Fermi-LAT* which provided stronger limits to the ones presented here. Using 24 months of *Fermi-LAT* data DM constraints to $\langle\sigma v\rangle$ as a function of the DM particle mass were derived, applying a joint likelihood analysis to 10 dwarf satellites galaxies. This work was performed by both the *Fermi-LAT* collaboration [210] and an independent group [211], which found similar results. Figure 6.9 shows the all-galaxies combined upper limits on the annihilation cross section for the $b\bar{b}$ final state. This procedure allows to rule out WIMP annihilation with cross sections predicted by the most generic cosmological calculation up to mass of ~ 27 GeV for the DM

annihilating purely into $b\bar{b}$, and up to mass of ~ 37 GeV for DM annihilating purely into $\tau^+\tau^-$. However, it is important to notice that these limits were derived assuming only a NFW profile for each of the galaxies. As it was showed in this work for the particular case of Sculptor and Carina, other assumptions on the DM halo profile, for example assuming cored profiles, or different anisotropy parameters, might induce less optimistic DM annihilation fluxes. Therefore the quoted errors on their astrophysical factor calculations may be underestimated. The H.E.S.S. collaboration, on the other

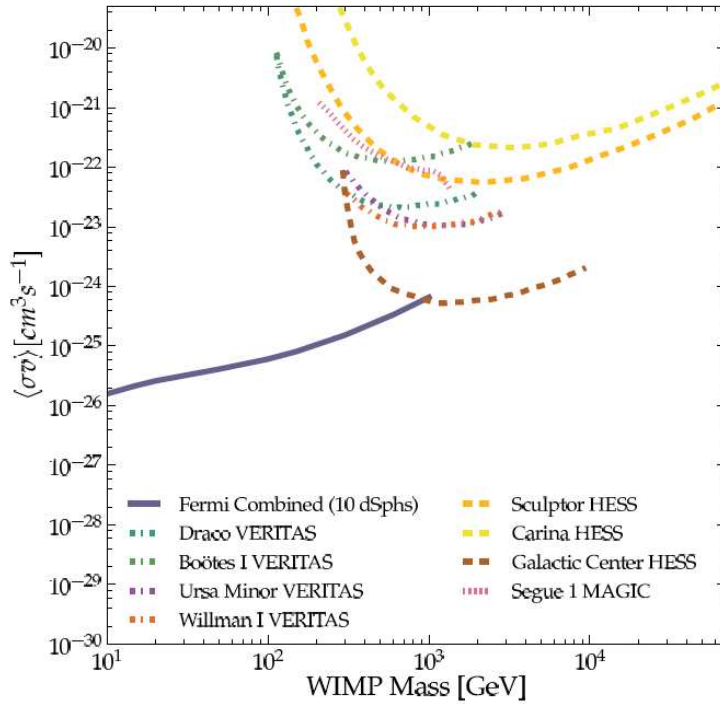


Figure 6.9: Summary of relevant constraints on the DM annihilation cross section with H.E.S.S., VERITAS and MAGIC, and the Fermi-LAT line is for a 24 months exposure. Ref. [212].

side, has reported limits on DM annihilation coming from an extended analysis of the Galactic Center halo [213]. The Figure 6.9 also presents the upper limits on $\langle\sigma v\rangle$ as a function of the DM particle mass for an Einasto DM density profile of the Milky Way. The limits on $\langle\sigma v\rangle$ are very strong in the TeV mass range, reaching $3 \times 10^{-25} \text{ cm}^3\text{s}^{-1}$ at 1 TeV for the assumption of a DM particle annihilating into quark-antiquark pairs. These limits are better than the *Fermi-LAT* limits on dwarf galaxies for DM masses above ~ 1 TeV. Nevertheless they also depend on the Milky Way DM halo profile assumption. For

6. Dark matter towards Sculptor and Carina dwarf galaxies

instance, assuming an isothermal DM halo profile would significantly loosen the given constraints.

Another very promising objects which might provide strong limits to a DM annihilation signal are the so-called ultra-faint dwarf galaxies. These are Milky Way satellites only recently discovered by the Sloan Digital Sky Survey (SDSS, [214]), and which are believed to even more DM dominated than the “classical” dwarf galaxies. On the other hand they suffer from an even more uncertain DM halo profile determination, since they harbors a very low number of luminous stars in their systems, and some of them may be tidal dwarf galaxies, or shreds from the violent building phase of the Milky Way [214]. In the next chapter the issue of well determine the DM halo distribution of tidal dwarf galaxies is addressed, for the particular case of the Sagittarius dwarf galaxy. Exclusion limits from the current generation and sensitivities of next generation of IACTs to a DM annihilation signal coming from the Sagittarius galaxy, as well as coming from the ultra-faint galaxy Segue 1 are then derived.

Chapter 7

Prospects for the Cherenkov Telescope Array towards dwarf galaxies

Contents

Introduction	138
7.1 CTA effective area	138
7.2 The Sagittarius dwarf galaxy	140
7.3 Modelling the Sagittarius dwarf dark matter halo	140
7.4 Exclusion and sensitivity limits to dark matter annihilation cross section	142
7.4.1 Sensitivity calculation and background estimates	142
7.4.2 Upper limits on the dark matter annihilation cross section	143
7.5 Astrophysical background emission	147
7.5.1 Millisecond pulsars in M54	148
7.5.2 Intermediate-Mass Black hole	150
7.6 Sensitivities predictions for Sculptor and Segue 1	150
7.7 Summary and conclusion	152

Introduction

In this chapter, an update at the constraints on a DM annihilation signal towards the Sagittarius dwarf galaxy (SgrDw) by the H.E.S.S. array of Imaging Atmospheric Cherenkov Telescopes is presented. The work presented here has been published in The Astrophysical Journal [215]. The current HESS constraints on SgrDw are based on the observation dataset collected in June 2006 and a work published in 2008. The constraints are updated in light of more realistic DM halo models than previously used [190, 216]. A prospect on the sensitivity of the future generation of IACTs, *i.e.* CTA (Cherenkov Telescope Array, 2010), for the detection of a DM annihilation signal is also given. The CTA design-study sensitivity is used to investigate the detection potential of possible conventional γ -ray emission, *e.g.* to the population of millisecond pulsars (MSP) in the globular cluster M54 at the center of SgrDw, or from the jet of a hypothetical central *intermediate-mass black hole* [217] (IMBH). Finally the potential of conservative performances of various telescope configurations of CTA are studied and sensitivity predictions to a DM annihilation signal coming from Sculptor dwarf galaxy and Segue 1 ultra-faint dwarf galaxy is given. The latter work is part of an article, which is about to be published in an special issue of the Astroparticle Physics Journal on CTA.

7.1 CTA effective area

As described in Sect. 2.3 CTA is expected to increase the flux sensitivity by a factor of 10 compared to current instruments, and enlarge the accessible energy range both towards the lower and higher energies. Based on the current CTA design study, a factor of about ten in effective area and at least a factor of two better in hadron rejection are expected. In the published “Conceptual Design Report” (CDR) of CTA, several conservative values of the effective area were calculated for various CTA telescopes configurations (CTA-array B, C and E are presented in the CDR). The conservative value of the effective areas comes mainly from the fact that the analysis cuts used in the Monte Carlo simulations were optimized for a detection of a Crab-like object, *i.e.*, point-like and with the same power-law spectrum as the Crab nebula (Hinton and Bernlohr private communication). An optimal cut was found at large telescope multiplicity, thus imposing a very high energy threshold and a low value

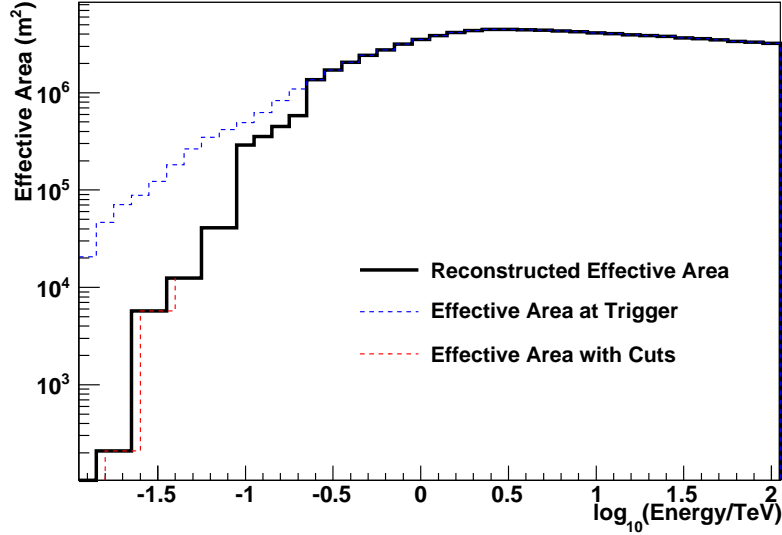


Figure 7.1: CTA effective area as function of the energy. The CTA effective area at the trigger level is smoothly connected below 200 GeV to the CTA effective of array E where γ -ray selection cuts were applied.

of the effective area below 1 TeV. These cuts are not necessarily optimal for DM searches.

In the study presented here, in the case of SgrDw, a higher value of the CTA effective area is used due to looser analysis cuts. The estimated CTA effective area at the trigger level (before offline analysis for gamma-hadron separation) is extracted from [218] and, from the experience with the H.E.S.S. effective area calculations, it is considered as a good estimate of the effective area at high energy (> 200 GeV). However, at lower energy (< 200 GeV), for actual observations, even applying very loose analysis cuts for the γ -rays selection, the effective area is expected to be much lower than the effective area at trigger level. So the trigger effective area is smoothly connected below 200 GeV to the published CTA effective area of array E (see for example Di Pierro et al. ICRC 2011). The effective area then decreases from $\sim 10^6$ m² at 200 GeV down to $\sim 10^3$ m² at about 20 GeV. In Figure 7.1 the CTA effective area as function of the γ -ray energy calculated at the trigger level and with the analysis cuts of the array E, as well as the reconstructed effective area used in this work are presented.

7.2 The Sagittarius dwarf galaxy

The Sagittarius dwarf galaxy is one of the nearest dwarf satellite galaxy, located at a distance of about 24 kpc from the Sun. Since the flux of the expected γ -ray signal is inversely proportional to the square of distance, one would expect the best dwarf spheroidal target to be the nearest one. However such dwarfs are also the closest to the Galactic Center and experience the tidal effect of the Milky Way. Recently, it has been shown that one could take advantage of this effect to trace back the evolution history of the object [219]. During the orbital motion of a dwarf galaxy, multiple crossings of the dwarf galaxy through the galactic disc of the Milky Way give rise to the formation of tidal streams, a careful study of which allows one to infer the gravitational potential of the dwarf galaxy.

In the case of the Sagittarius Dwarf galaxy (SgrDw), the tidal streams have been detected with multiple tracer populations [188, 220, 221, 222, 223, 224, 225, 226] and have been used to derive the DM halo potential. Furthermore, measurements of stars within SgrDw and the luminosity of its core and surrounding debris, allows the estimate of the DM content *prior* to tidal disruption [227, 228]. Other peculiar features of SgrDw include the presence of the M54 globular cluster coincident in position with its center of gravity [229], and hints for the presence of a central IMBH [217]. The latter point is supported by the observation of a deviation from a flat behavior in the surface brightness density profile towards the center of the object.

7.3 Modelling the Sagittarius dwarf dark matter halo

Sagittarius dwarf galaxy has experienced substantial tidal disruption by the Milky Way. Such effect inevitably modified the properties of the stellar and DM halo profiles. The initial luminosity and mass are larger than those observed today and depend on the history of the orbital motion of the galaxy around the Milky Way. The present luminosity in the stellar tidal debris can be used to reassemble the initial stellar profile of the galaxy [219, 230]. It has been estimated [227], using SDSS and 2MASS data, that 70% of SgrDw's luminosity now resides in the tidal debris. N-body simulations on the evolution of dwarf galaxies driven by galactic tides allows to recover the stellar and

DM halo profiles after evolution [230].

In a recent model, SgrDw is assumed to originate from a late-type, rotating disc galaxy [228]. In this model, the galaxy is composed of a stellar disk and a DM component. The DM halo profile is taken as an pseudo-isothermal (pISO) profile with the addition of an exponential cut-off, described by the density distribution

$$\rho_{\text{pISO}}(r) = \frac{m_{\text{h}}\alpha}{2\pi^{3/2}r_{\text{cut}}} \frac{\exp[-(r/r_{\text{cut}})^2]}{(r_{\text{c}}^2 + r^2)}, \quad (7.1)$$

where m_{h} is the halo mass, r_{c} is the core radius and $\alpha \simeq 1.156$ [228]. The DM halo mass can be estimated using the initial luminosity and a given mass-to-light ratio. Using the results from Niederste-Ostholt et al. [227] the initial luminosity was estimated to be $\sim 10^8 L_{\odot}$. Assuming a typical mass-to-light ratio for dwarf galaxies of 25 [188], the DM halo mass was found to be $m_{\text{h}} = 2.4 \times 10^9 M_{\odot}$. To account for the initial tidal disruption of the SgrDw halo by the Milky Way, a truncation of the halo profile was imposed at $r_{\text{cut}} = 12r_{\text{c}}$. The evolution of the SgrDw in the Milky Way potential was obtained via a N-body model of SgrDw using the particle-mesh gravity code SUPERBOX [231]. Peñarrubia et al. [228] applied this evolution code to recover the actual DM profile, by using the constraint of the observed stellar distribution. The values of the parameters found by Peñarrubia et al. [228] of the present ISO profile are given in Table 7.1.

Alternatively, cosmologically-motivated models of dwarf galaxies show that their DM halo can be described by a cuspy NFW profile (Eq. 5.5). To date, no N-body code simulates the evolution of SgrDw system with a NFW halo profile. Nevertheless, it was shown in [219] that the tightly bound central dark matter cusp is more resilient to disruption than a more loosely bound cored profile. Assuming that the external tidal field does not influence the kinematics of stars that locate the central regions of the dwarf, and ignoring the effects of tidal stripping on the outer ($r \gg r_s$) dark matter halo profile, one can use the Jeans equations to search the DM halo parameters that best fit the stellar central velocity dispersion for a observed King $\check{\Sigma}$ radius of this object. The assumption of isotropy and constant velocity dispersion implies in a King-NFW degeneracy, which gives rise to a family of NFW halo models which

7. Prospects for the CTA towards dwarf galaxies

can reproduce the stellar dynamics [230]. One way to break this degeneracy is using the relationship between the virial mass and concentration found in cosmological N-body simulations [see for instance, 232]. Using this procedure on the SDSS survey data provides a value of $r_s = 1.3$ kpc. Considering the scatter on the relationship between virial mass and concentration, the 2σ error on r_s is found to be ~ 0.2 kpc. This corresponds to the family of models with ρ_s spanning from 7.5×10^{-3} to $1.3 \times 10^{-2} M_\odot \text{pc}^{-3}$. In Table 7.1 the results of fits together with the astrophysical factors \bar{J} for different solid angles $\Delta\Omega$ are presented. Taking into account the error on the halo profile parameters the value of the astrophysical factor can vary by a factor of 2.

Table 7.1: Values of the *LOS*-integrated squared density averaged over the solid angle (\bar{J}) expressed in units of $10^{23} \text{ GeV}^2 \text{ cm}^{-5}$, for different solid angles $\Delta\Omega$. The values of \bar{J} are calculated for the NFW and pISO DM halo profiles. The parameters of these profiles are given in the first column.

DM halo profile	$\Delta\Omega = 10^{-3}$ sr	$\Delta\Omega = 2 \times 10^{-5}$ sr	$\Delta\Omega = 2 \times 10^{-6}$ sr
NFW	0.065	0.88	3.0
$r_s = 1.3$ kpc $\rho_s = 1.1 \times 10^{-2} M_\odot \text{pc}^{-3}$			
pISO	0.49	1.0	1.0
$r_c = 0.34$ kpc $m_h = 9.5 \times 10^8 M_\odot$			

7.4 Exclusion and sensitivity limits to the dark matter annihilation cross section

7.4.1 Sensitivity calculation and background estimates

The sensitivity for IACTs is calculated by comparing the number of events expected from an assumed γ -ray emission scenario with the expected level of background events. Following the procedure described in Sect. 5.5, in case of no γ -ray signal, a limit on the number of γ -rays at 95% confidence level (C.L.), $N_\gamma^{95\% \text{C.L.}}$, is calculated using the

7.4 Exclusion and sensitivity limits to dark matter annihilation cross section

method of Rolke et al. [185]. In what follows two cases are considered. In the case of current IACTs, the $N_\gamma^{95\%C.L.}$ calculation uses the numbers of γ -ray and background events extracted from 11h H.E.S.S. measurements of Sgdw [190]. The projected $N_\gamma^{95\%C.L.}$ for 50 h observation time is obtained by extrapolating both the numbers of γ -ray and background events from 11 h to 50 h. In the case of 95% C.L. sensitivity calculations, $N_\gamma^{95\%C.L.}$ is calculated assuming the background-only hypothesis. For the H.E.S.S. sensitivity the number of background events is taken from the extrapolation at 50 h of observation. For the CTA sensitivity, the number of background events is calculated from Eq. (5.40) of Sect. 5.5 after multiplication by the effective area of the detector and the observation time. $N_\gamma^{95\%C.L.}$ is then calculated using five off regions ($\alpha = 1/5$) (see Sect. 5.5 for details).

7.4.2 Upper limits on the dark matter annihilation cross section

Here the parametrization of the DM self-annihilation γ -ray spectrum dN_γ/dE_γ is taken from [186] for a typical DM particle annihilating into W and Z pairs. Fig. 7.2 shows the upper limits of current IACTs on $\langle\sigma v\rangle$ as a function of the DM mass m for $\Delta\Omega = 2 \times 10^{-5}$ sr. Using the HESS upper limits published in [190], the new upper limits are calculated for the NFW and pISO DM halo profiles of Section 7.3 and 11 h of observation time; the projected upper limits for 50 h of observation time is also plotted. The limits are at the level of 5×10^{-23} cm³s⁻¹ around 1 TeV for 50 h. The sensitivity of H.E.S.S. for 50 h observation time is also displayed. The limits now published with more realistic DM halo models loosen the existing constraints by more than one order of magnitude. However it is important to notice that older publications [e.g. 190, 216] on DM searches towards SgrDw used dark matter mass profiles which lead to somewhat optimistic constraints on particle dark matter self-annihilation cross sections. These models were used because no accurate modelling of SgrDw existed at that time.

The sensitivity limits for CTA on $\langle\sigma v\rangle$ as a function of the DM mass m are presented in Fig. 7.3 for 50 h and 200 h observation times. The limits are calculated with $\Delta\Omega = 2 \times 10^{-6}$ sr for the NFW DM halo profile and $\Delta\Omega = 10^{-3}$ sr for the ISO DM halo profile. The sensitivity limits at 95% C.L. reaches the level of 10^{-25} cm³s⁻¹

7. Prospects for the CTA towards dwarf galaxies

for DM masses of about 1 TeV in the case of the ISO DM halo profile.

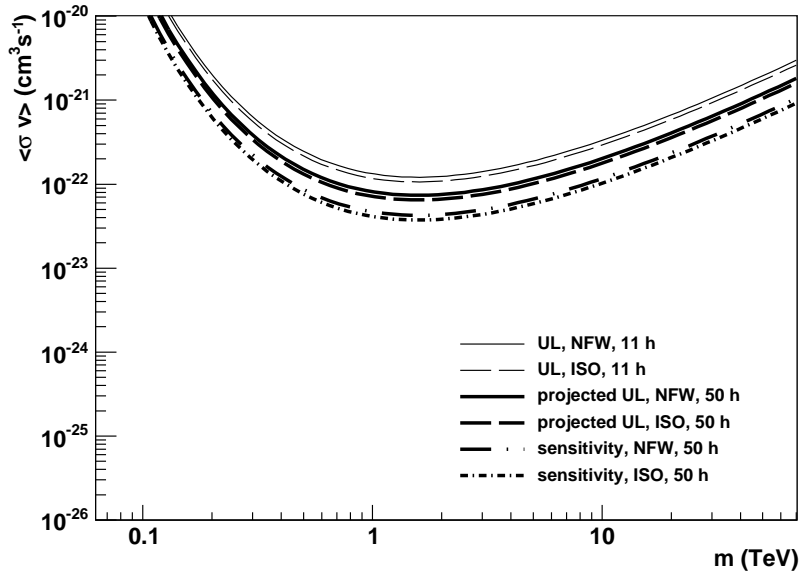


Figure 7.2: 95% C.L. upper limits on the velocity-weighted annihilation cross section $\langle\sigma v\rangle$ versus the DM mass m for a NFW (solid line) and Isothermal (ISO) (dashed line) DM halo profiles respectively for 11 h observation time and $\Delta\Omega = 2 \times 10^{-5}$ sr. The projected upper limits are displayed for 50 h observation time. The sensitivities at 95% C.L. for 50 h are also shown for NFW (long-dashed dotted line) and ISO (dashed dotted line) DM halo profiles.

Two additional contributions to the overall γ -ray flux that can modify the limits are considered: namely the *Sommerfeld effect* and *Internal Bremsstrahlung* (IB) from the DM annihilation. Assuming now that the DM particles only annihilate to a W boson (wino), the attractive potential created by the Z gauge boson through the weak force before annihilation would give rise to an enhancement of $\langle\sigma v\rangle$ through the Sommerfeld effect. Assuming that the DM velocity dispersion inside the halo is the same as for the stars, the value of the DM velocity dispersion is fixed at 11 km s^{-1} for SgrDw [188]. The value of the enhancement factor (S) is numerically calculated as done in [184] and then used to improve the upper limits on the velocity-weighted annihilation cross section, $\langle\sigma v\rangle/S$ as a function of the DM particle mass. The factor S also varies as

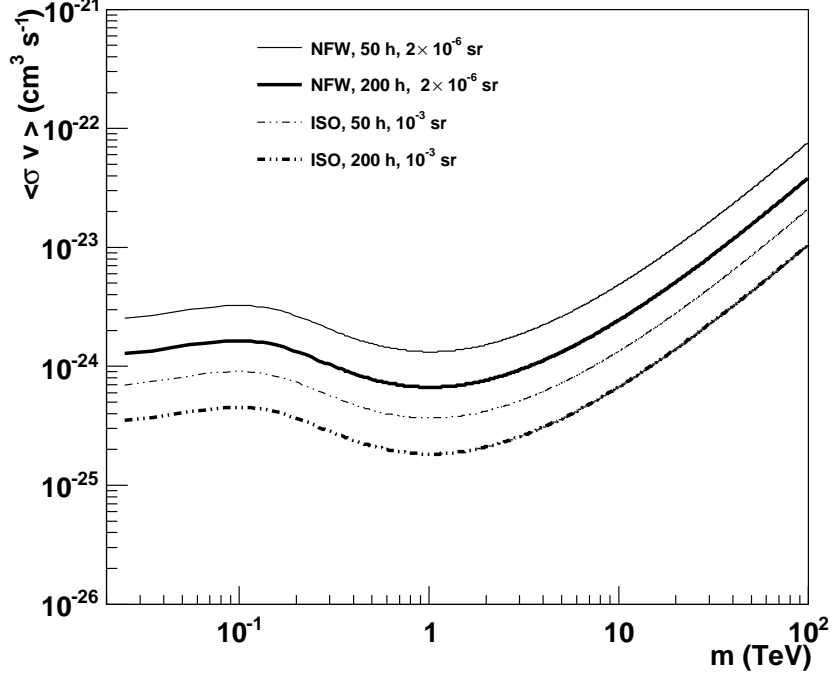


Figure 7.3: Sensitivity at 95% C.L. for CTA on the velocity-weighted annihilation cross section $\langle\sigma v\rangle$ versus the DM mass m for a NFW (solid line) and Isothermal (ISO) (dashed line) DM halo profiles, respectively. The sensitivity is shown for 50 and 200 h observation times. The solid angle of observation is taken as $\Delta\Omega = 2 \times 10^{-6}$ sr for the NFW DM halo profile and $\Delta\Omega = 10^{-3}$ sr for the ISO DM halo profile.

function of the mass.

Additionally, every time a DM particle annihilates into charged particles, the electromagnetic radiative correction to the main annihilation channel can give a more or less significant enhancement to the expected γ -ray flux in the observed environment due to internal Bremsstrahlung (IB) [181, 233]. As already discussed in Sect. 5.4.1 in the case of a wino DM particle the annihilation spectrum would receive a considerable contribution from Internal Bremsstrahlung [181]. Fig. 7.4 shows the 95% C.L. upper limits on $\langle\sigma v\rangle/S$ as a function of the DM mass m for current IACTs (H.E.S.S.). The projected upper limit is shown for the NFW profile, 50 h observation time and $\Delta\Omega = 2 \times 10^{-5}$ sr. The effect of the IB is only significant below ~ 1 TeV.

7. Prospects for the CTA towards dwarf galaxies

Some specific wino masses can be excluded due to the resonant enhancement in the Sommerfeld effect. Outside resonances, the projected upper limits are improved by more than one order of magnitude for DM masses above 1 TeV. The sensitivity at 95% C.L. for CTA on $\langle\sigma v\rangle/S$ as a function of the DM mass m is presented in Fig. 7.5. The limits are calculated for the ISO DM halo profile, with 200h observation time and $\Delta\Omega = 10^{-3}$ sr. The values of $\langle\sigma v\rangle$ corresponding to cosmological thermally-produced DM, $\langle\sigma v\rangle \sim 3 \times 10^{-26} \text{ cm}^3\text{s}^{-1}$, can be tested for specific wino masses in the resonance regions of the Sommerfeld effect. Outside the resonances the sensitivity on $\langle\sigma v\rangle/S$ is improved by more than one order of magnitude for TeV DM masses, reaching the level of $10^{-26} \text{ cm}^3\text{s}^{-1}$.

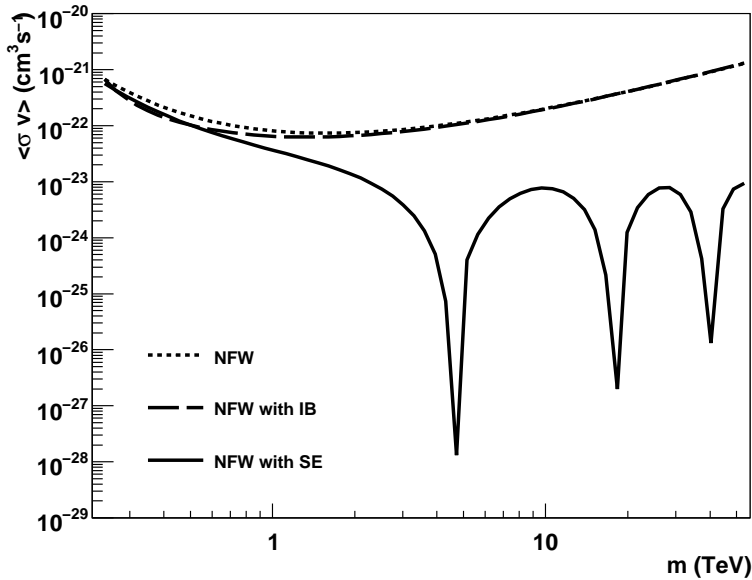


Figure 7.4: Projected upper limits at 95% C.L. on the $\langle\sigma v\rangle/S$ versus the DM mass m enhanced by the IB (dashed line) and SE (solid line) for the NFW profile. The projected upper limits are shown for 50 h observation times and $\Delta\Omega = 2 \times 10^{-5}$ sr.

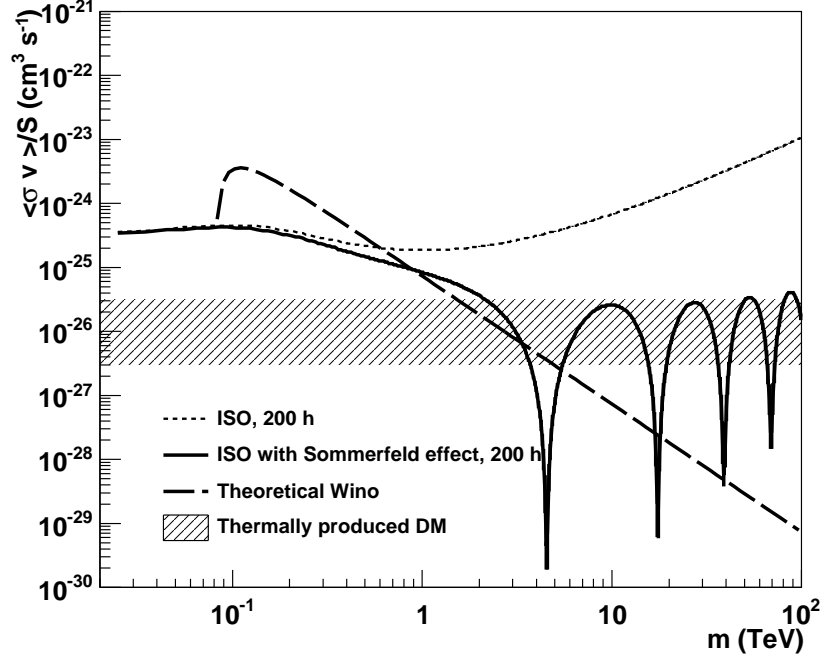


Figure 7.5: Sensitivity at 95% C.L. for CTA on the $\langle\sigma v\rangle/S$ versus the DM mass m enhanced by the SE for the ISO profile. The sensitivity is shown for 200 h observation times and $\Delta\Omega = 10^{-3}$ sr.

7.5 Astrophysical background emission

Dwarf galaxies are generally believed to contain very little background emission from conventional astrophysical sources at VHE energies, and are therefore easy targets for DM searches. This assumption is based on their low gas content and stellar formation rate. However, some γ -ray emitting sources may still exist within them: in particular from pulsars, and black hole accretion and/or jet emission processes. The Sagittarius and Carina dwarf galaxies both host globular clusters (the M54 globular cluster is located at the center of SgrDw), and globular clusters are known to host millisecond pulsars (MSPs). The collective emission of high energy γ -rays by MSPs in globular clusters has been detected by *Fermi-LAT* [20], and emission in the VHE energy range has been predicted by several models for these objects, but has not yet been observed. The possible emission of very high energy radiation by millisecond pulsars from the

7. Prospects for the CTA towards dwarf galaxies

M54 globular cluster is examined in section 7.5.1. Additionally, it has been suggested by some authors [see 234, 235, and references thereby] that globular clusters may host black holes with masses of around 10^2 to 10^4 solar masses (called *intermediate-mass black holes, or IMBHs*). Indeed, Ibata et al. [217] suggest SgrDw may also be a possible host for a $10^4 M_{\odot}$ IMBH. The high energy emission from the IMBH candidate in the center of M54 is discussed in section 7.5.2.

7.5.1 Millisecond pulsars in M54

The M54 globular cluster at the center of SgrDw is likely to harbor a large population of pulsars, especially MSPs. The number of MSPs in globular clusters has been shown by the *Fermi-LAT* collaboration [20] to be correlated with the stellar collision rate, Γ , inside the globular cluster. Γ is proportional to $\rho^{3/2} r_c^2$, where ρ is the cluster central luminosity and r_c its core radius. Taking a central surface brightness of $\mu_V \simeq (14.12 - 14.9) \text{ mag arcsec}^{-2}$ from Table 4 of [236] and a core radius $r_c = 0.9 \text{ pc}$, the stellar collision rate of M54 is scaled with respect to the collision rate of the M62 globular cluster (in M62 $\rho^{3/2} r_c^2 = 6.5 \times 10^6 L_{\odot}^{3/2} \text{ pc}^{-2.5}$):

$$\Gamma_{\text{M54}} \simeq (0.8 - 2.6) \times \Gamma_{\text{M62}}. \quad (7.2)$$

Γ_{M62} is the reference collision rate of the M62 globular cluster which was normalised in [20] so that it is equal to 100. In Figure 7.6 [20] the correlation between the predicted number N_{MSP} of MSPs and the collision rate is presented. The predicted number of MSPs in M54 is found to be: $N_{\text{MSP}} = 60 - 140$.

The collective very-high-energy γ -ray emission of millisecond pulsars from globular clusters has been predicted by several authors, notably Bednarek and Sitarek (BS) [21], Venter, deJager and Clapson (VJC) [22] and Cheng et al. (CCDHK) [23]. Using the effective area of CTA described in Section 7.1, one expects to observe respectively 1285, 181 and 71 γ -rays per hour towards the 47 Tucanae globular cluster, with the BS, CCDHK and VJC models, respectively. As suggested by Venter and de Jager (2008), a rough estimate of the collective VHE emission of M54 can be obtained from their predicted emission of 47 Tucanae by scaling by the factor:

$$x = \left(\frac{N_{\text{MSP}}}{100} \right) \left(\frac{d_{47\text{Tuc}}}{d_{\text{M54}}} \right)^2 \left(\frac{\langle u_{\text{M54}} \rangle}{\langle u_{47\text{Tuc}} \rangle} \right). \quad (7.3)$$

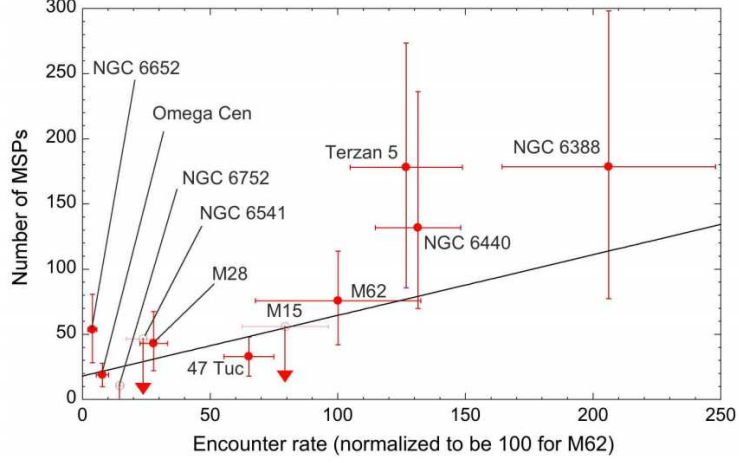


Figure 7.6: Predicted number of MSPs versus stellar encounter rate Γ_e . The data have been fitted by a linear relation $N_{\text{MSP}} = 0.5 \times \Gamma_e + 18$. (source Ref. [20])

In this equation, $d_{47\text{Tuc}}$ and d_{M54} are the distances to 47 Tucanae and M54, and $\langle u_{\text{M54}} \rangle$ and $\langle u_{47\text{Tuc}} \rangle$ the average luminosity per cubic parsec of the globular cluster. Taking the distances, luminosity and half-mass radii of M54 and 47 Tucanae from [238] (2010 edition), one finds a correction factor $x \simeq 1.6 \times 10^{-2}$, assuming that M54 contains 100 MSPs. The expected number of γ -rays per hour are thus 19.9 and 5.6 in the BS and CCDHK models. For the VJC model, the number of expected γ -rays per hour is about 1.1.

The signal extension are predicted to be almost point-like $\sim 1'$ in the BS and VJC models and as extended as $\simeq 12'$ for the CCDHK model. To estimate whether this signal is observable or not, the signal integration regions are taken as $3'$ for the BS and VJC models and $12'$ for the CCDHK model. With an hadron rejection factor of 10% as in section 5.5, the number of background per hour is calculated following the procedure of 7.4. The significance of the collective MSP signal depends thus on the observation time T_{obs} (in hours) as respectively $4.5 \sqrt{T_{\text{obs}}}$, $0.31 \sqrt{T_{\text{obs}}}$ and $0.25 \sqrt{T_{\text{obs}}}$ in the BS, CCDHK and VJC models. The BS model would give a signal at the 4.5σ level after just a one hour observation. The other models would give a much smaller signal, with a typical significance of 4σ after 200 hours of observation.

In summary, the millisecond pulsars of M54 could give a significant VHE γ -ray signal

7. Prospects for the CTA towards dwarf galaxies

in CTA with observation times of typically 200 hours. For a cosmological thermally produced DM particle, $\langle\sigma v\rangle = 3\times 10^{-26} \text{ cm}^3\text{s}^{-1}$, the corresponding signal would have a significance of 0.1σ , after 200 hours of observation and without any boost factor. The collective MSP signal would be a few orders of magnitude stronger than the DM annihilation signal.

7.5.2 Intermediate-Mass Black hole

Ibata et al. [217] reported evidence for density and kinematic stellar cusps in the globular cluster M54, possibly due to the presence of $10^4 M_{\odot}$ IMBH. An estimation of the largest contribution of the IMBH to a possible VHE γ -ray signal is done, assuming that the IMBH is active and has a jet inclined towards the line of sight with an angle θ . The contribution of the black hole to the VHE γ -ray emission is estimated using the model developed by [239], on the emission of relativistic jets associated with active galactic nuclei. The parameters of the model for the central black hole and jet are described in [239]. However at higher energies, in particular in the CTA energy range, the emission is in the $10^{-18} - 10^{-17} \text{ erg cm}^{-2} \text{ s}^{-1}$ flux range—too faint to be detected by CTA (for details see Viana et al. 2012 [215]).

7.6 Sensitivities predictions for Sculptor and Segue 1

In order to investigate the potential of various telescope configurations of CTA a study was performed using the effective areas for the CTA-arrays B, C and E of the CRD. A conservative sensitivity prediction to a DM annihilation signal is given for the “classical” dwarf galaxy Sculptor, and the ultra-faint dwarf galaxy Segue 1. Segue 1 is considered as one of the best targets for DM searches, although its nature is still under debate, due to its similarities with globular clusters.

Segue 1 was recently discovered in 2006 as an overdensity of resolved stars in the SDSS [214]. It is located at a distance of 23 ± 2 kpc from the Sun at (RA,Dec)=(10h07m03.2s,16° 04'25”), well above the galactic plane. Because of its proximity to the Sagittarius stream, the nature of the Segue 1 overdensity has recently been disputed, with some authors arguing that it was a tidally disrupted globular cluster originally associated with the SgrDw. However a metallicity and kinematics study of

7.6 Sensitivities predictions for Sculptor and Segue 1

a large number of Segue 1 star members (71 stars) demonstrated that Segue 1 is a dwarf galaxy. According to the study of its star kinematics, Segue 1 is probably one of the most dark matter-dominated dSph and is often highlighted as the most promising dSph target for indirect dark matter searches.

Table 7.2: Astrophysical factors \bar{J} for Sculptor and Segue 1. Dec. is the target declination and D the distance.

dSph	Dec. [deg]	D [kpc]	\bar{J} [GeV ² cm ⁻⁵]	Profile
Sculptor	-83.2	79	8.9×10^{17}	NFW
			2.7×10^{17}	ISO
Segue 1	+16.1	23	1.7×10^{19}	Einasto

The same procedure applied in the case of SgrDw in the past section can be applied in the case of Sculptor and Segue 1, with the caution of changing accordingly the effective area and the astrophysical factor \bar{J} in the calculation of the 95% C.L. limit on the velocity-weighted annihilation cross section (Eq. 5.41). The observation time is set to 100 hours. The integration solid angle to $\Delta\Omega$ is taken as $\Delta\Omega = 1 \times 10^{-5}$ sr. The astrophysical factors \bar{J} are extracted from Charbonnier et al. [240].

In the case of Sculptor two DM halo profiles are assumed, a NFW and an ISO profile. The DM halo of Segue 1 is modeled by an Einasto profile (see Sect. 5.2). The astrophysical factor for both galaxies are summarized in the Table 7.2. The sensitivity limits as a function of the DM particle mass m_{DM} for both the NFW and the ISO DM halo profiles of Sculptor are depicted in Figures 7.7. The sensitivity is calculated assuming that the DM particles annihilating exclusively into $b\bar{b}$, for arrays B, C and E at an observation zenith angle of 20° . Sensitivity limits as a function of the DM particle mass m_{DM} assuming DM particle annihilating into $b\bar{b}$, $\tau^+\tau^-$ and $mu^+\mu^-$ are presented in Figure 7.8 for the Segue 1 Einasto profile and the CTA-array E. In the same figure the sensitivity limit assuming the $b\bar{b}$ annihilation channel and the NFW profile of Sculptor (and Ursa Minor) is plotted for comparison purpose. Because of the much larger astrophysical factor of Segue 1 the sensitivity limits reach stronger values

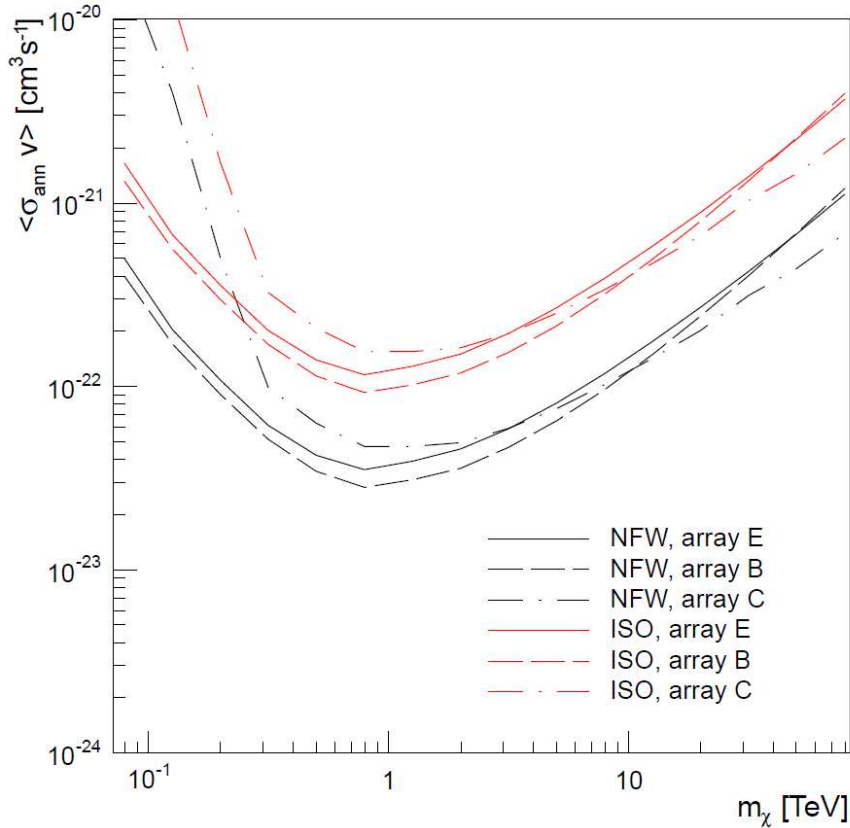


Figure 7.7: CTA sensitivities on the velocity-averaged annihilation cross section as a function of the DM mass for 100 hours observation of Sculptor with the CTA array E (solid line), B (dashed line) and C (dashed-dotted line). Both the NFW (black line) and cored isothermal (ISO, red line) DM halo profiles are shown, for an integration solid angle $\Delta\Omega = 1 \times 10^{-5}$ sr. Annihilations are assumed to occur with 100% branching ratio into $b\bar{b}$. Ref. [212].

than the ones of Sculptor. Nevertheless it is important to stress that no systematical analysis on the Segue 1 DM halo profile determination was ever done in the literature, and the uncertainties on its DM halo profile, when evaluated, may loosen the presented constraints.

7.7 Summary and conclusion

Older publications [e.g. 190, 216] on DM searches towards SgrDw used dark matter mass profiles which lead to somewhat optimistic constraints on particle dark matter

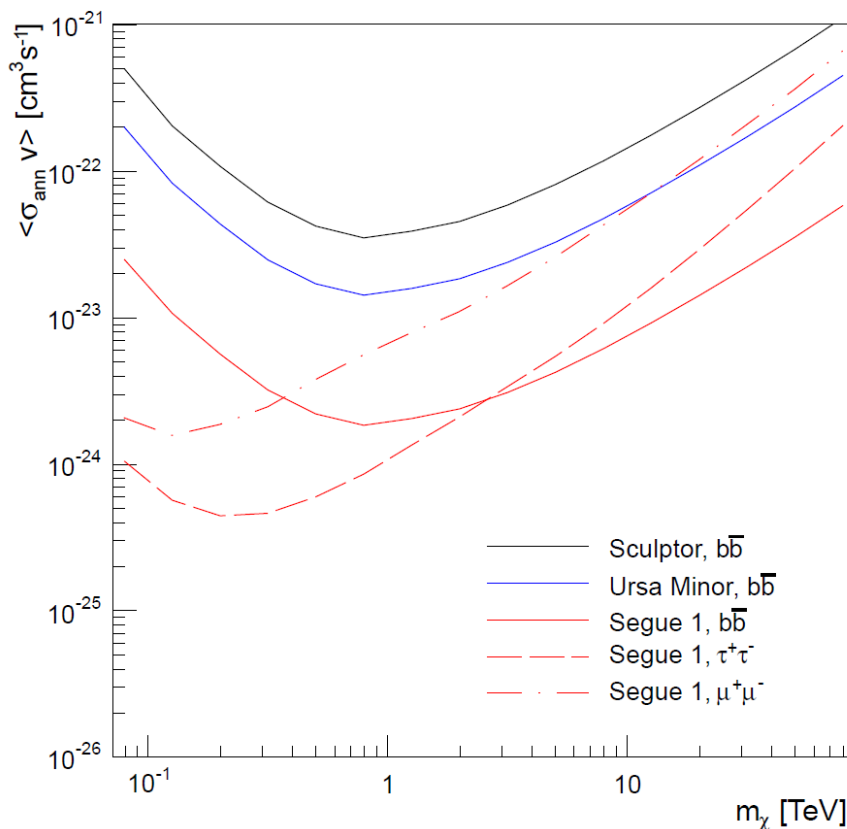


Figure 7.8: CTA sensitivities on the velocity-averaged annihilation cross section versus the WIMP mass for 100 hours observation towards Sculptor, Ursa Minor and Segue 1, assuming 100% branching ratio into $b\bar{b}$. For Segue 1 also annihilation with 100% branching ratio into $\tau^+\tau^-$ and $\mu^+\mu^-$ are shown. The calculations are done for array E and $\Delta\Omega = 1 \times 10^{-5}$ sr. Ref. [212].

self-annihilation cross sections. These models were used because no accurate modelling of SgrDw existed at that time. Several realistic models are now published that loosen the existing constraints by more than one order of magnitude. The future CTA array will be sensitive to $\langle\sigma v\rangle$ values around a few 10^{-24} $\text{cm}^3 \text{s}^{-1}$. Some models could be excluded after 200 hours of observation, if boosts factors are taken into account.

However, the very high energy emission of several astrophysical objects could give an observable signal for long-enough observation times. The collective very high energy emission of the MSPs of the M54 globular cluster, which is predicted by several models, could be much stronger than a DM signal. It could be observed in just a few tens of hours with CTA. The candidate IMBH located at the center is not expected to give

7. Prospects for the CTA towards dwarf galaxies

an observable signal. Under favorable circumstances (active black hole and jet aligned towards the line of sight), it might nevertheless be detectable in observations of SgrDw.

The potential of conservative performances of various telescope configurations of CTA are studied. Sensitivity predictions to $\langle\sigma v\rangle$ of a DM annihilation signal coming from Sculptor dwarf galaxy and Segue 1 ultra-faint dwarf galaxy reach values around a few $10^{-23} \text{ cm}^3 \text{ s}^{-1}$ and $10^{-24} \text{ cm}^3 \text{ s}^{-1}$, respectively. In the case of Segue 1, if the DM particle annihilates into $\tau^+\tau^-$, CTA could be sensitive to $\langle\sigma v\rangle$ of a few $10^{-25} \text{ cm}^3 \text{ s}^{-1}$ for a DM particle mass around 200 GeV.

In the past two chapters the current H.E.S.S. exclusion limits and sensitivities of future IACTs to a DM annihilation signal towards Milky Way dwarf satellite galaxies were presented. Investigations were done towards the “classical” dSph galaxies Sculptor and Carina, the tidal disrupted Sagittarius dwarf galaxy, and the ultra-faint dwarf galaxy Segue 1. Besides dwarf galaxies, another class of objects which have been considered as good targets for the indirect detection of DM are the galaxy clusters. DM, in fact, is supposed to be the dominant component of the galaxy clusters mass budget, accounting for up to 80% of its mass (the other components are the galaxies and the gas of the intra-cluster medium). In the next chapter the search for VHE γ -rays from DM annihilation coming from the Fornax galaxy cluster is presented.

Chapter 8

Gamma-rays from the Fornax galaxy cluster

Contents

Introduction	156
8.1 Target selection and dark matter content	157
8.1.1 Dark matter in the Fornax galaxy cluster	158
8.1.2 Dark matter halo substructures	160
8.2 Astrophysical non-thermal emission from Fornax	162
8.3 H.E.S.S. observations and data analysis	165
8.3.1 Fornax galaxy cluster observation by H.E.S.S.	165
8.3.2 Data analysis	165
8.4 Gamma-ray flux upper limits	167
8.5 Exclusion limits on dark matter annihilations	168
8.5.1 γ -ray flux enhancements	169
8.5.2 Inverse Compton emission	171
8.5.3 Enhancement from dark matter substructures	173
8.6 Summary and conclusion	173

Introduction

Galaxy clusters are the largest virialized objects observed in the Universe. Their main mass component is dark matter (DM), making up about 80% of their total mass budget, with the remainder provided by intracluster gas and galaxies, at 15% and 5% respectively [see e.g. 124]. Despite the fact that galaxy clusters are located at much further distances than the dwarf spheroidal galaxies around the Milky Way, the higher annihilation luminosity of clusters make them comparably good targets for indirect detection of dark matter. The flux of γ -rays from WIMP DM annihilation in clusters of galaxies is possibly large enough to be detected by current γ -ray telescopes [173, 241]. Also standard astrophysical scenarios have been proposed for a non-thermal γ -ray emission [see e.g. 242, for a review], in particular, collisions of intergalactic cosmic rays and target nuclei from the intracluster medium. Despite these predictions, no significant γ -ray emission has been observed in local clusters by H.E.S.S. [243, 244], MAGIC [245] and *Fermi*-LAT [246, 247] collaborations. Although γ -rays of a different astrophysical emission processes have already been detected from some central radio galaxies in clusters [e.g. 32, 248, 249, 250].

This chapter reports on the observation in VHE γ rays of the Fornax galaxy cluster (ACO S373) with the High Energy Stereoscopic System (H.E.S.S.). The work presented here has been published in The Astrophysical Journal [148]. Interdependent constraints on several DM properties are derived from the data, such as the DM particle mass and annihilation cross section. Different models of the DM density distribution of the cluster halo are studied. The chapter is structured as follows. In Section 8.1 the Fornax galaxy cluster is described. The choice of Fornax for a DM analysis is motivated, based on the DM content and distribution inside the cluster. Section 8.1 describes the most important non-thermal astrophysical phenomena taking place in the Fornax galaxy cluster. In Section 8.1 the data analysis and results are presented. Upper limits on the γ -ray flux for both standard astrophysical sources and DM annihilation are extracted in Section 4. Exclusion limits on the DM annihilation cross section versus the particle mass are given in Section 5. Several DM particle candidates are considered, with particular emphasis on possible particle physics and astrophysical enhancements to the

γ -ray annihilation flux.

8.1 Target selection and dark matter content

H.E.S.S. telescope has observed three galaxy clusters, Coma, Virgo and Fornax. All three clusters are in principle promising targets for indirect dark matter searches through γ -rays because of its high expected annihilation flux (Section 4.3.2). Nevertheless, the radio galaxy M 87 at the center of Virgo provides a strong astrophysical γ -ray signal [32], showing flux variabilities from daily to yearly timescales that exclude the bulk of the signal to be of a DM origin. Since a DM γ -ray signal would be hard to disentangle from this dominant standard astrophysical signal, Virgo is found not to be a prime target for DM searches.

Moreover, galaxy clusters are expected to harbor a significant population of relativistic cosmic-ray protons originating from different sources, such as large-scale shocks associated with accretion and merger processes [251, 252], or supernovae [253] and AGN activity [254]. The γ -ray emission arising from pion decays produced by the interaction of these cosmic-ray protons with the intracluster gas may be a potential astrophysical background to the DM-induced γ -ray signal. In the case of Coma, it was shown [241] that such astrophysical background is expected to be higher than the DM annihilation signal¹. On the other hand, the same study ranked Fornax as the most luminous cluster in DM-induced γ -ray emission among a sample of 106 clusters from the HIFLUGCS catalog [255]. The DM-to-cosmic-ray γ -ray flux ratio of Fornax was predicted to be larger than 100 (see Table 8.1) in the GeV energy range [241]. The cosmic-ray induced emission will be discussed in the case of Fornax in Section 8.2.

The center of Fornax galaxy cluster is located at $\text{RA}(J2000.0) = 03^{\text{h}}38^{\text{m}}29^{\text{s}}.3$ and $\text{Dec}(J2000.0) = -35^{\circ} 27' 00''.7$ in the Southern Hemisphere. For ground-based Cherenkov telescopes like H.E.S.S. (cf. Chap. 3), low zenith angle observations are required to guarantee the lowest possible energy threshold and the maximum sensitivity

¹Also the two brightest radio galaxies, NGC 4874 and NGC 4889, lying in the central region of Coma may be potential sources of a standard astrophysical γ -ray signal.

8. Gamma-rays from the Fornax galaxy cluster

Galaxy Cluster	Fornax	Coma	Virgo
RA (J2000.0)	3h38m40s	12h59m47s	12h26m32s
Dec. (J2000.0)	-35° 18' 37"	27° 56' 20"	12° 43' 23"
Distance (Mpc)	19	99	17
$\theta_{z,\min}$	12°	51°	35°
DM/CR flux ratio	108.1	3.6	no data

Table 8.1: Characteristics of the galaxy clusters observed by H.E.S.S.: first three lines show the coordinates in RADEC (J2000.0) and the distance in Mpc (taken from [255]). The fourth line show the minimum zenithal angle of observation by the H.E.S.S. telescope. The fifth line present DM-to-cosmic-ray γ -ray flux ratio extracted from [241] for Fornax and Coma; in the case of Virgo no DM induced γ -ray emission is studied due to the M 87 strong emission.

of the instrument. Given the location of H.E.S.S., this condition is best fulfilled for Fornax, compared to the Virgo and Coma clusters as it can be seen in Table 8.1. Therefore, Fornax is the preferred galaxy cluster target for dark matter searches for the H.E.S.S. experiment. The properties of its dark matter halo are discussed in more details in the following section.

8.1.1 Dark matter in the Fornax galaxy cluster

The first approach to determine the DM distribution in Fornax follows the method described in 4.3.2. Using the X-ray measurements of the gravitationally bound hot intracluster gas in the HIFLUGCS catalog [255], the virial mass and radius of Fornax are found to be $M_{\text{vir}} \sim 10^{14} M_{\odot}$ and $R_{\text{vir}} \sim 1$ Mpc, respectively. Under the assumption of a NFW halo profile, and the concentration parameter-virial mass relation from Eq. 5.11, the NFW halo parameters are expressed in terms of ρ_s and r_s . This model is hereafter referred as to RB02.

The second approach is based on the velocity dispersion measurements and the subsequent solution of the Jeans equation for different sets of dynamical tracers found in the Fornax cluster. From velocity dispersion measurements on dwarf galaxies observed up to about 1.4 Mpc, a dynamical analysis of the Fornax cluster by Drinkwater

et al. [256] constrained the cluster mass. The associated DM density profile, hereafter referred as to DW01, can be well described by a NFW profile [122] with parameters given in Table 8.2. Richtler et al. [122] have analyzed the DM distribution in the inner regions of Fornax by using the globular clusters (GCs) as dynamical tracers. This allowed an accurate DM mass profile measurement out to a radial distance of 80 kpc from the galactic cluster centre, corresponding to an angular distance of $\sim 0.25^\circ$. The resulting velocity dispersion measurements can be well fitted by a NFW DM halo profile with parameters given in Table 8.2. This density profile is referred in the next as to RS08.

Detailed analysis using the same data set but this time separating the data into different samples of subpopulations of globular clusters was done in [123]. The kinematics stellar data of Fornax was also used in different samples. As discussed in 5.15 the use of different samples to derive the DM halo helps to partially breaks the Jeans degeneracy. Both a NFW and a Burkert DM halo profiles can equally well fit the globular cluster and stars velocity dispersion measurements. Representative DM halo profiles using different sets of globular clusters samples, hereafter referred as to SR10 a₆ and SR10 a₁₀, are extracted from Table 6 of [123]. The parameters for both the NFW and Burkert DM halo profiles are given in Table 8.2.

Using the dark matter halo parameters derived from the above-mentioned methods, values of \bar{J} were derived for different angular integration radii. The point-spread-function of H.E.S.S. corresponds to an integration angle of $\sim 0.1^\circ$ [68], and most often the smallest possible angle is used in the search for dark matter signals in order to suppress background events. However, since a sizable contribution to the γ -ray flux may also arise from dark matter subhalos located at larger radii (see Section 5.2.2), integration angles of 0.5° and 1.0° were also considered.

The choice of the tracer samples induces a spread in the values of the astrophysical factor \bar{J} up to one order of magnitude for an integration angle of 0.1° . This spread can be better seen in Figure 8.1, which shows the astrophysical factor $\bar{J} \times \Delta\Omega$ as function of the integration angle. Note that the GCs and stars measurements of [122] and [123] trace the DM density distribution only up to 80 kpc from the center. In consequence the

8. Gamma-rays from the Fornax galaxy cluster

			$\bar{J}(\Delta\Omega) [10^{21} \text{ GeV}^2 \text{ cm}^{-5}]$		
Model	r_s [kpc]	$\rho_s [M_\odot \text{ pc}^{-3}]$	NFW profile		
			$\theta_{\text{max}} = 0.1^\circ$	$\theta_{\text{max}} = 0.5^\circ$	$\theta_{\text{max}} = 1.0^\circ$
RB02	98	0.0058	112.0	6.5	1.7
DW01	220	0.0005	6.2	0.5	0.1
RS08	50	0.0065	24.0	1.2	0.3
SR10 a ₁₀	34	0.0088	15.0	0.6	0.1
SR10 a ₆	200	0.00061	7.0	0.5	0.1
			Burkert profile		
Model	r_c [kpc]	$\rho_c [M_\odot \text{ pc}^{-3}]$	$\theta_{\text{max}} = 0.1^\circ$	$\theta_{\text{max}} = 0.5^\circ$	$\theta_{\text{max}} = 1.0^\circ$
SR10 a ₁₀	12	0.0728	15.0	0.6	0.2
SR10 a ₆	94	0.0031	2.4	0.5	0.1

Table 8.2: Dark matter halo models for the Fornax galaxy cluster. The first three columns show the selected profiles (see text for details) with their respective NFW or Burkert halo parameters. The last three columns show the astrophysical factor \bar{J} , calculated for three different integration radii.

derived values of the virial mass and radius are significantly smaller than those derived from X-ray measurements on larger distance scales (see Table 8.3). Thus the DM density values may be underestimated for distances larger than about 100 kpc in these models. On the other hand, for indirect DM searches this does not pose a real problem since it is well known that for an NFW profile about 90% of the DM annihilation signal comes from the volume within the scale radius r_s . This can be seen in Figure 8.2, where the normalized astrophysical factor $\bar{J} \times \Delta\Omega$ is plotted as function of the integration angle expressed in terms of radial distance to the center. Therefore, even for NFW models with large virial radii such as RB02 and DW01, the main contribution to the annihilation signal comes from the region inside about 98 kpc and 220 kpc, respectively.

8.1.2 Dark matter halo substructures

Figure 8.3 shows the substructure enhancement B_{sub} over the smooth halo as function of the opening integration angle for the NFW profile RB02 following the prescription described in Sect. 5.2.2. At the distance of Fornax, integration regions larger than

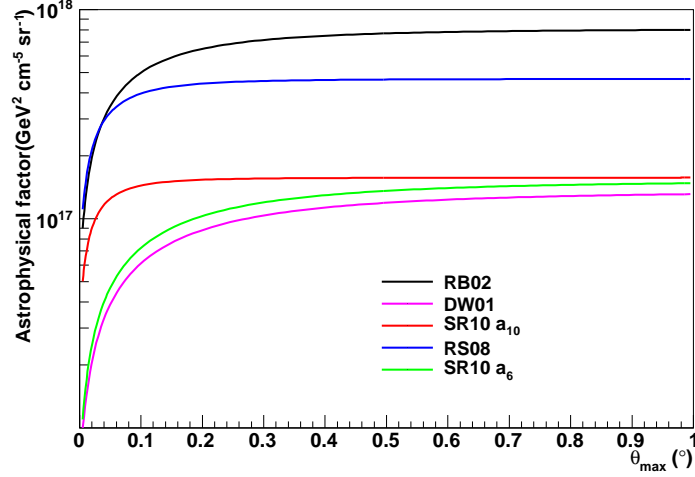


Figure 8.1: \bar{J} as function of the integration angle for all the DM halo models of Fornax presented in Table 8.2.

$\sim 0.2^\circ$ correspond to more than 65 kpc. Beyond these distances the substructure enhancement exceeds a factor 10. Two values of the limiting mass of substructures are used: $M_{\text{lim}} = 10^{-6} M_\odot$ and $M_{\text{lim}} = 5 \times 10^{-3} M_\odot$, inducing a *high* and a *medium* value of the enhancement, respectively. The values of B_{sub} for the opening angles of 0.1° , 0.5° and 1.0° and for both values of M_{lim} are given in Table 8.4.

Effect of the virial radius

As already mentioned in Sect. 5.2.2 numerical simulations of galactic halos are scale invariant. Since the virial radii of the different dark matter halo models in Table 8.2 are also different, the substructures contribution to the γ -ray flux will be renormalised at their maxima at different distances from the Fornax cluster center. As a consequence, for a fixed solid angle of observation the substructure enhancement will depend on the assumed halo model. This effect can be seen in Figure 8.4, where the substructure enhancement B_{sub} over the smooth halo as function of the opening integration angle is given for all the halo models of Table 8.2.

Nevertheless the NFW profile RB02 is chosen to be used as the DM density distribution of the smooth halo to derive γ -ray flux enhancements from substructures.

8. Gamma-rays from the Fornax galaxy cluster

Model	Tracers	Method	R_{vir} [Mpc]	M_{vir} [$10^{13}M_{\odot}$]
RB02	Hot intracluster gas	X-ray + c- M_{vir}	0.88	8.3
DW01	Dwarf galaxies	Jeans	0.72	4.6
RS08	GCs	Jeans	0.56	2.1
SR10 _{a10}	Red GCs + Stars	Jeans	0.39	0.7
SR10 _{a6}	Blue GCs	Jeans	0.72	4.5

Table 8.3: Dark matter halo models for the Fornax galaxy cluster. The first three columns show the selected profiles (see text for details) with the tracers and method used to derive the DM halo parameters. The last two columns show the predicted values of virial radius R_{vir} and virial mass M_{vir} for each DM halo model.

θ_{max}	0.1°	0.5°	1.0°
$M_{\text{lim}} = 10^{-6}M_{\odot}$	4.5	50.5	120
$M_{\text{lim}} = 5 \times 10^{-3}M_{\odot}$	1.5	8.2	18.3

Table 8.4: Enhancement B_{sub} due to the halo substructure contribution to the DM flux, for different opening angles of integration θ_{max} . The enhancement is calculated for two limiting masses of substructures M_{lim} and over the smooth DM halo RB02.

The choice of the RB02 profile among the others is based on the observation that substructures in the form of gravitationally bound dwarf galaxies to Fornax are actually observed up to about 1 Mpc from the center. They are thus included within the virial radius predicted by the RB02 profile ($R_{\text{vir}} \simeq 1$ Mpc), but not within the virial radii of the other halo profiles.

8.2 Astrophysical non-thermal emission from Fornax

Although not directly detected in galaxy cluster, relativistic cosmic-ray particles are expected to populate these objects. The most compelling evidence for relativistic particle populations in such objects is the non-thermal radio emission observed from several galaxy clusters (Giovannini et al. 1993, Feretti et al. 2004). Further evidence is provided by possible non-thermal X-rays observed from a few clusters (Rephaeli and Gruber 2002, Fusco-Femiano et al. 2004, Eckert et al. 2007). Moreover in

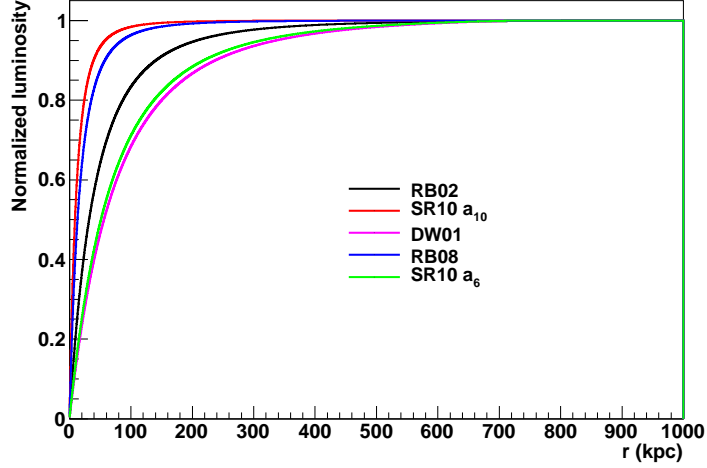


Figure 8.2: DM annihilation luminosity normalized at its maximum value as function of the integration radius for all the DM halo models of Fornax presented in Table 8.2.

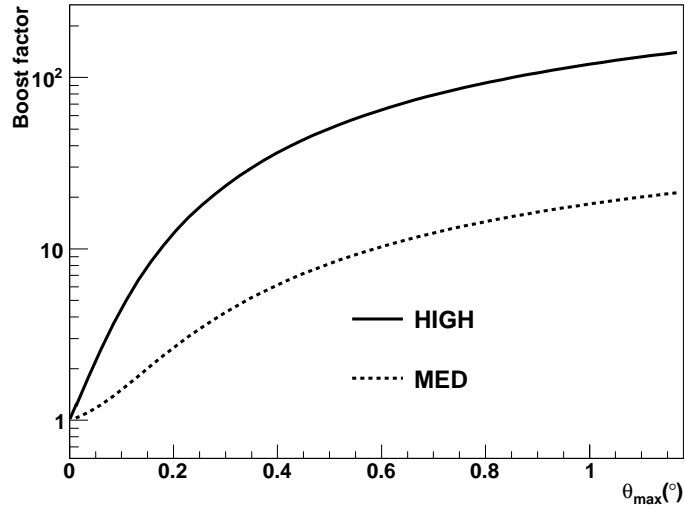


Figure 8.3: Substructure γ -ray flux enhancement as function of the opening angle of integration. Two values of the limiting mass of substructures are used: $M_{\text{lim}} = 10^{-6} M_{\odot}$, for the high (HIGH) boost (solid line), and $M_{\text{lim}} = 5 \times 10^{-3} M_{\odot}$, for the medium (MED) boost (dashed line). The RB02 profile is chosen as the smooth host DM halo.

supernovae remnants and on scales of galaxies, especially, in the MW, the cosmic rays are observed directly as well as indirectly through radio, X-ray, and γ -ray emission.

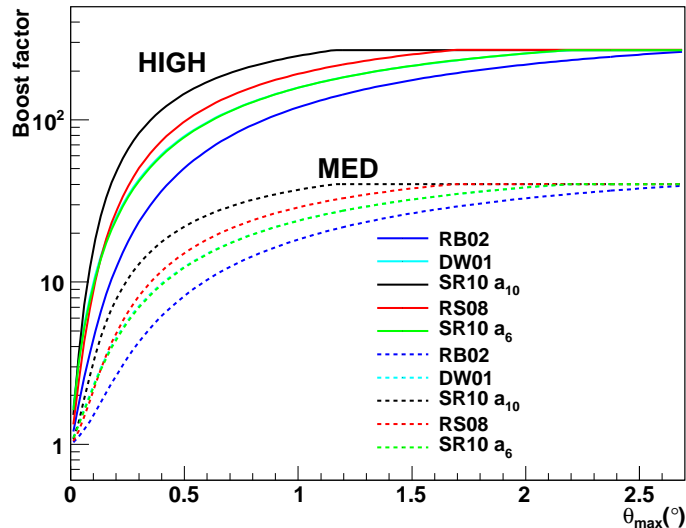


Figure 8.4: Substructure γ -ray flux enhancement for all the models of table 8.2 as function of the opening angle of integration. Two values of the limiting mass of substructures are used: $M_{\text{lim}} = 10^{-6} M_{\odot}$, for the high (HIGH) boost (solid line), and $M_{\text{lim}} = 5 \times 10^{-3} M_{\odot}$, for the medium (MED) boost (dashed line).

γ -ray emission is expected from inelastic collisions of relativistic protons on the intracluster gas, which produce, in their hadronic debris, neutral pions promptly decaying into two γ -rays. Relativistic electrons are also expected to produce γ -rays through inverse Compton up-scattering on the background radiation fields, such as the CMB. In this context the fraction η of thermal energy in the cluster volume in the form of relativistic non-thermal particles is an important parameter that can determine the level of γ -ray emission expected. Since the thermal energy content is a function of the cluster mass, the most massive and nearby clusters present the best targets to probe for such γ -ray emission.

Recent studies [173, 241, 257] have computed the cosmic-ray induced γ -ray flux from pion decays using a cosmological simulation of a sample of 14 galaxy clusters [258]. Since the electron induced γ -ray flux from inverse Compton is found to be systematically subdominant compared to the pion decay γ -ray flux [241], this contribution is not considered. Using the results of [173], the γ -ray flux above 260 GeV for Fornax is

calculated assuming an opening angle of observation of 1.0° and 10% of the thermal cluster energy in the form of cosmic-rays (efficiency $\eta = 0.1$) and it is found to be:

$$\Phi_\gamma(E_\gamma > 260\text{GeV}) = 6 - 12 \times 10^{-15} \text{ cm}^{-2} \text{ s}^{-1}, \quad (8.1)$$

depending if the emission from individual galaxies within Fornax are taken into account or not.

8.3 H.E.S.S. observations and data analysis

8.3.1 Fornax galaxy cluster observation by H.E.S.S.

Dedicated observations of the Fornax cluster were conducted in fall 2005 [259]. The nominal pointing position was fixed at the position of the central galaxy NGC 1399, $\text{RA}(\text{J2000.0}) = 03^{\text{h}}38^{\text{m}}29^{\text{s}}.3$ and $\text{Dec}(\text{J2000.0}) = -35^\circ 27' 00''.7$. The observations were carried out in *wobble mode* [68], with the target typically offset by 0.7° from the pointing direction, allowing simultaneous background estimation from the same field of view. The total data passing the standard H.E.S.S. data-quality selection described in chapter 3 yield an exposure of 14.5 hrs live time with a mean zenith angle of 21° . The Fornax cluster is a very extended object. Its DM halo possibly reaches distances as far as 1 Mpc of its center, which correspond to an angular distance of about 3° . Together with the fact that beyond 65 kpc ($\sim 0.2^\circ$) the γ -ray flux from DM substructures becomes very important, *extended* analyses using integration angles of 0.5° and 1.0° are performed in order to improve the chances of a signal detection.

8.3.2 Data analysis

The data analysis was performed using the improved *model* analysis described in the chapter 3 (Model++), with independent cross-checks performed with the *Hillas*-type analysis procedure. Both analyses give compatible results using standard cuts. The cosmic-ray background estimation for the three different signal integration angles 0.1° , 0.5° and 1° was done using the *template* model described in the Section 3.2. Because of the large integration ON region all the other background subtraction methods, based on ON-OFF regions, cannot be applied. Indeed for integration ON regions with radii too close or larger than the observation offset there is problem in defining the OFF regions,

8. Gamma-rays from the Fornax galaxy cluster

since an exclusion region needs to be taken at least as large as the ON region itself. The *template* model circumvent this problem by selecting the hadron-like events in the same region, but selecting only those which do not pass the analysis cuts as background.

No significant excess was found above the background level in any of the integration regions, as visible in Fig. 8.5 for an integration angle of 0.1° . An upper limit on the total number of observed γ -rays $N_\gamma^{95\% \text{ C.L.}}$, was calculated at 95% confidence level (C.L.). The calculation followed the Rolke et al. [185] method, using the number of γ -ray candidate events in the signal region N_{ON} and the *normalized* number of γ -ray events in the background region $\overline{N}_{\text{OFF}}$. Since the normalization is performed with respect to the direction-dependent acceptance and event rate, the background normalization factor for $\overline{N}_{\text{OFF}}$ as defined in [72] is $\alpha \equiv 1$. This is equivalent to the assumption that the uncertainty on the background determination is the same as for the signal, allowing a conservative estimate of the upper limits. This information is summarized in Table 8.5.

A minimal γ -ray energy (E_{min}) is defined as the energy at which the acceptance for point-like observations reaches 20% of its maximum value, which gives 260 GeV for the observations of Fornax. Limits on the number of γ -ray events above the minimal energy E_{min} have also been computed (see Table 8.6) and are used in Section 8.4 for the calculation of upper limits on the γ -ray flux.

θ_{max}	N_{ON}	$\overline{N}_{\text{OFF}}$	$N_\gamma^{95\% \text{ C.L.}}$	Significance
0.1°	160	122	71	2.3
0.5°	3062	2971	243	1.2
1.0°	11677	11588	388	0.6

Table 8.5: Numbers of VHE γ -ray events from the direction of the Fornax galaxy cluster centre, using three different opening angles for the observation. Column 1 gives the opening angle θ_{max} , columns 2 and 3 the numbers of γ -ray candidates in the ON region, N_{ON} , and the normalized number of γ -ray in the OFF region, $\overline{N}_{\text{OFF}}$, respectively. Column 4 gives the 95% C.L. upper limit on the number of γ -ray events according to [74]. The significance of the numbers of γ -ray candidates in the ON region is stated in column 5 according to Rolke et al. [185].

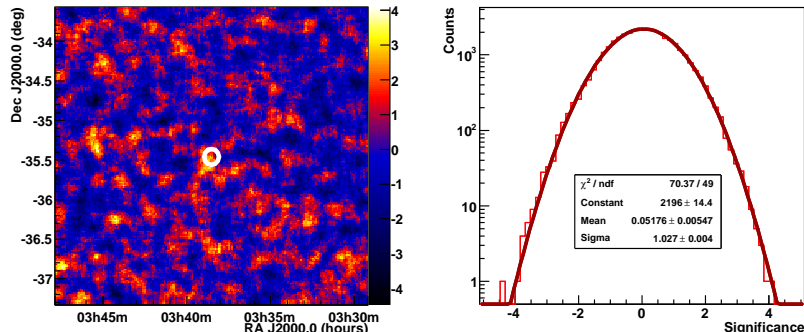


Figure 8.5: Left: Significance map in equatorial coordinates, calculated according to the Li & Ma method [73], with an oversampling radius of 0.1° . The white circle denotes the 0.1° integration region. No significant excess is seen at the target position. Right: Distribution of the significance. The solid line is a Gaussian fitted to the data. The significance distribution is well described by a normal distribution.

8.4 Gamma-ray flux upper limits

The upper limits on the number of observed γ -rays above the minimal energy E_{\min} are translated into the upper limit on the observed γ -ray flux Φ_γ with an assumed source energy spectrum dN_γ/dE_γ . For instance the intrinsic spectra of standard astrophysical VHE γ -ray sources typically follow power-law behavior of index $\Gamma \approx 2 - 3$. Upper limits at 95% C.L. on the integral flux above the minimum energy (cf. Section 6.2) are given in Table 8.6 for different source spectrum indices. Flux upper limits for a DM annihilation spectrum as function of the DM particle mass are presented in Figure 8.6 assuming DM annihilation purely into $b\bar{b}$, W^+W^- and $\tau^+\tau^-$ and an opening angle of the integration of 0.1° . Flux upper limits reaches $10^{-12} \text{ cm}^{-2} \text{ s}^{-1}$ for 1 TeV DM mass.

On the other hand, using the results from Section 8.2, the cosmic-ray induced γ -ray flux above 260 GeV for Fornax is expected to lie between a few $10^{-15} \text{ cm}^{-2} \text{ s}^{-1}$ and $10^{-14} \text{ cm}^{-2} \text{ s}^{-1}$ for an opening angle of observation of 1.0° . The flux is about 2-to-3 orders of magnitude lower than the upper limits presented in Table 8.6, thus this scenario cannot be constrained. In order to compare with a γ -ray emission from DM annihilation, a DM particle with mass of 1 TeV and a typical value of the annihilation cross section for thermally-produced DM, $\langle\sigma v\rangle = 3 \times 10^{-26} \text{ cm}^3 \text{ s}^{-1}$, and the NFW profile of DM density profile of Fornax RB02 assumed. In this scenario the

8. Gamma-rays from the Fornax galaxy cluster

θ_{\max}	$N_{\gamma}^{95\% \text{ C.L.}}(E_{\gamma} > E_{\min})$	$\Phi_{\gamma}^{95\% \text{ C.L.}}(E_{\gamma} > E_{\min})(10^{-12} \text{ cm}^{-2} \text{ s}^{-1})$	
		$\Gamma = 1.5$	$\Gamma = 2.5$
0.1°	41.3	0.8	1.0
0.5°	135.1	2.3	3.3
1.0°	403.5	6.8	10.0

Table 8.6: Upper limits on the VHE γ -ray flux from the direction of Fornax, assuming a power-law spectrum with spectral index Γ between 1.5 and 2.5. Column 1 gives the opening angle of the integration region θ_{\max} , column 2 the upper limits on the number of observed γ -rays above the minimum energy $E_{\min} = 260$ GeV, calculated at 95% C.L.. Columns 3 and 4 list the 95% C.L. integrated flux limits above the minimum energy, for two power law indices.

predicted DM γ -ray flux is found to be a few $10^{-13} \text{ cm}^{-2} \text{ s}^{-1}$. This estimate takes into account the γ -ray enhancement due to dark halo substructure and the Sommerfeld enhancement (see section 8.5) to the overall DM γ -ray flux. Therefore the dominant γ -ray signal is expected to originate from DM annihilations.

8.5 Exclusion limits on dark matter annihilations

Upper limits at 95% C.L. on the dark matter velocity-weighted annihilation cross section are derived for different DM halo profiles and annihilation spectra. The exclusion limits as a function of the DM particle mass m_{DM} for all the DM halo profile models of Table 8.2 are depicted in Figures 8.7 and 8.8 for DM particles annihilating exclusively into $b\bar{b}$ and $\tilde{B}^{(1)}$ particles, respectively. Predictions for the $\langle\sigma v\rangle$ as function of the mass are given in Figure 8.8 for the $\tilde{B}^{(1)}$ particle within the UED framework of Servant and Tait [136]. These predictions can change in extensions of this UED model [138]. A range of predicted $\langle\sigma v\rangle$ is given in the case of a mass splitting between the LKP and the next lightest KK particle down to 1%. In the TeV range the 95% C.L. upper limit on the annihilation cross section $\langle\sigma v\rangle$ reaches $10^{-22} \text{ cm}^3\text{s}^{-1}$. Exclusion limits as a function of the DM particle mass m_{DM} assuming DM particle annihilating into $b\bar{b}$, $\tau^+\tau^-$ and W^+W^- are presented in Figure 8.9 for the RB02 NFW profile. Stronger constraints are obtained for masses below 1 TeV in the $\tau^+\tau^-$ where the 95% C.L. upper limit on $\langle\sigma v\rangle$ reaches $10^{-23} \text{ cm}^3\text{s}^{-1}$. The *Fermi*-LAT exclusion limit for Fornax is added in Figure

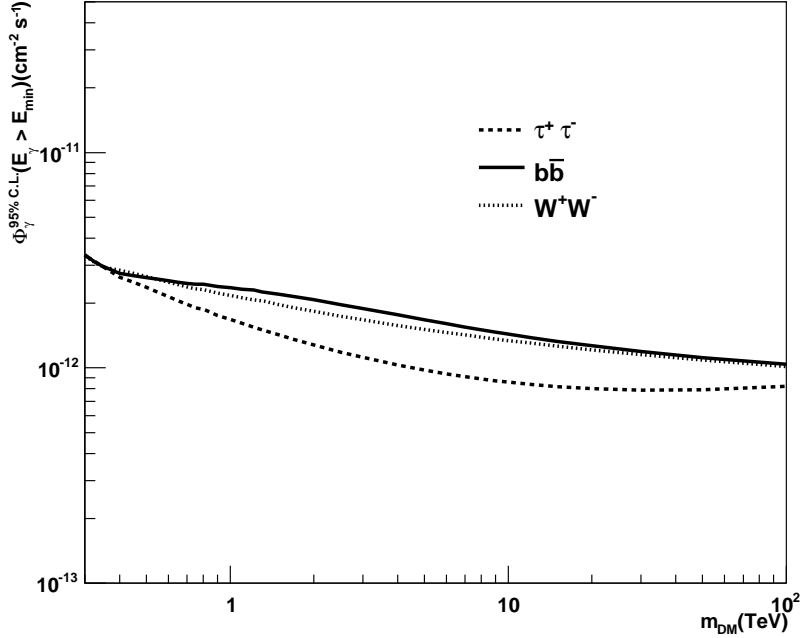


Figure 8.6: Upper limits 95% C.L. on the γ -ray flux as a function of the DM particle mass for $E_{\text{min}} = 260$ GeV from the direction of Fornax. DM particles annihilating into $b\bar{b}$ (solid line), W^+W^- (dotted line) and $\tau^+\tau^-$ (dashed line) pairs are considered.

8.7 (pink dashed-line), extending up to 1 TeV [246]. It is based on the RB02 NFW profile and a γ -ray spectrum which assumes annihilation to $b\bar{b}$ pairs. Below 1 TeV, the *Fermi*-LAT results provide stronger limits than the H.E.S.S. results. However, the H.E.S.S. limits well complement the DM constraints in the TeV range.

8.5.1 γ -ray flux enhancements

The flux enhancement caused by the internal bremsstrahlung and the Sommerfeld effect are taken into account in the exclusion limits calculation. A parametrization of the internal bremsstrahlung for DM particles annihilating uniquely into W^+W^- was given in Section 5.4.1. This parametrization is used in the calculation of the 95% C.L. upper limit on the velocity-weighted annihilation cross section as a function of the DM particle mass, presented in Figures 8.9 and 8.10. As already discussed in Section 5.4.1

8. Gamma-rays from the Fornax galaxy cluster

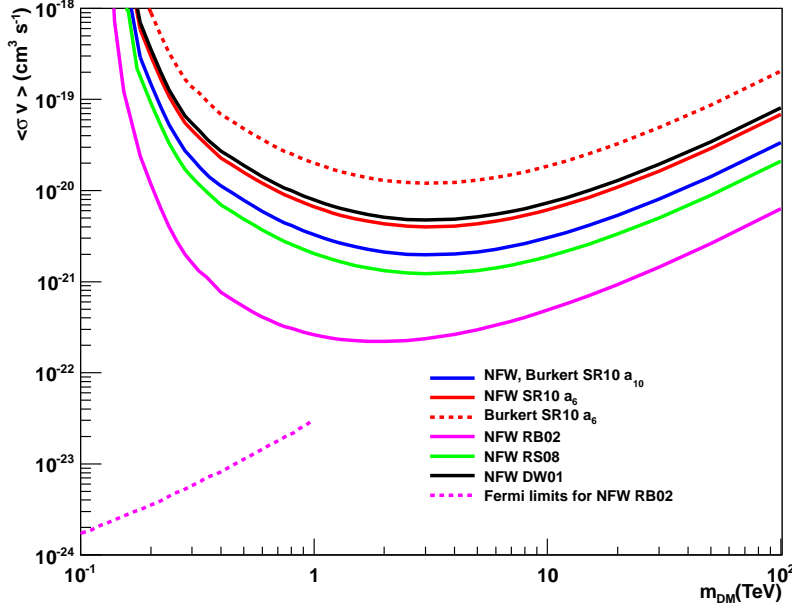


Figure 8.7: Upper limit at 95% C.L. on the velocity-weighted annihilation cross section $\langle\sigma v\rangle$ as a function of the DM particle mass, considering DM particles annihilating purely into $b\bar{b}$ pairs. The limits are given for an integration angle $\theta_{\text{max}} = 0.1^\circ$. Various DM halo profiles are considered: NFW profiles, SR10 a_{10} (blue solid line), DW01 (black solid line), RB02 (pink solid line) and RS08 (green solid line), and Burkert profiles, SR10 a_6 (red dotted line) and a_{10} (blue solid line). See Table 8.2 for more details. The *Fermi*-LAT upper limits [246] for the NFW profile RB02 are also plotted.

and in the previous chapter, the internal bremsstrahlung affects the exclusion limits mostly in the low mass DM particle regime, where its contribution to the total number of γ -rays in the H.E.S.S. acceptance is largest.

In the Fornax galaxy cluster, the velocity dispersion and thus the mean relative velocity of “test masses” such as stars, globular clusters or galaxies is of the order of a few 100 km s^{-1} [123], hence $\beta \approx 10^{-3}$. Assuming that the same velocity distribution holds true for DM particles, the Sommerfeld effect can take place on the assumption of a DM particle annihilation into W^+W^- (c.f. Section 5.4.3). The limits on $\langle\sigma v\rangle_{\text{eff}}/S$ are derived and shown in Figure 8.10 for a signal integration radius of 1.0° and the RB02 NFW profile. Although the DM velocity dispersion is about one

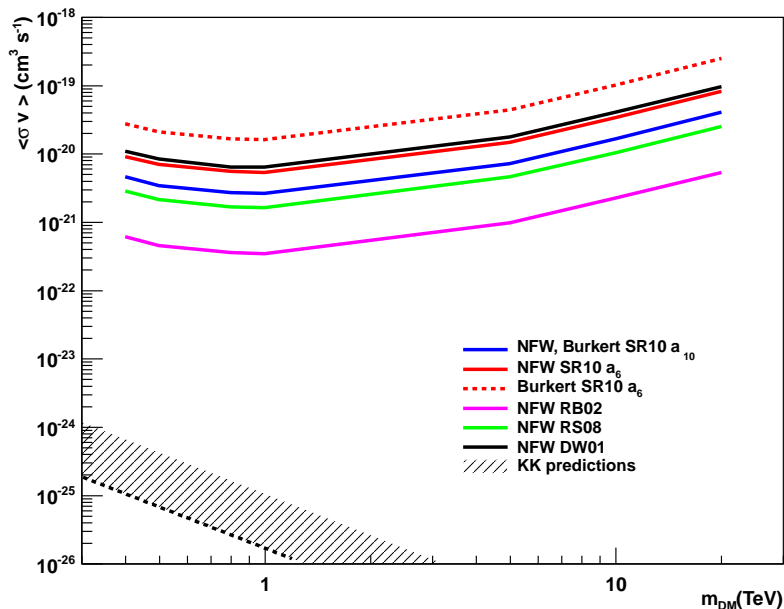


Figure 8.8: Kaluza-Klein hypergauge boson $\tilde{B}^{(1)}$ dark matter: Upper limit at 95% C.L. on $\langle\sigma v\rangle$ as function of the $\tilde{B}^{(1)}$ mass towards Fornax. The limits are given for an integration angle $\theta_{\text{max}} = 0.1^\circ$. The NFW profiles, SR10 a_{10} (blue solid line), DW01 (black solid line), RB02 (pink solid line) and RS08 (green solid line), and Burkert profiles, SR10 a_6 (red dotted line) and a_{10} (blue solid line). See Table 8.2 for more details. The prediction of $\langle\sigma v\rangle$ as function of the $\tilde{B}^{(1)}$ mass is given (dotted-line). A range for this predictions is given in case of a mass splitting between the LKP and the next LKP down to 1% (dashed area).

order of magnitude higher than in dwarf galaxies, a boost of $\sim 10^3$ is obtained for DM particle masses around 4.5 TeV. The resonance-like feature is clearly visible for masses above 4.5 TeV. Outside the resonances, the limits on $\langle\sigma v\rangle_{\text{eff}}/S$ are tightened by more than one order of magnitude for dark matter particles heavier than about 3 TeV.

8.5.2 Inverse Compton emission

Differently from dwarf spheroidal galaxies, in galaxy cluster the spatial diffusion time scale of positron/electrons is large enough to allow these particles to efficiently lose energy by Inverse Compton (IC) up-scattering on the CMB photons. Assuming a

8. Gamma-rays from the Fornax galaxy cluster

DM particle annihilating primarily into $\mu^+\mu^-$ pairs, the subsequent muon decay into positrons and electrons will lead to an additional γ -ray emission component by IC. The IC component of the annihilation spectrum is then added to the FSR spectrum. For instance, the scenario of a DM annihilation primarily into leptonic final states was proposed to explain measurements of cosmic electron and positron spectra by PAMELA [143], ATIC [144], H.E.S.S. [145] and *Fermi*-LAT [146], and are often referred as *leptophilic* models.

As discussed before (Section 5.4.2) the enhancement of the γ -ray flux by IC in

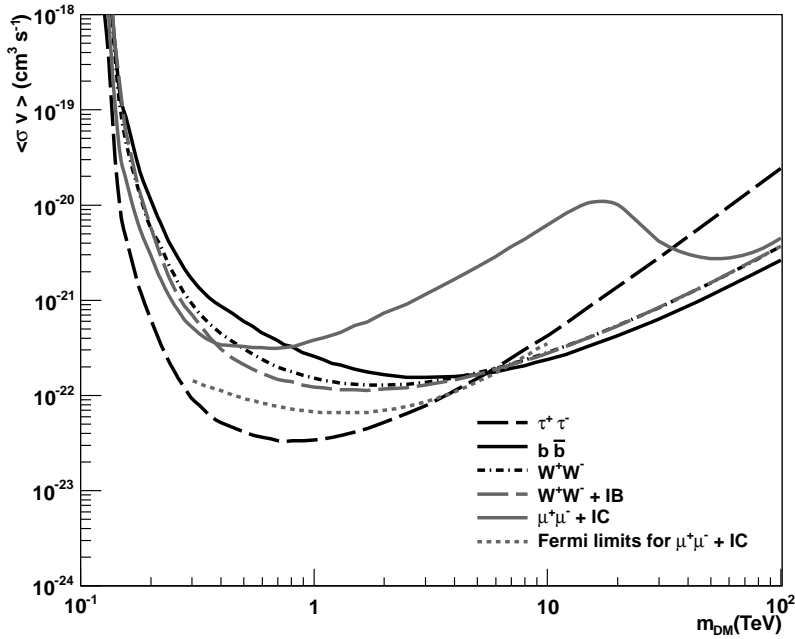


Figure 8.9: The effect of different DM particle models: Upper limit at 95% C.L. on $\langle\sigma v\rangle$ as function of the DM particle mass. The limits are given for $\theta_{\text{max}} = 0.1^\circ$ and the NFW profile RB02. The limits are shown for DM particles annihilating into $b\bar{b}$ (black solid line), W^+W^- (black dash-dotted line), $\tau^+\tau^-$ (gray long-dashed line) pairs. The effect of Internal Bremsstrahlung (IB) occurring for the W^+W^- channel is plotted in gray long-dashed line. The gray solid line shows the limits for DM annihilating into $\mu^+\mu^-$ pairs including the effect of inverse Compton (IC) scattering. The *Fermi*-LAT upper limits [246] for the NFW profile RB02 and for an DM annihilating into $\mu^+\mu^-$ pairs including the effect of IC scattering are also plotted (gray dotted line). See section 5.4.2 for more details on IC.

the H.E.S.S. energy range is found to lower the exclusion limits only for very high DM masses, $m_{\text{DM}} > 10$ TeV. The limits are enhanced by a factor of ~ 10 . The *Fermi*-LAT exclusion limit for Fornax is added (gray dashed-line), extending up to 10 TeV [246]. Due to the IC component, below a few tens of TeV the *Fermi*-LAT results provide stronger limits than the H.E.S.S. results. However, since for DM particle masses above 10 TeV the IC emission peak falls out of the *Fermi*-LAT energy acceptance, the IC spectra becomes harder in the same energy range. The *Fermi*-LAT limits for DM particle masses above 10 TeV would tend to raise with a stronger slope than the slope in between 1 and 10 TeV. Thus H.E.S.S. limits would well-complement the *Fermi*-LAT constraints in the DM mass range higher than 10 TeV.

8.5.3 Enhancement from dark matter substructures

The effect of DM substructures inside the opening angle of 0.1° and 1.0° are presented in Figure 8.11, using the enhancement values calculated in Section 8.1.2. The enhancements to the 95% C.L. upper limits on $\langle\sigma v\rangle$ are estimated using the two limiting masses of substructures M_{lim} . In the TeV range, the upper limit on $\langle\sigma v\rangle$ is at the 10^{-23} cm³s⁻¹ level. The joint enhancement due to the Sommerfeld effect added to the IB and the substructures contribution is plotted in Figure 8.10. In the most optimistic model, with the largest enhancement by substructures and the Sommerfeld effect, the 95% C.L. upper limit on $\langle\sigma v\rangle_{\text{eff}}$ reaches 10^{-26} cm³s⁻¹, thus probing natural values for thermally-produced DM.

8.6 Summary and conclusion

The Fornax galaxy cluster is the best galaxy cluster for indirect DM searches. Observations with the H.E.S.S. telescope array to search for VHE γ -rays were conducted and presented here. No significant γ -ray signal was found and upper limits on the γ -ray flux were derived for power-law and DM spectra, at the level of 10^{-12} cm⁻²s⁻¹ above 260 GeV .

Assuming several different models of particle dark matter and different models of the dark matter density distribution in the halo, exclusion limits on the DM

8. Gamma-rays from the Fornax galaxy cluster

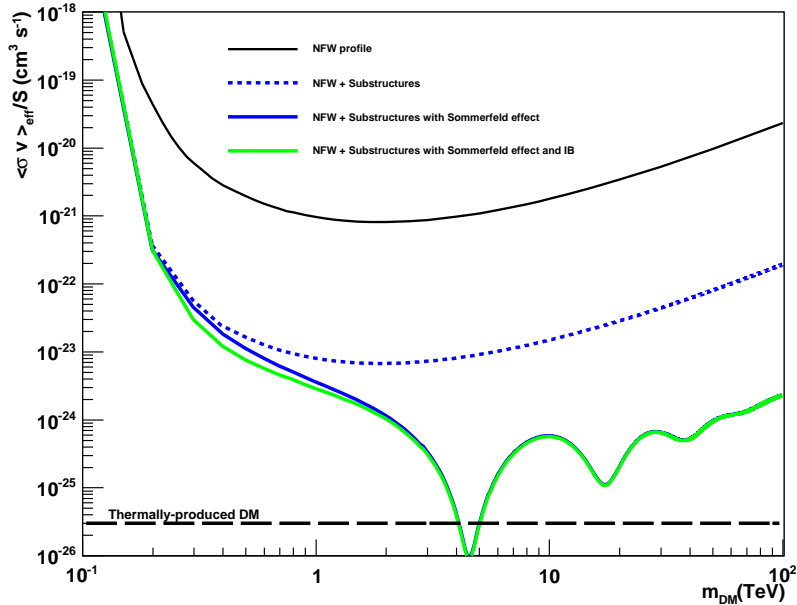


Figure 8.10: The Sommerfeld effect: Upper limits at 95% C.L. on the effective annihilation cross section $\langle\sigma v\rangle_{\text{eff}} = \langle\sigma v\rangle_0/S$ as a function of the DM particle mass annihilating into W pairs. The black line denotes the cross section limit for $\theta_{\text{max}} = 1.0^\circ$ without γ -ray flux enhancement, the dashed blue line shows the effect of halo substructure (using the “high boost”, cf. Fig. 8.11). The solid green and blue lines show the limit for the case of Wino dark matter annihilation enhanced by the Sommerfeld effect, with and without including Internal Bremsstrahlung, respectively. The DM halo model RB02 is used (see Table 8.2 and main text for more details). A typical value of the annihilation cross section for thermally-produced DM is also plotted.

self-annihilation cross section as a function of the DM particle mass were derived. Particular consideration was given to possible enhancements of the expected γ -ray flux which could be caused by DM halo substructure or the Sommerfeld effect. For a DM mass of 1 TeV, the exclusion limits reach values of $\langle\sigma v\rangle \approx 10^{-22} - 10^{-23} \text{ cm}^3 \text{s}^{-1}$, depending on DM model and halo properties, without the substructures contribution, and $\langle\sigma v\rangle \approx 10^{-23} - 10^{-24} \text{ cm}^3 \text{s}^{-1}$ when considering the substructures signal enhancement. At $M_{\text{DM}} \approx 4.5 \text{ TeV}$, a possible Sommerfeld resonance could lower the upper limit to $10^{-26} \text{ cm}^3 \text{s}^{-1}$.

Compared to observations of dwarf spheroidal galaxies (see chapters 7 and 6) or

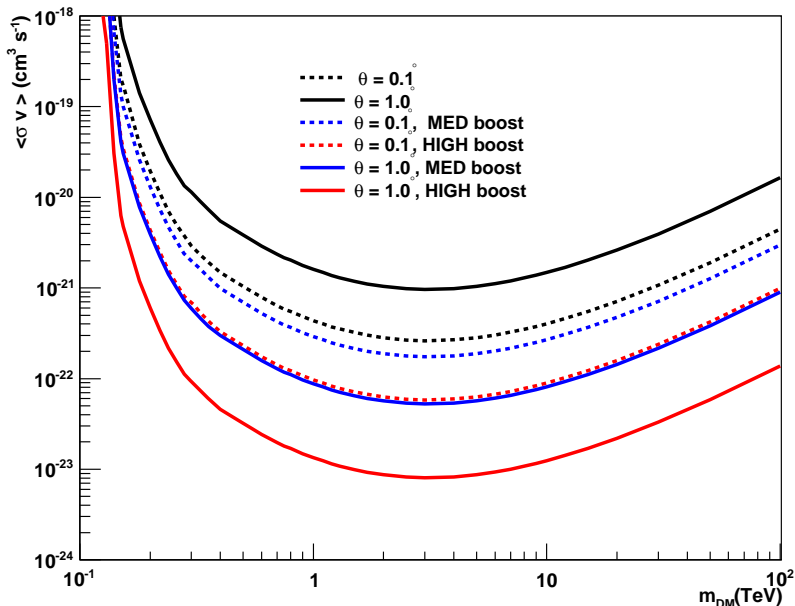


Figure 8.11: The effect of DM halo substructures: Upper limit at 95% C.L. on $\langle\sigma v\rangle$ as function of the DM particle mass annihilating purely into $b\bar{b}$ pairs. The limits are given for $\theta_{\text{max}} = 0.1^\circ$ (dashed lines) and $\theta_{\text{max}} = 1.0^\circ$ (solid lines). The DM halo model RB02 is used (see Table 8.2 and main text for more details). In addition, the effect of halo substructures on the $\langle\sigma v\rangle$ limits is plotted. The “medium boost” (MED) with $M_{\text{lim}} = 5 \times 10^{-3} M_\odot$ (blue lines) and the “high boost” (HIGH) with $M_{\text{lim}} = 10^{-6} M_\odot$ (red lines) are considered.

globular clusters [260]¹, these limits reach roughly the same order of magnitude. The choice of different tracers to derive the DM halo profile in Fornax galaxy cluster allows to well constraint the uncertainty in the expected signal. The poorly constrained, but plausibly stronger subhalo enhancement in the galaxy cluster induces an uncertainty in the expected signal of about two orders of magnitude.

With an optimistic joint γ -ray signal enhancement by halo substructures and the Sommerfeld effect, the limits on $\langle\sigma v\rangle$ reach the values predicted for thermal relic dark matter. Additionally, they extend the exclusions calculated from *Fermi*-LAT observations of galaxy clusters to higher DM particle masses.

¹However, it is important to notice that the presence of DM in globular clusters is very uncertain since their formation scenarios may not require a DM halo.

8. Gamma-rays from the Fornax galaxy cluster

Part III

The Galactic Center region

Chapter 9

The Galactic Center inner 500 pc

Contents

Introduction	180
9.1 Morphology and main components of the Galactic Center region	180
9.1.1 Central region morphology in radio	180
9.1.2 Central region morphology in X-rays	182
9.1.3 Central molecular zone	186
9.1.4 Sgr A complex	188
9.2 Gamma-ray emissions from the Galactic Center region	197
9.2.1 HESS J1745-290: counterparts and spectrum	197
9.2.2 The diffuse emission from the Galactic Center Ridge	200

Introduction

The center of our Galaxy is located at 8.5 ± 0.5 kpc from the Sun. The region surrounding the Galactic Center is one of the most complex regions studied in high-energy astrophysics harboring a variety of potential sources of high-energy radiation. In particular it hosts a super-massive black hole (SMBH) Sagittarius (Sgr) A* (2.87 ± 0.15) $\times 10^6 M_{\odot}$ [110] that was discovered in radio in 1974 [261]. Given its distance of 8.5 kpc [262], it is the closest SMBH to Earth and is therefore used to study the physical phenomena in such environments. Various observations in radio, microwave, infrared, X-rays and γ -rays followed that discovery and revealed an enormous density of emitting objects in every waveband, while optical and ultra-violet observations are completely obscured by dust along the line of sight. This inner part defines the so-called *zone of avoidance*, consisting of dust, stars and gas, with size and shape which depends on the wavelength. It surrounds the high density molecular cloud region called Central Molecular Zone (CMZ), which extends over about 600 pc in galactic longitude and 200 pc in latitude around the dynamical center of the Milky Way which corresponds to around $4^{\circ} \times \text{A}1.5^{\circ}$ in angular coordinates, thus completely included in the H.E.S.S. telescope field of view on this region of about $5^{\circ} \times \text{A}5^{\circ}$. This chapter describes, first the structure and morphology of the Galactic Center region in different wavelengths relevant for non-thermal interactions. Then the TeV observations, including published results from H.E.S.S. and other ground based Cherenkov telescopes are summarized and discussed.

9.1 Morphology and main components of the Galactic Center region

9.1.1 Central region morphology in radio

A wide-field radio image of the Galactic Center region taken by the *Very Large Array*¹ (VLA) at 90 cm of wavelength (330 MHz) is shown in Figure 9.1 [263]. At $\lambda = 90$ cm the VLA is sensitive to both thermal and non-thermal emission and the resulting image

¹The VLA is a radio astronomy observatory located on New Mexico (USA) observing with a frequency coverage of 74 MHz to 50 GHz. The angular resolution goes down to 0.04”.

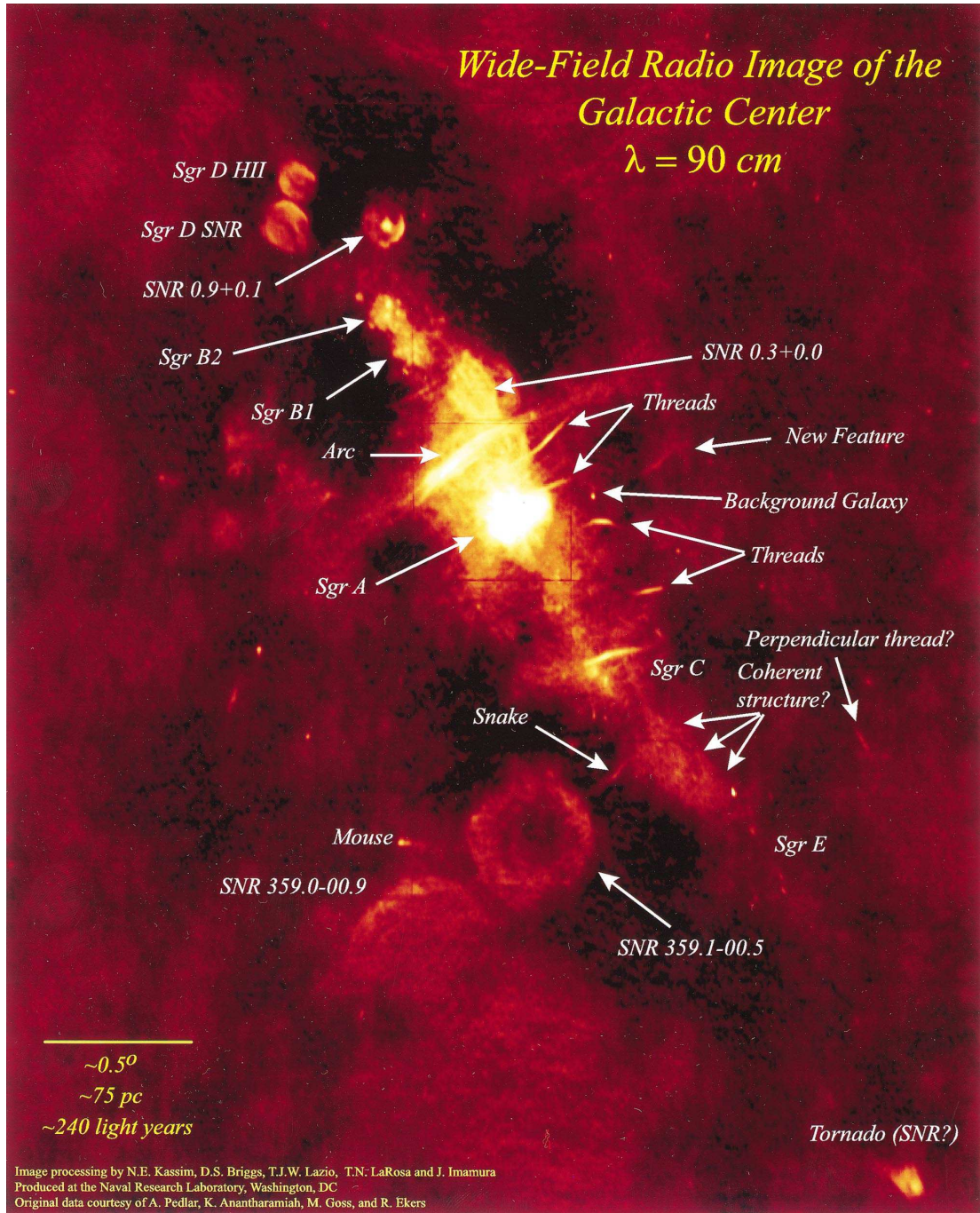


Figure 9.1: The galactic center region as observed by VLA at 90cm [263]. Numerous features like SNR shells, thin non-thermal filaments and HII regions are visible at this wavelength.

gives a detailed view of the structure and morphology of this region. The non-thermal emission seen in radio is due to synchrotron emission (see chapter 1.1). The central structure, Sgr A, has a compact synchrotron source which is related to the SMBH Sgr A*. Apart from the non-thermal emission from the SMBH, the region exhibits an expanding non-thermal shell from the SNR called Sgr A East, a thermal, spiral-shaped diffuse HII nebula Sgr A West, the stellar cluster IRS 16 and two GMCs [264]. Since these objects are located within just a few parsecs, their interactions are especially interesting from the point of view of high energy astrophysics, knowing that SMBHs, SNR shells and objects in stellar clusters ¹ can accelerate particles to relativistic energies, while regions of dense molecular gas provide the target for γ -ray production both from hadrons and leptons collisions. Other than the Sgr A complex, the Galactic Center region has lots of other sources and structures. For instance several thin filaments of non-thermal emission are visible within 0.5° from the GC, of which the Radio Arc and Sgr C are the most prominent one, that are believed to harbor a population of relativistic electrons that emit synchrotron photons [263]. Another radio sources includes supernova remnants, like SNR 0.9+0.1 (G0.9+0.1), which was also detected in γ -rays by H.E.S.S. [265], and the SNR 359.1-00.5 which was shown to possibly be associated to the VHE source HESS J1745-303 [266]. Thermal radio emission can also be seen coming from the molecular clouds Sgr B1 and Sgr B2, and from H II regions like Sgr D HII.

9.1.2 Central region morphology in X-rays

Soft X-rays observations

The most recent soft X-ray observations of the Galactic Center were performed by the satellites Chandra ² [267, 268], XMM-Newton ³ [269] and Suzako ⁴ [270], with an

¹It is also assumed that stellar clusters themselves can accelerate particles through collective effects such as colliding winds of massive stars or the interactions of several SNR ejecta [9].

²Chandra is an American satellite launched in July 1999. It observes X-rays in the energy band of 1 keV to 10 keV, with an angular resolution of $0.5''$ and an energy resolution of about 10%.

³XMM-Newton is an European satellite launched in December 1999. It observes X-rays in the energy band of 1 keV to 10 keV, with an angular resolution of $14'$ and an energy resolution of less than 0.5%.

⁴Suzako is an American-Japanese satellite launched in July 2005. It observes X-rays in the very wide energy band ranging from 0.2 keV to 700 keV, with an angular resolution about $1.0'$ and an energy

9.1 Morphology and main components of the Galactic Center region

unprecedented precision and resolution.

Figure 9.2a shows the Galactic Center map viewed by Chandra [271]. A large number of point and extended sources is visible, as well as a diffuse emission. The latter is strongly asymmetric and the east region from Sgr A is brighter than the west part. The energy spectrum of the diffuse emission was found to be harder than the expected spectrum from a purely thermal emission. Indeed, previous X-ray missions (ROSAT, ASCA, BeppoSAX) have shown that the diffuse emission was due to a combined thermal emission from hot gas at a temperature of 10^7 - 10^8 K, plus a non-thermal emission from point sources, generally X-ray binaries. Chandra has detected about 2300 point like sources in the Galactic Center region, of which 281 are foreground sources and about one hundred are far galaxies hosting an active galactic nucleus (AGN). The energy spectra of the local sources was found to be very hard, with a spectral index typically of smaller than 1, which is characteristic of a X-ray emission from white dwarf stars or neutron stars accreting mass. The non-thermal component to the diffuse emission was thus confirmed by Chandra. Sgr A* was also detected in X-rays [272], and it is clearly seen in Figure 9.2a, however its luminosity, $L = 2 \times 10^{33}$ erg s⁻¹ in the 2-10 keV band, is very low compared to other galactic nuclei.

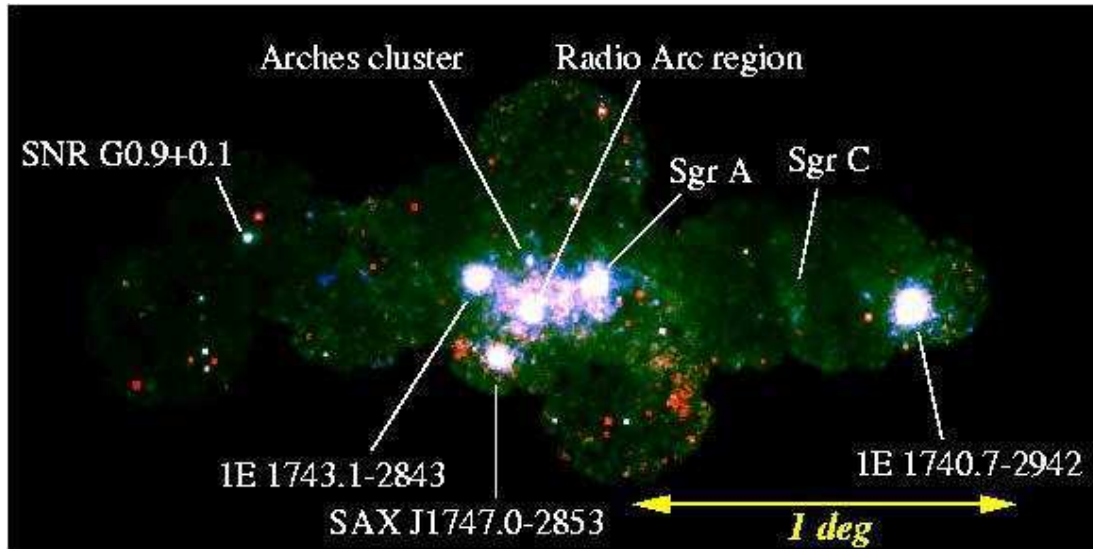
Beside emission from Sgr A*, X-ray emission was also detected by Chandra from Sgr A East [273]. However, in this frequency range, compared to the radio counterpart the source turns out to be smaller in diameter (≈ 4 pc vs ≈ 20 pc in radio) and reveals a non-thermal shell together with a thermal core region. The latter is explained by a reverse shock of the expanding shell that heats the matter inside the remnant. With the help of X-ray observations it was possible to estimate that the explosion took place $\approx (10 \pm 2.5) 10^3$ years ago and the mass of the exploding star was $M = 13$ - $20M_{\odot}$, contradicting earlier estimates based on radio observations that stated the emission seen from Sgr A East is a result of up to 40 supernova explosions [264]. Additionally, Chandra has discovered an energetic pulsar wind nebula G359.95-0.04 [274]. It is located only $8.7''$ away from the position of Sgr A*, making it a suitable candidate for TeV emission, since despite its low X-ray luminosity $L = 10^{34}$ erg s⁻¹, the very dense radiation fields of the GC region provide enough target photons for efficient inverse resolution of about 1%.

9. The Galactic Center inner 500 pc

Compton production.



(a) Galactic Center view by Chandra



(b) Galactic Center view by XMM-Newton

Figure 9.2: (a) The GC region as observed by Chandra (from Ref. [271]). The scale of both images is matched. A large number of point and extended sources is visible. The counterparts to the TeV point sources at the positions of G0.9+0.1 and Sgr A are visible. (b) XMM-Newton color image of the Galactic Centre Region along the Galactic Plane in the energy band 2-9 keV. Ref. [269]

Figure 9.2b exhibits a mosaic the Galactic Center observations by XMM-Newton [269], covering a region of $2.5^\circ \times 1.0^\circ$. Several bright sources are clearly distinguishable, two stable X-ray binaries (1E1240.7-2942 and 1E1743.1-2843) and one variable X-ray binary (SAXJ1747.0-2853). The X-ray emission from the Sgr A complex and from the

9.1 Morphology and main components of the Galactic Center region

SNR 0.9+0.1 (PWN 0.9+0.1 on the map) are also pointed out. The diffuse emission is clearly visible in the whole area. X-ray observations carried out by ASCA and Suzaku on the Galactic Center (see Figure 9.3, Koyama et al. [270] (2006) revealed that the Sgr B HII area, the non-thermal radio filament Sgr C and the complex with the SNRs 359.0-0.09 and 359.1-0.05 appear to be a so-called X-ray reflection nebulae [275, 276]. This term means that most part of the X-ray emission received from an object is not produced there but is rather due to reflection of and florescence caused by X-ray photons coming from a different site, with a strong fluorescent 6.4 keV iron line located on top of a non-thermal continuum as its main characteristic. Interestingly, there would be a connection between these sources and the γ -ray source HESS J1745-290, since in all three cases it is assumed that the source of primary emission is the SMBH Sgr A*. The flux produced by Sgr A* that is required to fit the observations from the reflection nebulae is about 10^6 times higher than the quiescent emission observed during the last years [264]. From the distance of Sgr B and Sgr C to the GC it was concluded that Sgr A* must have been very bright in X-rays some hundreds of years ago. Due to a possible correlation between X-ray flux and particle acceleration in the GC, this is an important fact for studies of TeV emission from this region.

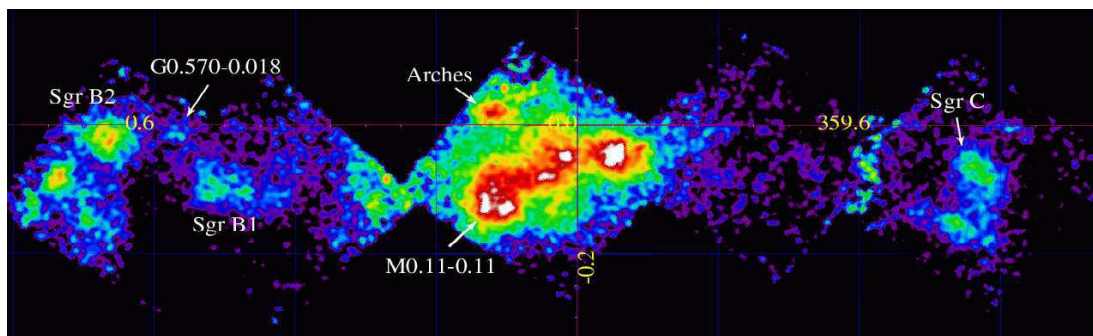


Figure 9.3: Narrow band map of the GC region as observed by Suzaku (from Ref.[270]) at the 6.4 keV line (the 6.34-6.46 keV band). Coordinates are galactic l and b in degrees.

Hard X-rays observations

Concerning higher energy X-rays, the INTEGRAL satellite performed a deep exposure the GC region in the energy range between 20 and 400 keV [277]. The Galactic

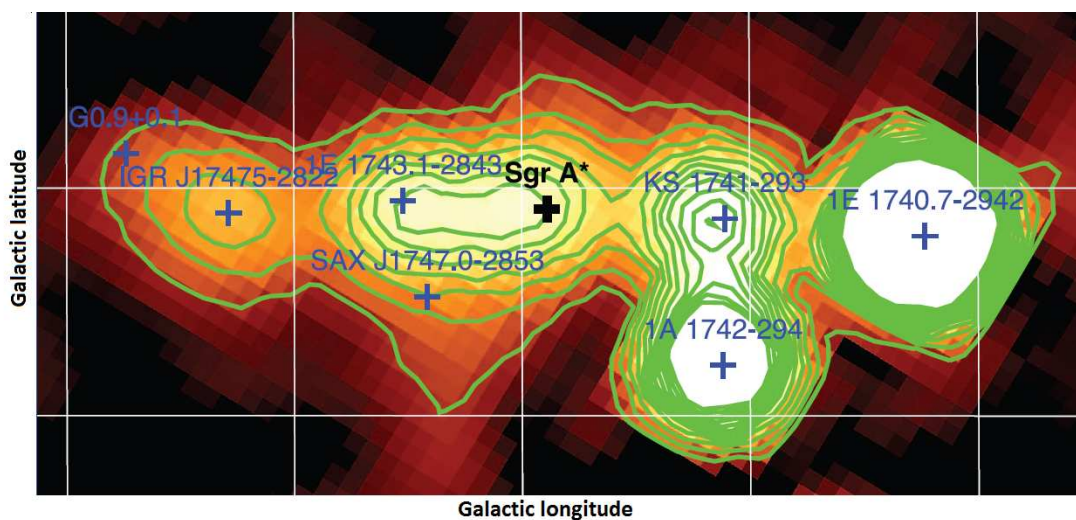
9. The Galactic Center inner 500 pc

Center region map obtained by the imager IBIS/ISGRI of INTEGRAL is presented in Figure 9.4. Six distinct sources are revealed in the region comprising $2.0^\circ \times 2.0^\circ$ around the Galactic Center. The central source IGR J17456-2901 has a position compatible with that of Sgr A*, however due to INTEGRAL's angular resolution of $\approx 10'$, it is not yet conclusive whether the emission has its origin directly at the SMBH or whether it is rather a diffuse radiation. The combined spectrum of soft and hard X-rays from the GC can be fitted by a thermal component, produced in hot plasma, in soft and a non-thermal power law component in hard X-rays, which origin is still under exploration. Additionally, some observations were carried out together with XMM-Newton and during that period several soft X-ray flares were detected, while the emission in hard X-rays stayed steady, therefore mostly favoring the diffuse hypothesis and a link to the VHE emission.

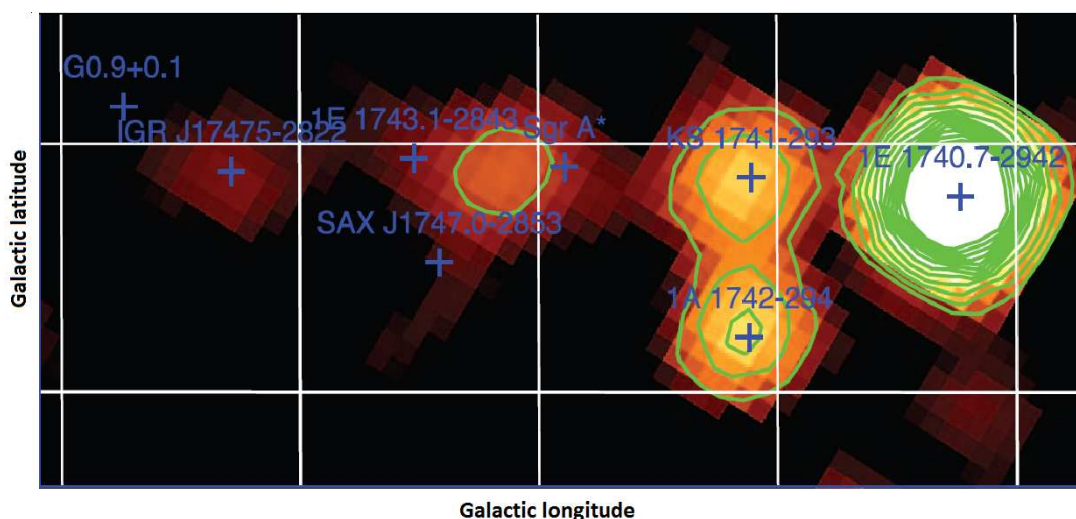
Another emission even harder in X-rays (56-85 keV band) was also detected between Sgr A* and the Radio Arc [278], as it can be seen in Fig. 9.4b at galactic longitude $l \sim 0.1^\circ$. This source was interpreted as coming from the central molecular cloud. The simultaneous observations performed by INTEGRAL and XMM-Newton in soft X-rays showed that most of INTEGRAL sources are associated to X-ray binaries, one of which might harbor a stellar-mass black-hole (1E 1740.7-2942). The unidentified source IGR J17475-2822 was also discovered by INTEGRAL and might be associated to the molecular cloud Sgr B2.

9.1.3 Central molecular zone

The Central Molecular Zone (CMZ) is a very dense region hosting, among other objects, about 10% of the total molecular mass of the Galaxy that can predominantly be found in Giant Molecular Clouds (GMC). As already mentioned, this region extends over about 600 pc in galactic longitude and 200 pc in latitude around the dynamical center of the Milky Way which corresponds to around $4^\circ \times 1.5^\circ$ in angular coordinates, revealing an ellipsoidal shape [262, 264]. Usually, its distribution is mapped using CO¹² and CO¹³ rotational state transition lines, which effectively trace the H₂ density profile [279, 280]. However, this method is inappropriate for the GC region, due to the high foreground and background contamination in the corresponding velocity bands. Instead, the emission line of the CS molecule (J=1-0) is used. Its advantage



(a) 20-40 keV band



(b) 56-85 keV band

Figure 9.4: INTEGRAL IBIS/ISGRI significance mosaic in two energy bands: 20-40 keV (*top*) and 56-85 keV (*bottom*). Black indicates a statistical significance below or equal to 3σ , and white indicates a significance greater than or equal to 50σ . Contours mark isosignificance levels from 9.5 to 75 linearly. The orientation is in Galactic coordinates. The grid lines indicate Galactic coordinates with a spacing of $0^\circ.5$ (source Ref. [278]).

is a higher critical density $n(\text{H}_2) \approx 10^4 \text{ cm}^{-3}$ of molecular material that is essentially only reached in the vicinity of the GC. Additionally, molecular clouds (MCs) with lower densities would be destroyed due to tidal forces present in this region [281], so

9. The Galactic Center inner 500 pc

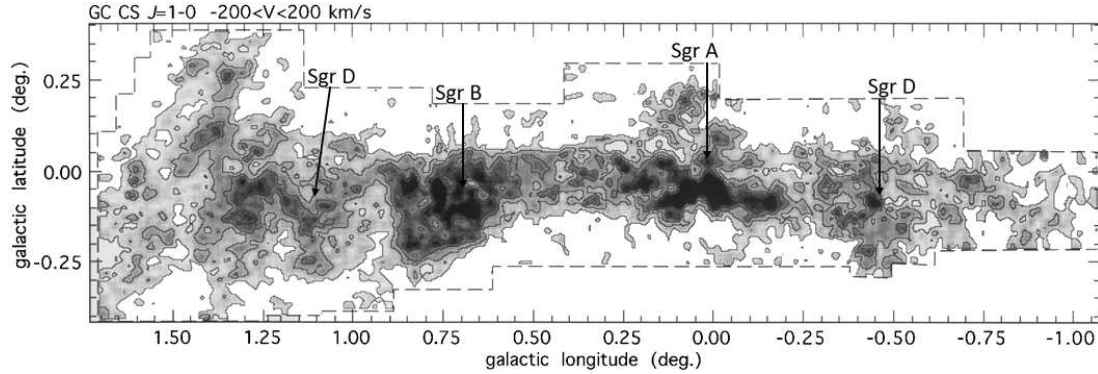


Figure 9.5: Velocity-integrated CS $J = 1-0$ emission in the Galactic center region. The observed area includes the Sgr A, Sgr B, Sgr C, and Sgr D complexes. The CS emission is a good tracer of high-density molecular clouds (source Ref. [281]).

one can expect the entire molecular content of the GC region to be properly imaged by such observations. The most complete measurement so far was achieved by the NRO telescope (see Fig. 9.5). Four high density regions are clearly distinct which are associated with strong X-ray and radio sources, the Sgr A, Sgr B, Sgr C, and Sgr D complexes. The total mass of the molecular clouds in the mapped area was estimated to be $(3-7) \times 10^7 M_{\odot}$. Most of the molecular material is found at low rotational velocities, organized in GMCs. Such a crowded and dense environment can provide a very efficient target region for interaction of cosmic rays accelerated in the GC vicinity.

9.1.4 Sgr A complex

Around a few parsecs from the Galactic Center, the multiwavelength emission is due to the Sgr A complex. The schematic diagram showing the sky locations and rough sizes and shapes of the Sgr A complex sources is presented in Figure 9.6 (e.g., Ref. [282]). In this paragraph the main sources of this region are detailed.

Central stellar cluster

The central parsecs of our Galaxy contain a dense and luminous star cluster. Infrared observations of this region revealed several comoving groups of stars (Fig. 9.7a). The brightest groups in central stellar cluster include the IRS 16 complex, which is located

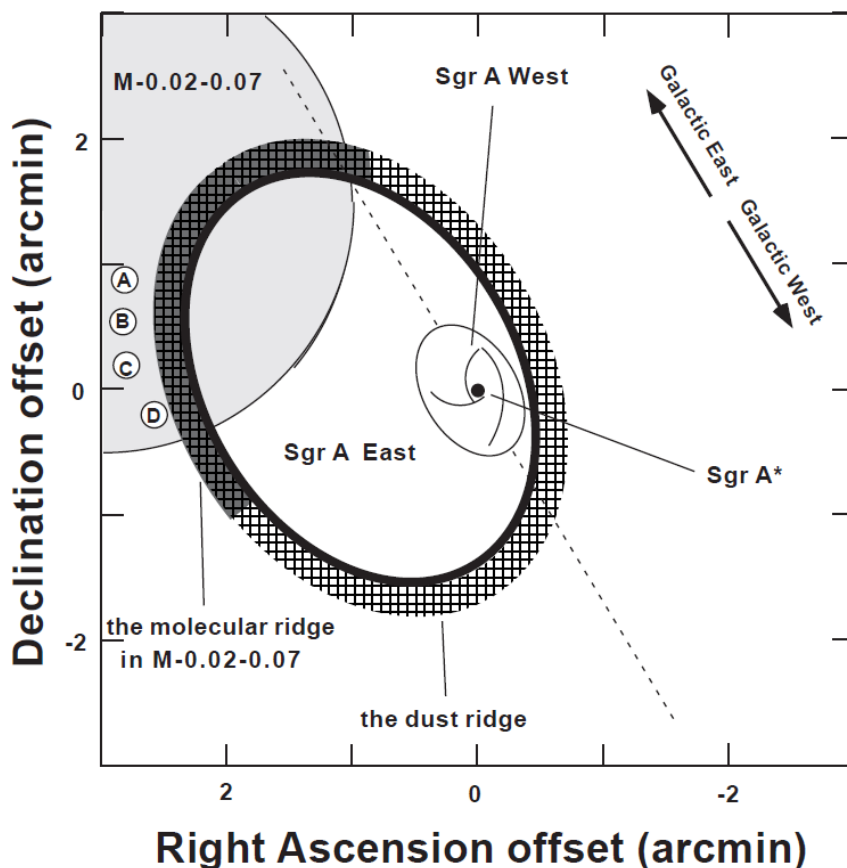
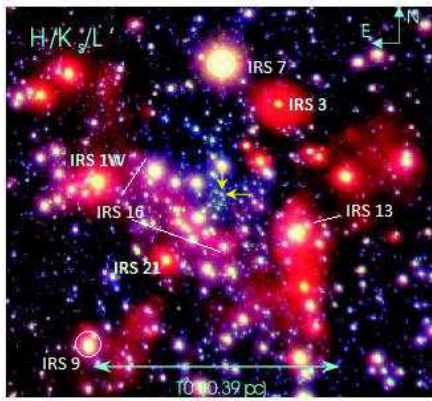


Figure 9.6: Schematic diagram showing the sky locations and rough sizes and shapes of Galactic center sources (e.g., Ref. [282]). The coordinate offsets are with respect to the compact non-thermal radio source Sgr A* which coincides with the MBH. Sgr A* is located at the center of the thermal radio source Sgr A West, which consists of a spiral-shaped group of thermal gas filaments. Sgr A West is surrounded by the molecular ring (also known as the circumnuclear disk), the radius of which is about 30sec. The non-thermal shell-like radio source Sgr A East is surrounding Sgr A West, but its center is offset by about 50sec. The non-thermal shell is surrounded by the dust and the molecular ridge. The molecular cloud M.0.02.0.07 (the +50 km s.l cloud) is located to the Galactic east of Sgr A East. At the eastern edge of the Sgr A East shell, the chain of HII regions (A-D) is seen. One arcminute corresponds to about 2.3 pc at the distance of 8 kpc.

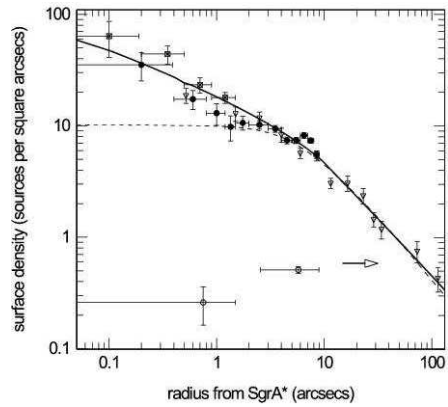
at about 1-2'' east of the radio source Sgr A*, the IRS 13 complex at 3.5'' south-east of Sgr A*, and the Sgr A* star cluster centered at the radio source with an extension of 1''. The central stellar cluster is composed of old stars but also about a hundred of young massive stars. The existence of these young massive stars indicates that star

9. The Galactic Center inner 500 pc

formation must have recently taken place at or near the Galactic Center within the last few million years. This is surprising, since regular star formation processes are likely to be suppressed by the tidal forces from the massive black hole. Many scenarios have been suggested for the origin of these stars [see 283, 284, for recent reviews]. These include in situ star formation through gravitational fragmentation of gas in disk(s) formed from infalling molecular cloud(s); transport of stars from far out by an infalling young stellar cluster, or through disruption of binary stars on highly elliptical orbits by the massive black hole; and rejuvenation of old stars due to stellar collisions and tidal stripping. The surface density distribution of stars as a function of projected radius from Sgr A* is shown in Figure 9.7b. The resulting profile has broken power law shape, with a power-law slope of $r^{-1.4}$ in the inner $r < 0.2 - 0.4$ pc and a break at larger distances with a slope of r^{-2} [109].



(a) Infrared image of the central stellar cluster



(b) Density profile of the central stellar cluster

Figure 9.7: (a) VLT infrared image of the central stellar cluster at the wavelength band of $1.65 \mu\text{m}$ to $3.76 \mu\text{m}$. Red color is defined as cold and blue as hot. The diffuse emission is caused by the interstellar dust. The two yellow arrows denote the position of Sgr A*. (b) Surface density of stars as a function of projected radius from Sgr A*. Different symbols correspond to stars detected in different wavelengths (H, K_s, ...). The dashed curve is the model of a flattened isothermal sphere of core radius 0.34 pc. The continuous curve is the broken power-law fit discussed in the text. Figures extracted from Ref. [109].

The supernova remnant Sgr A East

Sgr A East is a $3.5'' \times 2.5''$ ($8 \text{ pc} \times 6 \text{ pc}$) shell-like non-thermal structure, interpreted as a supernova remnant (see Figures 9.8a and 9.8b) [282]. It surrounds Sgr A* in projection, but its center is offset by about $50''$ (2 pc). The non-thermal radio emission coming from Sgr A East shell is mostly due to synchrotron radiation from relativistic electrons interacting with a strong magnetic field (2-4 mG). Radio observations have also showed that Sgr A East appears to be interacting with the $+50 \text{ km s}^{-1}$ molecular cloud M-0.02-0.07. The X-ray emitting region observed by Chandra and XMM-Newton is concentrated within the central $\approx 2 \text{ pc}$ of the larger radio shell. The combination of the radio and X-ray morphologies classifies Sgr A East as a new metal-rich “mixed morphology” (MM) SNR. The size of the Sgr A East radio shell is the smallest of the known MM SNRs, which strongly suggests that the ejecta have expanded into a very dense interstellar medium of about 10^3 cm^{-3} , which is about a thousand times denser than the average interstellar medium density. The very high chemical abundance of heavy elements, overabundant by roughly a factor of 4 with respect to solar abundances, support the hypothesis that Sgr A East is a supernova remnant (SNR), perhaps produced by the type II supernova explosion of a massive star with a main-sequence mass of $13\text{--}20 M_{\odot}$.

Sgr A west region

The region of Sgr A West corresponds to the inner two parsecs of the Galaxy. Sgr A West is identified as a spiral-shaped diffuse HII nebula which appears on the western side of the Sgr A complex. It has a complex shape, appearing in projection as a three-armed spiral of gas in the 6 cm radio wave band (Figure 9.8b). Sgr A West is composed of several dust and highly ionized gas clouds, which orbit and fall onto Sgr A*. The radial velocity structure varies regularly between -100 and $+100 \text{ km s}^{-1}$ in the south-north direction. The velocity within the inner $10''$ where there is a hole in the distribution of ionized gas, known as the mini-cavity, becomes increasingly more negative down to $\approx -350 \text{ km s}^{-1}$ toward Sgr A*. Surrounding Sgr A West there is a massive, clumpy torus of cooler molecular gas, the Circumnuclear Disk (CND) with a mass $> 10^4 M_{\odot}$. Figure 9.8c shows the radio continuum image of ionized gas (Sgr A

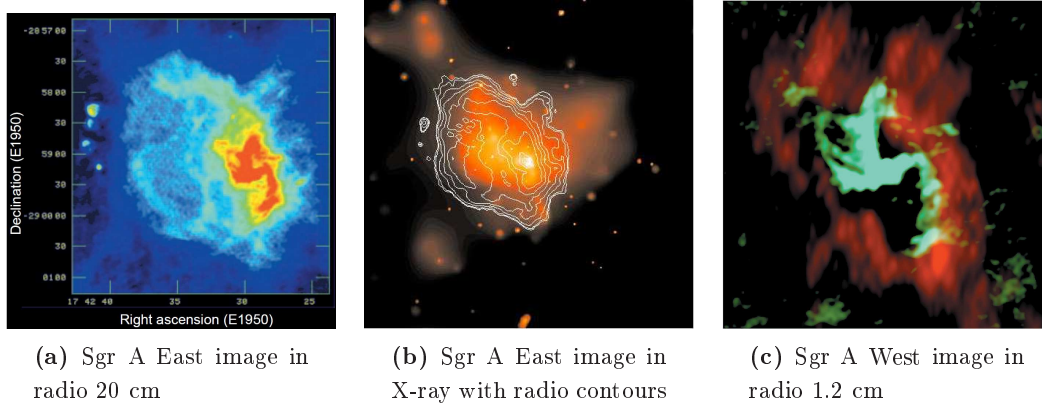


Figure 9.8: (a) VLA radio continuum image at $\lambda = 20$ cm of the Galactic center showing the shell-like structure of nonthermal Sgr A East (light blue and green) and the spiral-shaped structure of thermal Sgr A West (red) at radio 6 cm (b) Smoothed X-ray image by Chandra (1.5 - 7.0 keV) with 20 cm radio contours obtained with VLA. (c) A radio continuum image of Sgr A West at $\lambda = 1.2$ cm with its three-arm appearance, shown in blue, superimposed on the distribution of HCN emission, displayed in red. The HCN emission traces the ionized gas distributed in the molecular mini-cavity. (source [282])

West) at $\lambda = 1.2$ cm with its three-arm appearance, shown in blue, superimposed on the distribution of HCN emission, which traces the molecular clouds [282].

The pulsar wind nebula G359.95-0.04

Chandra observations of the Galactic Center region revealed the existence of a pulsar wind nebula (PWN G359.95-0.04) located at $8.7''$ (0.32 pc) from Sgr A* [274]. Figure 9.9 shows the 3.6 cm radio continuum observations superposed by the X-ray intensity contours obtained by Chandra in the energy band of 1 to 9 keV. The non-thermal X-ray emission has a particular comet-like shape, with a hypothetical pulsar on its head and a cometary tail. The tail extends back to a region centered at the massive stellar complex IRS 13 and surrounded by an enhanced diffuse X-ray emission, which may represent an associated supernova remnant. G359.95-0.04 has a hard and apparently nonthermal power-law energy spectrum that steepens with increasing distance from the putative pulsar. Also it has a high X-ray flux in contrast to little emission in both radio and infrared. These distinct spectral and spatial X-ray characteristics are similar to those belonging the rare class of ram-pressure confined pulsar wind nebulae. Interestingly, the

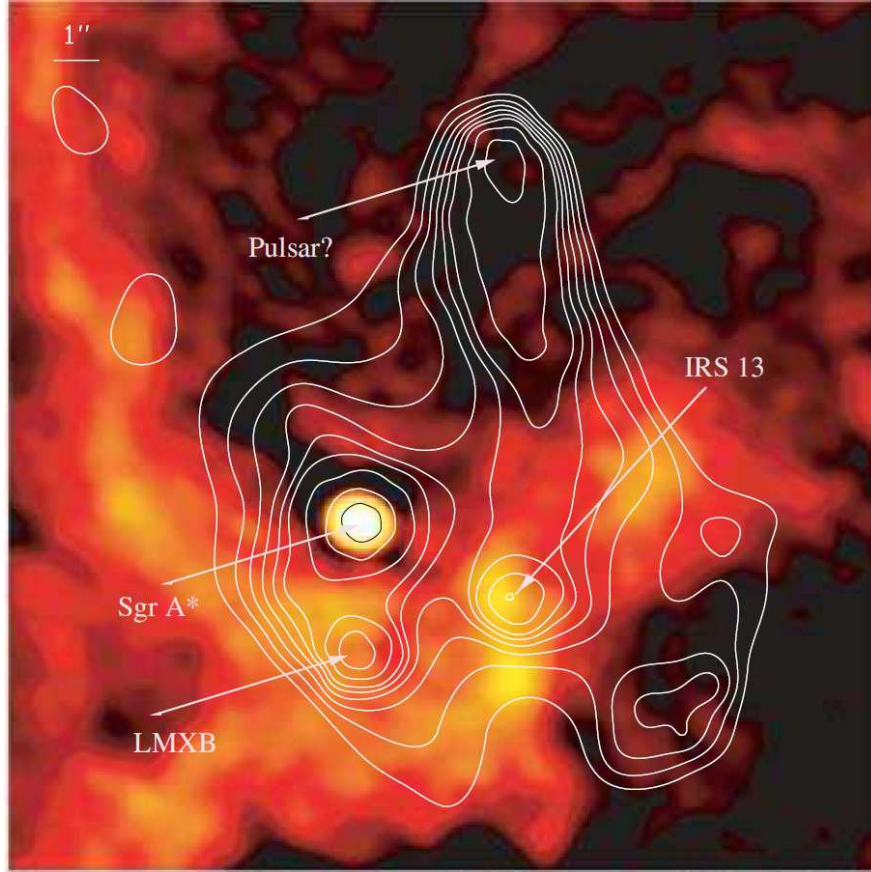


Figure 9.9: The immediate vicinity of Sgr A* in radio superposed by X-ray contours (north is up and east is to the left in galactic coordinates). The radio image is taken at the 3.6 cm energy band with the VLA. Chandra X-ray contours show a clear comet-like shape feature associated to the pulsar G359.95-0.04. Sgr A* is marked and it is located at $8''.7$ (0.32 pc) south-east of the pulsar. From [274].

presence of a young energetic pulsar, only $8.7''$ from Sgr A* , can also explain the very high energy γ -ray radiation observed from the GC by H.E.S.S. [e.g. 285, 286]. Indeed inverse Compton scattering (ICS) of leptons, which are accelerated by the pulsar wind, on the dense radiation fields in the Galactic Center may efficiently produce photons at TeV energies.

Sgr A* supermassive black-hole

Since the discovery of the radio source Sgr A*, many observations at different wavelengths have been carried out. The position of Sgr A* was measured very precisely

9. The Galactic Center inner 500 pc

by the VLT using a thirteen years dataset of stars in its vicinity [287]. In equatorial coordinates is

$$\alpha(2000) = 17^h 45^m 40.0383^s \pm 0.0007^s \quad (9.1)$$

$$\delta(2000) = -29^\circ 00' 28.069'' \pm 0.014'', \quad (9.2)$$

where the errors account for both statistical and systematic uncertainties on the measurements. Also, radio observations with the Very Long Baseline Array (VLBA) showed that the proper motions of Sgr A*, with respect to two extragalactic radio sources over a period of eight years, are consistent with that expected from the orbit of the Sun around the Galactic center [288]. Altogether these results confirm that Sgr A* is located in the dynamical center of the Galaxy. Constraints to the black hole mass were obtained by the study of the stars dynamics in their orbit around the dynamical center. Ghez et al. (2005) [108] have analysed the trajectories of 17 stars during 10 years of infra-red observations with the Keck telescope. Figure 9.10a shows the reconstructed orbit of 7 stars which were found to have non-rectilinear trajectories in the center of mass frame. The two stars passing the closest to the center of mass are S2, which has a pericenter of 120 AU ¹, and S0-16, which has a pericenter of 45 AU. The orbit gravitational center of both the stars corresponds to the Sgr A* position with an uncertainty of 1.3 milliarcseconds. The results allowed the conclusion that a mass of $(3.7 \pm 0.2) \times 10^6 M_\odot$ is confined within a radius of 45 AU, what in fact can be only fulfilled by the presence of a SMBH [288] accounting for about 10% of this mass. Figure 9.10b shows the enclosed mass profile as function of the distance to Sgr A*, taking into account the central mass and the central stars cluster mass.

The spectrum of Sgr A*, measured from radio to the infrared domain helped to establish the understanding of its quiescent non-thermal low energy radiation as synchrotron emission from relativistic electrons [289, 290]. Additionally, the overall flux level of near-infrared emission from Sgr A* was monitored by VLT [291], which measured the flaring activity of Sgr A* in the infrared domain, later confirmed by Keck [292]. The spectrum of flaring emission can again be explained by synchrotron emission from a population of electrons, accelerated to relativistic energies or, as an

¹AU \equiv astronomic units = 4.8×10^{-6} pc

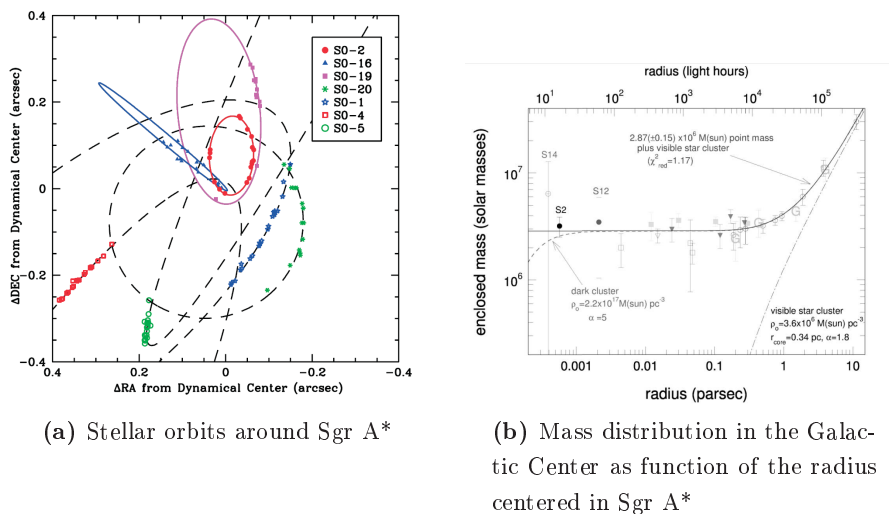


Figure 9.10: (a) Astrometric positions and orbital fits for the seven stars that show significant deviation from linear motion. The proper-motion measurements were obtained between 1995 and 2003 at the Keck telescopes, have uncertainties that are comparable to or smaller than the size of the points, and are plotted in the reference frame in which the central dark mass is at rest. Image from Ref. [108] (b) Mass distribution in the GC, assuming an 8 kpc distance [110]. The filled circles at the shortest projected distances denote the masses derived from the orbits of S2, S12, and S14. At larger distances the mass measurements depend on the central stellar cluster modelling (triangles, rectangle and open circles). The solid curve shows the overall best-fit model to all data. It is the sum of a $(2.87 \pm 0.15) \times 10^6 M_{\odot}$ point mass and a stellar cluster of central density $3.6 \times 10^6 M_{\odot} \text{pc}^{-3}$, core radius 0.34 pc, and power-law index $\alpha = 1.8$. The long-dash-short-dashed curve shows the same stellar cluster separately, but for an infinitely small core. The dashed curve shows the sum of the visible cluster and a hypothetical very compact dark cluster formed by neutron stars and black holes. This last scenario was excluded by Ghez et al. [108]

alternative explanation, by expansion of hot plasma, occurring like in extragalactic radio jets [264].

Sgr A* was also detected in X-Rays [272], however its luminosity, $L = 2 \times 10^{33} \text{ erg s}^{-1}$ in the 2-10 keV band, is very low compared to other galactic nuclei [293]. This fact is explained by a now widely accepted theory of Radiative Inefficient Accretion Flow, which explains that the inefficiency of the accretion activity of Sgr A*, suggested by the level of X-ray emission, is due to convection effects, leading to outflow or

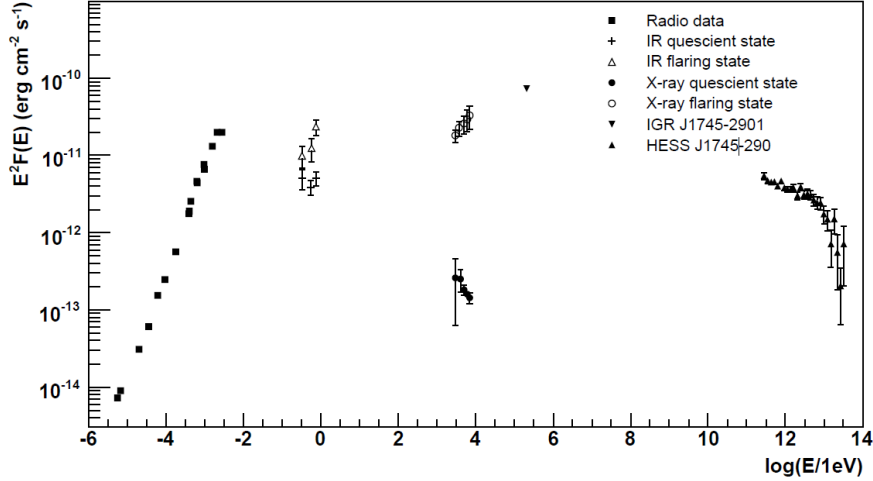


Figure 9.11: A composite spectral energy distribution of the Galactic Center source. The data and references are given in Ref. [297]. The measured spectrum during the flare states in X-rays and infrared are also plotted. The HESS J1745-290 spectral points are shown by filled triangles.

winds of accreting material [264]. The observational results for X-rays and for other wavelengths must be taken into account by models that describe possible mechanisms for particle acceleration in the vicinity of the SMBH. At the same time, the low luminosity of Sgr A* from IR to optical, which accounts to $10^{-8} L_{\text{edd}}$, with L_{edd} being the Eddington luminosity¹, makes the vicinity of the SMBH transparent to γ -rays otherwise shielded by pair-production of very high-energy γ -rays with ambient radiation [294]. Furthermore, X-ray satellites detected bright flares from Sgr A* and also took part in multiwavelength campaigns monitoring its flaring activity [295, 296]. Like already discussed above, synchrotron emission from relativistic electrons close to the SMBH is one way to explain the observed spectra. But expanding hot plasma can also account for at least some of the flare emission [264]. The broadband spectral energy distribution (SED) in the direction of Sgr A* is presented in Figure 9.11. The measured spectrum during the flare states in X-rays and infrared are also plotted.

¹The Eddington luminosity denotes the level of electromagnetic radiation of an object, for which the gravitational and radiative pressures cancel against each other.

9.2 Gamma-ray emissions from the Galactic Center region

The γ -ray emission from the Galactic Center was first detected by the EGRET satellite in the energy band 100 MeV to 10 GeV (3EG J1746-2852). In the case of observations with Imaging Atmospheric Cherenkov telescopes (IACTs), and detection of very high energy (VHE, $E \gtrsim 100$ GeV) gamma rays was reported by the CANGAROO [298], VERITAS [299], H.E.S.S. [285] and MAGIC[286] from the direction of the Galactic Center (GC). The nature of this VHE source is still unknown. The *Fermi-LAT* satellite has detected a source at the Galactic Center in the energy range between 20 MeV to more than 300 GeV [300], however due to the strong γ -ray diffuse background in this energy range no conclusion was taken about associations of the *Fermi-LAT* source with other γ -ray sources. The H.E.S.S. observations of the GC region led to the detection of a point-like source of VHE gamma-rays at the gravitational center of the Galaxy (HESS J1745-290), compatible with the positions of the SMBH Sgr A*, the supernova remnant (SNR) Sgr A East, and the plerion G359.95-0.04. A larger exposure of the region in 2004 revealed a second point-like source: the supernova remnant G0.9+0.1 [265]. The subtraction of these two sources revealed a ridge of diffuse emission extending along the Galactic plane for roughly 2° (Fig. 9.12), which was found to be correlated spatially to the GMCs. Among all the IACTs, H.E.S.S. is the most sensitive instrument to map the Galactic plane, thanks to its location in the southern hemisphere, its wide field of view ($5^\circ \times 5^\circ$) and the excellent hardware performances (see chapter 3). The H.E.S.S. experiment has been taking observations of the Galactic Center region for the past eight years, and with the data collected it provide the most detailed γ -ray picture of the GC region to date. In this paragraph the H.E.S.S. results on the GC are summarized.

9.2.1 HESS J1745-290: counterparts and spectrum

In December 2004, H.E.S.S. reported the detection of VHE gamma rays from the center of our Galaxy, at the time based on data obtained with the first two H.E.S.S. telescopes during 16h of observations in 2003. Within the - at the time unprecedented - precision of $30''$ in RA and Dec, the location of the source HESS J1745-290 was consistent with the Galactic gravitational center, and the spectrum of gamma rays was consistent with a power law up to 10 TeV. Towards identifying the origin of the

gamma rays, a multi-year effort was invested aimed at improving the pointing position of the H.E.S.S. telescopes. After a careful investigation of the pointing systematics of the H.E.S.S. telescopes, the systematic error on the centroid position was reduced from 30" to 6" per axis, with a comparable statistical error - by far the best source location achieved in gamma rays so far [59]. The thus determined source position is within $8'' \pm 9''_{\text{stat}} \pm 9''_{\text{sys}}$ from Sgr A*, well consistent with the location of the black hole and the pulsar wind nebula (PWL) G359.95-0.04 but it is inconsistent with the regions of intense radio emission from Sgr A East. It excludes Sgr A East remnant as the main counterpart of the VHE emission at the level of 7σ , if the assumed position of the VHE emission in Sgr A East is taken as the radio observations maximum, and at the level of 5σ if the assumed position is the best-fit centroid position of the radio emission from Sgr A East (Fig. 9.13, left) [see 59, for more details].

Using 93h of data on the central source accumulated in the years 2004, 2005 and 2006, the energy spectrum of the gamma rays was measured with high precision, revealing an energy break or cutoff in the spectrum around 15 TeV (Fig. 9.13, right). No signs of variability has been found [297]. Different mechanisms have been suggested to explain the broadband spectrum of the GC. Firstly, the stochastic acceleration of electrons interacting with the turbulent magnetic field in the vicinity of Sgr A*, as discussed by [301], has been advocated to explain the millimeter and sub-millimeter emission. This model would also reproduce the IR and X-ray flaring. In addition, it assumes that charged particles are accreted onto the black hole, and predicts the escape of protons from the accretion disk and their acceleration [301]. These protons produce π^0 mesons by inelastic collisions with the interstellar medium in the central star cluster of the Galaxy. The cut-off energy found in the gamma-ray spectrum could reflect a cut-off $E_{\text{cut},p}$ in the primary proton spectrum. In that case, one would expect a cut-off in the gamma-ray spectral shape at $E_{\text{cut}} \simeq E_{\text{cut},p}/30$. The measured value of ~ 15 TeV would correspond in this scenario to a cut-off energy in the primary proton spectrum between 100-400 TeV depending on the strength of the exponential cut-off. Energy-dependent diffusion models of protons to the outside of the central few parsecs of the Milky Way [294] are alternative plausible mechanisms to explain the TeV emission observed with the H.E.S.S. instrument. They would lead to a spectral break as in the measured spectrum due to competition between injection and escape of

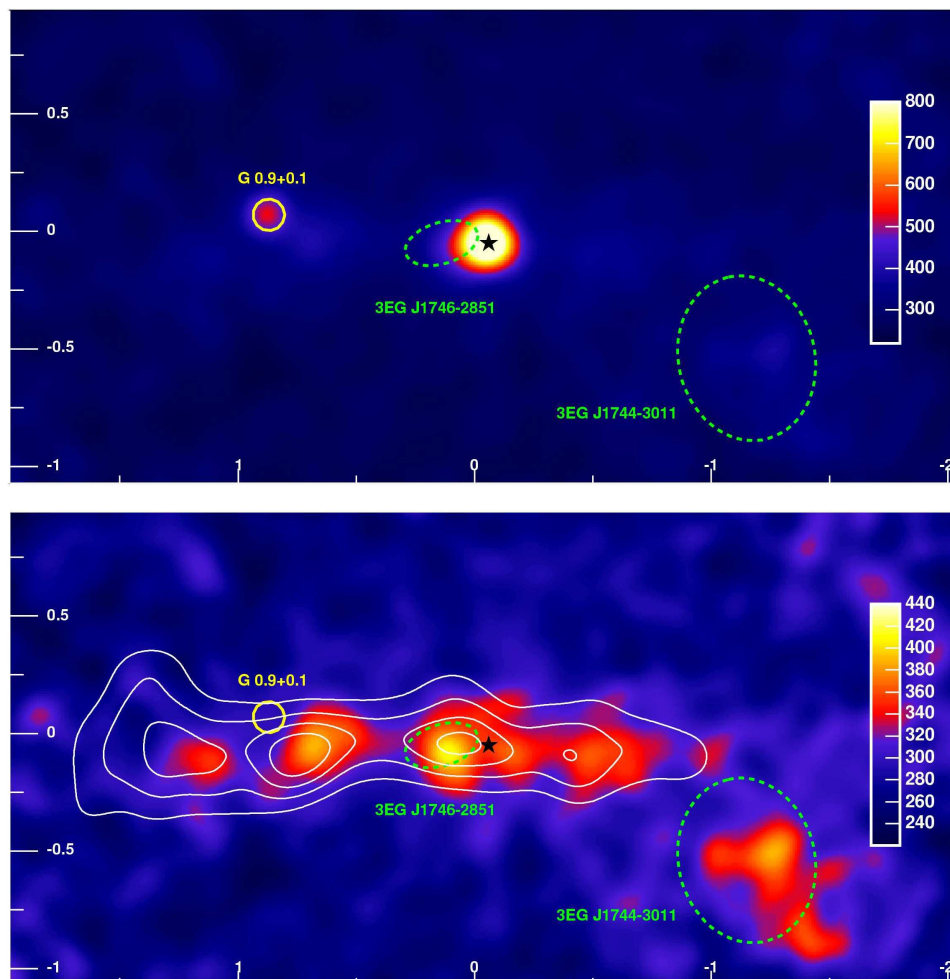


Figure 9.12: VHE gamma-ray images of the GC region. Top: gamma-ray count map, bottom: the same map after subtraction of the two dominant point sources, showing an extended band of gamma-ray emission. White contour lines indicate the density of molecular gas, traced by its CS emission. The position and size of the composite SNR G0.9+0.1 is shown with a yellow circle. The position of Sgr A* is marked with a black star. Figure extracted from [189].

protons outside the vicinity of the GC.

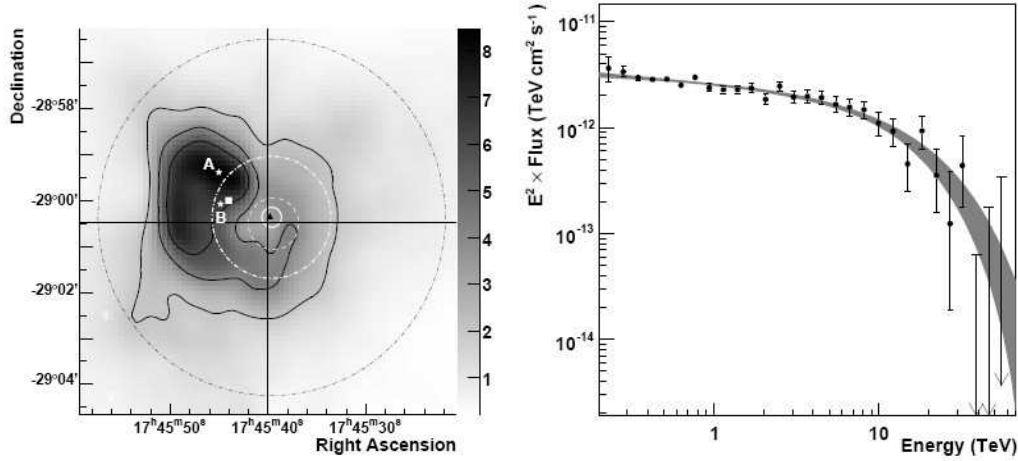


Figure 9.13: **Left:** 90 cm VLA radio flux density map of the innermost 20 pc of the GC, showing emission from the supernova remnant Sgr A East. The crossing lines show the position of the Galactic Center Sgr A*. The 68% CL error contour for the position of the gamma ray source HESS J1745-290 is given by the small white circle. The white stars marked A and B denote the position of the radio maximum and the centroid of a radio emission from Sgr A East, respectively. Figure extracted from [59]. **Right:** Energy spectrum of gamma rays from HESS J1745-290 as determined from the data sets obtained in the years 2004, 2005 and 2006. The shaded band shows the best fit to data for a power law with an exponential cutoff. Figure extracted from [297].

9.2.2 The diffuse emission from the Galactic Center Ridge

In order to search for much fainter emission, an analysis of the GC region was made [189] subtracting the best fit model for point-like emission at the position of HESS J1745-290 and the SNR G0.9+0.1. Two significant features are apparent after subtraction: extended emission spatially coincident with the unidentified EGRET source 3EGJ1744-3011 and emission extending along the Galactic plane for roughly 2° . The latter emission is not only clearly extended in longitude l , but also significantly extended in latitude b with a characteristic root mean square (rms) width of 0.2° , as can be seen in Fig. 9.12. The reconstructed gamma-ray spectrum for the region $-0.8^\circ < l < 0.8^\circ$, $|b| < 0.3^\circ$ (with point-source emission subtracted) is well described by a power law with photon index $\Gamma = 2.29 \pm 0.07_{\text{stat}} \pm 0.20_{\text{sys}}$ (Fig. 9.14).

Given the plausible assumption that the gamma-ray emission takes place near the center of the Galaxy, at a distance of about 8.5 kpc, the observed rms extension in

latitude of 0.2° corresponds to a scale of ≈ 30 pc. This extension value is similar to that of the interstellar material in giant molecular clouds in this region, as traced by their CS emission [281]. At least for $|l| < 1.$, a close match between the distribution of the VHE gamma-ray emission and the density of dense interstellar gas is found [see 189, for more details]. The close correlation between gamma-ray emission and available target material in the central 200 pc of our galaxy is a strong indication for an origin of this emission in the interactions of CRs. The hardness of the gamma-ray spectrum and the tight correlation of the intensity distribution with the molecular gas indicates a pion-decay process, so that the cosmic rays giving rise to the gamma-rays are likely to be protons and nuclei rather than electrons. Indeed, it was shown in [302] that electrons accelerated in a distribution of point sources, such as pulsar wind nebulae dispersed along the Galactic plane, do not produce a TeV emission profile consistent with the HESS map. Since in the case of a power-law energy distribution the spectral index of the gamma-rays closely traces the spectral index of the CRs themselves, the measured gamma-ray spectrum implies a CR spectrum near the GC with a spectral index close to 2.3, significantly harder than in the solar neighborhood¹. Given the probable proximity and young age of particle accelerators, propagation effects are likely to be less pronounced than in the Galaxy as a whole, providing a natural explanation for the harder spectrum which is closer to the intrinsic CR-source spectra. In addition, the key experimental facts of a harder than expected spectrum, and a higher than expected TeV flux, imply that there is an additional young component to the GC cosmic-ray population above the CR 'sea' which fills the Galaxy. This is the first time that such direct evidence for recently accelerated (hadronic) CRs in any part of our galaxy has been found.

The observation of a deficit in VHE emission at $l = 1.3^\circ$ relative to the available target material (see Fig. 9.12, bottom) suggests that CRs, which were recently accelerated in a source or sources in the GC region, have not yet diffused out beyond $|l| = 1^\circ$. Therefore the central CRs accelerators would only been active in the GC for the past 10.000 years. The fact that the diffuse emission exhibits a photon index which is the same - within errors - as that of HESS J1745-290 suggests that the underlying astrophysical emitter of HESS J1745-290 could be the source in question. Within the $1'$ error box of HESS J1745-290 are two compelling candidates for such a CR accelerator.

¹The measured CR spectrum in the solar neighborhood has an index of 2.75.

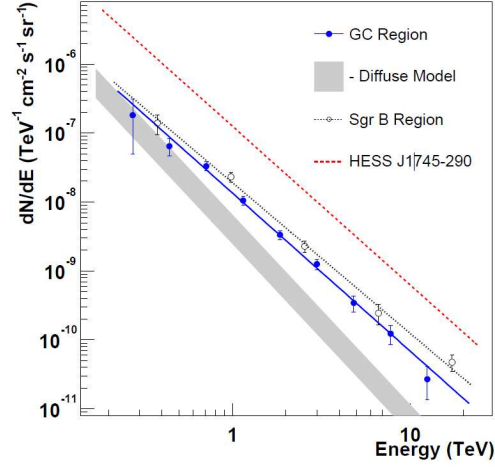


Figure 9.14: γ -ray flux per unit solid angle in the GC region (data points), in comparison with the expected flux assuming a cosmic-ray spectrum as measured in the solar neighbourhood (shaded band). The strongest emission away from the bright central source HESS J1745-290 occurs close to the Sagittarius B complex of giant molecular clouds. The energy spectrum of this region is shown using open circles. The 2006 spectrum of the central source HESS J1745-290 is shown for comparison (using an integration radius of 0.14°). Figure extracted from [189].

The first is the SNR Sgr A East with its estimated age around 10 kyr. The second is the SMBH Sgr A* which may have been more active in the past [294].

Chapter 10

Analysis of the VHE diffuse emission in the Galactic Center region

Contents

10.1 Update on the Galactic Center observations	204
10.1.1 Data selection	204
10.1.2 HESS J1745-290 data analysis and spectrum	205
10.2 Subtraction of the diffuse spectral contamination	208
10.2.1 Diffuse emission spectrum	209
10.2.2 A Diffuse model	212
10.2.3 Final spectrum	214
10.2.4 A closer look on the highest energy events	215
10.3 Spectral morphology of the diffuse region	217
10.3.1 Spectral analysis of annular regions around the Galactic Center	218
10.3.2 Systematics uncertainties on the energy cut-off reconstruction	219
10.3.3 Sagittarius B, C and D spectra	220
10.4 Summary and conclusion	221

In this chapter the new analysis of the Galactic Center region with the H.E.S.S. array is described. First, in Section 10.1, the analysis of H.E.S.S. data is presented, from which an energy spectral reconstruction of the HESS J1745-290 source is performed. In Section 10.2 the energy spectrum of the diffuse emission around the central VHE source is calculated. The contribution of the diffuse emission signal as foreground for the central source is determined based on a diffuse model. A spectral subtraction of the diffuse component under the HESS J1745-290 signal is performed, which allows to recover the intrinsic spectrum of the central source. Finally, in Section 10.3, a study on the spectral morphology of the Galactic Center region in VHE γ -rays is presented.

10.1 Update on the Galactic Center observations

10.1.1 Data selection

Since the last published results on the Galactic Center using data accumulated in the years 2004, 2005 and 2006 [297], more observations have been done every year. A selection of all the runs with dedicated observation of the central source or observations of sources with angular distances inferior to 2.5° of Sgr A* nominal position was done for the present work. These selected runs comprise observations performed between 2003 and 2011. In order to improve the statistics and constrain the shape of the high energy part of the spectrum ($E_\gamma \geq 10\text{TeV}$) observation at high zenith angles ($40^\circ \leq \theta_z \leq 70^\circ$) were performed in 2005 and 2006, and following the discovery of an exponential energy cut-off in the HESS J1745-290 spectrum around 15 TeV dedicated observations at high θ_z were also taken in 2011. Indeed showers energetic enough to trigger the telescopes at high θ_z are more likely to have been initiated by very-high energy γ -rays. The dedicated observations of the Galactic Center were performed in *wobble mode*, i.e. with the target typically offset by 0.7° to 1.1° from the direction of Sgr A*. The data sets used for the analysis include only the observation runs that meet the standard quality control criteria described in chapter 3. The total data set amounts to 198 hrs of live time after the quality selection. This is the largest exposure ever taken on any source at VHE γ -rays observations. Table 10.1 summarizes the H.E.S.S. observation campaigns towards the Galactic Center over the years.

Year	θ_z [$^\circ$]	T_{obs} [h]	Excess γ -events	Significance σ
2004	21.8	48.5	2270	56.6
2005	28.8	69.2	1522	43.3
2006	18.7	29.3	725.2	30.4
2007	11.2	11.5	245.2	17.7
2008	15.3	13.4	408	22.7
2009	17.8	6.0	180.5	18.3
2010	10.8	11.6	301	21.0
2011	33.6	10.1	196	15.4
Total	22.5	198.0	6468.1	95.0

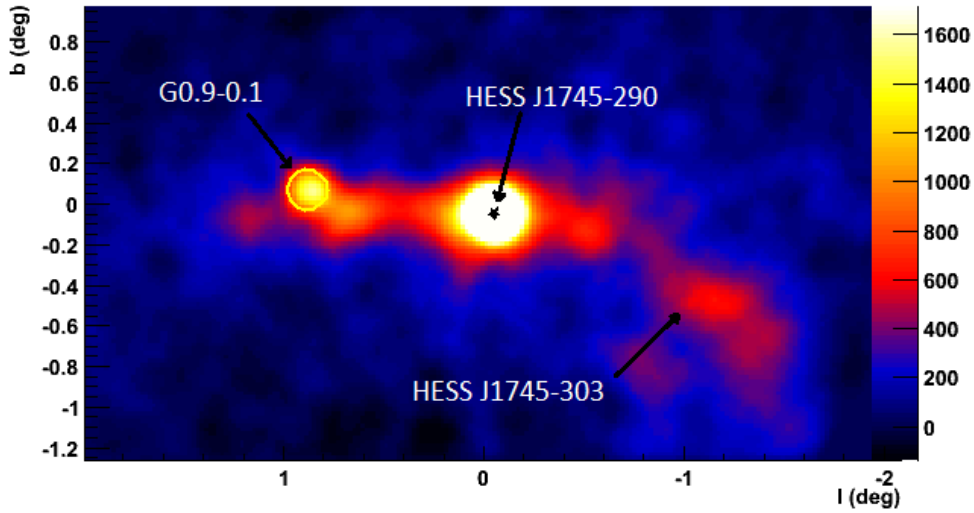
Table 10.1: Details on the H.E.S.S. observation campaigns towards the Galactic Center over the years. θ_z indicates the mean zenith angle of observation, and T_{obs} the observation live time. The excess is calculated in a circular region of 0.1° around the position of Sgr A*. The significance is calculated after Eq. 3.9.

10.1.2 HESS J1745-290 data analysis and spectrum

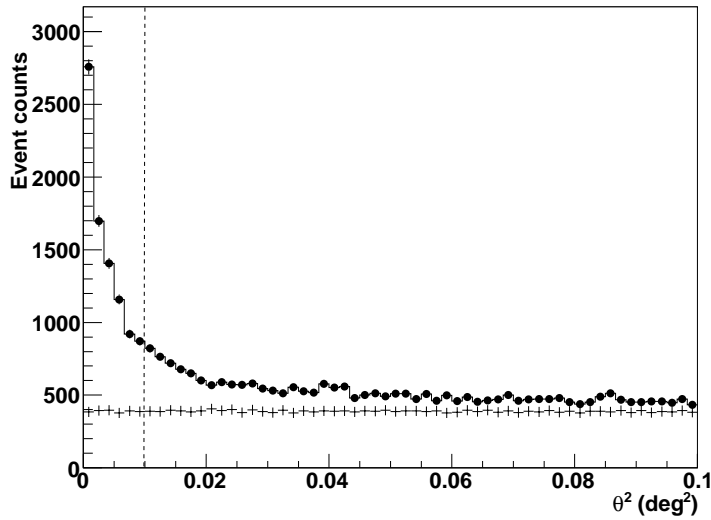
The full data is analyzed using the *model analysis* described in the chapter 3 (Model++) applying the *standard cuts* for the events selection. The cosmic-ray background was determined by the ring-background technique (see Section 3.2 for more details), calculating the background for each position in the field-of-view using the background rate contained in a ring around the target. Exclusion regions for the background determination were defined excluding the whole diffuse emission region for background events selection. These exclusion regions are shown in Figure 10.1a where the excess map of the GC region centered on the position of Sgr A* is presented.

Three sources are clearly seen: the HESS J1745-290, the supernova remnant G0.9+0.1 and the HESS J1745-303. The data analysis in a circular region with an opening angle of 0.1° around Sgr A* shows an excess of 6468 γ events with a significance of 95.0σ . The γ events distribution as function of the square of the angular distance θ is presented in Figure 10.1b. An excess outside the central source region, $\theta^2 \geq 0.01^\circ$, is clearly seen and it is related to the diffuse emission on the galactic plane. The contamination of the diffuse component under the central source is estimated in

Sect. 10.2.



(a) Excess map (number of γ -rays)



(b) Angular distribution of γ -rays

Figure 10.1: (a) γ -ray excess map in galactic coordinates. The positions of the sources HESS J1745-290, G0.9+0.1 and HESS J1745-303 are indicated. (b) Angular distribution of γ -rays plotted as function of θ^2 where θ is the angle between the γ -ray direction and Sgr A*. γ -ray candidates (*full circles*) and residual hadronic background (*crosses*) are plotted. The dotted line indicates the ON region, from where the signal is extracted.

Applying the forward-folding likelihood method described in Section 3.2 the energy spectrum of HESS J1745-290 is obtained for the full dataset of 2004 to 2011. Two spectral shapes are used in the fitting procedure a power-law,

$$\frac{dN}{dE} = \Phi_0 \times \left(\frac{E}{E_{\text{norm}}} \right)^\Gamma, \quad (10.1)$$

and a power-law with exponential cut-off,

$$\frac{dN}{dE} = \Phi_0 \times \left(\frac{E}{E_{\text{norm}}} \right)^\Gamma \times e^{-\frac{E}{E_c}}, \quad (10.2)$$

where Φ_0 is the flux normalisation in $\text{TeV}^{-1} \text{m}^{-2} \text{s}^{-1}$, E_{norm} is the energy normalisation at 1 TeV, Γ the spectral index and E_c the exponential cut-off energy.

The energy spectrum fittings are presented in Fig. 10.2. It clearly deviates from a pure power-law spectrum shape. The spectrum is well described by a power-law with exponential cut-off, confirming the tendency found in the published paper [297]. The power-law spectrum index is found to be:

$$\Gamma = 2.22 \pm 0.04_{\text{stat}} \pm 0.10_{\text{syst}}, \quad (10.3)$$

with an exponential cut-off at

$$E_c = 6.35 \pm 1.10_{\text{stat}} \pm 1.00_{\text{syst}} \text{ TeV}, \quad (10.4)$$

and an integrated flux above 1 TeV of

$$\Phi(\geq 1\text{TeV}) = (1.52 \pm 0.08_{\text{stat}} \pm 0.28_{\text{syst}}) 10^{-8} \text{ m}^{-2} \text{ s}^{-1}. \quad (10.5)$$

The systematic errors, 5 % for the spectral index, 17 % for the cut-off energy and 15 % for the integrated flux, are estimated in Ref. [48] (see also chapter 3). The values of Γ and $\Phi(\geq 1\text{TeV})$ found with the full dataset are in good agreement with the published 2006 spectrum. The value of E_c has a smaller value than the published one, which was measured at 15.7 ± 6.0 TeV, but it is still compatible at a 2σ deviation. To investigate the evolution of the spectral parameters with time, the same spectral analysis was performed using datasets from 2004-2008, 2004-2009 and 2004-2010. Table 10.2 presents the spectral parameters of power-law with exponential energy cut-off for all

the different datasets. It is clear that the rise in the number of detected γ -rays due to the additional 100 hours of observations since 2006, especially at very high energy, allows a more precise measurement of the spectrum shape at the TeV energy range.

DataSet	Index Γ	E_c [TeV]	$\Phi(\geq 1\text{TeV})$ [$\text{cm}^{-2} \text{s}^{-1}$]
2004-2008	2.13 ± 0.04	11.8 ± 3.21	$(1.69 \pm 0.05) \times 10^{-12}$
2004-2009	2.23 ± 0.04	8.1 ± 1.5	$(1.59 \pm 0.07) \times 10^{-12}$
2004-2010	2.21 ± 0.04	7.2 ± 1.3	$(1.57 \pm 0.07) \times 10^{-12}$
2004-2011	2.22 ± 0.04	6.3 ± 1.1	$(1.52 \pm 0.08) \times 10^{-12}$

Table 10.2: Values of the spectral parameters of the HESS J1745-290 energy spectrum with different datasets. The spectrum is fitted with a power-law with index Γ and an exponential energy cut-off at the energy E_c .

10.2 Subtraction of the diffuse emission spectral contamination from the HESS J1745-290 spectrum

Although the main contribution to the HESS J1745-290 spectrum must come from one (or two) astrophysical emitter, definitely a part of the γ -rays detected under the central source comes from the diffuse emission. In Figure 10.1b the diffuse emission is clearly seen at $\theta \geq 0.1^\circ$. The theta-squared distribution can be fitted under the assumption of central point-like source plus a linear component to account for the diffuse emission. Figure 10.3 shows the result of the fitting procedure. Extending the linear part under the central source gives a first and rough estimation of the diffuse emission contamination, which by this procedure is found to be about 9 %. However a proper estimation of the diffuse emission under the central source can be done by modeling this emission as coming from the interaction of hadronic cosmic-rays accelerated at the center, which then diffuse to the ambient space. Details of this modeling are given in Section 10.2.2 (where a different percentage of contamination is found).

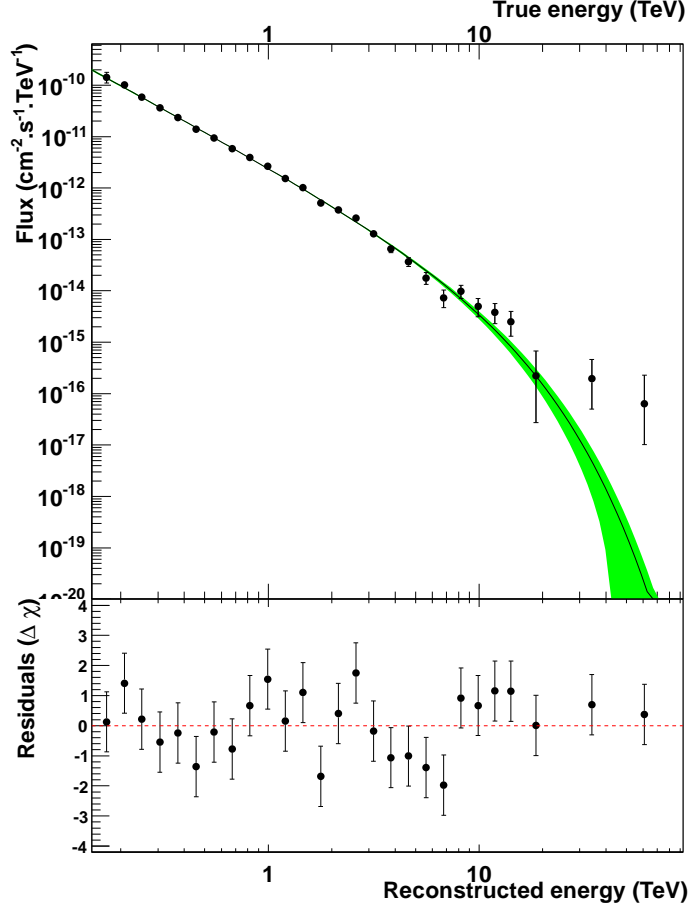


Figure 10.2: HESS J1745-290 spectrum derived with the dataset from 2004 to 2011. The green region correspond to the best-fit with a power-law with exponential energy cut-off shape. The residuals $(N_\gamma - N_{\gamma,\text{th}})/N_{\gamma,\text{th}}$ are also presented, where $N_{\gamma,\text{th}}$ is the predicted number of γ -rays for the fitted spectrum. It is well centered on 0, which indicates a good fit.

10.2.1 Diffuse emission spectrum

In order to correctly subtract the diffuse emission, a target region needs to be defined to derive the γ -ray energy spectrum. The test region is defined as a ring around the central source with inner radius $r_{\text{in}} = 0.1^\circ$ and out radius $r_{\text{out}} = 0.4^\circ$, as visualized in Figure 10.4. Assuming that the diffuse emission has azimuthal symmetry along the galactic plane, γ -rays with the same energy spectrum should be contributing to the central source spectrum. The data analysis was performed with the same criteria for

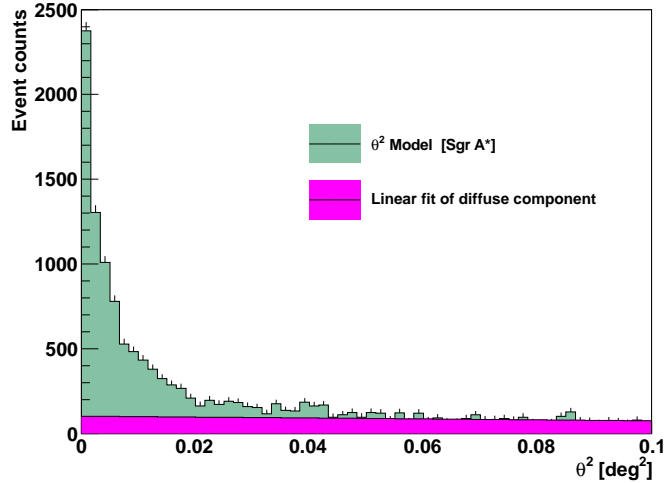


Figure 10.3: Angular distribution of γ -rays plotted as function of θ^2 . The green histogram correspond to the actual observed γ -rays distribution. The pink histogram is the predicted distribution of γ -rays of the diffuse emission, found by fitting the actual γ -ray distribution by a central point-like source (double-gaussian psf) plus a linear component and taking the linear component as the diffuse emission.

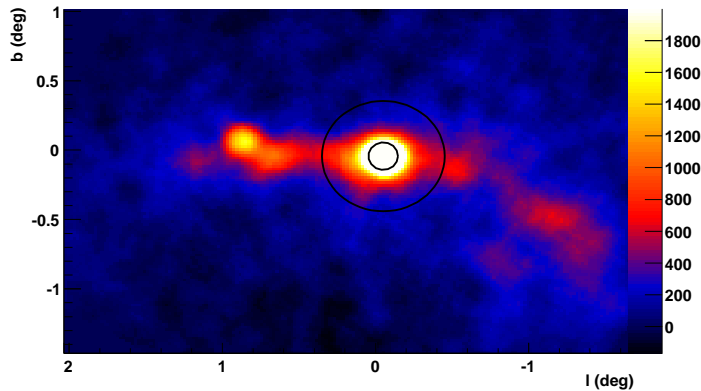


Figure 10.4: Test region to extract the γ -ray diffuse emission spectrum. The region is defined as a ring delimited by the two black circles. The inner radius $r_{\text{in}} = 0.1^\circ$ and out radius $r_{\text{out}} = 0.4^\circ$.

the events selection as the analysis of HESS J1745-290, and the cosmic-ray background was determined by the ring-background technique.

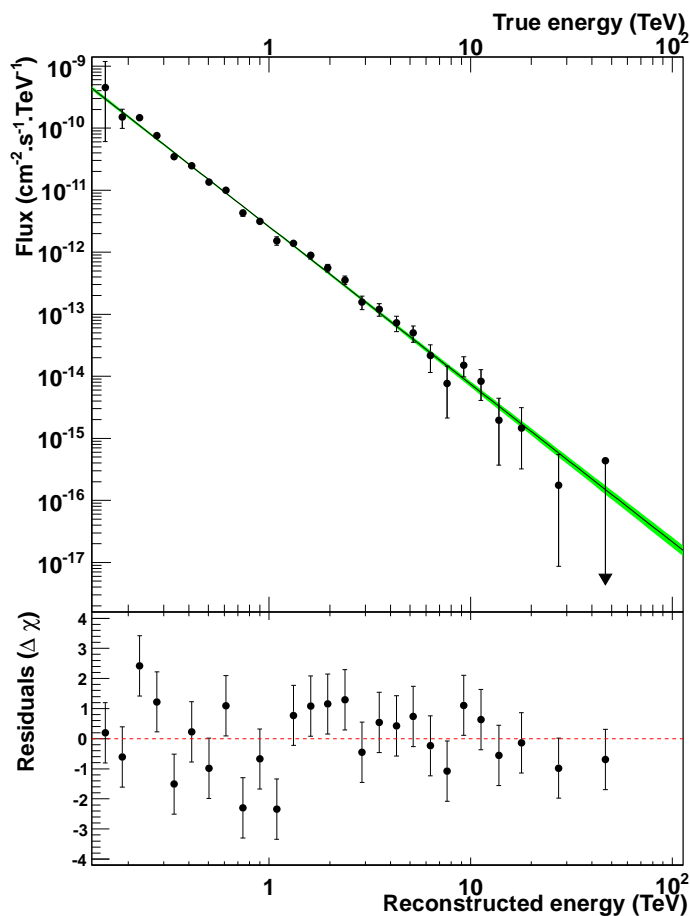


Figure 10.5: Diffuse emission spectrum. The green region correspond to the best-fit with a power-law shape. A power-law index of $\Gamma = 2.53 \pm 0.04_{\text{stat}} \pm 0.10_{\text{sys}}$ is found.

An excess of 7000 γ -rays is found and the energy spectrum is well fitted by a power-law with index

$$\Gamma = 2.53 \pm 0.04_{\text{stat}} \pm 0.10_{\text{sys}} , \quad (10.6)$$

and an integrated flux above 1 TeV of

$$\Phi(\geq 1\text{TeV}) = (1.67 \pm 0.08_{\text{stat}} \pm 0.25_{\text{sys}})10^{-8} \text{ m}^{-2}\text{s}^{-1} , \quad (10.7)$$

as it can be seen in Figure 10.5.

10.2.2 A Diffuse model

The basic concept of diffusion of CRs is understood as a result of interactions between the CR particles and the magnetic field in the Galaxy. After leaving the acceleration region, CRs perform a diffusive random walk in the galaxy due to irregularities in the galactic magnetic field structure. During its diffusion the interaction between the CRs and the interstellar material in giant molecular clouds (GMCs) would give rise to a γ -ray emission. This model was first proposed by Aharonian et al. (2006) [189] and a more elaborate model based on the first was developed in Ref. [303] and it is used here.

The starting point for the diffusion model comes from the diffusion equation, which connects the net flow of particles $\vec{J}(\vec{r}, E, t)$ with spatial gradient of particles density $\vec{\nabla}n(\vec{r}, E, t)$ by

$$\vec{J}(\vec{r}, E, t) = -D(\vec{r}, E, t)\vec{\nabla}n(\vec{r}, E, t), \quad (10.8)$$

where $D(\vec{r}, E, t)$ is called the diffusion coefficient. Since $\vec{\nabla}\vec{J}(\vec{r}, E, t) = \frac{\partial n(\vec{r}, E, t)}{\partial t}$ one obtains following differential equation:

$$\frac{\partial n(\vec{r}, E, t)}{\partial t} = -\vec{\nabla}D(\vec{r}, E, t)\vec{\nabla}n(\vec{r}, E, t). \quad (10.9)$$

For scalar, constant diffusion $D(\vec{r}, E, t) = D(E)$, and assuming spherical symmetry $n(\vec{r}, E, t) = n(r, E, t)$ the solution is

$$n(r, E, t) = \frac{n(0, E, t)}{[4\pi D(E)t]^{1/2}} \exp\left[\frac{-r^2}{4D(E)t}\right]. \quad (10.10)$$

The relation $n(t)/n(0)$ simply gives the probability of finding a particle at a distance r for a given time t . It is evidently a Gaussian function with a width of $\sigma = \sqrt{2Dt^2}$. From this relation it follows that the mean distance a particle travels away from its source is proportional to the square-root of time: $\langle r(t) \rangle = \sigma \propto \sqrt{Dt}$. The diffusion coefficient contains the magnetic field structure dependence, as it is assumed that particles are scattered by perturbations in a magnetohydrodynamic fluid, consisting of the magnetic field, ions and electrons. Here, both small and large-scale characteristics of the magnetic field play an important role. But until now, the knowledge about its configuration on various scales is still insufficient, specially in the galactic center region. Nevertheless, it is still possible to search for an optimal value for the diffusion coefficient of

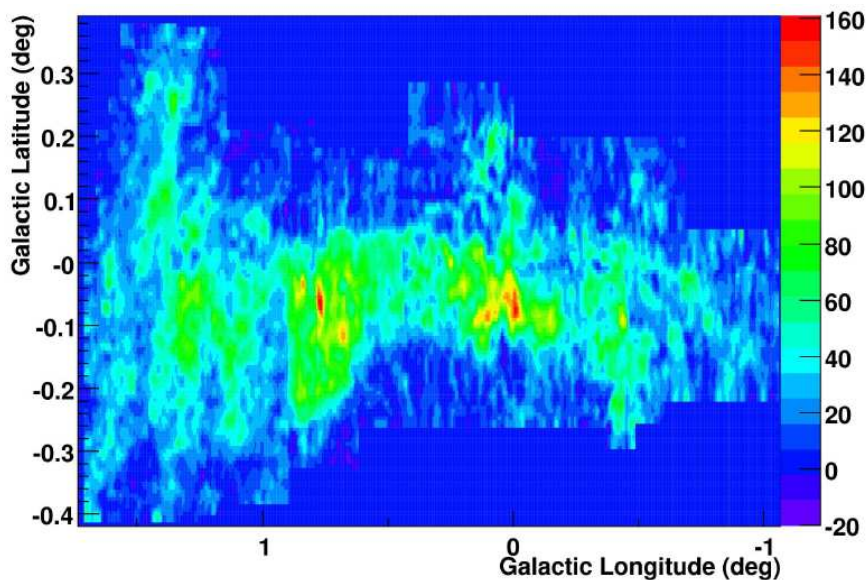


Figure 10.6: A map of molecular clouds in the galactic center region obtained by NRO telescope imaging the CS line (units are arbitrary).

protons in the GC region from the observed morphology of diffuse emission by H.E.S.S..

In Aharonian et al. (2006)[189] and Nekrassov (2010) [303], this was done using a simple model, where the diffusion coefficient and the diffusion time were assumed as constants. Because of the close correlation between the γ -ray emission and the density of interstellar material in GMCs, the γ -ray flux is assumed to be proportional to the matter density. The diffusion emission is then estimated by folding the two-dimensional map of molecular material, obtained by means of CS observations [281] (Fig. 10.6), with the solution of the diffusion equation (Eq. 10.10), assuming a burst-like injection of the primary hadrons. For each bin of this map, the hadron density $n(r)$ is obtained by calculating the distance r between the bin center and the center of the map, while assuming a certain diffusion coefficient D and diffusion time t . The normalisation is arbitrary and is later matched to the data. If, for example, Sgr A East is taken as the source of protons, assuming that the progenitor star exploded 10^4 years ago, the diffuse coefficient can be completely determined. In Aharonian et al. (2006) [189] an upper limit on the diffusion coefficient was estimated at $D \leq 3.5 \text{ kpc}^2 \text{ Myr}^{-1}$ ($10^{30} \text{ cm}^2/\text{s}$). The resulting diffusion emission model map assuming a diffusion coefficient of $D = 3.0$

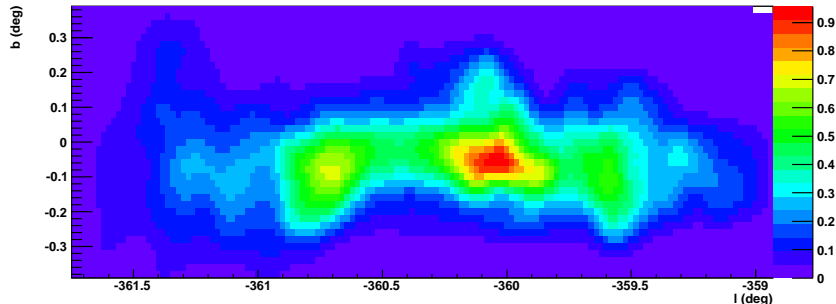


Figure 10.7: The resulting γ -ray count map for the diffusion model from [189]. The underlying CS-map was folded with a Gaussian, of which the width σ corresponds to the diffusion coefficient of $3 \text{ kpc}^2 \text{ Myr}^{-1}$ (see Eq. 10.10), smoothed to match the angular resolution of H.E.S.S..

$\text{kpc}^2 \text{ Myr}^{-1}$ and an arbitrary diffusion time can be seen in Fig. 10.7.

The estimation of the diffuse emission contamination under the central source can now be performed based on this diffusion model. Figure 10.8 shows the events distribution in the diffuse model as function of θ^2 . A linear regression between the model and the observed events for $\theta^2 \geq 0.05^\circ$ was performed in order to normalize the diffuse model. In this case the contamination is estimated at 27 % of the events in the central source ($\theta \leq 0.1^\circ$) as coming from the diffuse component. The linear regression error at 1σ , gives an uncertainty of $\pm 5\%$ on the contamination estimate.

10.2.3 Final spectrum

The intrinsic spectrum of the central source can be recovered by subtracting the diffuse spectral contamination. The diffuse emission spectrum has to be renormalised so that the expected number of γ -rays due to the diffuse component match the 27 % of the expected number of γ -rays due to the central GC emission. The expected number of γ -rays per unit of time coming from a given source is found by folding the source spectrum with the detector acceptance, obtained from the observational dataset, and integrating for all energies. The renormalisation factor α of the diffuse spectrum can then be found by the following relation:

$$\alpha \int \frac{dN^{\text{diff}}}{dE} A_{\text{eff}}(E) dE = 0.25 \int \frac{dN^{\text{GC}}}{dE} A_{\text{eff}}(E) dE, \quad (10.11)$$

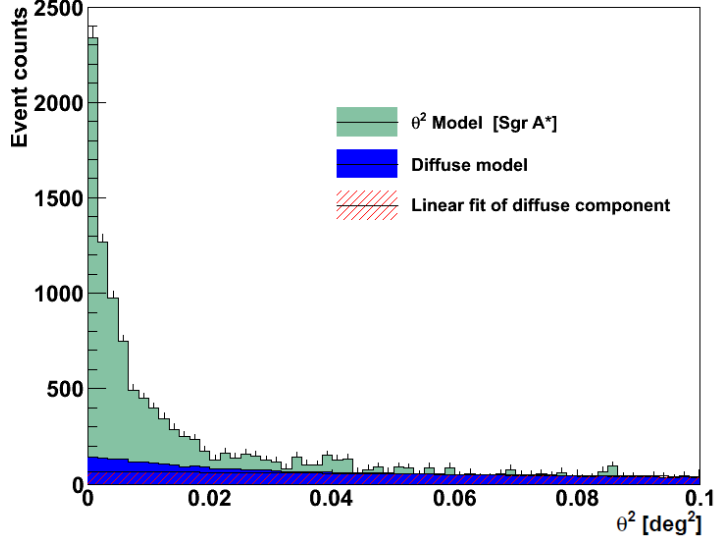


Figure 10.8: Angular distribution of γ -rays plotted as function of θ^2 . The green histogram correspond to the actual observed γ -rays distribution. The blue region correspond to the γ -ray angular distribution of the diffuse model showed in Fig. 10.7. The model was renormalised in order to match the observed number of γ -rays for $\theta^2 \geq 0.05^\circ$.

where dN^{diff}/dE and dN^{diff}/dE are the diffuse and central GC source spectra, respectively, and A_{eff} is the effective area of the detector.

After renormalisation, the expected diffuse emission spectrum under the central source is recovered. In Figure 10.9 the diffuse emission is finally subtracted from the central source spectrum. The central source intrinsic spectrum reveals a stronger energy cut-off at energies around 10 TeV. Plus γ -rays from the diffuse emission are predicted to dominate the full spectrum at energies $E \gtrsim 20\text{TeV}$. With more statistics, the detected flux should go as a power-law at this energy range.

10.2.4 A closer look on the highest energy events

The prediction of a dominance of the diffuse emission at energies above 20 TeV can already be tested. From the residuals in Fig.10.2 it is possible to identify the presence of some γ -ray events with energy superior to 20 TeV. In Fig. 10.10 the energy of each γ -ray event in the signal (ON) region with $E \geq 20$ TeV is plotted as function of the

10. Analysis of the VHE diffuse emission in the Galactic Center region

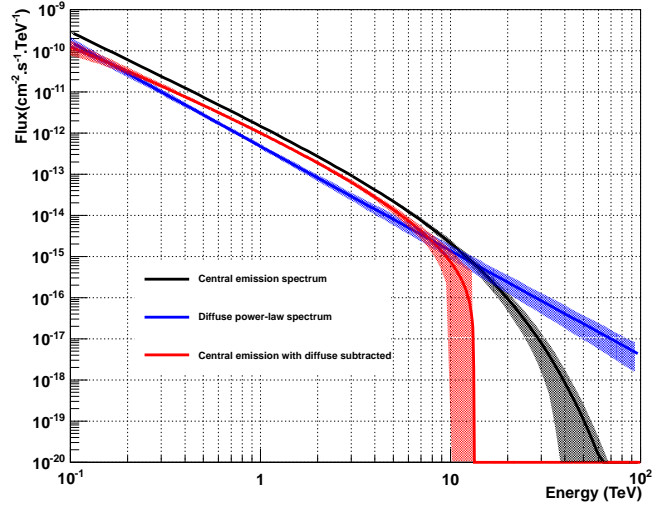


Figure 10.9: Final spectrum of the central VHE γ -ray source after the subtraction of the diffuse foreground component. The HESS J1745-290 spectrum (black line) is the sum of the diffuse spectrum (blue line) and the a central γ -ray source (red line). The colored bands give the statistical uncertainties on the reconstructed spectra.

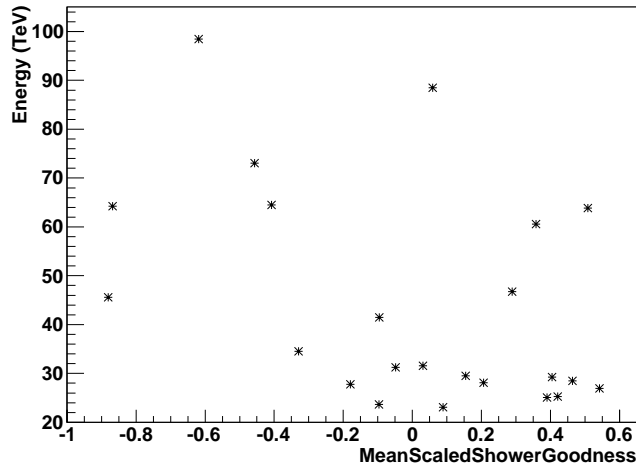


Figure 10.10: γ -ray events from the Galactic Center central source with $E \geq 20$ TeV. The energy of each single event is plotted as function of its *Mean Scaled Shower Goodness* (MSSG) variable.

γ -ray discriminating variable *Mean Scaled Shower Goodness*(MSSG).

10.3 Spectral morphology of the diffuse region

There are 23 γ -like events passing the γ -ray selection cuts. The background level above 20 TeV is estimated at 18 γ -like events in the signal region, which gives an excess of 5 events. This excess is compatible with a background fluctuation at about 1.2σ . The same procedure was applied using different cuts on energy, as presented in Table 10.3 for 20, 25 and 30 TeV. It is interesting to notice that while all these excesses are compatible with a background fluctuation up to 2σ , they cannot be explained as coming from the GC HESS J1745-290 source. On the other hand, the diffuse emission predicts a number of events in the same order of magnitude as the observed excesses.

	$E \geq 20$ TeV	$E \geq 25$ TeV	$E \geq 30$ TeV
γ -ray events	23	21	13
Background events	18	13	10
Excess	5	8	3
Diffuse emission prediction	6.1	4.1	3.0
HESS J1745-290 prediction	0.9	0.3	0.1

Table 10.3: Estimation on the number of γ -ray events above different energy thresholds coming from different origins in the Galactic Center. The predictions for diffuse emission is based on its expected spectrum under the central source, from Section 10.2.3. The predictions for HESS J1745-290 are based on the measured spectrum from Section 10.1.2.

10.3 Spectral morphology of the diffuse region

Although the diffusion picture seems to be in good agreement with the H.E.S.S. observations, small scale deviations from the predictions of the diffusion models are still visible. The diffusion models often represent only the space-averaged diffusion process, where $D = \langle D(E) \rangle$. One consequence of these models is that the γ -ray energy spectrum in the whole diffuse area is predicted to be the same. In reality the diffusion coefficient is certainly space-dependent, which would definitely induce a spatial change of the measured energy spectra in the region. Besides, it is unclear how deep CRs of different energies can penetrate dense molecular clouds [304], i.e. if the diffusion can take place everywhere in the GC region. Alternative scenarios propose that the observed emission could be due to a population of extended sources having the same longitude and latitude distribution as the GMCs. In this section the spectral

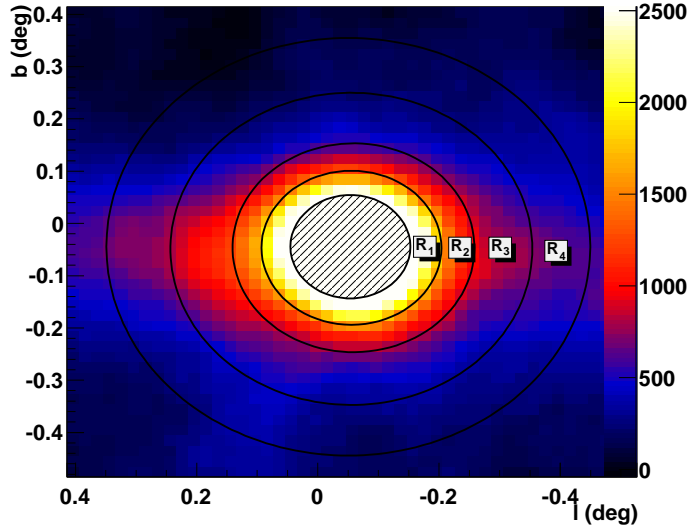


Figure 10.11: Concentric annular regions centered on Sgr A*. Four ring regions are defined based on their inner radius r_{in} and out radius r_{out} by $[r_{\text{in}}, r_{\text{out}}]$: $R_1 = [0.1^\circ, 0.15^\circ]$, $R_2 = [0.15^\circ, 0.2^\circ]$, $R_3 = [0.2^\circ, 0.3^\circ]$ and $R_4 = [0.3^\circ, 0.4^\circ]$.

morphology of the diffusion emission is studied. Because of the increase in statistical data from the Galactic Center region, local measurements of the γ -ray energy spectrum now becomes possible.

10.3.1 Spectral analysis of annular regions around the Galactic Center

The ring area used in Sect. 10.2.1 to derive the space-averaged diffusion emission spectrum is now sliced in four smaller ring regions $R_1 = [0.1^\circ, 0.15^\circ]$, $R_2 = [0.15^\circ, 0.2^\circ]$, $R_3 = [0.2^\circ, 0.3^\circ]$ and $R_4 = [0.3^\circ, 0.4^\circ]$ (see Figure 10.11). Independent data analysis is performed in each of these regions applying the Model++ and Hillas analysis with *standard cuts* for the events selection. The background is estimated by the ring-background technique. The energy spectra is measured assuming two spectral shapes, a power-law and a power-law with exponential cut-off. The spectra best fit parameters are summarized in Table 10.4 and Table 10.5, for the power-law and power-law with exponential cut-off shapes, respectively. There is no evidence of any energy cut-off, and the spectra are well described by a pure power-law. The central values of the power-law indexes

measured in the rings are softer than the HESS J1745-290 spectral index. However, these values are still compatible within 2σ , if a systematic error of 0.1 is taken into account.

Ring	$r_{\text{in}}-r_{\text{out}}$ [deg]	Γ (Model++)	Γ (Hillas)
R ₁	0.1° – 0.15°	2.41 ± 0.04	2.43 ± 0.04
R ₂	0.15° – 0.2°	2.33 ± 0.05	2.33 ± 0.05
R ₃	0.2° – 0.3°	2.32 ± 0.08	2.41 ± 0.05
R ₄	0.3° – 0.4°	2.40 ± 0.08	2.21 ± 0.1

Table 10.4: Spectral results from the analyses of the set of annular region defined on the text covering the diffuse emission around Sgr A*. The best-fit parameters for power-law of index Γ are presented for both Model++ and Hillas analysis, with their respective statistical errors.

Ring	$r_{\text{in}}-r_{\text{out}}$ [deg]	1/ E_{cut} (Model++) [TeV ⁻¹]	1/ E_{cut} (Hillas) [TeV ⁻¹]
R ₁	0.1° – 0.15°	0.02 ± 0.02	0.04 ± 0.02
R ₂	0.15° – 0.2°	0.04 ± 0.04	≤ 0.04
R ₃	0.2° – 0.3°	≤ 0.04	≤ 0.04
R ₄	0.3° – 0.4°	≤ 0.04	≤ 0.04

Table 10.5: Spectral results from the analyses of the set of annular region defined on the text covering the diffuse emission around Sgr A*. The best-fit parameters for power-law of index Γ with an exponential energy cut-off at E_{cut} are presented for both Model++ and Hillas analysis, with their respective statistical errors.

10.3.2 Systematics uncertainties on the energy cut-off reconstruction

In order to check the validity of the spectral reconstruction and in particular the energy cut-off E_c estimation, Monte-Carlo simulations of showers generated by γ -rays with a primary power-law spectra were performed. γ -rays with primary power-law with an exponential cut-off are generated by weighting the high energy events of the first spectrum : for each event with energy E , a weight $\exp(-E/E_c)$ is calculated and then compared to a number between 0 and 1 drawn randomly with a uniform

10. Analysis of the VHE diffuse emission in the Galactic Center region

probability distribution. If the weight is bigger than the drawn number then the event is kept. All the showers were simulated with south azimuth, a spectral index of 2.23 corresponding to the HESS J1745-290 spectrum index, zenith angle of 30° and with a camera offset of 0.7° to account for the *wobble mode* observations. The energy cut-off in the primary γ -ray spectra is applied at 6 TeV. For each spectrum 200.000 showers were simulated. The trigger requirements are set at the normal requirements for stereoscopic observations, i.e., if more than 3 pixels within a camera sector receive a signal of more than 4 photo-electrons (p.e.) within a time window of 1.5 ns. The events analysis and spectral reconstruction follows the same chain as the Galactic Center region data analysis. Each primary γ -ray spectrum is reconstructed assuming power-law with exponential cut-off shape.

Figure 10.12 shows the distribution of the measured $1/E_c$ for each primary spectrum shape. The $1/E_c$ of γ -rays with primary spectra of power-law with exponential cut-off at 6 TeV have a gaussian distribution with center at 0.162 ($E_c = 6.1$ TeV) and $\sigma = 0.044$. If the primary spectrum is a pure power-law the reconstructed $1/E_c$ distribution was found to be well described by gaussian distribution centered at 0 and $\sigma = 0.047$. These distributions can be used to derive the probability of reconstruction of an energy cut-off assuming the two primary spectra hypothesis. By applying the Neyman Pearson hypothesis test it is possible to define a region of the parameter space where a hypothesis can be rejected or accepted. The hypothesis of a primary spectrum with a pure power-law can be excluded at more than 95% of confidence level for reconstructed spectrum with E_c at $1/E_c > 0.09$ ($E_c < 11$ TeV). On the other hand a primary power-law spectrum with exponential cut-off at 6 TeV can be excluded at more than 95% of confidence level for any reconstructed spectrum with E_c at $1/E_c < 0.07$ ($E_c > 14$ TeV). The reconstructed energy cut-offs from the annular regions in Table 10.5 imply that the a pure power-law spectrum is completely consistent with the measured spectra. On the other hand, the existence of an energy cut-off at 6 TeV is excluded at 95 % of C.L. for all the rings.

10.3.3 Sagittarius B, C and D spectra

Four regions with high density of molecular gas are distinctly observed in Figure 10.6, and each of them can be related to a Sagittarius (Sgr) complex, the Sgr A ($l = 0.0^\circ$),

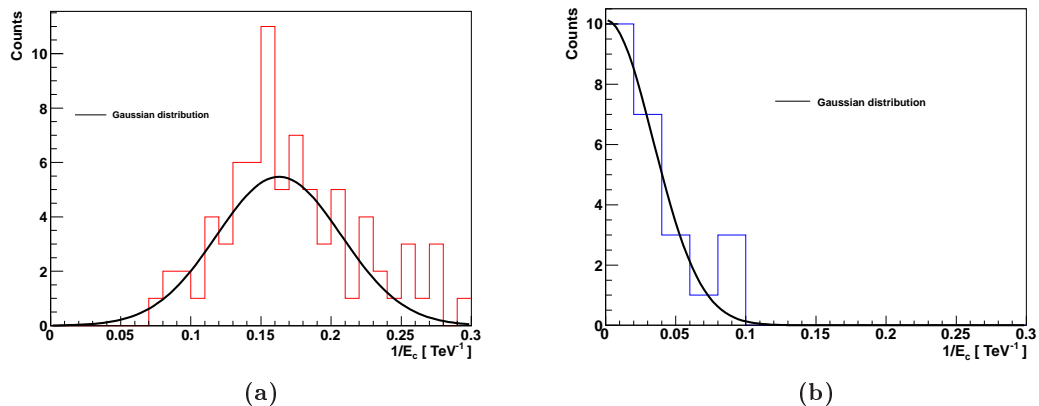


Figure 10.12: Histograms of the reconstructed energy cut-offs produced after air-showers simulations of a source emitting γ -rays with a primary spectrum following: (a) power-law with index 2.23; (b) a power-law with spectral index 2.23 and exponential energy cut-off at 6 TeV.

Sgr B ($l = 0.4^\circ$), Sgr C ($l = -0.6^\circ$) and Sgr D ($l = 1.2^\circ$) complexes (see chapter 9 for details). The γ -ray emission of the Sgr A complex is completely dominated by the central source emission, and the treatment of the foreground from the diffuse emission was done previously in this chapter. Analysis of the other regions, which are called here B, C and D for the complex of the same name, are performed in order to extract the γ -ray energy spectrum. The Model++ analysis with *standard cuts* for the events selection, and the ring-background technique for background estimation are used. The chosen positions are detailed in Table 10.6 as well as the γ -ray events excess and significance. An opening angle of observation is fixed at 0.2° in order to increase statistics for the spectral reconstruction. The energy spectra are well described by a power-law distributions. The best-fit spectral parameters are summarized in Table 10.6. The power-law indexes measured in these regions are again much softer than the HESS J1745-290 spectral index. For instance, a deviation at more than 3σ , considering statistical and systematic errors, is found between the region C and the HESS J1745-290 measured spectral indexes.

10.4 Summary and conclusion

The new analysis of the Galactic Center region, using the whole H.E.S.S. dataset from 2004 to 2011, was presented in this chapter. The energy spectrum of the central HESS

10. Analysis of the VHE diffuse emission in the Galactic Center region

Region	l [deg]	b [deg]	Excess	Significance	Γ
Region B	+0.4	-0.07	2283	23.9	2.54 ± 0.06
Region C	-0.6	-0.14	1857	20.55	2.66 ± 0.08
Region D	+1.2	-0.06	1591	17.3	2.54 ± 0.08

Table 10.6: Diffuse regions observation parameters. The first three columns defines the regions and the position of their center in galactic coordinates. The signal is integrated inside a radius of 0.2° around the center. The fourth and fifth columns give the γ -ray excess and excess significance. The final column presents the best-fit power-law spectral index in each region, with their respective statistical errors.

J1745-290 still shows a clear deviation from pure power-law, with an energy cut-off at $(6.35 \pm 1.10_{\text{stat}} \pm 1.00_{\text{syst}})$ TeV. The energy spectrum of the diffuse emission around the central source was found to follow a power-law distribution with an spectral index of $(2.53 \pm 0.04_{\text{stat}} \pm 0.10_{\text{syst}})$. The foreground contribution of the diffuse emission to the central source is determined based on a diffuse model, which is found to account for 27 ± 5 % of the total signal of HESS J1745-290. The intrinsic spectrum of the central source is found after a spectral subtraction of the diffuse component under the HESS J1745-290 signal, revealing a stronger energy cut-off at energies around 10 TeV. Additionally γ -rays from the diffuse emission are predicted to dominate the full HESS J1745-290 spectrum at energies above ~ 20 TeV.

The spectral morphology study of the diffuse emission showed the evolution of the energy spectrum with the distance to the central GC source. With the help of Monte Carlo simulations of air showers to test the systematical uncertainties of the spectral reconstruction method, it was possible to confirm that the energy cut-off on the spectrum of the γ -ray emission vanishes when moving away from the central source. The cut-off should thus come from an intrinsic acceleration mechanism of the central emitter. Moreover specific regions in the whole diffuse emission region were selected and their energy spectrum were calculated.

The high correlation between the observed γ -ray diffuse emission and dense molecular regions leave no question about the role of these molecular clouds as target for energetic CRs propagating in the GC region. On the other hand the source which accelerates these CRs remains unknown. The fact that the power-law index of HESS J1745-290 is significantly different from the indexes in some of the diffuse regions ana-

lyzed here, in particular the region C where a much softer spectrum is found, suggests that maybe different accelerators are generating the observed emission. Additionally, the diffuse emission models may not well reproduce the observed emission at Sgr D region. However further investigation is still needed in order to treat these regions as independent sources. A detailed analysis of their spatial morphology as well as new observations from the upcoming H.E.S.S. 2 array will bring new light upon this matter.

10. Analysis of the VHE diffuse emission in the Galactic Center region

General conclusion

In this work detailed studies on indirect searches of dark matter through VHE γ -rays towards dwarf galaxies and galaxy clusters, and the analysis of the Galactic Center at VHE γ -rays with the H.E.S.S. telescope were presented.

The first subject of study of this thesis was the search for signals of DM annihilations in the H.E.S.S. data, and the estimation of the sensitivity of the future generation of IACTs to such a signal. Interdependent constraints on several DM properties, such as the DM particle mass and annihilation cross section were obtained after the H.E.S.S. observations of the Sculptor and Carina dwarf galaxies, and later on the Fornax galaxy cluster. Particular consideration was given to possible enhancements of the expected γ -ray flux which could be caused by DM halo substructure, the Sommerfeld effect or additional contributions to the DM particles annihilation spectra. The sensitivity of the future generation of IACTs, *i.e.* CTA (Cherenkov Telescope Array), towards the tidal disrupted Sagittarius dwarf galaxy, the Sculptor dwarf galaxy, and the ultra-faint dwarf galaxy Segue 1 were calculated. CTA will improve by a factor of ten the sensitivity to a DM annihilation signal in the TeV particle mass range, when compared to current experiments. For lower DM particle masses, below 100 GeV, the data of the currently operating Fermi satellite [40] will improve the existing limits proportionally to the squared-root of the observation time. Complementarity between these two experiments will be of the utmost importance for the searches of a DM annihilation signal.

A problem which is inherent to indirect DM searches is the systematic uncertainties coming from the DM haloes modelling. Throughout this work a particular effort was made to properly consider a large class of DM haloes which can well describe the DM distribution within galaxies and galaxy cluster. In the case of the Sculptor dwarf galaxy, different globular clusters populations were used to derive the DM halo profiles,

and several different assumptions on the DM halo properties were made, for example assuming cored profiles, or different anisotropy parameters. The tidal streams of the Sagittarius dwarf galaxy were used to trace back its evolution history, providing a robust estimation of its DM halo profile and content. Finally, multiple populations of dynamical tracers were used to derive the DM halo profile in Fornax galaxy cluster. All these different methods allowed to better constraint the uncertainty in the expected signal, due to the DM halo modelling in these objects.

The second subject of this thesis provided a detailed analysis of the VHE γ -ray data from the Galactic Center region observed by H.E.S.S. This was possible thanks to the deep exposure of this region, achieved by the H.E.S.S. experiment throughout the last 8 years. The signal measured by H.E.S.S. in the direction of the Galactic Center indicates that at least one particle accelerator is present in that region. Although there exist astrophysical objects which can explain such emission, such as the SMBH Sgr A* or the SNR Sgr A East, the exact underlying astrophysical emitter is still under debate. In order to better understand the astrophysical processes ongoing in the Galactic Center region, a detailed analysis of the energy spectral distribution of this region is crucial. The spectrum of the central HESS J1745-290 source follows a power-law distribution with an exponential energy cut-off around 6 TeV, and a surrounding diffuse emission is surely contaminating this signal. The diffuse emission is assumed to originate from interactions of highly energetic hadrons, which were accelerated at a central source and subsequently diffused to the ambient medium, with the matter bound in local GMCs. The H.E.S.S. observations allow the first measurement where the propagation of CRs can be directly observed. The diffuse emission energy spectrum close to the central source (radial distance $\lesssim 60$ pc) is for the first time calculated, and subtracted from the HESS J1745-290 energy spectrum. The central source intrinsic spectrum is derived for the first time. Finally the spectral morphology analysis of the whole diffuse region suggests that maybe various accelerators are generating the observed emission. A further detailed analysis of their spatial morphology as well as new observation from the upcoming H.E.S.S. 2 array are expected to shine new light upon this subject.

List of Figures

1.1	Shell-type supernova remnants RXJ1713.7-3946 and RXJ0852.0-4622 . . .	12
1.2	Crab nebula emission model	14
2.1	Schematic view of satellites detector and the Fermi-LAT instrument . . .	19
2.2	Comparison between shower shapes induced by a γ -ray and by a proton	24
2.3	Illustration of the imaging principle used in IACTs	26
2.4	Examples of air showers images observed in the H.E.S.S. cameras	27
2.5	Artistic view of the Cherenkov Telescope Array (CTA)	29
2.6	Sensitivity, given in $E \times F$, as function of the energy of current and future IACTs, compared with satellite telescopes and EAS arrays	30
3.1	Aerial view of the H.E.S.S. telescope array	33
3.2	H.E.S.S. telescope structure and mirrors arrangement	34
3.3	H.E.S.S. point spread function	35
3.4	Mechanics of the H.E.S.S. camera	36
3.5	H.E.S.S. cameras drawer	37
3.6	Illustration of the Hillas parameters	41
3.7	Distributions of mean reduced scaled width and mean reduced scale length parameters	42
3.8	Distribution of Shower Goodness of PKS 2155-304 compared with a simulation of γ -rays	46
3.9	θ^2 distribution of PKS 2155-3042	47
3.10	Illustration of the radial acceptance calculation method	49
3.11	Schematic illustration of the exposition map calculation	50
3.12	Schematic illustration of the bi-dimensional acceptance map calculation	51

LIST OF FIGURES

3.13	OFF regions definitions for the residual hadronic background estimate . . .	52
3.14	Illustration of the template background geometry	53
3.15	H.E.S.S. effective areas as function of the energy	56
3.16	Energy resolution and bias as function of energy for Model and Hillas based analysis	57
4.1	Contours at 68.3%, 95.5% and 99.7% confidence levels in the $(\Omega_m, \Omega_\Lambda)$ plane	69
4.2	Rotational curve of the NGC6503 galaxy, broken down to its individual components	71
4.3	Chandra X-ray and Hubble optical images of Abell 2390 and MS2137.3-2353	72
4.4	Composite image of the Bullet cluster (1E 0657-56)	73
4.5	The abundances of ^4He , D, ^3He , and $7\text{Li}^7\text{Li}$ as predicted by the Big-Bang nucleosynthesis	75
4.6	Observed cosmic microwave background (CMB) temperature power spectrum	76
4.7	Projected DM density-square maps of the simulated Milky Way-size halo Via Lactea-1	77
4.8	DM density distribution of the MW normalized to the local DM density	79
4.9	Projected velocity dispersion profiles for eight bright dwarf spheroidal galaxies	81
4.10	Radial mass profile of M87	83
4.11	Standard Model particles and their superpartners in the MSSM	87
4.12	Representation of different Kaluza-Klein states	88
4.13	LKP effective annihilation cross section $\sigma_{eff}v$ as a function of the mass splitting Δ_{q_1} between the LKP and the next LKP	89
5.1	The current status of searches for dark matter using high-energy neutrinos	93
5.2	Cosmic positron flux measured by PAMELA and e^+e^- flux measured by ATIC, Fermi, and other experiments	94
5.3	Concentration parameter c as function of the virial mass M_{vir}	100
5.4	Photon spectra for 1 TeV dark matter particles self-annihilating in different channels	107

5.5	Diagrams that contribute to the first order QED corrections to WIMP annihilations into a pair of charged particle final states	108
5.6	γ -ray spectrum for 1 TeV wino	109
5.7	Comparison between the time scales for the energy losses due to various mechanisms	111
5.8	Ladder diagram giving rise to the Sommerfeld enhancement for DM particle	112
5.9	Sommerfeld effect dependence with respect to several parameters	113
6.1	Significance maps of Sculptor and Carina dSphs	121
6.2	95% C.L. upper limits on the γ -ray fluxes of Carina and Sculptor for DM annihilation spectra	124
6.3	Upper limit at 95% C.L. of $\langle\sigma v\rangle$ as function of the DM particle mass for different DM halos of Sculptor dSph	128
6.4	Upper limit at 95% C.L. of $\langle\sigma v\rangle$ as function of the DM particle mass for different DM halos of Carina dSph	129
6.5	Upper limit at 95% C.L. of $\langle\sigma v\rangle$ as function of the Kaluza-Klein DM particle mass for all DM profiles of Sculptor	130
6.6	Upper limit at 95% C.L. on $\langle\sigma v\rangle/S$ as function of the DM particle mass enhanced by the Sommerfeld effect for Sculptor	131
6.7	Upper limit at 95% C.L. on $\langle\sigma v\rangle/S$ as function of the DM particle mass enhanced by the Sommerfeld effect for Carina	132
6.8	Upper limit at 95% C.L. on $\langle\sigma v\rangle/S$ as function of the DM particle mass enhanced by the Sommerfeld effect and the internal Bremsstrahlung for a NFW profile of Sculptor	133
6.9	Summary of relevant constraints on the DM annihilation cross section with H.E.S.S., VERITAS and MAGIC, and the Fermi-LAT	135
7.1	CTA effective area as function of the energy	139
7.2	Upper limit at 95% C.L. of $\langle\sigma v\rangle$ as function of the DM particle mass for different DM halos of SgrDw	144
7.3	Sensitivity at 95% C.L. for CTA on $\langle\sigma v\rangle$ versus the DM mass for different DM halos of SgrDw	145
7.4	Projected upper limits at 95% C.L. on $\langle\sigma v\rangle/S$ versus the DM mass enhanced by the IB and SE for the NFW profile of SgrDw	146

LIST OF FIGURES

7.5	Sensitivity at 95% C.L. for CTA on $\langle\sigma v\rangle/S$ versus the DM mass enhanced by the IB and SE for the ISO profile of SgrDw	147
7.6	Predicted number of MSPs versus stellar encounter rate	149
7.7	CTA sensitivities on $\langle\sigma v\rangle$ as a function of the DM mass for 100 hours observation of Sculptor	152
7.8	CTA sensitivities on $\langle\sigma v\rangle$ as a function of the DM mass for 100 hours observation towards Sculptor, Ursa Minor and Segue 1	153
8.1	\bar{J} as function of the integration angle for all the DM halo models of Fornax	161
8.2	DM annihilation luminosity as function of the radius for all DM halo models of Fornax	163
8.3	Substructure γ -ray flux enhancement as function of the opening angle of integration for the RB02 DM halo profile of Fornax	163
8.4	Substructure γ -ray flux enhancement for all the DM halo models of Fornax	164
8.5	Significance map and distribution of H.E.S.S. observations of Fornax . . .	167
8.6	Upper limits 95% C.L. on the γ -ray flux as a function of the DM particle mass from the direction of Fornax	169
8.7	Upper limit at 95% C.L. on $\langle\sigma v\rangle$ as a function of the DM particle mass for all DM halo models of Fornax	170
8.8	Upper limit at 95% C.L. on $\langle\sigma v\rangle$ as function of the Kaluza-Klein particle $\tilde{B}^{(1)}$ mass towards Fornax	171
8.9	Upper limit at 95% C.L. on $\langle\sigma v\rangle$ as function of the DM particle mass for different DM particle models	172
8.10	Upper limits at 95% C.L. on the effective annihilation cross section $\langle\sigma v\rangle_{\text{eff}} = \langle\sigma v\rangle_0/S$ as a function of the DM particle mass enhanced by the Sommerfeld effect	174
8.11	Upper limit at 95% C.L. on $\langle\sigma v\rangle$ as function of the DM particle mass enhanced by DM halo substructures	175
9.1	The galactic center region as observed by VLA at 90cm	181
9.2	Galactic Center view in X-rays by Chandra and XMM-Newton	184
9.3	Galactic Center view by Suzaku in X-rays	185
9.4	Galactic Center view by INTEGRAL in hard X-rays	187
9.5	Velocity-integrated CS J = 1-0 emission in the Galactic center region . .	188

9.6 Schematic diagram showing the sky locations and rough sizes and shapes of Galactic center sources	189
9.7 VLT infrared image and density profile of the central stellar cluster	190
9.8 Sgr A East images in radio and X-ray, and Sgr West image in radio	192
9.9 The immediate vicinity of Sgr A* in radio superposed by X-ray contours showing the pulsar G359.95-0.04	193
9.10 Stellar orbits and mass distribution as function of the radius around Sgr A*	195
9.11 A composite spectral energy distribution of the Galactic Center source	196
9.12 VHE γ -ray images of the GC region	199
9.13 Position and spectrum of the VHE γ -ray source HESS J1745-290	200
9.14 Sgr B region γ -ray spectrum compared with HESS J1745-290 and diffuse model spectra	202
10.1 Excess map and θ^2 -distribution centered on HESS J1745-290	206
10.2 HESS J1745-290 spectrum derived with the dataset from 2004 to 2011	209
10.3 Angular distribution of γ -rays plotted as function of θ^2 : linear diffuse component superposed to HESS J1745-290	210
10.4 Test region to extract the γ -ray diffuse emission spectrum	210
10.5 Diffuse emission spectrum	211
10.6 A map of molecular clouds in the galactic center region	213
10.7 γ -ray count map for diffusion model	214
10.8 Angular distribution of γ -rays plotted as function of θ^2 : diffuse model superposed to HESS J1745-290	215
10.9 Final spectrum of the central VHE γ -ray source after the subtraction of the diffuse foreground component	216
10.10 γ -ray events from the Galactic Center central source with $E \geq 20$ TeV	216
10.11 Concentric annular regions centered on Sgr A*	218
10.12 Histograms of the reconstructed energy cut-offs produced after air-showers simulations with two spectra hypothesis : power-law and power-law with energy cut-off	221

LIST OF FIGURES

List of Tables

2.1	Performances comparison between EGRET and Fermi-LAT	20
2.2	Comparative table of IACTs	29
3.1	Main sources of systematic errors and their value for the reconstruction of the spectral index and fluxes.	61
4.1	Most recent set of cosmological parameters	68
4.2	Branching ratios of the different annihilation channels of the $\tilde{B}^{(1)}$ particle.	88
6.1	Coordinates for the Sculptor and Carina dSphs	119
6.2	Table of Sculptor and Carina H.E.S.S. observation characteristics	120
6.3	95% C.L. upper limits on the γ -ray fluxes of Carina and Sculptor for power-law spectra	123
6.4	Structural DM halo parameters of the eight best fits for Sculptor dSph	126
6.5	Structural DM halo parameters of the two best fits for Carina dSph	127
7.1	Values of \bar{J} for different solid angles and DM halo profiles of Sagittarius dwarf galaxy	142
7.2	Astrophysical factors \bar{J} for Sculptor and Segue 1	151
8.1	Characteristics of the galaxy clusters observed by H.E.S.S. : Fornax, Coma and Virgo	158
8.2	Dark matter halo models for the Fornax galaxy cluster : Parameters and \bar{J}	160
8.3	Dark matter halo models for the Fornax galaxy cluster : Tracers, method and virial radius/mass	162

LIST OF TABLES

8.4	Substructures enhancement to the DM flux for different opening angles of integration and M_{lim}	162
8.5	Numbers of VHE N_{ON} and \bar{N}_{OFF} γ -ray events from the direction of the Fornax galaxy cluster center	166
8.6	Upper limits on the VHE γ -ray flux from the direction of Fornax, assuming power-law spectra	168
10.1	Details on the H.E.S.S. observation campaigns towards the Galactic Center over the years	205
10.2	Values of the spectral parameters of the HESS J1745-290 energy spectrum with different datasets	208
10.3	Highest γ -ray events from the Galactic Center	217
10.4	Best-fit parameters for a power-law from the analyses of the set of annular region around Sgr A*	219
10.5	Best-fit parameters for a power-law with exponential cut-off from the analyses of the set of annular region around Sgr A*	219
10.6	Diffuse regions observation parameters	222

References

- [1] V. Hess, “Über Beobachtungen der durchdringenden Strahlung bei sieben Freiballonfahrten,” *Physikalische Zeitschrift*, vol. 13, pp. 1084–1091, 1912. [4](#)
- [2] M. S. Longair, “*High Energy Astrophysics: Volume 1, Particles, Photons and their Detection*”. Cambridge University Press, 1992. [5](#), [6](#), [110](#)
- [3] E. Fermi, *Physical Review*, vol. 75, pp. 1169–1174, Apr. 1949. [5](#)
- [4] G. Krimsky, *Sov. Phys. Dokl.*, vol. 23, p. 327, 1977. [6](#)
- [5] A. R. Bell, *MNRAS*, vol. 182, pp. 147–156, Jan. 1978. [6](#)
- [6] W. I. Axford, E. Leer, and G. Skadron, in *International Cosmic Ray Conference*, ser. International Cosmic Ray Conference, vol. 11, 1977, pp. 132–137. [6](#)
- [7] R. D. Blandford and J. P. Ostriker, *ApJ*, vol. 221, pp. L29–L32, Apr. 1978. [6](#)
- [8] V. L. Ginzburg and S. I. Syrovatskii, *ARA&A*, vol. 3, p. 297, 1965. [7](#)
- [9] F. A. Aharonian, *Very high energy cosmic gamma radiation : a crucial window on the extreme Universe*, 2004. [7](#), [9](#), [11](#), [182](#)
- [10] G. R. Blumenthal and R. J. Gould, *Reviews of Modern Physics*, vol. 42, pp. 237–271, 1970. [8](#), [9](#)
- [11] G. W. Clark, G. P. Garmire, and W. L. Kraushaar, *ApJ*, vol. 153, p. L203, Sep. 1968. [10](#)
- [12] *WHIPPLE* : <http://veritas.sao.arizona.edu/whipple-10m-topmenu-117>, 2012. [10](#), [28](#)

REFERENCES

- [13] P. L. Nolan *et al.*, *ApJS*, vol. 199, p. 31, Apr. 2012. [10](#), [20](#)
- [14] *TeVCat* : <http://tevcad.uchicago.edu/>, 2012. [10](#)
- [15] F. Aharonian *et al.*, *A&A*, vol. 449, pp. 223–242, Apr. 2006. [11](#), [12](#)
- [16] ———, *A&A*, vol. 437, pp. L7–L10, Jul. 2005. [11](#), [12](#)
- [17] F. Acero *et al.*, *A&A*, vol. 516, p. A62, Jun. 2010. [11](#)
- [18] E. VERITAS Collaboration, Aliu *et al.*, *Science*, vol. 334, pp. 69–, Oct. 2011. [13](#)
- [19] J. Aleksić *et al.*, *A&A*, vol. 540, p. A69, Apr. 2012. [13](#)
- [20] A. A. Abdo *et al.*, “(Fermi-LAT Collaboration),” *A&A*, vol. 524, pp. A75+, Dec. 2010. [13](#), [147](#), [148](#), [149](#)
- [21] W. Bednarek and J. Sitarek, *MNRAS*, vol. 377, p. 920, May 2007. [13](#), [148](#)
- [22] C. Venter, O. C. De Jager, and A. Clapson, *ApJ*, vol. 696, p. L52, May 2009. [13](#), [148](#)
- [23] K. S. Cheng *et al.*, *ApJ*, vol. 723, p. 1219, Nov. 2010. [13](#), [148](#)
- [24] A. Abramowski *et al.*, *A&A*, vol. 531, p. L18, Jul. 2011. [13](#)
- [25] R. Buehler *et al.*, *ApJ*, vol. 749, p. 26, Apr. 2012. [13](#)
- [26] D. Horns and F. A. Aharonian, in *5th INTEGRAL Workshop on the INTEGRAL Universe*, ser. ESA Special Publication, V. Schoenfelder, G. Lichti, and C. Winkler, Eds., vol. 552, Oct. 2004, p. 439. [13](#), [14](#)
- [27] F. Aharonian *et al.*, *Science*, vol. 309, pp. 746–749, Jul. 2005. [14](#)
- [28] A. A. Abdo *et al.*, *ApJ*, vol. 706, pp. L56–L61, Nov. 2009. [15](#)
- [29] J. Albert *et al.*, *Science*, vol. 312, pp. 1771–1773, Jun. 2006. [15](#)
- [30] F. Aharonian *et al.*, *A&A*, vol. 442, pp. 1–10, Oct. 2005. [15](#)
- [31] F. A. Aharonian *et al.*, *A&A*, vol. 469, pp. L1–L4, Jul. 2007. [15](#)

-
- [32] F. Aharonian *et al.*, “(H.E.S.S. Collaboration),” *Science*, vol. 314, p. 1424, Dec. 2006. [15](#), [156](#), [157](#)
- [33] ———, *A&A*, vol. 430, pp. 865–875, Feb. 2005. [15](#)
- [34] A. Abramowski *et al.*, *ApJ*, vol. 746, p. 151, Feb. 2012. [15](#)
- [35] G. Vedrenne and J.-L. Atteia, *Gamma-Ray Bursts*, 2009. [15](#), [16](#)
- [36] L. Piro *et al.*, *A&A*, vol. 329, pp. 906–910, Jan. 1998. [16](#)
- [37] A. A. e. a. Abdo, *Nature*, vol. 462, pp. 331–334, Nov. 2009. [16](#)
- [38] A. A. Abdo *et al.*, *ApJ*, vol. 706, pp. L138–L144, Nov. 2009. [16](#)
- [39] *EGRET* : <http://heasarc.gsfc.nasa.gov/docs/cgro/egret/>, 2012. [18](#), [20](#)
- [40] *Fermi* : <http://fermi.gsfc.nasa.gov/>, 2012. [18](#), [19](#), [20](#), [225](#)
- [41] *AMS-02* : <http://www.ams02.org/>, 2012. [18](#)
- [42] A. A. Abdo *et al.*, *ApJS*, vol. 188, pp. 405–436, Jun. 2010. [20](#)
- [43] *ARGO-YBJ* : <http://argo.na.infn.it/>, 2012. [25](#)
- [44] *Milagro* : <http://www.lanl.gov/milagro/>, 2012. [25](#)
- [45] *HAWC* : <http://hawc.umd.edu/>, 2012. [25](#)
- [46] *LHAASO* : <http://english.ihep.cas.cn/ic/ip/LHAASO/>, 2012. [25](#)
- [47] S. Hoppe, Ph.D. dissertation, Ruperto-Carola Univ. of Heidelberg, Germany, 2008. [26](#), [54](#)
- [48] M. Vivier, Ph.D. dissertation, Univ. Paris XI, France, 2009. [27](#), [52](#), [56](#), [207](#)
- [49] *HEGRA* : <http://www.mpi-hd.mpg.de/hfm/CT/CT.html>, 2012. [28](#)
- [50] *H.E.S.S.* : <http://www.mpi-hd.mpg.de/hfm/HESS/>, 2012. [28](#), [32](#), [94](#)
- [51] *MAGIC* : <http://www.magic.mppmu.mpg.de/>, 2012. [28](#), [94](#)
- [52] *VERITAS* : <http://veritas.sao.arizona.edu/>, 2012. [28](#), [94](#)

REFERENCES

- [53] *CANGAROO-III* : <http://icrhp9.icrr.u-tokyo.ac.jp/>, 2012. 28
- [54] *The CTA Consortium*, 2010, [arXiv:1008.3703](https://arxiv.org/abs/1008.3703). 29, 138
- [55] *CAT* : <http://lppnp90.in2p3.fr/cat/>, 2012. 30
- [56] K. Bernlöhner *et al.*, *Astroparticle Physics*, vol. 20, p. 111, Nov. 2003. 34
- [57] J. Davies and E. Cotton, *J. Solar Energy Sci. and Eng.*, vol. 1, p. 16, 1957. 34
- [58] R. Cornils *et al.*, *Astroparticle Physics*, vol. 20, pp. 129–143, Nov. 2003. 34, 35
- [59] F. Acero *et al.*, *MNRAS*, vol. 402, pp. 1877–1882, Mar. 2010. 35, 198, 200
- [60] M. Punch and H.E.S.S. Collaboration, in *International Cosmic Ray Conference*, ser. International Cosmic Ray Conference, vol. 7, Aug. 2001, p. 2814. 35, 36
- [61] F. Aharonian *et al.*, *Astroparticle Physics*, vol. 22, pp. 109–125, Nov. 2004. 36, 37
- [62] S. Funk *et al.*, *Astroparticle Physics*, vol. 22, p. 285, Nov. 2004. 37
- [63] L. Rolland, Ph.D. dissertation, Univ. Paris 6, France, 2005. 39, 58, 61
- [64] D. Heck, J. Knapp, J. N. Capdevielle, G. Schatz, and T. Thouw, *CORSIKA: a Monte Carlo code to simulate extensive air showers.*, Feb. 1998. 40
- [65] M. P. Kertzman and G. H. Sembroski, *Nuclear Instruments and Methods in Physics Research A*, vol. 343, pp. 629–643, Apr. 1994. 40
- [66] J. Guy, Ph.D. dissertation, Univ. Paris 6, France, 2003. 40
- [67] A. M. Hillas, in *International Cosmic Ray Conference*, ser. International Cosmic Ray Conference, F. C. Jones, Ed., vol. 3, Aug. 1985, pp. 445–448. 40
- [68] F. Aharonian *et al.*, “(H.E.S.S. Collaboration),” *A&A*, vol. 457, p. 899, Oct. 2006. 42, 43, 159, 165
- [69] S. Le Bohec *et al.*, *Nuclear Instruments and Methods in Physics Research A*, vol. 416, pp. 425–437, Oct. 1998. 43
- [70] M. de Naurois and L. Rolland, *Astroparticle Physics*, vol. 32, p. 231, Dec. 2009. 43, 46, 47, 56, 57

-
- [71] D. Berge, S. Funk, and J. Hinton, *A&A*, vol. 466, pp. 1219–1229, May 2007. [53](#)
- [72] G. P. Rowell, *A&A*, vol. 410, p. 389, Oct. 2003. [54](#), [166](#)
- [73] T. Li and Y. Ma, *ApJ*, vol. 272, p. 317, Sep. 1983. [54](#), [121](#), [167](#)
- [74] G. J. Feldman and R. D. Cousins, *Phys. Rev. D*, vol. 57, p. 3873, Apr. 1998. [60](#), [115](#), [116](#), [121](#), [122](#), [166](#)
- [75] F. Zwicky, “Die Rotverschiebung von extragalaktischen Nebeln,” *Helvetica Physica Acta*, vol. 6, pp. 110–127, 1933. [66](#)
- [76] H. W. Babcock, *Lick Observatory Bulletin*, vol. 19, pp. 41–51, 1939. [66](#)
- [77] P. J. E. Peebles, *ApJ*, vol. 263, pp. L1–L5, Dec. 1982. [66](#)
- [78] L. Bergstrom, “Saas-Fee Lecture Notes: Multi-messenger Astronomy and Dark Matter,” *ArXiv e-prints*, Feb. 2012. [66](#)
- [79] C. Tao, in *EAS Publications Series*, ser. EAS Publications Series, F. Mayet and D. Santos, Eds., vol. 53, Feb. 2012, pp. 97–104. [66](#)
- [80] J. Beringer *et al.*, “(Particle Data Group),” *Phys.Rev.*, vol. D86, p. 010001, 2012. [67](#), [68](#), [73](#), [75](#), [84](#), [97](#)
- [81] E. W. Kolb and M. S. Turner, *The early universe.*, 1990. [68](#), [70](#)
- [82] A. R. Liddle and D. H. Lyth, Apr. 2000. [68](#)
- [83] E. Komatsu *et al.*, *ApJS*, vol. 192, p. 18, Feb. 2011. [68](#), [76](#)
- [84] N. Suzuki *et al.*, *ApJ*, vol. 746, p. 85, Feb. 2012. [68](#), [69](#)
- [85] L. Bergström, *New Journal of Physics*, vol. 11, no. 10, p. 105006, Oct. 2009. [69](#), [85](#), [86](#)
- [86] C. Boehm and J. Lesgourgues, “course on “Dark Matter and Dark Energy” given at EPFL in the frame of the Ecole Doctorale de Suisse Romande,” 2008. [70](#), [76](#)
- [87] K. G. Begeman, A. H. Broeils, and R. H. Sanders, *MNRAS*, vol. 249, pp. 523–537, Apr. 1991. [71](#)

REFERENCES

- [88] G. Bertone, D. Hooper, and J. Silk, *Phys. Rept.*, vol. 405, p. 279, 2005. [71](#), [72](#), [74](#), [78](#), [82](#), [84](#), [86](#), [87](#)
- [89] M. Milgrom, *ApJ*, vol. 270, pp. 371–389, Jul. 1983. [71](#)
- [90] J. A. Tyson, G. P. Kochanski, and I. P. dell’Antonio, *ApJ*, vol. 498, p. L107, May 1998. [72](#)
- [91] *Chandra* : <http://chandra.harvard.edu>, 2012. [73](#)
- [92] W. Hu and S. Dodelson, *ARA&A*, vol. 40, pp. 171–216, 2002. [75](#)
- [93] D. Larson *et al.*, *ApJS*, vol. 192, p. 16, Feb. 2011. [76](#)
- [94] C. L. Reichardt *et al.*, *ApJ*, vol. 694, pp. 1200–1219, Apr. 2009. [76](#)
- [95] M. L. Brown *et al.*, *ApJ*, vol. 705, pp. 978–999, Nov. 2009. [76](#)
- [96] C. W. Misner, *Nature*, vol. 214, pp. 40–41, Apr. 1967. [76](#)
- [97] P. J. E. Peebles, *ApJ*, vol. 142, p. 1317, Nov. 1965. [76](#)
- [98] J. Silk, *Nature*, vol. 215, pp. 1155–1156, Sep. 1967. [76](#)
- [99] —, *ApJ*, vol. 151, p. 459, Feb. 1968. [76](#)
- [100] V. Springel *et al.*, *MNRAS*, vol. 391, p. 1685, Dec. 2008. [77](#), [78](#), [104](#)
- [101] J. Diemand, M. Kuhlen, P. Madau, M. Zemp, B. Moore, D. Potter, and J. Stadel, *Nature*, vol. 454, p. 735, Aug. 2008. [77](#), [78](#)
- [102] W. J. G. de Blok, S. S. McGaugh, A. Bosma, and V. C. Rubin, *ApJ*, vol. 552, pp. L23–L26, May 2001. [78](#)
- [103] F. Governato *et al.*, *MNRAS*, vol. 422, pp. 1231–1240, May 2012. [78](#)
- [104] A. V. Macciò *et al.*, *ApJ*, vol. 744, p. L9, Jan. 2012. [78](#)
- [105] C. Hamadache *et al.*, *A&A*, vol. 454, pp. 185–199, Jul. 2006. [79](#)
- [106] P. Englmaier and O. Gerhard, *Celestial Mechanics and Dynamical Astronomy*, vol. 94, pp. 369–379, Apr. 2006. [79](#)

-
- [107] J. Bovy and S. Tremaine, *ArXiv e-prints*, May 2012. [80](#)
- [108] A. M. Ghez *et al.*, *ApJ*, vol. 620, pp. 744–757, Feb. 2005. [80](#), [194](#), [195](#)
- [109] R. Genzel *et al.*, *ApJ*, vol. 594, pp. 812–832, Sep. 2003. [80](#), [190](#)
- [110] R. Schödel, T. Ott, R. Genzel, A. Eckart, N. Mouawad, and T. Alexander, *ApJ*, vol. 596, pp. 1015–1034, Oct. 2003. [80](#), [180](#), [195](#)
- [111] P. J. E. Peebles, *General Relativity and Gravitation*, vol. 3, pp. 63–82, Jun. 1972. [80](#)
- [112] P. Young, *ApJ*, vol. 242, pp. 1232–1237, Dec. 1980. [80](#)
- [113] P. Gondolo and J. Silk, *Physical Review Letters*, vol. 83, pp. 1719–1722, Aug. 1999. [80](#)
- [114] V. Belokurov *et al.*, *Astrophys. J.*, vol. 642, pp. L137–L140, 2006. [80](#)
- [115] B. Willman and others., *AJ*, vol. 129, pp. 2692–2700, Jun. 2005. [80](#)
- [116] J. S. Bullock, *ArXiv e-prints*, Sep. 2010. [80](#)
- [117] G. Gilmore *et al.*, *ApJ*, vol. 663, p. 948, Jul. 2007. [81](#), [125](#), [127](#)
- [118] M. G. Walker *et al.*, *ApJ*, vol. 667, p. L53, Sep. 2007. [81](#), [99](#), [125](#), [127](#)
- [119] M. G. Walker, M. Mateo, E. W. Olszewski, J. Peñarrubia, N. Wyn Evans, and G. Gilmore, *ApJ*, vol. 704, pp. 1274–1287, Oct. 2009. [81](#)
- [120] A. J. Romanowsky and C. S. Kochanek, *ApJ*, vol. 553, pp. 722–732, Jun. 2001. [83](#)
- [121] S. Colafrancesco, S. Profumo, and P. Ullio, *A&A*, vol. 455, p. 21, Aug. 2006. [82](#), [97](#), [109](#), [111](#)
- [122] T. Richtler, Y. Schuberth, M. Hilker, B. Dirsch, L. Bassino, and A. J. Romanowsky, *A&A*, vol. 478, p. L23, Feb. 2008. [82](#), [97](#), [159](#)
- [123] Y. Schuberth, T. Richtler, M. Hilker, B. Dirsch, L. P. Bassino, A. J. Romanowsky, and L. Infante, *A&A*, vol. 513, p. A52, Apr. 2010. [82](#), [97](#), [99](#), [159](#), [170](#)

REFERENCES

- [124] G. M. Voit, *Reviews of Modern Physics*, vol. 77, p. 207, Apr. 2005. [82](#), [97](#), [100](#), [156](#)
- [125] D. J. Sand, T. Treu, and R. S. Ellis, *ApJ*, vol. 574, pp. L129–L133, Aug. 2002. [82](#)
- [126] A. El-Zant, I. Shlosman, and Y. Hoffman, *ApJ*, vol. 560, p. 636, Oct. 2001. [82](#)
- [127] J. Lesgourgues and S. Pastor, *Phys. Rep.*, vol. 429, pp. 307–379, Jul. 2006. [84](#)
- [128] S. Fukuda *et al.*, *Physical Review Letters*, vol. 85, pp. 3999–4003, Nov. 2000. [84](#)
- [129] V. N. Aseev *et al.*, *Phys. Rev. D*, vol. 84, no. 11, p. 112003, Dec. 2011. [84](#)
- [130] K. Eitel, *Nuclear Physics B Proceedings Supplements*, vol. 143, pp. 197–204, Jun. 2005. [84](#)
- [131] S. H. Hansen, J. Lesgourgues, S. Pastor, and J. Silk, *MNRAS*, vol. 333, pp. 544–546, Jul. 2002. [84](#)
- [132] A. H. Chamseddine, R. Arnowitt, and P. Nath, *Physical Review Letters*, vol. 49, pp. 970–974, Oct. 1982. [85](#)
- [133] N. Arkani-Hamed, S. Dimopoulos, and G. Dvali, *Physics Letters B*, vol. 429, pp. 263–272, Jun. 1998. [86](#)
- [134] L. Randall and R. Sundrum, *Physical Review Letters*, vol. 83, pp. 3370–3373, Oct. 1999. [86](#)
- [135] P. Brun, Ph.D. dissertation, Univ. de Savoie, France, 2007. [88](#)
- [136] G. Servant and T. M. P. Tait, *Nuclear Physics B*, vol. 650, p. 391, Feb. 2003. [87](#), [88](#), [89](#), [106](#), [126](#), [168](#)
- [137] H.-C. Cheng, K. T. Matchev, and M. Schmaltz, *Phys. Rev. D*, vol. 66, no. 3, p. 036005, Aug. 2002. [88](#)
- [138] S. Arrenberg, L. Baudis, K. Kong, K. T. Matchev, and J. Yoo, *Phys. Rev. D*, vol. 78, no. 5, p. 056002, Sep. 2008. [89](#), [168](#)
- [139] J. L. Feng, *ARA&A*, vol. 48, pp. 495–545, Sep. 2010. [92](#), [93](#)

-
- [140] R. Abbasi and et al., *Phys. Rev. D*, vol. 84, no. 2, p. 022004, Jul. 2011. [92](#), [93](#)
- [141] G. Bertone, *Particle Dark Matter : Observations, Models and Searches*. Cambridge University Press, 2010. [93](#)
- [142] J. Braun, D. Hubert, and for the IceCube Collaboration, *ArXiv e-prints*, Jun. 2009. [93](#)
- [143] O. Adriani *et al.*, “(PAMELA Collaboration),” *Nature*, vol. 458, p. 607, 2009. [93](#), [172](#)
- [144] J. Chang, J. Adams, H. Ahn, G. Bashindzhagyan, M. Christl *et al.*, *Nature*, vol. 456, p. 362, 2008. [93](#), [172](#)
- [145] F. Aharonian *et al.*, “(H.E.S.S. Collaboration),” *Astron. Astrophys.*, vol. 508, p. 561, 2009. [93](#), [172](#)
- [146] M. Ackermann *et al.*, “(Fermi-LAT Collaboration),” *Phys. Rev.*, vol. D82, p. 092004, 2010. [93](#), [172](#)
- [147] A. E. Vladimirov, S. W. Digel, G. Jóhannesson, P. F. Michelson, I. V. Moskalenko, P. L. Nolan, E. Orlando, T. A. Porter, and A. W. Strong, *Computer Physics Communications*, vol. 182, pp. 1156–1161, May 2011. [93](#), [94](#)
- [148] A. Abramowski *et al.*, *ApJ*, vol. 750, p. 123, May 2012. [94](#), [156](#)
- [149] M. Cirelli, M. Kadastik, M. Raidal, and A. Strumia, *Nucl.Phys.*, vol. B813, p. 1, 2009. [94](#)
- [150] A. A. Abdo *et al.*, *Physical Review Letters*, vol. 102, no. 18, p. 181101, May 2009. [94](#)
- [151] J. Binney and S. Tremaine. Princeton University Press, 2008. [96](#), [101](#), [110](#)
- [152] J. F. Navarro, C. S. Frenk, and S. D. M. White, *ApJ*, vol. 462, p. 563, May 1996. [97](#)
- [153] A. Burkert, *IAU Symp.*, vol. 171, p. 175, 1996. [97](#)
- [154] Y. P. Jing and Y. Suto, *ApJ*, vol. 529, p. L69, Feb. 2000. [99](#), [125](#)

REFERENCES

- [155] A. Koch *et al.*, *ApJ*, vol. 657, p. 241, Mar. 2007. [99](#)
- [156] D. A. Buote *et al.*, *Astrophys. J.*, vol. 664, pp. 123–134, 2007. [99](#)
- [157] M. Cappellari *et al.*, *MNRAS*, vol. 366, pp. 1126–1150, Mar. 2006. [100](#), [101](#)
- [158] A. J. Romanowsky *et al.*, *Science*, vol. 301, pp. 1696–1698, Sep. 2003. [100](#)
- [159] M. Arnaboldi *et al.*, *ApJ*, vol. 614, pp. L33–L36, Oct. 2004. [100](#)
- [160] N. R. Napolitano *et al.*, *MNRAS*, vol. 393, pp. 329–353, Feb. 2009. [100](#)
- [161] G. Bertin *et al.*, *A&A*, vol. 292, pp. 381–391, Dec. 1994. [101](#)
- [162] A. van der Wel and R. P. van der Marel, *ApJ*, vol. 684, pp. 260–269, Sep. 2008. [101](#)
- [163] D. C. Jackson, E. D. Skillman, J. M. Cannon, and S. Côté, *AJ*, vol. 128, pp. 1219–1227, Sep. 2004. [101](#)
- [164] L. D. Matthews and J. M. Uson, *AJ*, vol. 135, pp. 291–318, Jan. 2008. [101](#)
- [165] T. G. Brainerd, R. D. Blandford, and I. Smail, *ApJ*, vol. 466, p. 623, Aug. 1996. [101](#)
- [166] L. C. Parker, H. Hoekstra, M. J. Hudson, L. van Waerbeke, and Y. Mellier, *ApJ*, vol. 669, pp. 21–31, Nov. 2007. [101](#)
- [167] J. Binney and G. A. Mamon, *MNRAS*, vol. 200, p. 361, Jul. 1982. [102](#)
- [168] L. P. Osipkov, *Pis ma Astronomicheskii Zhurnal*, vol. 5, p. 77, Feb. 1979. [102](#), [125](#)
- [169] D. Merritt, *AJ*, vol. 90, p. 1027, Jun. 1985. [102](#), [125](#)
- [170] J. H. An and N. W. Evans, *ApJ*, vol. 701, p. 1500, Aug. 2009. [103](#)
- [171] L. L. Watkins, N. W. Evans, and J. H. An, *MNRAS*, vol. 406, pp. 264–278, Jul. 2010. [103](#)
- [172] G. Battaglia, A. Helmi, E. Tolstoy, M. Irwin, V. Hill, and P. Jablonka, *ApJ*, vol. 681, pp. L13–L16, Jul. 2008. [103](#), [125](#), [126](#)

-
- [173] A. Pinzke, C. Pfrommer, and L. Bergström, *Physical Review Letters*, vol. 103, no. 18, p. 181302, Oct. 2009. [103](#), [104](#), [105](#), [156](#), [164](#)
- [174] T. Bringmann, *New Journal of Physics*, vol. 11, no. 10, p. 105027, Oct. 2009. [105](#)
- [175] J. Diemand, M. Kuhlen, and P. Madau, *ApJ*, vol. 649, p. 1, Sep. 2006. [105](#)
- [176] M. Cirelli, G. Corcella, A. Hektor, G. Hutsi, M. Kadastik *et al.*, *JCAP*, vol. 1103, p. 051, 2011. [106](#), [107](#), [110](#)
- [177] T. Sjöstrand *et al.*, *Computer Physics Communications*, vol. 135, p. 238, Apr. 2001. [106](#), [123](#), [124](#)
- [178] T. Bringmann, F. Calore, G. Vertongen, and C. Weniger, *Phys. Rev. D*, vol. 84, no. 10, p. 103525, Nov. 2011. [106](#)
- [179] T. Sjöstrand, S. Mrenna, and P. Skands, *Computer Physics Communications*, vol. 178, pp. 852–867, Jun. 2008. [107](#)
- [180] L. Bergström, T. Bringmann, M. Eriksson, and M. Gustafsson, *Physical Review Letters*, vol. 95, no. 24, p. 241301, Dec. 2005. [108](#)
- [181] T. Bringmann, L. Bergström, and J. Edsjö, *JHEP*, vol. 1, p. 49, Jan. 2008. [108](#), [131](#), [145](#)
- [182] T. Moroi and L. Randall, *Nuclear Physics B*, vol. 570, p. 455, Mar. 2000. [108](#), [130](#), [131](#), [132](#)
- [183] J. Hisano, S. Matsumoto, and M. M. Nojiri, *Physical Review Letters*, vol. 92, no. 3, p. 031303, Jan. 2004. [112](#)
- [184] M. Lattanzi and J. Silk, *Phys. Rev. D*, vol. 79, no. 8, p. 083523, Apr. 2009. [112](#), [113](#), [114](#), [144](#)
- [185] W. A. Rolke, A. M. Lopez, and J. Conrad, *Nucl. Instrum. Meth.*, vol. A551, pp. 493–503, 2005. [115](#), [116](#), [143](#), [166](#)
- [186] L. Bergström, P. Ullio, and J. H. Buckley, *Astropart. Phys.*, vol. 9, p. 137, Aug. 1998. [116](#), [122](#), [124](#), [126](#), [127](#), [143](#)

REFERENCES

- [187] F. Di Pierro *et al.*, in *Proceedings 32nd ICRC Beijing 2011*, 2011. [116](#)
- [188] M. L. Mateo, *ARA&A*, vol. 36, p. 435, 1998. [118](#), [119](#), [140](#), [141](#), [144](#)
- [189] F. Aharonian *et al.*, “(H.E.S.S. Collaboration),” *Nature*, vol. 439, p. 695, Feb. 2006. [118](#), [199](#), [200](#), [201](#), [202](#), [212](#), [213](#), [214](#)
- [190] ———, “(H.E.S.S. Collaboration),” *Astropart. Phys.*, vol. 29, p. 55, Feb. 2008, erratum-ibid: (2010) 33, 274. [118](#), [138](#), [143](#), [152](#)
- [191] ———, “(H.E.S.S. Collaboration),” *Astropart. Phys.*, vol. 33, p. 274, May 2010. [118](#)
- [192] ———, “(H.E.S.S. Collaboration),” *ApJ*, vol. 691, p. 175, Jan. 2009. [118](#)
- [193] H. Shapley, *Harvard College Observatory Bulletin*, vol. 908, p. 1, Mar. 1938. [118](#)
- [194] R. D. Cannon, T. G. Hawarden, and S. B. Tritton, *MNRAS*, vol. 180, p. 81P, Sep. 1977. [118](#)
- [195] S. Piatek *et al.*, *AJ*, vol. 126, p. 2346, Nov. 2003. [118](#)
- [196] ———, *AJ*, vol. 131, p. 1445, Mar. 2006. [118](#)
- [197] A. Abramowski *et al.*, “(H.E.S.S. Collaboration),” *Astropart. Phys.*, vol. 34, p. 608, 2011. [118](#), [134](#)
- [198] W. B. Atwood *et al.*, “(Fermi-LAT Collaboration),” *ApJ*, vol. 697, p. 1071, Jun. 2009. [119](#)
- [199] A. A. Abdo *et al.*, “(Fermi-LAT Collaboration),” *ApJ*, vol. 712, p. 147, Mar. 2010. [119](#), [123](#), [124](#), [127](#), [128](#), [134](#)
- [200] F. Aharonian, J. Buckley, T. Kifune, and G. Sinnis, *Reports on Progress in Physics*, vol. 71, no. 9, p. 096901, Sep. 2008. [122](#)
- [201] G. Battaglia, Ph.D. dissertation, Univ. Groningen, The Netherlands, 2007. [125](#)
- [202] M. I. Wilkinson, *Private Communication*, 2010. [125](#)
- [203] S. R. Majewski *et al.*, *AJ*, vol. 130, p. 2677, Dec. 2005. [126](#)
- [204] R. R. Muñoz *et al.*, *ApJ*, vol. 649, p. 201, Sep. 2006. [126](#)

-
- [205] G. Jungman, M. Kamionkowski, and K. Griest, *Phys. Rep.*, vol. 267, p. 195, Mar. 1996. [131](#)
- [206] E. Komatsu *et al.*, *arXiv:1001.4538*, Jan. 2010. [Online]. Available: <http://arxiv.org/abs/1001.4538> [134](#)
- [207] J. Albert *et al.*, “(MAGIC Collaboration),” *Astrophys. J.*, vol. 679, p. 428, 2008. [134](#)
- [208] V. A. Acciari *et al.*, “(VERITAS Collaboration),” *ApJ*, vol. 720, p. 1174, 2010. [134](#)
- [209] C. de los Heros, *arXiv:1012.0184*, 2010. [134](#)
- [210] M. Ackermann *et al.*, *Physical Review Letters*, vol. 107, no. 24, p. 241302, Dec. 2011. [134](#)
- [211] A. Geringer-Sameth and S. M. Koushiappas, *Physical Review Letters*, vol. 107, no. 24, p. 241303, Dec. 2011. [134](#)
- [212] M. Doro *et al.*, *ArXiv e-prints*, Aug. 2012. [135](#), [152](#), [153](#)
- [213] A. Abramowski *et al.*, *Physical Review Letters*, vol. 106, no. 16, p. 161301, Apr. 2011. [135](#)
- [214] V. Belokurov *et al.*, *ApJ*, vol. 654, pp. 897–906, Jan. 2007. [136](#), [150](#)
- [215] A. Viana *et al.*, *ApJ*, vol. 746, p. 77, Feb. 2012. [138](#), [150](#)
- [216] N. W. Evans, F. Ferrer, and S. Sarkar, *Phys. Rev. D*, vol. 69, no. 12, p. 123501, Jun. 2004. [138](#), [143](#), [152](#)
- [217] R. Ibata *et al.*, *ApJ*, vol. 699, p. L169, Jul. 2009. [138](#), [140](#), [148](#), [150](#)
- [218] M. Paz Arribas, *Master thesis, Humbolt University Berlin*, 2008. [139](#)
- [219] J. Peñarrubia, J. F. Navarro, and A. W. McConnachie, *ApJ*, vol. 673, pp. 226–240, Jan. 2008. [140](#), [141](#)
- [220] B. Yanny *et al.*, *ApJ*, vol. 540, p. 825, 2000. [140](#)

REFERENCES

- [221] A. K. Vivas *et al.*, *ApJ*, vol. 554, p. L33, 2001. [140](#)
- [222] L. Watkins *et al.*, *MNRAS*, vol. 398, p. 1757, 2009. [140](#)
- [223] S. Majewski *et al.*, *Astron. J.*, vol. 118, p. 1709, 1999. [140](#)
- [224] D. Martinez-Delgado, A. Aparicio, M. A. G. Flechoso, and R. Carrera, *ApJ*, vol. 549, p. L199, 2001. [140](#)
- [225] H. J. Newberg *et al.*, *ApJ*, vol. 569, p. 245, 2002. [140](#)
- [226] S. R. Majewski, M. Skrutskie, M. D. Weinberg, and J. C. Ostheimer, *ApJ*, vol. 599, p. 1082, 2003. [140](#)
- [227] M. Niederste-Ostholt, V. Belokurov, N. W. Evans, and J. Peñarrubia, *ApJ*, vol. 712, p. 516, 2010. [140](#), [141](#)
- [228] J. Peñarrubia *et al.*, *MNRAS*, vol. 408, p. L26, Oct. 2010. [140](#), [141](#)
- [229] R. Ibata, G. Gilmore, and M. Irwin, *Nature*, vol. 370, p. 194, 1994. [140](#)
- [230] J. Peñarrubia, A. W. McConnachie, and J. F. Navarro, *ApJ*, vol. 672, pp. 904–913, Jan. 2008. [140](#), [141](#), [142](#)
- [231] M. Fellhauer *et al.*, *New A*, vol. 5, pp. 305–326, Sep. 2000. [141](#)
- [232] J. S. Bullock *et al.*, *MNRAS*, vol. 321, p. 559, Mar. 2001. [142](#)
- [233] L. Bergström, *Phys. Lett. B*, vol. 225, p. 372, Jul. 1989. [145](#)
- [234] B. Lanzoni *et al.*, *ApJ*, vol. 668, p. L139, Oct. 2007. [148](#)
- [235] E. Noyola, K. Gebhardt, and M. Bergmann, *ApJ*, vol. 676, p. 1008, Apr. 2008. [148](#)
- [236] M. Bellazzini *et al.*, *AJ*, vol. 136, p. 1147, Sep. 2008. [148](#)
- [237] C. Venter and O. C. de Jager, in *American Institute of Physics Conference Series*, ser. American Institute of Physics Conference Series, F. A. Aharonian, W. Hofmann, & F. Rieger, Ed., vol. 1085, Dec. 2008, p. 277. [148](#)
- [238] W. E. Harris, *AJ*, vol. 112, pp. 1487–+, Oct. 1996. [149](#)

-
- [239] M. M. Reynoso, M. C. Medina, and G. E. Romero, *A&A*, vol. 531, p. A30, Jul. 2011. [150](#)
- [240] A. Charbonnier *et al.*, *MNRAS*, vol. 418, pp. 1526–1556, Dec. 2011. [151](#)
- [241] T. E. Jeltema, J. Kehayias, and S. Profumo, *Phys. Rev. D*, vol. 80, no. 2, p. 023005, Jul. 2009. [156](#), [157](#), [158](#), [164](#)
- [242] P. Blasi, S. Gabici, and G. Brunetti, *Int. J. Mod. Phys.*, vol. A22, p. 681, 2007. [156](#)
- [243] F. Aharonian *et al.*, “(H.E.S.S. Collaboration),” *A&A*, vol. 495, p. 27, 2009. [156](#)
- [244] F. A. Aharonian *et al.*, “(H.E.S.S. Collaboration),” *A&A*, vol. 502, p. 437, 2009. [156](#)
- [245] J. Aleksić *et al.*, “(MAGIC Collaboration),” *ApJ*, vol. 710, p. 634, Feb. 2010. [156](#)
- [246] M. Ackermann *et al.*, “(Fermi-LAT Collaboration),” *J. Cosmology Astropart. Phys.*, vol. 5, p. 25, May 2010. [156](#), [169](#), [170](#), [172](#), [173](#)
- [247] ———, “(Fermi-LAT Collaboration),” *ApJ*, vol. 717, p. L71, Jul. 2010. [156](#)
- [248] V. A. Acciari *et al.*, “(VERITAS Collaboration),” *ApJ*, vol. 679, p. 397, May 2008. [156](#)
- [249] J. Aleksić *et al.*, “(MAGIC Collaboration),” *ApJ*, vol. 723, p. L207, Nov. 2010. [156](#)
- [250] A. A. Abdo *et al.*, “(Fermi-LAT Collaboration),” *Astrophys. J.*, vol. 707, p. 55, 2009. [156](#)
- [251] S. Colafrancesco and P. Blasi, *Astroparticle Physics*, vol. 9, p. 227, Oct. 1998. [157](#)
- [252] D. Ryu, H. Kang, E. Hallman, and T. W. Jones, *ApJ*, vol. 593, p. 599, Aug. 2003. [157](#)
- [253] H. J. Völk, F. A. Aharonian, and D. Breitschwerdt, *Space Sci. Rev.*, vol. 75, p. 279, Jan. 1996. [157](#)
- [254] J. A. Hinton, W. Domainko, and E. C. D. Pope, *MNRAS*, vol. 382, p. 466, Nov. 2007. [157](#)

REFERENCES

- [255] T. H. Reiprich and H. Böhringer, *ApJ*, vol. 567, p. 716, Mar. 2002. [157](#), [158](#)
- [256] M. J. Drinkwater, M. D. Gregg, and M. Colless, *ApJ*, vol. 548, p. L139, Feb. 2001. [159](#)
- [257] A. Pinzke and C. Pfrommer, *MNRAS*, vol. 409, p. 449, Dec. 2010. [164](#)
- [258] C. Pfrommer, T. A. Enßlin, and V. Springel, *MNRAS*, vol. 385, p. 1211, Apr. 2008. [164](#)
- [259] G. Pedalletti, S. Wagner, and W. Benbow, in *International Cosmic Ray Conference*, ser. International Cosmic Ray Conference, vol. 3, 2008, p. 933. [165](#)
- [260] A. Abramowski *et al.*, “(H.E.S.S. Collaboration),” *Astrophys. J.*, vol. 735, p. 12, 2011. [175](#)
- [261] B. Balick and R. L. Brown, *ApJ*, vol. 194, pp. 265–270, Dec. 1974. [180](#)
- [262] K. Ferrière, W. Gillard, and P. Jean, *A&A*, vol. 467, pp. 611–627, May 2007. [180](#), [186](#)
- [263] T. N. LaRosa, N. E. Kassim, T. J. W. Lazio, and S. D. Hyman, *AJ*, vol. 119, pp. 207–240, Jan. 2000. [180](#), [181](#), [182](#)
- [264] A. Goldwurm, in *American Institute of Physics Conference Series*, ser. American Institute of Physics Conference Series, F. A. Aharonian, W. Hofmann, and F. Rieger, Eds., vol. 1085, Dec. 2008, pp. 135–145. [182](#), [183](#), [185](#), [186](#), [195](#), [196](#)
- [265] F. Aharonian *et al.*, *Astron. Astrophys.*, vol. 432, pp. L25–L29, 2005. [182](#), [197](#)
- [266] F. Aharonian *et al.*, *A&A*, vol. 483, pp. 509–517, May 2008. [182](#)
- [267] M. P. Muno *et al.*, *ApJ*, vol. 589, pp. 225–241, May 2003. [182](#)
- [268] F. K. Baganoff *et al.*, *ApJ*, vol. 591, pp. 891–915, Jul. 2003. [182](#)
- [269] M. Sakano, R. S. Warwick, and A. Decourchelle, in *Workshop on Galaxies and Clusters of Galaxies*, Feb. 2003, p. 9. [182](#), [184](#)
- [270] K. Koyama, Y. Hyodo, and T. Inui, *Journal of Physics Conference Series*, vol. 54, pp. 95–102, Dec. 2006. [182](#), [185](#)

-
- [271] M. P. Muno *et al.*, *ApJS*, vol. 181, pp. 110–128, Mar. 2009. [183](#), [184](#)
- [272] ———, *ApJ*, vol. 613, pp. 1179–1201, Oct. 2004. [183](#), [195](#)
- [273] Y. Maeda *et al.*, *ApJ*, vol. 570, pp. 671–687, May 2002. [183](#)
- [274] Q. D. Wang, F. J. Lu, and E. V. Gotthelf, *MNRAS*, vol. 367, pp. 937–944, Apr. 2006. [183](#), [192](#), [193](#)
- [275] H. Murakami, K. Koyama, M. Sakano, M. Tsujimoto, and Y. Maeda, *ApJ*, vol. 534, pp. 283–290, May 2000. [185](#)
- [276] S. G. Ryu, K. Koyama, M. Nobukawa, R. Fukuoka, and T. G. Tsuru, *PASJ*, vol. 61, pp. 751–, Aug. 2009. [185](#)
- [277] G. Bélanger *et al.*, *ApJ*, vol. 636, pp. 275–289, Jan. 2006. [185](#)
- [278] M. G. Revnivtsev *et al.*, *Astronomy Letters*, vol. 30, pp. 382–389, Jun. 2004. [186](#), [187](#)
- [279] T. M. Bania, *ApJ*, vol. 216, pp. 381–403, Sep. 1977. [186](#)
- [280] T. M. Dame, D. Hartmann, and P. Thaddeus, *ApJ*, vol. 547, pp. 792–813, Feb. 2001. [186](#)
- [281] M. Tsuboi, T. Handa, and N. Ukita, *ApJS*, vol. 120, pp. 1–39, Jan. 1999. [187](#), [188](#), [201](#), [213](#)
- [282] F. Yusef-Zadeh, F. Melia, and M. Wardle, *Science*, vol. 287, pp. 85–91, Jan. 2000. [188](#), [189](#), [191](#), [192](#)
- [283] T. Alexander, *Phys. Rep.*, vol. 419, pp. 65–142, Nov. 2005. [190](#)
- [284] T. Paumard, *Journal of Physics Conference Series*, vol. 131, no. 1, p. 012009, Oct. 2008. [190](#)
- [285] F. Aharonian *et al.*, *Astron. Astrophys.*, vol. 425, pp. L13–L17, 2004. [193](#), [197](#)
- [286] J. Albert *et al.*, *Astrophys. J.*, vol. 638, pp. L101–L104, 2006. [193](#), [197](#)
- [287] F. Yusef-Zadeh, D. Choate, and W. Cotton, *ApJ*, vol. 518, pp. L33–L35, Jun. 1999. [194](#)

REFERENCES

- [288] M. J. Reid and A. Brunthaler, *ApJ*, vol. 616, pp. 872–884, Dec. 2004. [194](#)
- [289] W. J. Duschl and H. Lesch, *A&A*, vol. 286, pp. 431–436, Jun. 1994. [194](#)
- [290] F. Melia, S. Liu, and R. Coker, *ApJ*, vol. 545, pp. L117–L120, Dec. 2000. [194](#)
- [291] R. Genzel *et al.*, *Nature*, vol. 425, pp. 934–937, Oct. 2003. [194](#)
- [292] A. M. Ghez *et al.*, *ApJ*, vol. 601, pp. L159–L162, Feb. 2004. [194](#)
- [293] R. Narayan, R. Mahadevan, J. E. Grindlay, R. G. Popham, and C. Gammie, *ApJ*, vol. 492, pp. 554–568, Jan. 1998. [195](#)
- [294] F. Aharonian and A. Neronov, *Astrophys.J.*, vol. 619, pp. 306–313, 2005. [196](#), [198](#), [202](#)
- [295] F. Baganoff, in *APS April Meeting Abstracts*, Apr. 2005, p. 3001. [196](#)
- [296] A. Goldwurm, E. Brion, P. Goldoni, P. Ferrando, F. Daigne, A. Decourchelle, R. S. Warwick, and P. Predehl, *ApJ*, vol. 584, pp. 751–757, Feb. 2003. [196](#)
- [297] F. Aharonian *et al.*, *Astron.Astrophys.*, vol. 503, p. 817, 2009. [196](#), [198](#), [200](#), [204](#), [207](#)
- [298] K. Tsuchiya *et al.*, *Astrophys.J.*, vol. 606, pp. L115–L118, 2004. [197](#)
- [299] K. Kosack *et al.*, *Astrophys.J.*, vol. 608, pp. L97–L100, 2004. [197](#)
- [300] A. A. Abdo *et al.*, *ApJS*, vol. 183, pp. 46–66, Jul. 2009. [197](#)
- [301] S.-M. Liu, F. Melia, V. Petrosian, and M. Fatuzzo, *Astrophys.J.*, vol. 647, pp. 1099–1105, 2006. [198](#)
- [302] E. Wommer, F. Melia, and M. Fatuzzo, *MNRAS*, vol. 387, pp. 987–997, Jul. 2008. [201](#)
- [303] D. Nekrassov, Ph.D. dissertation, Ruperto-Carola Univ. of Heidelberg, Germany, 2010. [212](#), [213](#)
- [304] S. Gabici, F. A. Aharonian, and S. Casanova, *MNRAS*, vol. 396, pp. 1629–1639, Jul. 2009. [217](#)

Abstract

H.E.S.S. (*High Energy Stereoscopic System*) is an array of four identical imaging atmospheric Cherenkov telescopes, designed to observe very high energy γ -rays ($E > 100$ GeV). The observation of such γ -rays plays a crucial role in the understanding of extreme non-thermal phenomena in the Universe. These γ -rays can be used for instance to search for annihilations of dark matter particles in dense environments of the Universe.

This thesis presents a series of data analysis and phenomenological studies on two main subject of the γ -ray astronomy: the indirect searches of dark matter, and the study of the Galactic Center region. The indirect dark matter searches focus on the study of two classes of targets: dwarf galaxies and galaxy clusters. A detailed study of the H.E.S.S. observations towards the Sculptor and Carina dwarf galaxies, and towards the Fornax galaxy cluster are presented. In the absence of a significant signal coming from these object, constraints on the annihilation cross section of dark matter particle candidates are derived. Particular consideration is given to different processes from particle physics and astrophysics which might give rise to additional contributions to the signal expected from a dark matter particle annihilation, such as the *Sommerfeld effect* and *dark matter halo substructures*. The current H.E.S.S. dark matter constraints towards the Sagittarius are updated in light of recent realistic dark matter halo models. A prospect on the sensitivity of the future generation of Cherenkov telescopes, *i.e.* CTA (Cherenkov Telescope Array), for the detection of a dark matter annihilation signal and conventional γ -ray emissions are also given.

The second subject of this thesis provides a detailed analysis of the VHE γ -ray data from the Galactic Center region observed by H.E.S.S. This was possible thanks to the deep exposure of this region, achieved by the H.E.S.S. experiment throughout the 2004-2011 period. The analysis and spectral reconstruction of the central source and the diffuse emission around this region are presented. A spectral subtraction of the diffuse emission contribution to the HESS J1745-290 spectral is performed and allows to recover the intrinsic central source spectrum. The spectral morphology of the diffuse emission region suggests the possibility of various accelerators being responsible for the observed emission.

Keywords : γ -ray astronomy, imaging atmospheric Cherenkov technique, dark matter, dark matter halo, Sommerfeld effect, dwarf galaxies, galaxy clusters, Galactic Center, non-thermal radiation, spectral reconstruction, diffuse emission.

Résumé

H.E.S.S. (*High Energy Stereoscopic System*) est un réseau de quatre imageurs Cherenkov atmosphériques, conçu pour détecter des rayons γ de très haute énergie ($E > 100$ GeV). L'observation de ces rayons γ de très haute énergie joue un rôle essentiel dans la compréhension des phénomènes non-thermiques les plus violents à l'œuvre dans l'Univers. Ils s'avèrent être des sondes très utiles pour la recherche de l'annihilation de particules de matière noire ayant lieu dans des environnements denses de l'Univers.

Cette thèse présente un ensemble de travaux d'analyse de données et phénoménologiques relatifs à deux sujets majeurs de l'astronomie γ : la recherche indirecte de matière noire et l'étude de la région du Centre Galactique. La recherche indirecte de matière noire se concentre sur l'étude de deux classes d'objets privilégiées: les galaxies naines, satellites de la Voie Lactée, et les amas de galaxies. Les études détaillées des observations des galaxies naines Sculptor et Carina, et de l'amas de galaxies Fornax par H.E.S.S. sont présentées. En l'absence de détection des signaux significatifs venant de ces objets, des contraintes sur la section efficace d'annihilation de particules de matière noire ont été calculées. Des considérations particulières ont été données à des différents processus de physique des particules et d'astrophysiques susceptibles d'apporter des contributions supplémentaires au signal de matière noire attendu, comme par exemple *l'effet Sommerfeld* et les *sous-structures des halos de matière noire*. D'autre part, les contraintes H.E.S.S. en direction de la galaxie naine Sagittarius sont mises à jour en lumière des profils de halos de matière noire les plus réalistes à l'heure actuelle. Le potentiel de la future génération de télescopes Cherenkov au sol, CTA (*Cherenkov Telescope Array*), à la détection d'un signal d'annihilation de matière noire et des signaux astrophysiques standards est aussi défini.

Le deuxième thème de cette thèse est consacré à l'étude détaillée de la région du Centre Galactique observée par H.E.S.S., grâce à la profonde exposition en temps sur cette région, obtenue dans la période entre 2004 et 2011. L'analyse et la reconstruction spectrale de la source centrale et de l'émission diffuse dans cette région sont présentées. La soustraction de la contamination spectrale de l'émission diffuse dans le spectre de HESS J1745-290 permet de retrouver le spectre intrinsèque de la source centrale. L'analyse de la morphologie spectrale de la région d'émission diffuse suggère finalement que plusieurs accélérateurs peuvent être à l'origine de cette émission.

Mots-clés : astronomie γ , technique d'imagerie Cherenkov atmosphérique, matière noire, halo de matière noire, effet Sommerfeld, galaxies naines, amas de galaxies, Centre Galactique, radiation non-thermique, reconstruction spectrale, émission diffuse.